UNIVERSITY OF OXFORD

DEPARTMENT OF ENGINEERING SCIENCE

Liquid Crystal Technologies for Enhanced Optical System Functionality

Yihan JIN

Lady Margaret Hall

A thesis submitted for the degree of

Doctor of Philosophy

in the

Department of Engineering Science

October 2, 2023

Abstract

Liquid Crystal Technologies for Enhanced Optical System Functionality

Yihan JIN

This thesis aims to investigate and develop novel liquid crystal (LC) technologies that can either manipulate the optical wavefront (phase) of light in a controlled way or improve the imaging quality by reducing the appearance of laser speckle by manipulating the optical wavefront in a pseudo-random way. Control of these properties is of great importance for a vast range of photonics and optics applications; for example, in LC spatial light modulators (LC-SLMs), near-eye displays, laser projectors and bio-medical microscopes. Among these applications, laser sources have been an indispensable element in modern imaging applications. This is because they exhibit many essential features (e.g., a high intensity, a narrow spectral linewidth, and directionality). However, due to the high coherence of laser light, the issue of speckle arises, which can badly plague the clarity and the appearance of an image. The essential reason for such degradation is because the coherent laser light will scatter when it interacts with an optically rough surface and forms constructive or destructive interference on the imaging plane.

To combat the formation of speckle and improve the performance of a laser-based imaging system, one approach is to generate as many decorrelated speckle patterns as possible within a short period of time. Existing methods for reducing speckle typically suffer from being either bulky, consisting of motors that introduce vibration to the system, or they do not provide an acceptable degree of speckle suppression. A key part of the research presented in this thesis aims to develop LC diffusers that can reduce the appearance of speckle in a range of different display and imaging applications, including laser projector, laser microscopy, head-up display, holography and polarimetry. The technique involves using highly twisted (helicoidal) liquid crystalline mesophases, doped with various dopants in the form of redox and zwitterionic dopants, to act as tuneable volume scatterers. The recipe for the optimum performance is BL006 + 3 wt.% R5011 + 0.5 wt.% Reichardt's dye (zwitterion dopant) filled into a 40 μm anti-parallel cell. Not only does this approach provide direct control of the speckle contrast (C), allowing it to be reduced to very low levels, $C = 0.07$ (93% reduction of the speckle noise), but it does so without the need for bulky mechanical parts, moving components or expensive optical elements.

Another important optical element that this thesis investigates are potential configurations for next-generation LC-SLMs. LC-SLMs are a key element in both imaging and optical wireless communication systems. In general, an LC-SLM can be used to control and shape the wavefront of light propagating in an optical system and hence control the structure of optical illumination,

by adjusting the voltage applied to the active LC layer. Among all wavefront correction applications, the phase-only mode is found to be the most promising for applications such as augmented reality near-eye displays and free-space optical beam-steering. The research presented in the latter part of the thesis explores new configurations, such as the nematic Pi-cell, nematic Fréedericksz cell, uniform lying helix chiral flexoelectro-optic LC device, and hybrid aligned nematic cell, that improve the switching speed of an SLM, but also maintain analogue control of the phase (from 0 to 2π) at room temperature via controlled modulation of the optical wavefront. Simulations that take into account factors such as the thickness of the boundary layer, the back-flow effect in the context of the LC hydrodynamic behaviour, and dielectric coupling in a flexoelectro-optic material are examined. These simulations play a crucial role in guiding the optimisation of the device configuration. The development of an analogue, fast-switching phase modulator would enable SLM technology to be used in a wider range of applications.

Acknowledgements

There are no demonstrative words in the English language that can exactly and adequately express my deep and sincere gratitude, worship and affection to my fabulous supervisors Professors Stephen Morris and Steve Elston. For the very first time since I was born to live and study in a totally different country, and get used to a brand new culture, their immense help and guidance were like beacons in the vast sea, for the lost ship direction. It has been the luckiest thing in my life that I decided to come to Oxford and have Steves as my supervisors, and my friends in life.

I would like to thank Steve M for his endless help and support since the start of my D.Phil study. The whole story began with the interview on that winter night. Your tremendous supports encourage me to keep going from the DPhil application to the DPhil thesis writing. I had never thought about I could have pursued a DPhil. It was you who helped me to transfer from a MRes to a DPhil. I am truly grateful for you managing the group and dealing with my capricious requests, big or small. The SMP group cannot grow to the present scale without your effort and perfect management. Obviously, people can't cook them unless they have them, for our group, we can't realise those 'whimsical' ideas, try out various recipes or have opportunities to travel abroad for international conferences and networking with other talented researchers without your support. It is hard to find a word in English to describe how difficult it is to have two roles, a gifted manager and a splendid academic supervisor, at the same time, but you really make it possible and take care of every single student conscientiously.

Thank you Steve E, for your valuable advice and endless patience when I was suffering from the most difficult time in my life. Your humour and intelligence dragged me out of the shadow and built my confidence without which

I could not proceed to the next. Not to mention your tremendous teaching and guidance in my research. I can still remember and will never forget those mornings and nights when you gave up your sleeping time, coming to the lab, giving tutorials and guiding in person. I have learnt a lot from this hands-on education and I grew fast because of that. You treat everyone in this group as your own child and consider our career paths as your own career seriously. I have always been telling my parents, and my colleagues, that if I could be a teacher, a scholar one day, you would be my role model in my entire career. Thanks again Steve, I will always remember the tea and chat we had at Gail's, the music recommendation, and the life motto.

I would also like to thank my first mentee, Nathan. This is my first time taking the responsibility of supervising a 4YP student. Thank you for your tolerance and gentleness which are the good in you that I lack of. The questions you raised and the discussion we had were inspiring and deep-going. I feel lucky that I can have you as my mentee in my last year. The work we did together will always be the highlight of my DPhil.

To Peng, it is my huge pleasure to work with you in my second and third years. Your astounding experience and assistance opened my eyes to not only the research but also the world around me. You are not only a responsible postdoc but also a great career development mentor to me. It is my honour to be able to work with you and I wish I could work with you even longer. And to Yunuen, thank you for the punting and supporting the group social when it was my turn. Your talk was really helpful and I will always remember it.

I would also like to thank you to all the members of the Soft Matter Photonics group, particularly to David, Taimoor and John. You are the first three senior group members I met since I arrived and thank you for helping me join the

group smoothly and start the project step by step. To Julian, I could not commence the phase modulator projects without your generous material supply. To Jia-De, you are my first Taiwanese friend and I still miss your incredible warmth and kindness. To Waqas, thank you for the company and encouragement throughout the pandemic. Since the old generation left, you were like my elder brother. Those lunches and strolls in Port Meadow really relieved my stress. To the new blood joining the group, Zipei you are the smartest student I have ever met in Oxford. Your sensitiveness and wisdom made you thoughtful. To Linpei, Bohan, Xuke, Mengmeng, Guanxiong and Zimo I am really happy to have you as my team-mates. Those drinks, chats, trips to Finland and working out in the gym really vitalized my DPhil life. Thank you for being such supportive colleagues over the past two years. And I would also like to thank Camron, Bradley, and Andrew you guys are awesome!

I would extend my sincere thanks to the members of the Dynamic Optics and Photonics Group. Special gratitude goes to my examiner Martin, whose guidance and presence throughout my D.Phil journey have been invaluable. Chao, your knowledge, explanations, and guidance were greatly appreciated. Patrick, your intelligence, kindness, humour, and smile have made my time here memorable. Thank you for your support and the stimulating environment.

Last but not least, I would like to express my heartfelt gratitude to my examiner, Steve Sheard. Your insightful questions, valuable suggestions, and timely assistance throughout my entire D.Phil. journey have been truly invaluable. I consider myself incredibly fortunate and blessed to have had such a supportive professor as my examiner from the very beginning of my

investigative journey at Oxford.

Outside the group, I am so lucky to have many of you as my best friends: Dinglan, Xuanxiao, Daohe, Xinpei and Shaoyu. You guys made up the most highlight three years in my life and I never stop thanking god that I could meet and make friends with you! Though Dinglan abandoned me and went to America for a postdoc, I am really proud of you and wish we could play Catan again!

Finally, this trip, this adventure could never be possible without my incredible family. Your infinite support and help form the strong foundations of my DPhil. Thank you, Xinyi, thank you for coming into my life. The memory I have of being with you is so valuable. I love you all so much and I dedicate this thesis to you all.

Publications

Primary Research Contributions

Jin, Y., Spiller, N.P., He, C., Booth, M.J., Elston, S.J., and Morris, S.M., 2023. Zwitterion-doped liquid crystal speckle reducers for immersive displays and vectorial imaging. *Light: Science & Applications*, 12(1), p.242.

Jin, Y., Zhao, Z., Elston, S.J., and Morris, S.M., 2023. Optical Phase Modulation of Fast-Switching Flexoelectro-optic Liquid Crystal Devices. *(in submission)*.

Jin, Y., Elston, S.J., Fells, J.A., Chen, B., Li, M., Kamal, W., Zhao, Z. and Morris, S.M., 2022. Backflow-assisted time-resolved phase modulation in nematic liquid crystal Pi-Cells. *Optics & Laser Technology*, 156, p.108596.

Jin, Y., Hansford, D.J., Elston, S.J. and Morris, S.M., 2021. Laser Speckle Reduction Using a Liquid Crystal Diffuser Enhanced with Redox Dopants. *Advanced Photonics Research*, 2(6), p.2000184.

Hansford, D.J., **Jin, Y.**, Elston, S.J. and Morris, S.M., 2021. Enhancing laser speckle reduction by decreasing the pitch of a chiral nematic liquid crystal diffuser. *Scientific reports*, 11(1), pp.1-12.

Jin, Y., Elston, S.J., Fells, J.A., Booth, M.J., Welch, C., Mehl, G.H. and Morris, S.M., 2020. Millisecond optical phase modulation using multipass configurations with liquid-crystal devices. *Physical Review Applied*, 14(2), p.024007.

Collaborative Contributions

Xue, L., **Jin, Y.**, Elston, S.J., 2023. Fast Analogue 2π Phase Modulation using a Liquid Crystal Pi-Cell. *Optics & Laser Technology*, 167, p.109773.

Fells, J.A., Salter, P.S., Welch, C., **Jin, Y.**, Wilkinson, T.D., Booth, M.J., Mehl, G.H., Elston, S.J. and Morris, S.M., 2022. Dynamic phase measurement of fast liquid crystal phase modulators. *Optics Express*, 30(14), pp.24788-24803.

He, C., Chang, J., Salter, P.S., Shen, Y., Dai, B., Li, P., **Jin, Y.**, Thodika, S.C., Li, M., Tariq, A. and Wang, J., 2022. Revealing complex optical phenomena through vectorial metrics. *Advanced Photonics*, 4(2), p.026001.

Kamal, W., Li, M., Lin, J.D., Parry, E., **Jin, Y.**, Elston, S.J., Castrejón-Pita, A.A. and Morris, S.M., 2022. Spatially Patterned Polymer Dispersed Liquid Crystals for Image-Integrated Smart Windows. *Advanced Optical Materials*, 10(3), p.2101748.

Conference Presentations

SPIE Photonics West

San Francisco-Feb 2023 (Presentation)

"Liquid crystal speckle reducers for head-up displays and polarization imaging "

University of Oxford Photonics Day

Oxford-Sep 2022 (Poster)

"Tunable Liquid Crystal Optical Phase Modulators for Fast Photonics Technologies "

University of Oxford Department of Engineering Science Researchers Conference

Oxford-June 2022 (Poster)

"Full Range Tunable Liquid Crystal Phase Modulators for Fast Optical Switching"

28th International Liquid Crystal Conference (ILCC)

Lisbon-July 2020 (Oral Presentation) *(Accepted but cancelled due to COVID-19 pandemic)*

"Laser speckle reduction using a liquid crystal diffuser"

Awards

Anwyl Burton Graduate Bursary 2021

Return to Research Grant, Rank Prize 2021

Ethel Ginsburg Graduate Bursary 2020

Contents

List of Figures

Chapter 1

Introduction

1.1 Overview

This DPhil thesis describes work aiming to bring new and enhanced optical system functionality to next-generation photonics technologies through the development and application of liquid crystal (LC) devices. Specifically, the thesis investigates the use of dynamic scattering for laser speckle reduction and fast-switching phase modulation for spatial light modulators (SLMs).

Both laser speckle reduction and optical phase modulation are of significant importance for a wide-range of 21st-century technologies including virtual reality (VR) and augmented reality (AR) displays [1, 2], holography [3–5], head-up displays (HUD) [6–8], pico laser projectors [9, 10], laser microscopy [9], high-power laser fabrication techniques [11, 12], free space communications [3, 10], optical switching and beam steering [13, 14]. Fundamentally, this thesis considers techniques and approaches that enable the optical wavefront (phase) to be manipulated in either a pseudo-random way or a controlled way.

Control of the optical phase properties of light in a random way is of great importance in improving the imaging quality of laser imaging systems

by reducing the appearance of laser speckle, which has plagued laser-based imaging systems since the invention of the laser. Today, lasers are of importance for a broad range of technologies and industries including cinema projectors and medical endoscopes, to name but a few. However, despite their numerous advantages (e.g., spectral purity, directionality etc) they are often fundamentally limited by the appearance of the granular noise (known as speckle) superimposed on the image that is being formed. The issue of speckle arises from the high-coherence of laser light which can badly degrade the appearance of an image. As an example, when light interacts with an optically rough surface, constructive and destructive interference occur which results in an intensity interference pattern that is overlaid on an image [15]. This combination of constructive and destructive interference results in the formation of bright and dark spots that corrupt the appearance of the image.

Historically, methods that have been developed to reduce speckle have relied on the superposition of multiple uncorrelated speckle patterns [15]. Such methods are based on the theory that when two or more statistically independent (or partially decorrelated) speckle patterns are superimposed, the random intensity fluctuations will be 'averaged out' across the image. Developing methods with which to reduce the appearance of speckle in a range of imaging and display applications using LC devices forms the first half of the thesis.

Liquid crystalline materials, which are well known for forming a mesophase between the crystalline solid and isotropic liquid phases, are known to have substantial optical and electrical anisotropies such that the refractive indices along different directions are different and can be changed by altering the orientation of the director (the average pointing direction of the LC molecules). Furthermore, the ability to reorient the director when applying external stimuli has made LCs of significant interest for generating

uncorrelated speckle patterns [16]. In this thesis, chiral nematic LCs doped with additional ionic species are used in order to excite a phenomenon called electrohydrodynamic instabilities (EHDI). The turbulent behaviour of the LC director results in a dynamic scattering mode that causes a phase and polarisation variation to the laser light and as a result, breaks up the coherence of the light.

The second part of the thesis focuses on the development of LC electro-optic modes that enable the fast modulation of the optical phase of light. Rapid analogue control of the optical phase of light is particularly important for new SLM technologies that are targeted for use in applications such as optical communications as well as light detection and ranging (LiDAR). The objective is to develop active elements that control the shape of the overall wavefront and the resulting polarisation properties.

Traditional methods of phase modulation are usually divided into two categories. Specifically, the optical phase can be changed either by changing the refractive index (or effective refractive index) of a material through which light is propagating or by physically changing the optical path-length for the incident light. In integrated optics technology, such as in the Mach-Zehnder interferometer, very high modulation speeds can be obtained, and LCs are not generally suitable materials in these applications. However, if a spatially structured phase modulation of a propagating optical wave-front is required (e.g., using an SLM) then LCs are highly desirable.

SLM technologies can be broken down into two principal categories: one that provides a digital, binary, or quantised phase modulation (0 and π phase states are commonly chosen) and one that provides analogue phase modulation (a phase range of 0 to 2π is commonly used). Binary SLMs can

achieve switching times substantially less than 1 ms. Analogue SLM technology on the other hand has longer switching times, generally being many milliseconds, with the very best (and most expensive) technology having a switching time that is still greater than 1 ms. There are alternatives to LC-based SLMs, using electro-mechanical technology, but these are generally either slow, bulky, or lacking in spatial resolution (i.e., have a small pixel density). Thus, the ultimate goal is to fabricate a device that can demonstrate analogue phase modulation as well as achieve sub-millisecond switching times.

While the development of the two technologies in this thesis may seem somewhat distinct (i.e., speckle reducers and phase modulators) there are areas where there is significant overlap. For example, it is shown how chiral nematic LCs can be used for speckle reduction (through the use of EHDI) and fast phase modulation (through the use of the flexoelectro-optic effect). In the former case, EHDI leads to dynamic scattering of the light whereas for the optical phase modulation flexoelectric coupling leads to a fast modulation of the optic axis of the LC. When an electric field is applied, the LC director can rotate to align either parallel or perpendicular to the electric field due to dielectric coupling. Additionally, because of the asymmetry of the molecular shape, an LC can couple to an electric field through flexoelectricity, which can result in a fast modulation of the optic axis in chiral nematic LCs. A number of different LC mixture compositions and phases are considered in this thesis as well as different device configurations. Where possible, these devices are demonstrated in optical systems to evaluate their performance and new measurement systems are developed to characterise the behaviour of the LC devices.

1.2 Layout of Thesis

The next chapter (Chapter 2) will provide the relevant theory and background on LC materials and electro-optic effects, phase modulators, and speckle phenomena so that the results in the following chapters can be explained.

Chapter 3 will detail the experimental methods used in this thesis including the LC alignment techniques, LC device assembly, and device characterisation. The purpose of the chapter is to explain in detail the experimental techniques that have been employed to obtain the results presented in this thesis. The relevant terminology and methods used throughout will first be introduced in this chapter.

Chapter 4 then describes the development of LC speckle reducers using two different redox dopants and considers how the reduction in the laser speckle is related to the concentration of the dopants. The chapter also demonstrates the improvement of the quality of an image generated using a modified commercial projector fitted with a monochromatic laser source and in a microscopic imaging scenario as well. The work presented in this chapter has been presented in two separate publications: *Advanced Photonics Research*, 2(6), p.2000184 (2021) [17].

Following on from Chapter 4, Chapter 5 further explores another type of additive that can elevate the LC speckle reducer performance. In this work, a novel dopant, a zwitterionic dopant, is applied to LC speckle reducers and the rest of the chapter investigates how the device performance depends upon a range of material and environmental parameters including the pitch of the chiral nematic LC helical structure, the concentration of dopants, and the temperature. The extraordinary performance of the LC speckle reducer is then demonstrated in five different display and imaging scenarios.

The subsequent chapters are on the development of LC devices for sub-millisecond analogue phase modulation. Chapter 6 reviews the current state-of-the-art of LC-SLMs and gives a more detailed introduction to the fundamental theory of optical phase manipulation. The chapter then presents two different configurations for analogue 0 to 2π optical phase modulation using LCs, each of which achieves switching times that are 1 ms or less. Both configurations exploit a multipass optical arrangement to enhance the available optical phase range while maintaining a fast-switching speed at room temperature. The work presented in this chapter has been published in *Physical Review Applied*, 14(2), p.024007 (2020) [18].

Chapter 7 further discusses results related to advanced phase modulator techniques, but also introduces an experimental method to extract the time-resolved phase modulation of three different nematic LC devices: pi-cell (parallel-rubbed alignment layers), Freedericskz cell (anti-parallel rubbed alignment layers), and a hybrid aligned nematic (HAN) device. Results are shown to be in good agreement with simulations of the phase modulation for the three nematic devices when backflow is taken into consideration. The work presented in this chapter has been published in *Optics & Laser Technology*, 156, p.108596 (2022) [19].

The last research chapter, Chapter 8, considers how the phase modulation depth of a flexoelectro-optic phase modulator can be improved. It is shown through careful design of the device configuration, that full 2π analogue phase modulation can be achieved even when the tilt of the optic axis is less than ideal (i.e., less than 45°). Modelling is employed to determine the phase shift for the chiral nematic LC and the experimental results are shown to be in good agreement with the results from simulations.

Finally, Chapter 9 serves as a conclusion and discussion for all of the

work presented in the previous chapters. This chapter will summarise the research that has been presented in this thesis and plot a route forward for future work.

Chapter 2

Background

2.1 Introduction to Liquid Crystals

As suggested by its name, liquid crystal (LC) is a unique phase that is more ordered than molecules in liquids but less ordered than crystalline solids [20]. The molecules inside such materials have a tendency to point in one direction and may also show positional order [20]. The different degrees of order, and combinations thereof, result in the formation of different LC phases [20]. The simplest LC phase, in terms of the order, is one where all the molecular axes statistically point in the same direction throughout the whole sample and this is called the nematic phase. In order to measure the orientational distribution of the sample, this preferred direction is denoted by the unit vector $\vec{n}$ and is called the director. Such a phase is illustrated in Figure 2.1.

Another well-known LC phase that is considered in this thesis is the chiral nematic phase (often referred by the alternative name of cholesteric phase) and is presented in Figure 2.2(a). The chiral nematic phase and nematic phase are similar in that molecules exhibit orientational order but no positional order. Yet, the significant difference between these two phases is that the director of a chiral nematic LC rotates about a helix axis which is perpendicular to the director [20]. The distance over which the director rotates

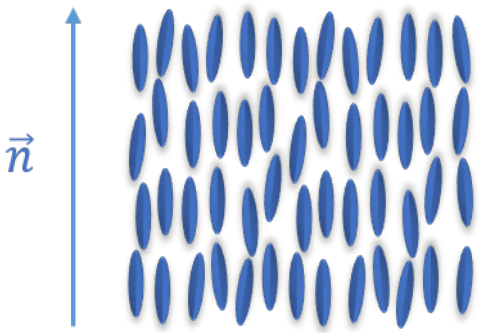

FIGURE 2.1: Molecules in a nematic phase. The average orientation of the molecules is given by the director $\vec{n}$.

a full 2π is called the pitch (P) as can be seen in Figure 2.2(b). The pitch of a chiral nematic changes with chemical composition, temperature and external stimuli such as electric field. It is common to mix chiral dopants with nematic LCs to make chiral nematic LCs with a certain pitch [21].

(a) (b)

FIGURE 2.2: Molecules in a chiral nematic LC (cholesteric) phase. (a) shows the macroscopic configuration of the director of a chiral nematic LC phase. The orientations of the specific molecules are given by the director $\vec{n}$. The grey dashed line in (a) and (b) represents the helical axis of the chiral structure. (b) illustrates half of the pitch within which the director gradually rotates from 0 to π.

Additionally, as a result of the molecular structure, for the different LC phases, they all share a common interesting physical property: anisotropy. This anisotropy appears in various physical parameters, including elastic modulus, conductivity, flexoelectric constant, dielectric constant, and refractive index. Anisotropy in parameters such as the refractive indices and the dielectric permittivities is what makes these materials particularly interesting for optoelectronic engineering.

2.1.1 Nematic Phase

The LC molecules discussed in this subsection and in the rest of the thesis are referred to as calamitic, meaning rod-like, which is the most common type of LC used in technologies such as flat panel displays [22]. This type of molecule is the most common molecule that can form the nematic phase (N). These rod-shaped compounds have one molecular axis that is significantly longer than the other two (the other two are typically about the same length). A typical calamitic LC molecule, 4-Cyano-4'-pentylbiphenyl (5CB), looks like the rod shaped object in Figure 2.3. Different calamitic LCs can be synthesised via different schemes, with various aromatic units and functional groups. However, as the molecules have a rather rigid length along a certain direction, and share the same ellipsoid shape, they can all be represented by the simplest and most classical calamitic LC shape.

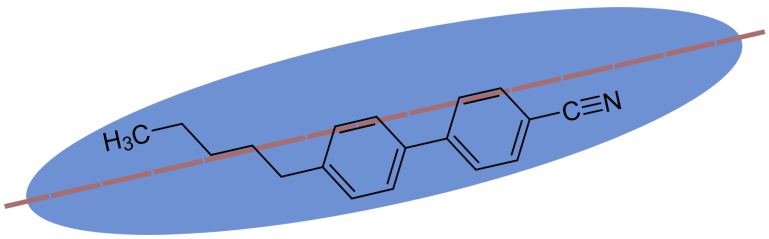

FIGURE 2.3: An example of a calamitic LC molecule. The figure depicts the chemical structure and shape of a typical calamitic LC molecule, 5CB. The rigid longer axis is highlighted by the red dashed line

The nematic phase is characterized by having orientational order but no positional order. It is thermodynamically stable within a temperature range between an isotropic liquid phase and a crystalline solid phase. LCs with such a phase are fluid and possess an ordered structure as depicted in Figure 2.1. To describe such a phase, we can ignore individual molecular motions and instead adopt a set of macroscopic parameters. It is historically common to use a macroscopic theory rather than considering the LC on an

atomistic level to describe the properties of different phases. The continuum theory for nematic LCs was developed by Sir Charles Frank in the 1950s [23], based on the pioneering contributions of Oseen and Zocher in 1933 [24]. By adopting the director $\vec{n}$, which is a unit vector oriented parallel to the average axis of the molecules in a local region, or alternatively, the time averaged axis of a single molecule, we can describe the amount and direction of orientational order. This is the key thing that needs to be considered for the nematic phase because the molecules in such a phase are free to flow relative to each other and show no positional order as emphasized previously. Here, the macroscopic order parameter, S, is defined in order to characterize the variance of the orientations of individual molecules with respect to the overall-averaged director. For a uniaxial nematic, S can be determined from the second Legendre polynomial [25],

$$S = \left\langle \frac{3}{2}\cos^2\theta - \frac{1}{2} \right\rangle \tag{2.1}$$

where θ is the angle of a molecule with respect to the local director $\vec{n}$. When all the molecules are aligned without deviation from the director, $S = 1$, whilst $S = 0$ for the isotropic case. For nematic LCs, S is between 0 and 1, and usually has an S between 0.3 and 0.8 [26], and varies with the molecular constitution and temperature. The order parameter S decreases with increasing temperature and abruptly drops to 0 when the temperature reaches the clearing point, T_c, the transition from the nematic phase to the isotropic phase.

2.1.2 Chiral Nematic Phase

There is another LC phase that is investigated in this thesis which is the chiral nematic phase (N*), also called the cholesteric phase as it was first observed in cholesterol derivatives. The director of a chiral nematic LC rotates about a

helix axis which is perpendicular to the director (as shown in Figure 2.2(a)). The other unique property of the chiral nematic phase is its pitch over which the director rotates a full 2π. However, this is not to say that in practice that the properties of the structure are considered over the whole pitch. In fact, because of the symmetry of the rod-shaped nematic molecules, $\vec{n}$ and -$\vec{n}$ are equivalent. Thus when we talk about the periodicity of a chiral nematic LC system, it should often be half of the pitch. In practical use, a certain pitch for a specified chiral nematic LC material is achieved by mixing nematic LCs and chiral dopants in different concentrations by weight. It is not obligatory that the dopant has to be liquid crystalline. Different chiral dopants have different helical twisting powers. The dopant can generate a chiral environment for any achiral molecules in the mixture, causing a slight asymmetry of the orientation of the molecules and as a result a gradual helical macrostructure is formed.

The intrinsic difference between the nematic phase and the chiral nematic phase in terms of periodic structure and enantiomorphism makes the chiral nematic phase particularly interesting. The helix can be either right-handed or left-handed, and the pitch can be much smaller, around the same order or much greater than the wavelength of the light propagating through the chiral nematic LC material. Chiral nematic LCs exhibit the following optical properties:

- circular birefringence: a chiral nematic LC is not linearly birefringent for light propagating along the helical axis but shows different retardation for different handedness of circularly polarised light;
- optical activity: also known as optical rotation which is a result of circular birefringence that the orientation of the incident linear polarised light has either a clockwise or anti-clockwise rotation;

- selective reflection: a phenomenon that is much like constructive interference of X-rays that the periodic structure of the chiral nematic LC phase causes a band of wavelengths to be reflected;

- waveguide regime: when the pitch is much longer than the wavelength of the incident light, the incident light sees each 'slice' of chiral nematic LC as a nematic LC, and the polarisation of the light simply follows the rotation of the director when propagating along the helical axis.

2.2 Elastic Energy and Continuum Theory for LCs

The LC molecules tend to have a preferred and uniform director field, therefore any state other than the equilibrium state for a LC is disfavoured and will increase the internal energy of the system. Distortions in the director field lead to elastic energy, the value of which depends on the type of distortion and the properties of the LC. The effect of elastic energy is important when there is an external stimulus applied to the LCs molecules, e.g., an electric field. The molecules will tend to rotate with the electric field because of dielectric coupling, but the elastic energy works to negate the reorientation.

It is common to use a macroscopic continuum model to simulate the behaviour of LCs when the director reorients from the equilibrium state to a deformation state or vice versa. Continuum theory treats the material as a continuum: rather than considering discrete molecules the macroscopic averages are assumed to be continuous within the material. Continuum theory has been widely used for LCs and is mainly derived from the work of Oseen [27, 28] and Zocher [24, 29] originally and the general phase classifications of LCs expressed by Friedel [30]. Later, Frank [23] further formulated the direct energy function needed for the continuum theory in 1958 and this led to Ericksen's work in developing a theory for nematic LCs which is a result

of the balance laws for dynamical behaviour [31]. Following this, Leslie [32, 33] made the last step to the formulation of the constitutive equations for a dynamic theory for nematic LCs.

As introduced previously in Section 2.1.1, the continuum theory employs the director $\vec{n}$ to portray an ensemble of molecules. Frank utilized that notation and defined the three types of distortion in LCs which are splay, twist and bend. When one end of a bulk of molecules is pulled away from adjacent molecules, while the other end of the bulk of molecules is pressed close to each other, a splay distortion will be generated. When a torque produces a rotation in the director through an ensemble of molecules, a twist distortion will be present. Twist distortion exists naturally in chiral nematic LCs. Bend distortion is parallel to the director and molecular axis. To illustrate these three types of distortion, diagrams of each distortion are shown in Figure 2.4.

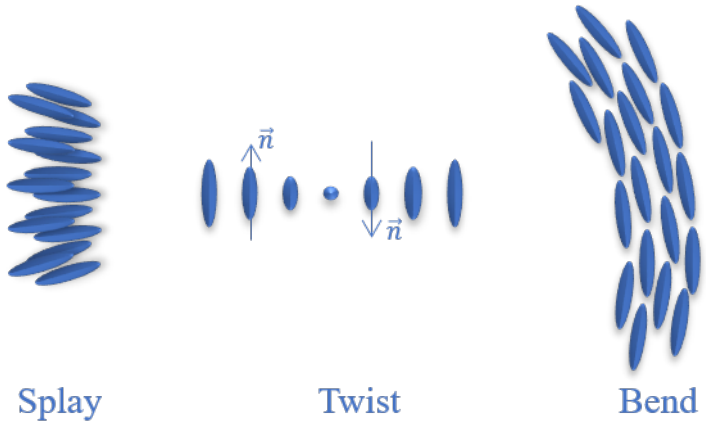

FIGURE 2.4: The three types of distortion developed by Frank: splay, twist, and bend.

With these premises, the elastic energy formulated by Frank can be comprehended. The Frank elastic energy equation is a function of the director $\vec{n}$ and gradients of $\vec{n}$. In the equation, the splay distortion is associated with $\nabla \cdot \vec{n}$, the twist deformation is related to $\vec{n} \cdot (\nabla \times \vec{n})$, and the bending

of the director is described as $\vec{n} \times (\nabla \times \vec{n})$. The description of these three distortions leads to the Frank-Oseen elastic free-energy density [23, 28],

$$\begin{aligned} f_{elastic}(\vec{n}) &= f_{splay}(\vec{n}) + f_{twist}(\vec{n}) + f_{bend}(\vec{n}) \\ &= \frac{1}{2}K_{11}[\nabla \cdot \vec{n}]^2 + \frac{1}{2}K_{22}[\vec{n} \cdot (\nabla \times \vec{n}) + q_0]^2 + \frac{1}{2}K_{33}[\vec{n} \times (\nabla \times \vec{n})]^2 \end{aligned} \tag{2.2}$$

The K_{11}, K_{22}, K_{33} are splay, twist and bend coefficients, respectively, and the unit of these constants are Newtons or Joules/metre. These three parameters are specific to each LC material, are temperature dependent and are called the Frank elastic constants. Usually, these constant are about 10^{-11} Joule/metre and K_{33} is around two or three times larger than K_{11} and K_{22}. The constant q_0 is the natural twist of the material which is nonzero only in chiral nematics and is equal to $\frac{2\pi}{P}$ where P is the helical pitch of the LC. This equation allows a relatively simple calculation of the free-energy per unit volume of a N phase and N* phase. Together with the illustration of the director for different types of deformation in Figure 2.4, the meaning of each term in Equation 2.2 is reasonable. For the splay distortion, the configuration is exactly what a divergence describes. Imagining there is a point source and the director radially points outwards from that source, this is exactly what a splay looks like in LCs. The director forms a vector field and the divergence of this vector field represents the degree of the splay distortion. For twist and bend, they can be described by the curl of the director. The difference is that for twist the direction of curl ($\vec{n}$) is parallel to the director $\vec{n}$, while, it is perpendicular to $\vec{n}$ for a bend deformation.

2.3 Liquid Crystals in Electric Fields

For an ideal N or N* non-conductive LC phase, an external electric field triggers at least two different reactions: 1) the dielectric anisotropy along the different directions of molecules, and 2) the flexoelectric effect, which is small in common rod-shaped calamitic LCs but has a significant impact on deformation of pear-shaped or banana-shaped LCs. This section will discuss these two different electric field effects in detail and introduce parameters that will be repeatedly mentioned in the following chapters.

2.3.1 Dielectric Coupling in Nematic LCs

To understand the dielectric coupling, an introduction to dielectric permittivity and dielectric anisotropy of LCs is necessary. Each axis of a LC molecule has a specific component of permittivity, and for an ideal uniaxial nematic LC molecule, the dielectric permittivities along the two short axes are the same but the one along the longest axis is different from the other two. The dielectric constant or dielectric permittivity is written as $\varepsilon_{\perp}$ measured perpendicular to the director and $\varepsilon_{\parallel}$ measured parallel to the director. The dielectric permittivity is then defined as $\Delta\varepsilon = \varepsilon_{\parallel} - \varepsilon_{\perp}$. The different permittivity along different directions occurs as a result of electric field induced dipoles, owing to the polarisability of a molecule, and/or the natural permanent dipole because of the chemical structure and molecule shape.

In practice, in order to realize a large dielectric anisotropy, a key way is to attach a strong polar group to one end of the molecule, such as the $-C \equiv N$ group in a 5CB molecule [34–36]. Also, the applied electric field, $\vec{E}$, will rearrange the free charges of the phenyl rings [36] and this contributes to the electrically induced dipole. Therefore, there are two contributions to the dielectric permittivity, one is through induced dipole moments

in the molecules by applying external fields, and the other one is through re-orientations of the permanent dipole moments of molecules, which can be strong in a LC system. In the 5CB case, the LC molecules carry a rather strong permanent dipole moment along (or nearly parallel to) the director so that the electric field can introduce stronger polarisation in this direction compared with the other two, thus it has positive dielectric anisotropy. The presence of the permanent dipole dominates over the induced dipole moment for 5CB-like molecules and usually such LCs have a rather large $\Delta\varepsilon \approx 12$ [36].

Alternatively, if there is a specific polar group that makes the permanent dipole moment somewhat normal to the director, for example, the N–O groups in (para-Azoxyanisole) PAA LC molecules, then the resulting $\Delta\varepsilon$ becomes negative. Such materials usually possess quite small $\Delta\varepsilon \approx -0.2$.

With an understanding of the origin of dielectric anisotropy, then we can consider how nematic and chiral nematic LCs behave in an electric field. We can consider this from a free-energy perspective. The overall dipole moment density is denoted as $\vec{P}$ (polarisation of molecules), and it is in the same direction as the average molecular dipole moment (pointing from the negative charge to the positive charge). For isotropic materials under a small electric field, the direction of $\vec{P}$ and the external $\vec{E}$ are parallel, and they are linearly proportional, which can be written as

$$\vec{P} = \varepsilon_0 \chi_e \vec{E} \tag{2.3}$$

where the ε_0 represents the free space permittivity 8.85×10^{-12} $\mathrm{C^2/Nm^2}$. χ_e is termed the electric susceptibility of a dielectric material, which is a measurement of how easily polarisation can be induced by an electric field. It is a dimensionless quantity.

However, for materials with a dielectric anisotropy, such as LCs, the induced molecular polarisation in response to an electric field is different when the relative direction between the $\vec{E}$ and the director is different. If we consider a LC molecule with a fixed direction, say along the z-axis, and there is an angle between the direction of $\vec{E}$ and the director, then due to the anisotropic property, the induced polarisation (electric susceptibility), along the three dimensions are not all equal. Decomposing the $\vec{E}$ along the x, y, z-axis, the polarisations it produces can be given by

$$\begin{aligned} P_x &= \varepsilon_0 \chi_\perp E_x \\ P_y &= \varepsilon_0 \chi_\perp E_y \\ P_z &= \varepsilon_0 \chi_\parallel E_z \end{aligned} \tag{2.4}$$

The three equations can be formulated into one tensor for the electric susceptibility. In this way, converting $\vec{E}$ to a vector, Equation 2.4 is then given by

$$\begin{pmatrix} P_x \\ P_y \\ P_z \end{pmatrix} = \varepsilon_0 \begin{pmatrix} \chi_\perp & 0 & 0 \\ 0 & \chi_\perp & 0 \\ 0 & 0 & \chi_\parallel \end{pmatrix} \begin{pmatrix} E_x \\ E_y \\ E_z \end{pmatrix} \tag{2.5}$$

The matrix, $\overleftrightarrow{\chi_e} = \begin{pmatrix} \chi_\perp & 0 & 0 \\ 0 & \chi_\perp & 0 \\ 0 & 0 & \chi_\parallel \end{pmatrix}$ is diagonal only when one of the axes is along the director. For director orientation at other angles, the tensor will not be diagonal but must be symmetric.

Now, with the definition of $\overleftrightarrow{\chi_e}$, the electric displacement within a nematic LC material is proportional to the electric field after replacing the polarisation with Equation 2.3,

$$\vec{D} = \varepsilon_0 \vec{E} + \vec{P} = \varepsilon_0 \vec{E} + \varepsilon_0 \overleftrightarrow{\chi_e}\, \vec{E} = \varepsilon_0 (\overleftrightarrow{1} + \overleftrightarrow{\chi_e}) \vec{E} = \varepsilon_0 \overleftrightarrow{\varepsilon_r}\, \vec{E} \tag{2.6}$$

where $\overleftrightarrow{\varepsilon_r}$ is the relative permittivity (or can also be termed as dielectric constant), and is related to the electric susceptibility, $\overleftrightarrow{\varepsilon_r} = \overleftrightarrow{1} + \overleftrightarrow{\chi_e}$, and therefore the dielectric constant is also anisotropic and can be further written as

$$\overleftrightarrow{\varepsilon_r} = \begin{pmatrix} \varepsilon_\perp & 0 & 0 \\ 0 & \varepsilon_\perp & 0 \\ 0 & 0 & \varepsilon_\parallel \end{pmatrix} \tag{2.7}$$

We can now determine the dielectric free-energy density by substituting equations and parameters mentioned above into the following LC dielectric energy density equation,

$$\begin{aligned} f_{dielectric} &= -\frac{1}{2} \vec{D} \cdot \vec{E} \\ &= -\frac{1}{2} \varepsilon_0 \begin{pmatrix} \varepsilon_\perp & 0 & 0 \\ 0 & \varepsilon_\perp & 0 \\ 0 & 0 & \varepsilon_\parallel \end{pmatrix} \begin{pmatrix} E_x \\ E_y \\ E_z \end{pmatrix} \cdot \vec{E} \\ &= -\frac{1}{2} \varepsilon_0 \left[\varepsilon_\perp \begin{pmatrix} 1 & 0 & 0 \\ 0 & 1 & 0 \\ 0 & 0 & 1 \end{pmatrix} + \begin{pmatrix} 0 & 0 & 0 \\ 0 & 0 & 0 \\ 0 & 0 & \Delta\varepsilon \end{pmatrix} \right] \begin{pmatrix} E_x \\ E_y \\ E_z \end{pmatrix} \cdot \vec{E} \\ &= -\frac{1}{2} \varepsilon_0 (\varepsilon_\perp \vec{E}\vec{E} + \Delta\varepsilon E_z \vec{n} \cdot \vec{E}) = -\frac{1}{2} \varepsilon_0 [\varepsilon_\perp \vec{E} + \Delta\varepsilon (\vec{n} \cdot \vec{E}) \vec{n}] \cdot \vec{E} \\ &= -\frac{1}{2} \varepsilon_0 [\varepsilon_\perp E^2 + \Delta\varepsilon (\vec{n} \cdot \vec{E})^2] \overset{simplify}{\Longrightarrow} = -\frac{1}{2} \varepsilon_0 \Delta\varepsilon (\vec{n} \cdot \vec{E})^2 \end{aligned} \tag{2.8}$$

where the $\vec{n} = \begin{pmatrix} 0 \\ 0 \\ 1 \end{pmatrix}$ along the z-axis. In Equation 2.8, for a LC, only the second term contains $\vec{n}$ which is important for director orientation evaluation, thus the first term is discarded. With a positive $\Delta\varepsilon$ the director tends to align parallel with the direction of $\vec{E}$, in order to reach an equilibrium state where the free-energy is minimum; for a LC material which possesses a negative $\Delta\varepsilon$, the director will rotate to be perpendicular to $\vec{E}$ for the same reason.

2.3.2 Dielectric Coupling in Chiral Nematic LCs

In a chiral nematic LC, the dielectric interaction can be used to reorient the helicoidal axis (Figure 2.5(b)), and dielectric coupling is also able to unwind the helix completely at a larger electric field (Figure 2.5(c)).

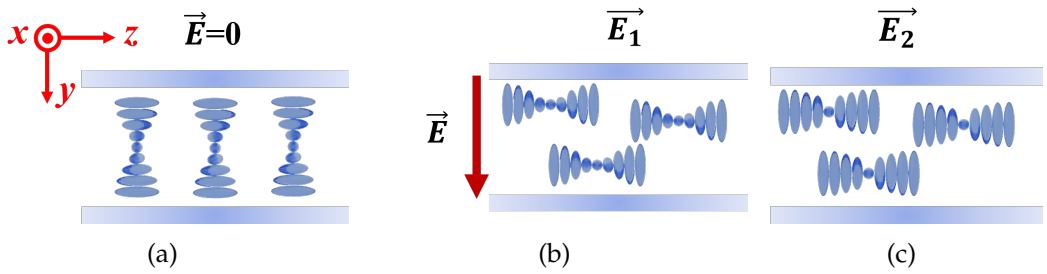

FIGURE 2.5: Schematics of chiral nematic LC phase when it is (a) at 0V, (b) reoriented so that the helix aligns with the substrates and (c) unwound. The $\Delta\varepsilon$ of the chiral nematic LC is positive and $\vec{E}_2 > \vec{E}_1 > 0$

For a chiral nematic LC with an electric field applied, there will be a torque that makes the director reorient to align either parallel or perpendicular to the field in the plane in which the director is uniform (depends on the sign of $\Delta\varepsilon$). In order to determine the amplitude of such in-plane distortion, we firstly consider an ideal chiral nematic LC model, whose pitch is P=P_0, where P_0 is the natural pitch, and the helicoidal axis is parallel to the y-axis at first when there is no electric field applied. After applying an electric field,

because of $\Delta\varepsilon > 0$, the helical axis will reorient to align parallel to the z-axis, and the director (in Figure 2.5(b)) can then be written as [37]

$$\vec{n} = \begin{pmatrix} n_x \\ n_y \\ n_z \end{pmatrix} = \begin{pmatrix} \cos\theta \\ \sin\theta \\ 0 \end{pmatrix} \tag{2.9}$$

the angle, θ, is defined as $\theta(z) = qz$. Combining the elastic and dielectric energy from Equation 2.2 and 2.8, respectively, if the applied field is parallel to y-axis, $\vec{E} = E_y\vec{y}$, then the free-energy of the system is given by,

$$\begin{aligned} F(\vec{n}) &= f_{elastic} + f_{dielectric} \\ &= \frac{1}{2}K_{22}\left(-\frac{\partial\theta}{\partial z} + q_0\right)^2 - \frac{1}{2}\Delta\varepsilon\varepsilon_0 E_y^2 \sin^2\theta \end{aligned} \tag{2.10}$$

because θ is only a function of z (as can be seen in Figure 2.5(b)). If the amplitude of the applied electric field is low, we can assume that the dielectric coupling causes a perturbation to θ which can be described as,

$$\theta(z) = q_0 z + \theta_0 \sin 2q_0 z \tag{2.11}$$

where the θ_0 is the twist distortion perturbation amplitude. In order to know the rotation of the director along the helix, we need to figure out an expression for θ_0 which we find by minimizing the total energy with respect to θ_0 over a pitch. By substituting $\frac{\partial\theta}{\partial z}$ and using a double-angle identity as well as taking the approximation that θ_0 is small, Eqaution 2.10 can be written as, writing out the elastic and dielectric terms separately,

$$f_{elastic} = \frac{1}{2}K_{22}(q_0^2\theta_0^2(1 + \cos 4q_0 z)) \tag{2.12}$$

$$f_{dielectric} = -\frac{1}{4}\Delta\varepsilon\varepsilon_0 E_y^2(1+\theta_0-\cos 2q_0 z-\cos 4q_0 z) \tag{2.13}$$

We then integrate the energy density over a half pitch repeating unit of the structure, $\frac{P}{2} = \frac{\pi}{q_0}$. Any cosine and sine terms integrate to zero, and the result becomes,

$$\int_0^{\pi/q_0} F(\vec{n})dz = \int_0^{\pi/q_0}(f_{elastic}+f_{dielectric})dz = \frac{\pi}{q_0}(\frac{1}{2}K_{22}q_0^2\theta_0^2 - \frac{1}{4}\Delta\varepsilon\varepsilon_0 E^2(1+\theta_0)) \tag{2.14}$$

By minimizing Equation 2.14 with respect to θ_0 it becomes,

$$\theta_0(E) = \frac{\Delta\varepsilon\varepsilon_0}{4\pi K_{22}q_0}E^2 \tag{2.15}$$

Finally, substituting Equation 2.15 back into Equation 2.11, an expression for the equilibrium twist component of the director is derived as,

$$\theta(z) = q_0 z + \frac{\Delta\varepsilon\varepsilon_0}{4\pi K_{22}q_0}E^2 \sin 2q_0 z \tag{2.16}$$

In chiral nematic LCs formed from a negative $\Delta\varepsilon$ nematic LC host, the sample will tend to align with the helical axis parallel to the field as the spatially rotating director will then always be perpendicular to the applied field. For a positive $\Delta\varepsilon$ material, the director tends to align parallel with the electric field direction. At low field amplitudes, the helical axis will be aligned perpendicular to the field, and as the field amplitude is increased the director is increasingly rotated to align parallel with the field in the way described above. If the pitch is not "constrained" this will also result in a lengthening of the pitch, which leads to unwinding of the helical structure above a certain

threshold electric field. We introduce E_c to describe the critical unwinding field, above which the material enters a homeotropic nematic alignment. E_c can be expressed as [38, 39]

$$E_c = \frac{\pi^2}{P_0}\left(\frac{K_{22}}{\Delta\varepsilon\varepsilon_0}\right)^{\frac{1}{2}} \tag{2.17}$$

2.3.3 The Flexoelectric Effect

As mentioned above LC molecules have different components of a permanent dipole parallel and perpendicular to the molecular axis, and with an external $\vec{E}$ there can be additional electric induced polarisation. However, in the absence of an applied electric field or bulk distortion, there is no net polarisation in the nematic phase. This is because the equilibrium thermodynamic distribution of the director has rotational symmetry about the director and is invariant under the inversion transformation $\vec{n} = -\vec{n}$, which guarantees the nematic uniaxial symmetry. A net polarisation will be induced and the equilibrium distribution will be disturbed once there is an electric field applied to the LC. The 'dielectric effect' discussed in Section 2.3.2 is the reorienting torque due to the anisotropy in the polarisability, which is a result of the coupling to the induced polarisation and permanent dipole moment. However, the coupling between the electric field and director-reorienting torques is further complicated by an effect called flexoelectricity [40].

If the LC molecules possess shape anisotropy, (such as banana-shaped or pear-shaped, Figure 2.6(a) presents pear-shaped nematic flexoelectric LC molecules), then a field-induced population bias in molecular orientations reduces the molecular packing efficiency at a cost to the free-energy. This cost in energy effectively reduces the material's polarisability and the resultant dielectric torque on the molecules [41, 42]. However, the LC molecules

can mitigate the reduced packing efficiency by forming curvature distortion spontaneously and thus form a coupling between electric field and director curvature distortions which is shown in Figure 2.6(c). Usually, this distortion is presented as a splay-bend distortion. The effect can also be applied in reverse. If a curvature distortion is present, a spontaneous population bias in the dipole orientations occurs that results in a net electric polarisation. This polarisation produces an internal field at a free-energy cost [37].

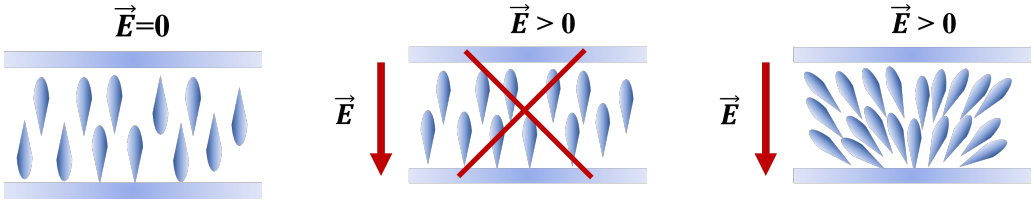

FIGURE 2.6: Illustration of the flexoelectric-induced director distortion. (a) demonstrates the orientation when there is no electric field applied; (b) shows an incorrect director-reorientation for a nematic flexoelectric LC; (c) presents the correct reorientation of the director for flexoelectric coupling. Instead of pointing in the same direction, the director will adopt a splay-bend structure to increase the packing efficiency.

The free-energy related to the flexoelectric polarisation can be written as,

$$f_{flexo}(\vec{n}) = -\vec{P}_{flexo} \cdot \vec{E} \tag{2.18}$$

where $\vec{P}_{flexo}$ is given by,

$$\vec{P}_{flexo} = e_1 \vec{n}(\nabla \cdot \vec{n}) + e_3(\nabla \times \vec{n}) \times \vec{n} \tag{2.19}$$

where e_1 and e_3 are the bend and splay flexoelectric coefficients in the original Meyer sign convention for flexoelectric polarisation [40]. Equation 2.19 shows the relationship between bend and splay distortions and flexoelectric

polarisation. Substituting the flexoelectric energy term into the elastic free-energy and dielectric free-energy equations, then we can get an expression for the total free-energy density,

$$\begin{aligned} F(\vec{n}) &= f_{elastic} + f_{dielectric} + f_{flexo} \\ &= \frac{1}{2}K_{11}[\nabla \cdot \vec{n}]^2 + \frac{1}{2}K_{22}[\vec{n} \cdot (\nabla \times \vec{n}) + q_0]^2 + \frac{1}{2}K_{33}[\vec{n} \times (\nabla \times \vec{n})]^2 \\ &- \frac{1}{2}\varepsilon_0 \Delta\varepsilon(\vec{n} \cdot \vec{E})^2 - [e_1\vec{n}(\nabla \cdot \vec{n}) + e_3(\nabla \times \vec{n}) \times \vec{n}] \cdot \vec{E} \end{aligned} \tag{2.20}$$

This equation is sufficient to simulate the behaviour of a large variety of devices. Note that the dielectric free-energy is proportional to $\vec{E}^2$ whilst the flexoelectric contribution is proportional to $\vec{E}$, which means that the dielectric contribution is independent of the sign of the electric field. However, the flexoelectric contribution is related to the sign of the applied electric field. Finally, the flexoelectric effect can also be described as a result of the torque on the director [43–46]. The flexoelectric torque can be expressed ($\vec{n} \times \vec{h}_{flexo}$) where,

$$\vec{h}_{flexo} = (e_1 - e_3)(\vec{E}(\nabla \cdot \vec{n}) - (\nabla \otimes \vec{n})\vec{E}) - (e_1 + e_3)(\vec{n} \cdot \nabla)\vec{E} \tag{2.21}$$

Flexoelectricity in chiral nematic LCs couples to electric field components perpendicular to the helicoidal axis and can produce a rotation of the director about the field direction. When a chiral nematic LC is in equilibrium with no applied electric field or polarisation, there is a natural twist structure that results in a periodic helicoidal director structure, as illustrated in Figure 2.7(a)

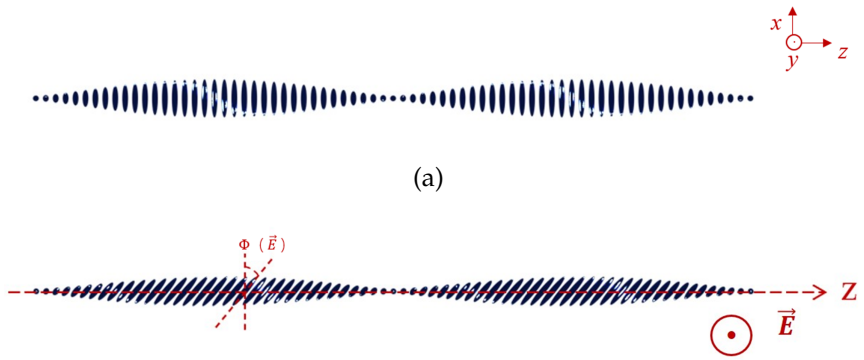

FIGURE 2.7: Illustration of the flexoelectro-optic effect in a chiral nematic LC (a) without and (b) with an applied electric field.

The planes perpendicular to the helicoidal axis contain a uniform director orientation. However, if there is an applied electric field perpendicular to the helix axis and the director is tilted by ϕ, which is shown in Figure 2.7(b), then the director in the plane exhibits a periodic splay-bend structure where the flexoelectric polarisation becomes greatest. The period of the splay-bend deformation [47] can be written as,

$$\gamma_{splay} = \frac{P}{\sin\phi} \tag{2.22}$$

where P is the chiral pitch and ϕ is the director tilt angle as defined in Figure 2.7(b). When $\phi = \frac{\pi}{2}$, the structure will be purely a splay-bend deformation with no twist at all. In practice, the resultant tilt angle ϕ is a balance between the elastic and flexoelectric free-energy. A full analytical treatment of this effect was first developed by Patel and Meyer [48–50] and further expanded by Rudquist to include the dynamics [51]. Following the approach developed by Rudquist of the tilt in the director of a chiral nematic LC due to flexoelectricity [51], consider the axis and director field in Figure 2.7. The method describes the director in terms of a spherical coordinate system, and uses this director in the free-energy expression from Equation 2.20, and then averages

this energy over a repeating unit of the chiral nematic LC structure to determine the relative total energy. The total free-energy is then minimized with respect to the flexoelectric tilt angle, ϕ. The ϕ rotates as shown in Figure 2.7 and the applied electric field is $\vec{E} = (0, E_y, 0)$. Then we can determine the value of ϕ that minimizes the total energy, which is given by

$$\tan\phi = \frac{e_1 - e_3}{2K_2 q_0} E - \frac{K_1 - 2K_2 + K_3}{2K_2} \sin\phi \tag{2.23}$$

For small angles, we can apply the approximation $\sin\phi \approx \tan\phi \approx \phi$ and simplify the expression as,

$$\phi(E) = \frac{e_1 - e_3}{K_1 + K_3} \frac{E}{q_0} \tag{2.24}$$

Sometimes, researchers replace $e_1 - e_3$ with $e = \frac{1}{2}(e_1 - e_3)$ and replace $K_1 + K_3$ with $K = \frac{1}{2}(K_1 + K_3)$. The resulting $\frac{e}{K}$ is then called the flexoelastic ratio and is considered as a figure of merit in the production of materials with optimal flexoelectro-optic switching properties.

As LCs are liquid-like materials, they, therefore, take time for the director to realign from an undistorted state to a distorted state with the application of the electric field. Here we define the time it takes for the tilt angle to reach within $\frac{1}{e}$ of the equilibrium value as the characteristic time τ. Considering the chiral nematic LC as a viscous system, the characteristic time is dependent upon the viscosity, the elastic constants, and the characteristic length scale of the distortion, which depends on the pitch in chiral nematic LCs or depends on the device thickness for achiral nematic LCs. Based on the derivation by Rudquist for the dynamic change of the flexoelectro-optic effect, the expression for the characteristic time is

$$\tau = \frac{2\gamma}{(K_1 + K_3)q_0^2} \tag{2.25}$$

where γ is viscosity and τ is proportional to P ($P = \frac{2\pi}{q_0}$), and thus depends on pitch. For a material in which $nP < \lambda$, the director rotation about the field direction manifests as a rotation of the optic axis of the material, which means if the pitch is shorter than the wavelength of light, then the macroscopic optic axis tilts with the flexoelectric tilt angle. As a result, electro-optic technologies that exploit fast-switching chiral nematic LCs have been hotly researched and developed, especially from a display engineering perspective [52–57].

2.3.4 Conductivity

An ideal pure LC material should be an insulating dielectric material. However, in practice, in real applications, there are always impurities and usually, these are in the form of ions[20]. Additionally, the physical anisotropy of typical nematic LC molecules may influence the circulation of the ion movement when there is an external electric field. The conductivity along the director and the other two axes are different. For a uniaxial anisotropy nematic LC, the conductivity parallel to the director is defined as $\sigma_{\parallel}$ while the conductivities for the other two axes perpendicular to the director are written as $\sigma_{\perp}$. The value of this parameter is rather small, ranging from 10^{-12} to 10^{-8} $/\Omega$cm[58]. In some applications, such impurities are useful and can be introduced on purpose by doping ionic dopants in the mixtures. As a result of this anisotropy, the ionic mobility is different along different directions. By adjusting the frequency and amplitude of the applied electric field, the motion of ions through the LC can cause continuous turbulence.

2.4 Optical Properties of Liquid Crystals

The optical birefringence of LCs allows them to be used in optical phase modulation, polarisation modulation and coherence control because of the unique electric response. LCs have already been widely used in liquid crystal displays (LCDs) [59] and LC-SLMs [60]. This thesis involves the development of LC technologies for phase and coherence control, and thus the fundamental optical properties of LCs are outlined here.

Light, or more specifically visible light, covers a wavelength range from 400 nm to 700 nm [61]. In the context of the research presented here, the wavelength is considered to be between 400 nm to 700 nm which is relevant for human perception. Light is an electromagnetic wave which has two perpendicular electric and magnetic field components oscillating perpendicularly to the direction of the propagating direction. For that reason, when investigating and explaining how LCs interact and change the various properties of light, and perform different kinds of optical properties, the best way is to consider this from the perspective of the refractive index.

2.4.1 Birefringence and Optical Retardation Manipulation

As an electromagnetic wave, light can travel in different materials and media and in a vacuum the light travels with a velocity of $c = 3 \times 10^8$ m/s and the relevant repeat spatial period is called the wavelength and is denoted as λ_0. The relation between those two parameters is $c = \lambda_0 f$, where f is the frequency of the photon from the source. The direct impact that a material can have on the light passing through is the decrease in the velocity and the factor by which it decreases is called the refractive index. Based on Maxwell equations, in non-magnetic materials, the velocity of the electromagnetic wave in a material is described as $v = \frac{c}{\sqrt{\varepsilon_r}}$. Comparing this with the velocity of light

travelling in a material, we can easily obtain an equation that can define the refractive index which is $n = \sqrt{\varepsilon_r}$ which is also related to the frequency of the light. With the introduction of the refractive index, the change in the velocity, wavelength and the phase of an incident light travelling through a medium is given by the following equations

$$\begin{aligned} v &= \frac{c}{n} \\ \lambda &= \frac{\lambda_0}{n} \\ \Delta\varphi &= nd\frac{2\pi}{\lambda} \end{aligned} \tag{2.26}$$

where d is the path of the light propagating through the material and nd is the so-called optical path length.

As calamitic nematic LCs are uniaxially anisotropic, the relative dielectric permittivity ε_r has a different value for electric field in different directions, so therefore does the n for light with different polarisation directions and this is what we call birefringence. For the refractive index along the director, this is called $n_{\parallel}$ and for the perpendicular one, this is denoted as $n_{\perp}$. Birefringence is a property shared by all anisotropic materials and the refractive index is different between one and the other two directions for uniaxially material (LCs). The refractive index for light polarised parallel to the director is called the extraordinary refractive index, n_e and for light polarised in the other two directions (perpendicular to the previous direction) we have the ordinary refractive index, n_o. For nematic LCs that are uniformly aligned, the n_e and $n_{\parallel}$ are the same things and the n_o and $n_{\perp}$ are the same things. Thus we can quantify the birefringence as

$$\Delta n = n_e - n_o \tag{2.27}$$

which varies for different temperatures and wavelengths. Because the order parameter changes with temperature so too does the birefringence. The higher the order parameter is, the higher the birefringence. Additionally, as the relative dielectric constant of the LC molecules changes with wavelength, as a result of the different interactions with the medium, so too does the refractive index vary with wavelength. The relationship between refractive index and wavelength is governed by Cauchy's equation.

Consider light propagating along the y-axis and the director of the LC material is aligned with the z-axis. Furthermore, consider that the electric field of the electromagnetic wave is oscillating along $z = x$ which is illustrated in Figure 2.8.

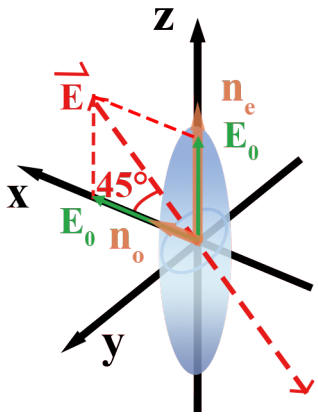

FIGURE 2.8: Light polarised at 45° relative to the x and z axes.

E_0 is the x and z components of the maximum amplitude of $\vec{E}$, the formulation of $\vec{E}$ can then be decomposed into

$$\begin{aligned} E_x = E_0 \cos wt &\overset{retardation}{\Longrightarrow} E_0 \cos\left(n_o y \frac{2\pi}{\lambda_0} - wt\right) \\ E_z = E_0 \cos wt &\overset{retardation}{\Longrightarrow} E_0 \cos\left(n_e y \frac{2\pi}{\lambda_0} - wt\right) \end{aligned} \tag{2.28}$$

where the $E_0 \cos wt$ represents the waveform right before interacting with the LC molecules at y=0. Substituting Equation 2.27 into Equation 2.28,we get,

$$\begin{aligned} E_x &= E_0 \cos\left(n_o d\frac{2\pi}{\lambda_0} - wt\right) \\ E_z &= E_0 \cos\left(n_o d\frac{2\pi}{\lambda_0} - wt + \Delta n d\frac{2\pi}{\lambda_0}\right) \end{aligned} \tag{2.29}$$

and this set of equations represents the light wave at the $y = d$ position. The phase difference between the E_x and E_z components is because of the optical retardation phenomenon, and the phase difference between the two components is represented by $\Delta\varphi = \Delta n d\frac{2\pi}{\lambda_0}$. This effect will result in a polarisation change after the light passes through the material and for different values of $\Delta\varphi$ the exit light can be linearly, circularly or elliptically polarised.

Before moving on, it is also interesting to consider the optical properties of chiral nematic LCs. Because of the dielectric coupling, the twist distortion induces optical biaxiality which means breaking the uniaxial optical symmetry of the chiral nematic LC such that the material has three refractive indices corresponding to three orthogonal directions. This can be described by considering the average of the perpendicular and parallel components of the permittivity and the corresponding local ordinary and extraordinary refractive indices, n_e and n_o, averaged over one pitch. Thus, we have effective biaxial refractive index components,

$$\begin{pmatrix} n_1 \\ n_2 \\ n_3 \end{pmatrix} = \begin{pmatrix} \sqrt{\langle n_e^2 \cos\theta^2 + n_o^2 \sin\theta^2 \rangle} \\ \sqrt{\langle n_e^2 \sin\theta^2 + n_o^2 \cos\theta^2 \rangle} \\ n_o \end{pmatrix} \tag{2.30}$$

where n_1, n_2 and n_3 are the refractive indices corresponding to x-, y- and z-axes, respectively, (Figure 2.5(b)). By substituting the following equations

into Equation 2.30 we obtain,

$$
\begin{aligned}
2\sin^2\theta &= 1-\cos 2\theta \\
&= 1-\cos[2qz+2\theta_0\sin(2qz)] \\
&= 1-\{\cos(2qz)\cos[2\theta_0\sin(2qz)]-\sin(2qz)\sin[2\theta_0\sin(2qz)]\} \\
&\overset{\theta_0 \text{ is small}}{\Longrightarrow} \approx 1-\cos(2qz)+2\theta_0\sin^2(2qz) \\
&\approx 1+\theta_0-\cos(2qz)-\cos(4qz)
\end{aligned}
$$

$$
\begin{aligned}
\langle\sin^2\theta\rangle &\approx \frac{1}{2}\langle[1+\theta_0-\cos(2qz)-\cos(4qz)]\rangle \\
&\approx \frac{1}{2}\Big[\frac{1}{d}\int_0^d 1+\theta_0-\cos(2qz)-\cos(4qz)dz\Big] \\
&\approx \frac{1}{2}\Big[1+\theta_0+\frac{\sin(2qd)}{2qd}+\frac{\sin(4qd)}{4qd}\Big] \\
&\xrightarrow{d \text{ equals half pitch, } P/2=\pi/q} \\
&\approx \frac{1}{2}(1+\theta_0)
\end{aligned}
$$

$$
\begin{aligned}
\langle\sin^2\theta\rangle &\approx \frac{1}{2}(1+\theta_0) \\
\langle\cos^2\theta\rangle &\approx \frac{1}{2}(1-\theta_0)
\end{aligned}
\tag{2.31}
$$

and thus,

$$
\begin{pmatrix} n_1 \\ n_2 \\ n_3 \end{pmatrix} = \begin{pmatrix} \sqrt{\frac{n_e^2+n_o^2}{2}}\sqrt{1-\theta_0(\frac{n_e^2-n_o^2}{n_e^2+n_o^2})} \\ \sqrt{\frac{n_e^2+n_o^2}{2}}\sqrt{1+\theta_0(\frac{n_e^2-n_o^2}{n_e^2+n_o^2})} \\ n_o \end{pmatrix} \tag{2.32}
$$

where θ_0 is defined by Equation 2.15.

2.4.2 Unique Optical Effects in Chiral Nematic LCs

In addition to the birefringence of a distorted chiral nematic LC system, there are other unique optical properties that can only be observed in a chiral nematic LC material but not in a nematic LC system, as described briefly in Section 2.1.2.

Consider a bulk chiral nematic LC with the helix parallel to the z-axis. The whole material can be dived into 'slices' and the average director of individual slices changes gradually from the bottom slice to the top slice. If the pitch of the chiral nematic LC is significantly smaller than the wavelength of the light, say $P \ll \lambda_0$, then the chiral nematic LC 'units' are similar to a discotic nematic phase. For light polarised in the plane perpendicular to the helical axis, the refractive index is the same for any direction and this shows an isotropic, transparent appearance.

An interesting phenomenon of chiral nematic LCs to consider is when the pitch is smaller than the wavelength of the incident light. In this case it falls into the optical activity (optical rotation) regime. The chiral nematic LCs now has two different refractive index values for right or left handed circularly polarised light and this is called circular birefringence and the anisotropy is defined as n_L and n_R, respectively. The consequence of such circular birefringence is that linearly polarised light will rotate either clockwise or anti-clockwise but not change the amplitude. The rotated angle relative to the x-axis is given by $\theta = \frac{(n_R - n_L)k_0 d}{2}$, where $k_0 = \frac{2\pi}{\lambda_0}$ is the wave vector in vacuum. Another interesting regime is when the chiral pitch is around the same order as the wavelength of visible light. Under such conditions, the chiral nematic LCs fall into the Bragg reflection regime.

Now, a more normal situation where the light incidents the chiral nematic LC at an angle θ away from the helical axis and with a reflected light

at an angle of ϕ because of the Bragg reflection. The repeating plane distance here is $\frac{P}{2}$ and the constructive interference can only occur when

$$m\lambda = \frac{nP}{2\cos\theta}[1 + \cos(\theta + \phi)] \overset{\theta=\phi}{\Longrightarrow} m\lambda = nP\cos\theta \tag{2.33}$$

where m is an integer and $m \geq 1$. λ is the wavelength of the incident light in LCs and n is the effective refractive index of the LCs. Apparently, one can only receive a specific band of wavelength reflected by the chiral nematic LCs when observing the sample under a white light source as a result of constructive interference. With the viewing angle changing from left to right, the colour of the sample will change as well. Such an effect is also called selective reflection. This might appear contradictory to the property introduced in the previous paragraph. It should be pointed out that for linearly polarised light such selective reflection can only occur if the wavelength is between $n_e P$ and $n_o P$, and for wavelength out of this regime, both right- and left-handed circularly light can propagate through but with different velocities.

It is also interesting to consider when the pitch is much longer, and significantly exceeds the wavelength of light, say $P \gg \lambda_0$, in this case, another special optical property will occur which is called the waveguide regime. In this case, the average director of each slice changes very little and the light can be considered as travelling through slices of nematic LCs. After propagating through each 'slice', linearly polarised light will be retarded and become elliptically polarised light with its semi-major axis parallel to the director orientation in the second slice. Since $P \gg \lambda_0$, and the slices are considered infinitesimally thin which means $d \ll \lambda_0$, the induced phase difference in the x and y components of the incident linear polarised light, $\Delta n k_0 d$, is extremely small. As a result, the emergent light is still linearly polarised but has rotated a small angle. The direction of the polarisation of the light will gradually

rotate, following the director orientation while still maintaining linear polarisation.

2.5 Laser Speckle and Optical Coherence Control

Laser speckle is a phenomenon that occurs in laser light and has been investigated since the invention of the laser. Numerous bright and dark spots are typical of the grainy speckle pattern that can be observed in an image, or perceived image, which is a key issue limiting imaging quality [15]. The degree of speckle present in, for example, a projected laser image with uniform average intensity is quantified by the speckle contrast, C, of the interference pattern [15]. To calculate C, we use the equation as follows:

$$C = \frac{\sigma_I}{\bar{I}} \tag{2.34}$$

where σ_I is the standard deviation of intensity values and $\bar{I}$ is the average intensity value. The equation is actually the reciprocal of the signal-to-noise ratio.

Historically, several methods for reducing C have been implemented, most of which rely on the superposition of multiple uncorrelated speckle patterns [15]. Methods of reducing C are based on the principle that when two or more statistically independent (or partially decorrelated) speckle patterns are superimposed, the random intensity fluctuations will be 'averaged out' across the image. Speckle reduction techniques can be separated according to whether the statistically independent speckle patterns are created instantaneously or time sequentially. Time sequential methods take advantage of the finite integration time of the observer, thus reducing speckle to zero for a human viewer. The reduction techniques can be further separated

into four different ways by which these speckle patterns are mutually decorrelated: spectral decorrelation, spatial decorrelation, angular decorrelation, and polarisation decorrelation. However, many of these methods have notable drawbacks when put into practice, such as the requirement for bulky mechanical parts, vibrations, or expensive components. To overcome these issues, previous work has studied a method [16] that takes advantage of the rapid, random movement of a local LC director to construct a compact diffuser device that is capable of reducing speckle.

In the ideal case when N completely uncorrelated speckle patterns are superimposed, the speckle contrast is given by [15]

$$C = \frac{\sqrt{\sum_{n=1}^{N} \bar{I}_n^2}}{\sum_{n=1}^{N} \bar{I}_n} \tag{2.35}$$

If the intensities of all speckle patterns have the same mean intensity, the minimum speckle contrast becomes $\frac{1}{\sqrt{N}}$. Depending on whether the statistically independent speckle patterns are created instantaneously or time sequentially, the categories of speckle reduction technologies can be further separated into two classes. For example, the human eye can be modelled to have an integration time of approximately 50 ms [62], and then the time sequential methods take advantage of the finite integration time of the observer.

Spectral decorrelation uses two or more independent monochromatic sources with wavelength λ_1 and λ_2 which illuminate a rough screen from the same position and angle leading to form two speckle patterns which will be decorrelated because of the wavelength variation $\Delta\lambda$. The decorrelation increases when $\Delta\lambda$ increases. Speckle reduction using spectral decorrelation techniques can also be achieved through wavelength chirping, changing the wavelength of laser emission within the integration time of the detector (such

as the eye). For the spatial decorrelation methods, the key is to make the spatial resolution larger than the size of the coherence area so that the spots of speckle patterns will be blurred together. To make this possible, researchers use a light source with low spatial coherence and therefore very small coherence areas at the screen. For example, B. Reading realized this through using a random laser [63].

Speckle contrast can also be reduced instantaneously by illuminating the screen with multiple light sources that vary in illumination angle. The greater the variation in angle between sources, the more decorrelated the resulting speckle patterns will be. A time sequential variation in angle can be achieved by passing light through a moving diffuser, for example, the most common way to reduce speckle contrast is to place a rotating glass diffuser in front of the light source [64–66]. A typical polarisation decorrelation technique is to use a projection screen which exhibits volume scattering of light so that when linearly polarised light is shone at such a screen the reflected light is shown to be depolarised because of the light being diffusely scattered from the surface and some light undergoing multiple scattering as it penetrates a short distance into the surface.

Considering these speckle reduction techniques and comparing them with the optical properties of LCs, the possibility of using LC thin film devices and other optical elements to reduce speckle contrast has been investigated by a number of researchers. The birefringence of LCs and the ability to reorient the director when applying external stimulus has made LCs of significant interest for technological applications, especially in the display industry, and the properties can also be used to control laser speckle.

For example, a planar-aligned nematic LC device can easily modulate the polarisation of incident light because the two orthogonal polarisation components of light in a LC experience different refractive indices, i.e., they travel through the device at different speeds and therefore exit with an added phase difference. An electric field can be used to reorient the bulk into homeotropic alignment, such that the orthogonal polarisation components of light experience the same refractive index n_0, causing no change to the polarisation state of the light. Varying the electric field amplitude to allow alignment between these extremes also allows for variable added phase difference for the propagating light. This is the fundamental effect used in most LC-based displays to control the amount of light transmitted for each primary colour at each pixel, but could also be used to add polarisation decorrelation to reduce speckle. Additionally, for a chiral nematic LC material, if the helical axis orientation varies randomly through a sample then a highly scattering state is observed.

LCs appear to be an ideal medium for reducing speckle contrast as it is possible to change the optical properties externally with an electric field. This can be used to apply a phase, polarisation or intensity variation to incident light that varies in time and space. This in turn can potentially create multiple statistically independent speckle patterns, reducing the appearance of speckle contrast. Furthermore, this can be achieved vibration free, and LC devices are small, light and relatively simple to make, and the power consumption is low due to the small conductivity.

The first research in this area used a nematic LC device with a gap of 15µm [43, 67]. One substrate was coated in PVA to form an alignment layer, the other was coated in a mixture of PVA and azo dye molecules to form a controllable alignment layer. The application of UV light of wavelength close to the absorption maximum of the dye causes a rotation in the

double bond to transform the cell from its stable *trans* form to its unstable *cis* form. When this light is removed, the molecule will fall back into the *trans* form with either its original molecular shape, or one that differs by approximately 90°, preferring the direction that matches the polarisation of UV light. By exposing this layer to UV light with a checkerboard pattern of orthogonal polarisations, the alignment layer forms a related checkboard pattern of orthogonal alignment properties. When filled with nematic LC this creates a cell that aligns itself according to the alignment surface. A reduction in speckle contrast of $\frac{1}{\sqrt{2}}$ has been reported when used in conjunction with a stationary diffuser plate, as a result of the two simultaneous orthogonal polarisation states present in the transmitted light [15]. In this case, speckle contrast was measured with a CCD directly in the path of the laser, instead of in reflection from a screen. This approach cannot be improved without introducing movement to the diffuser or LC cell, as there are only two distinct polarisation states, and this does not reduce speckle any further than a depolarising screen used in applications such as laser projection.

The field induced turbulence in LC was mentioned above, and EHDI (electrohydrodynamic instability) is a phenomenon that we take advantage of in speckle reduction. Conductivity and dielectric anisotropy can be used to apply competing torques to the LC director that then create instability in the macroscopic alignment of a device. If a thin layer (approximately 10-50 µm) of nematic LC with negative $\Delta\varepsilon$ and positive $\Delta\sigma$ is exposed to a DC or low-frequency AC electric field perpendicular to the device substrates, the director will tend to orient perpendicular to this field but the ionic impurities will try to move through the material towards the oppositely charged electrodes, applying a torque on the director back in the direction of the field. The instabilities caused by these competing torques lead to a range of induced patterns that change with field amplitude and frequency [20].

When the voltage is increased above a threshold voltage, then a periodic distortion of the alignment is seen that appears as a series of parallel lines perpendicular to the director which are called Williams domains. This is because of a convective instability in the LC that results in ions flowing in a closed circle. The circle's diameter is approximately the cell thickness d. The observation of parallel lines is due to the convective flow causing a reorientation of the director to be perpendicular to the substrates where flow is perpendicular, and parallel where the flow is parallel.

As the voltage is further increased these Williams domains become more agitated by the increasing flow velocity until, above a larger threshold voltage, the flow becomes turbulent and completely disordered. In this state, the director is randomly aligned both in space and time. This causes the material to become highly scattering, appearing opaque and with a milky white appearance to the eye. This is known as the dynamic scattering mode (DSM) [68].

EHDI has been observed not only in nematics but also in chiral nematics and smectic LCs and all of them have DSM phenomena. Chiral nematics are known to exhibit a highly scattering, stationary focal conic state, which is used for optical storage of information. For this reason, our work aims to use EHDI effects in chiral nematic mixtures to provide maximum scattering and optimum speckle reduction.

To help induce instability of the LC, it is possible to dope the LCs with ionic dopants such as Cetyltrimethylammonium bromide (CTAB) [16], nanoparticles [69], polymer structure [70], fine particles [71] or redox dopants [72]. The ultimate goal of this thesis is to reduce the speckle contrast to close to $C = 0.04$, below which the human eye cannot perceive speckle any more [15].

2.6 Optical Phase Modulation and LC-SLMs

To recap, Sections 2.3.1 and 2.4 have introduced the properties of nematic and chiral nematic LCs in electric field and how they can manipulate the phase, polarisation, colour and the intensity of the light. The birefringence and dielectric anisotropy provides a solution for optical phase modulation and this forms the basic idea of LC-SLMs. Based on these fundamental LC properties, we can say that not only nematic but also chiral nematic LCs could be promising materials in modulating the optical phase of light. Electro-optic technologies that exploit fast-switching chiral nematic LCs have been researched and developed, especially from a display engineering perspective [52–57]. Optical phase modulation is important in many aspects of optical and optoelectronic technology. Phase modulation can be obtained either by changing the refractive index (or effective refractive index) of a material through which light is propagating, or by physically changing the optical path-length for the light. As mentioned in the previous chapter, LC materials are not suitable for integrated optics technology where a fundamental high modulation speed is required. However, LC materials are of importance for SLM technology to shape the wave-front of propagating light.

As discussed in Chapter 1, LC-SLM technology can be classified into two categories, which are either providing a digital, binary, or quantised phase modulation (0 and π phase states are commonly chosen) or providing analogue phase modulation (a phase range of 0 to 2π is commonly used). Binary SLM typically exhibits substantially less than 1 ms switching times, however, analogue SLM technology has a long switching time, commonly being many milliseconds. Of course, there are some alternatives which are based on electro-mechanical technology, but they suffer from various disadvantages which have been listed in Chapter 1.

Improving the switching speed, whilst maintaining access to a full range of phase states (from 0 to 2π) would allow SLM technology to be used in a wider range of systems, such as in faster optical laser beam tracking and steering [73], and in higher-speed optical aberration correction in imaging systems [74]. There has been much work in this area, with a number of proposals and demonstrations of configurations that can enhance the switching speed (reduce the response time) in a useful way [75–77]. There also has been work on incorporating polymer networks into LC layers to obtain submillisecond switching times [14].

There is another approach demonstrated by using the flexoelectro-optic effect in chiral nematic LC [48] which takes advantage of the characteristic lengthscale of a chiral nematic LC. While the electro-optic effect offers submillisecond switching times, the optical response is generally quite small for most LC compounds and mixtures, with switching angles of just a few degrees. LC dimers (bimesogens), however, can show much larger switching angles, allowing useful electro-optic effects to be exploited [78]. However, the attempt demonstrated in [78] has other issues which is that the devices have to operate at elevated temperatures over 100°C which is impractical for most technological applications. Unfortunately, room-temperature materials showing a large and high-speed flexoelectro-optic effect are not yet commonly available. A LC that shows substantial switching angles at room temperature has recently been demonstrated, but it requires a large electric field (equivalent to 100 V across a 5-µm-thick device to achieve a switching angle of 40°) [78]. The ultimate goal of the work in this thesis is to overcome the impracticality of elevated temperatures and large voltages as well as achieve robust analogue full 2 π phase modulation in a compact optical system (Chapter 6). Additionally, a detailed exploration of the most suitable cell configuration (Chapter 7) is also carried out in order to make the best

use of the switching characteristics of the LC material. Simulations have also been developed to guide the experiments so that the phase modulation is maximized as well as eliminating unwanted intensity modulation (Chapter 8).

2.7 Summary

In this chapter, a detailed introduction of the most important properties of LC materials relevant to this thesis has been presented. The discussion is further divided into four parts, which starts with an introduction to the nematic and chiral nematic LC phases, then describes the elastic energy before moving on to a discussion about the dielectric and flexoelectric effects. The optical properties of both nematic and chiral nematic LCs are then considered before a comprehensive summary of previous related research on laser speckle and phase modulation is provided.

Chapter 3

Experimental Techniques

3.1 Liquid Crystal Mixtures

In this thesis, the liquid crystal (LC) mixtures prepared can be divided into two categories: one set of mixtures was developed for the speckle reduction and one set of mixtures was developed for the optical phase modulation. For the speckle reduction devices, chiral nematic LC mixtures have been prepared that have been doped with an ionic additive. On the other hand, for the optical phase modulation studies (Chapters 6, 7 and 8), both nematic and chiral nematic LC mixtures have been considered. The nematic LC materials used in this thesis are either commercially-available from suppliers such as Synthon Chemicals Ltd or bespoke materials that have been synthesised by research collaborators, such as the group of Prof. Georg Mehl at the University of Hull. One of the nematic mixtures used in this thesis was the eutectic nematic LC mixture E7, which was sourced from Synthon Chemicals and used without further purification. E7 contains four different compounds, the chemical structures of which are shown in Figure 3.1, with their corresponding concentration by weight. Each LC mixture was then capillary filled into a glass cell for characterisation of their electro-optic properties.

The glass cells used to obtain the results presented in the following

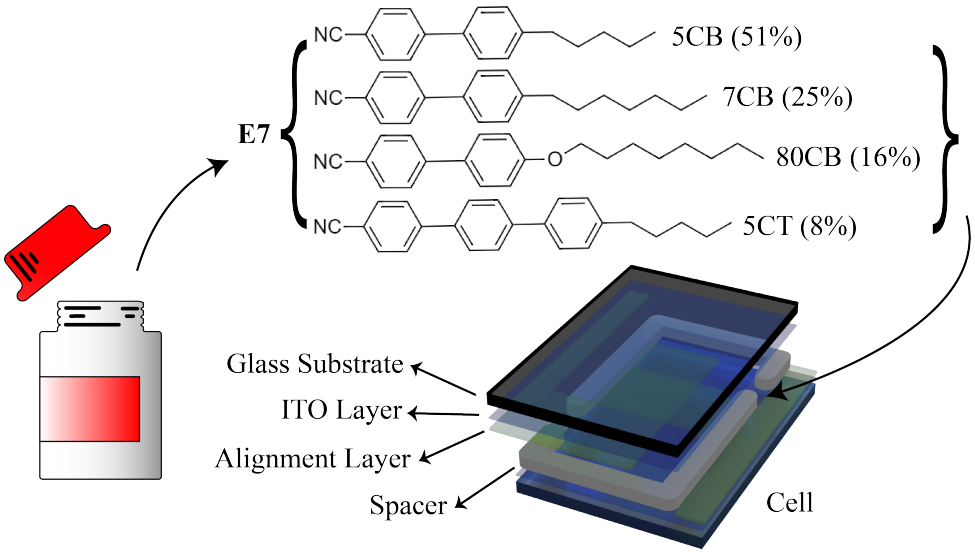

FIGURE 3.1: An illustration of E7 composition and the concentration of each of the components by weight. The mixture is filled into the glass cell by capillary action.

chapters were either sourced commercially from Instec or were fabricated in-house. Some of the studies also employed the use of glass cells that had been kindly provided by Samsung. In all cases, a cell is constructed with two glass substrates separated by a small distance, d, such that a thin film of LC is formed, as illustrated in Figure 3.1. The cell shown in Figure 3.1 is a typical cell configuration from INSTEC [79]. The cell thickness determines the film thickness, which is typically between 2 µm and 20 µm. There are spacer beads or spacer thin films between the alignment layers to control the cell gap. The substrate surfaces are usually treated with a variety of additional functional layers. For example, in order to apply an electric field across the LC layer, transparent electrodes are coated onto the inner substrates in the form of indium tin oxide (ITO).

Alignment layers can be used to control the director orientation at each surface interface to set the initial overall average director orientation inside the LC thin film. For the glass cells that were fabricated in-house, this was achieved by using a rubbing machine to align spin-coated polyvinyl alcohol (PVA) polymer layers. With different alignment layer pretreatment,

the cells can have different pretilts. In the case of anti-parallel rubbing, we can obtain a so-called Fréedericksz cell. Conventional Fréedericksz cells have a uniform alignment of the director with a pretilt angle in the same direction on the two substrates, which is resultant from anti-parallel rubbing. After the electric field is switched on and then off, the director starts to relax back to the original state, causing a flow. Another kind of cell that is of relevance to this work is the so-called Pi-cell. In the Pi-cell, the pretilt angles on both substrates are in opposite directions, which is because of the parallel rubbing on the top and bottom substrates, and this is called parallel alignment. An alternative configuration that is considered in this thesis involves coating one substrate with a homeotropic alignment layer and the other substrate with a planar alignment. This results in the so-called hybrid aligned nematic (HAN) cell. The homeotropic alignment layer is often lecithin [80]. Diagrams for each cell are shown in Figure 3.2.

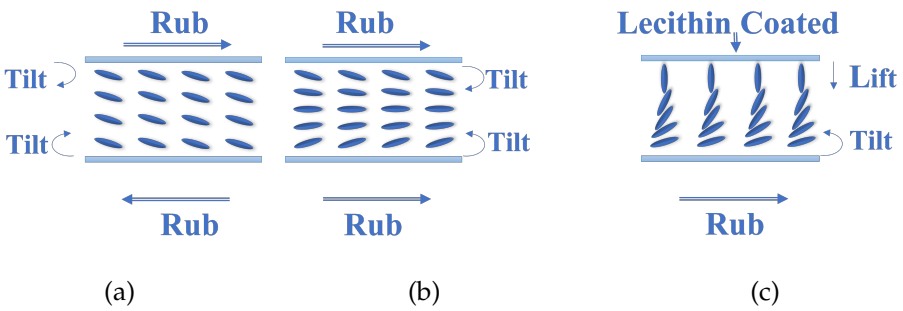

FIGURE 3.2: The initial orientation of the director inside (a) conventional Fréedericksz cell, (b)Pi-cell and (c) HAN cell without an applied electric field.

Chiral nematic mixtures for the speckle reduction and optical phase modulation studies were prepared by weighing the LC and the dopants using a precision microbalance which has an accuracy of 0.1 mg (Mettler Toledo AB104-S) [81]. The liquid materials are extracted by a pipette whereas the solid materials are extracted by a spatula. For illustration purposes, a chiral nematic LC mixture prepared for the speckle reduction studies involved a sample of BL006 (Merck KGaA), 3 wt.% R5011 (Merck KGaA) right-handed

chiral dopant, and 0.1 wt.% ionic dopant. The nematic LC phase of BL006 is between -20°C and 113°C thus at room temperature the host nematic LC is in a liquid crystalline state and the other two are in powder form. After weighing the appropriate amount of these three materials, they are placed in a vial (Wheaton sample vials). The samples are usually prepared in a batch of more than 100 mg or 200 mg to match the accuracy of the analytic balance. The process is depicted in Figure 3.3(a) and the temperature used for thermal mixing is typically around 10°C above the clearing point of the host LC. Figure 3.3(b) shows the process of filling a cell via capillary action, the mixture again is heated above the clearing point when filling the cell, following which a slow and gentle annealing and cooling process allows the material to form a uniform Grandjean texture.

3.2 Polarisation Optical Microscopy

Observing the texture and colour of an LC cell under polarised optical microscopy is of great importance in understanding and investigating some of the physical and optical properties of an LC device. In this study, all microscope images, unless otherwise indicated, are taken on the polarised microscope shown in Figure 3.4. The microscope is an Olympus BX51 model with a QImaging camera, model 'Retiga R6 6.0 megapixel CCD camera'. The light coming out of the halogen bulb first passes through a polariser and then is formed by the condenser. An optical bandpass filter can be inserted after the condenser if the specimen on the mechanical stage is sensitive to certain wavelengths of light. After passing through all of these elements, the incident light finally illuminates the LC device. The objective lens turret, which covers a wide selection of lenses, including a magnification of 4x, 10x, 20x, 40x and 50x, is positioned directly above the cell. A second linear polariser is the next element, which acts as an analyser. The analyser is

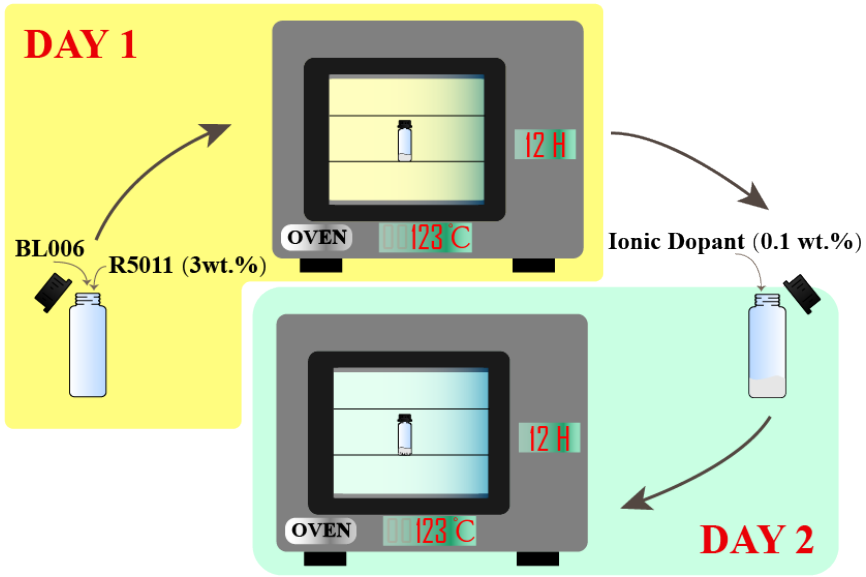

(a)

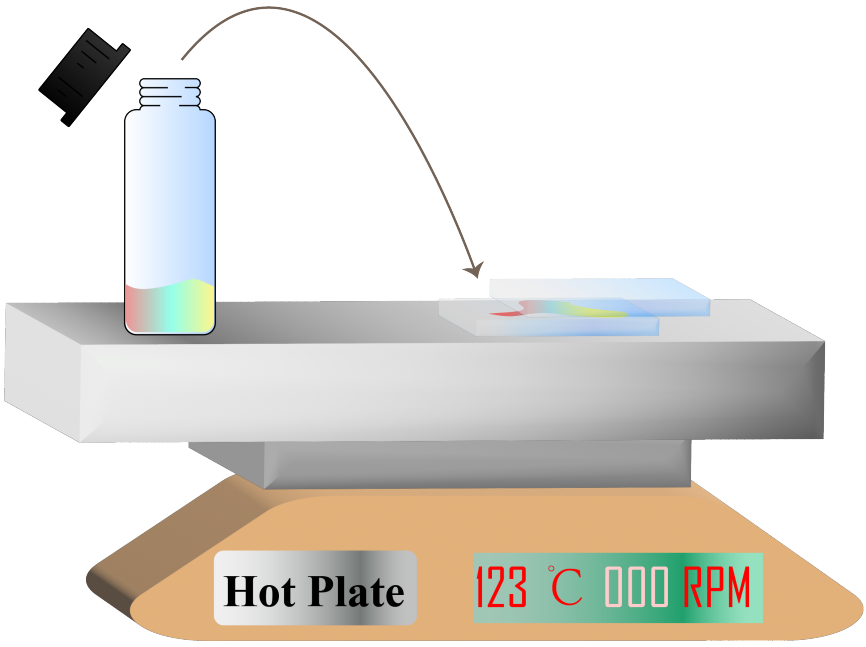

(b)

FIGURE 3.3: Schematic of the cell-filling procedure from (a) mixture preparation to (b) fill a cell. In (a), the vial is first filled with BL006 and 3 wt.% of R5011 on DAY 1 and placed in an oven set at 123°C for 12 hours. On DAY 2 the selected ionic dopant is added to the completely-mixed chiral nematic LC host and placed in the oven, mixing at the temperature where the LC material is isotropic, for another 12 hours. (b) The well-mixed sample after two days of preparation is transferred to a hot-plate set at the same temperature as the mixing process and the cell is placed next to it on the same hot-plate, filled via capillary action. The cell here is an anti-parallel Fréedericksz cell. The RPM on the hot-plate represents the revolutions per minute.

FIGURE 3.4: A photograph of the BX51 Olympus microscope and QImaging camera used in this thesis.

usually set perpendicular to the first linear polariser so that we can differentiate an anisotropic material from an isotropic material. For a nematic LC device, when rotating the microscope stage by 2π, under single-wavelength illumination, it will show four cycles of light transmission increasing from zero to maximum and falling back to zero. If the device is illuminated by a

white light source in Figure 3.4, then still the device demonstrates different intensity when the sample stage is rotated by different angles relative to the polarisers. In this case, the colour also fades and the intensity of the transmitted light drops to zero when the optic axis of the LC is parallel to the polarisers.

A hot-stage (Linkam Scientific Instruments LTD, LinkPad, LTS420, temperature range < -195°C to 420°C, stability <0.1°C) and a combination of a waveform generator (dual-channel, Tektronix AFG 3022 [82]) and an amplifier (dual-channel, 10x, FLC Electronics F10AD [83] were used during the inspection on the polarised microscope. The hot-stage was placed directly on the microscope rotation stage and was used to investigate the phase transition temperatures of the mixtures. The waveform generator together with the amplifier was able to supply up to $\pm$200 V which allows us to characterise the device for different applied voltages.

3.3 UV-Vis Spectroscopy

In this thesis, the cell gap and the pitch of the chiral nematic LCs are critical for the resulting performance of the devices, and thus a quantitative analysis is employed via an ultra-violet-visible (UV-Vis) spectrometer, Agilent Cary 8454 UV-Visible Spectroscopy System [84]. The spectrometer provides a transmission spectrum from 190 nm to 1100 nm with an interval of 0.9 nm [84]. The spectrum is realised by combining a deuterium gas lamp and a tungsten lamp. The light is firstly collimated by the source lens and then passed through the sample. A spectrograph lens and a slit placed after the sample make sure each proportion of wavelength is projected onto the appropriate photodiode only [84]. The spectrometer has an array of 1024 individual photodiodes. A blank measurement was always taken before any

measurements of device parameters in order to remove ambient light or extraneous reflections.

The method of measuring the thickness of an empty cell is based on the theory of a Fabry–Pérot interferometer in which light undergoes multiple reflections between two parallel glass substrates and the transmitted light forms an interference pattern. The intensity of the transmitted light is shown as transmission on the plot in Figure 3.5 and the peaks of the interference wave are highlighted by the blue dots. We can write:

$$I_t = \mid E_t \mid^2 = \frac{1}{1 + F\sin^2(\frac{2\pi nd}{\lambda})} I_0 \tag{3.1}$$

where F is the coefficient of finesse, I_0 is the intensity of the incident light, n is the refractive index of the air which is equal to 1, and d represents the cell gap. By analysing Equation 3.1, we can see that only when $\frac{2\pi d}{\lambda} = i\pi, (i \in N)$ then I_t reaches a maxima. Accordingly, a Matlab script was written and the cell gap can be calculated by the following equation

$$\begin{aligned} d &= -\frac{1}{2}\frac{\Delta x}{\Delta y} \\ \Delta y &= \frac{1}{\lambda_1} - \frac{1}{\lambda_{\Delta N}} \\ \Delta x &= -\Delta N \end{aligned} \tag{3.2}$$

where definitions for Δy, Δx, and ΔN are illustrated in Figure 3.5(b).

In a practical measurement, we select as many peaks as possible provided the waveform is not distorted. Such a case could happen because of the defects on the films coated on the glass substrates, which is not common for commercial devices, but can be easily seen for home-made devices. The reason why we didn't select all the peaks in Figure 3.5 is to demonstrate that the MATLAB script written for this thesis is able to select preferred peaks out

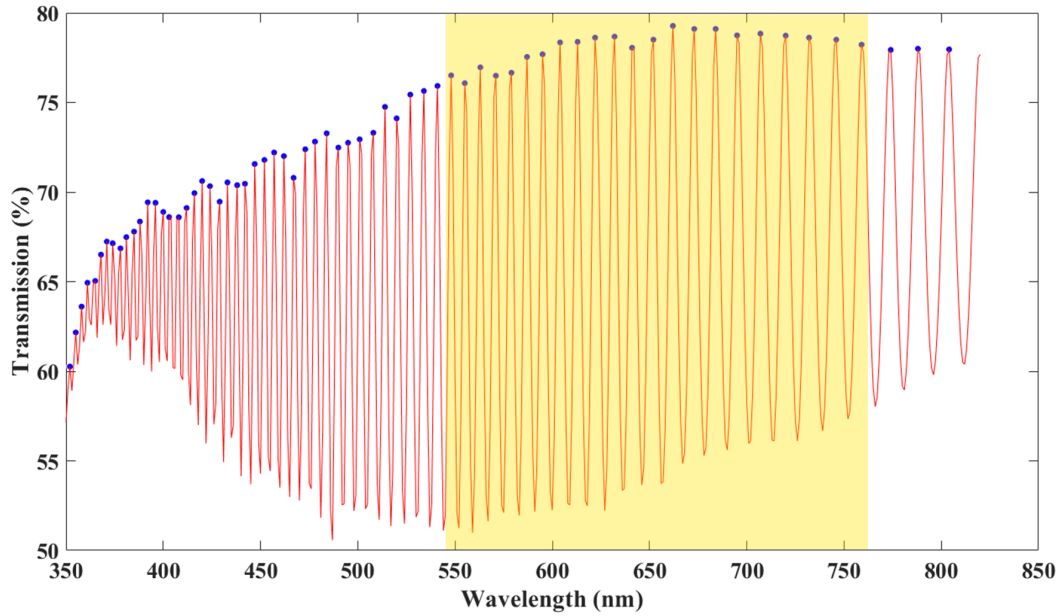

(a)

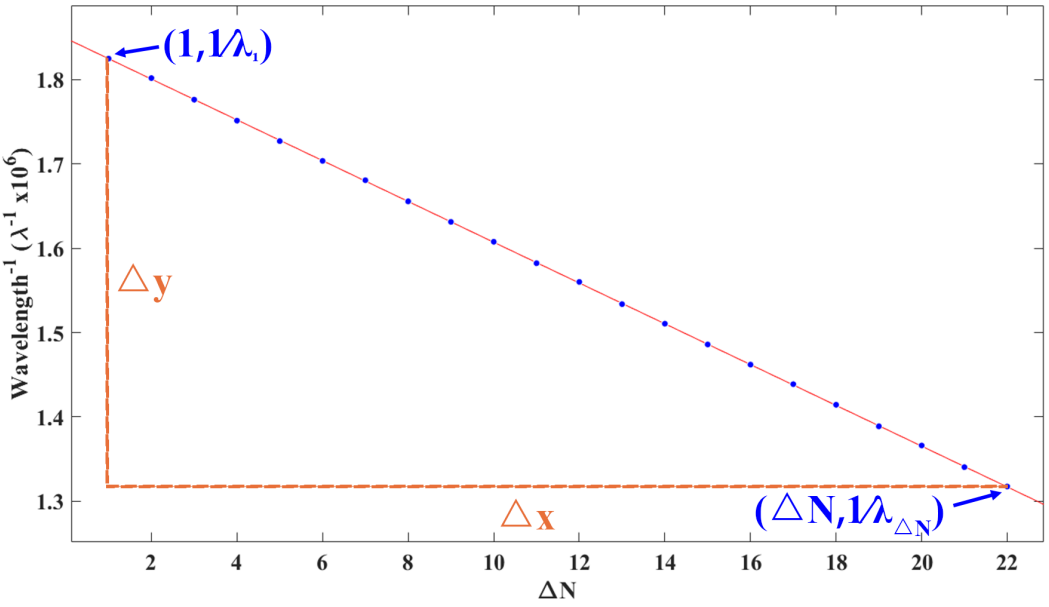

(b)

FIGURE 3.5: Example transmission spectrum of an anti-parallel rubbed 20 µm-thick Instec glass cell. (a) is the spectrum obtained via the Agilent Cary 8454 UV-Visible spectrometer, because of the natural attenuation of the glass material, the spectrum starts from 350 nm. The peaks in the interference pattern are highlighted by the blue dots and the selected successive peaks (highlighted by the yellow block in (a)) are plotted in (b) as a function of $\frac{1}{\lambda_{\Delta N}}$-$\Delta N$, where ΔN is the peak number. The gradient of the plot in (b) is related to the cell gap and is found to be 20.65 µm which is within 5% of the standard value of 20 µm given by the manufacturer.

of all detected peaks.

UV-Vis spectroscopy was also used to determine the pitch of a chiral nematic LC mixture/device. After filling the anti-parallel device with the chiral nematic LC material and carefully annealing to obtain a Grandjean texture (confirmed by inspecting the structure under the polarised microscope), the cell was placed after the light source and before the spectrograph lens. According to the theory mentioned in Section 2.4.2, the selective reflection is related to the pitch, P, and the refractive index of the LC material. Here the refractive index of BL006 is quoted as $n_e = 1.7988$ and $n_o = 1.5249$ [85]. According to Equation 2.33, we can find that

$$\lambda_{central} = \frac{\lambda_{low} + \lambda_{high}}{2} = \frac{(n_e + n_o)P}{2} \tag{3.3}$$

which is clearly demonstrated in Figure 3.6. In the real calculation, we use a fixed refractive index for both the extraordinary and ordinary refractive indices which are measured at λ=633 nm. Because over the commonly seen band-gap in this thesis (the $\lambda_{central}$ is around 400 nm to 700 nm), the refractive index does not change very much, so we always use a fixed value for the refractive indices to estimate the pitch.

3.4 Speckle Contrast Characterisation

In order to quantify the exact speckle contrast value a dedicated characterisation experiment was developed by D. H. Hansford [36], which has been further developed and adapted in this thesis.

As mentioned previously in Equation 2.34, to evaluate the degree of speckle noise, it is important to obtain the profile of the intensity on the

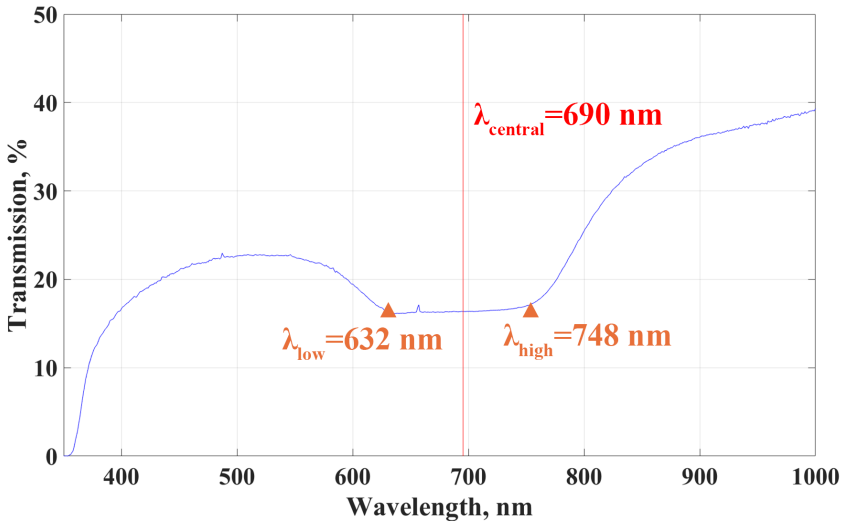

FIGURE 3.6: An example transmission spectrum of a chiral nematic LC device showing Bragg reflection. The bandgap is confined by the λ_{low} and λ_{high}, while the central wavelength is highlighted by the red solid line. In this case, the chiral nematic LC mixture was BL006+2.5 wt.%R5011 and the pitch was found to be 415 nm.

imaging plane. There are two ways to capture this, as introduced by Goodman [15]; it can be either taken in a subjective way or in an objective way. Considering real applications, such as a laser projector or a HUD, human vision tends to perceive the granular noise subjectively. As a result, the experimental system employed in this work focused exclusively on subjective speckle to best relate the results of the speckle contrast value to human perception. The experimental configuration is shown in Figure 3.7, which is the same as that used in previous work except for the use of two ground glass diffusers (GGDs) and a light-pipe (LP) (MKS Instruments, Inc., LPH-PIP-4).

In previous work, conditioning optics as well as settings for the CCD-camera were investigated and subsequently chosen to mimic the response of the human eye [36]. Here, we will only introduce some of the salient features that both Figure 3.7(a) and Figure 3.7(b) share. The light source is a coherent laser, JDS Uniphase 1122P, emitting at a wavelength of $\lambda = 632.8$ nm. The output light beam has a diameter of 0.63 mm and the beam divergence is only

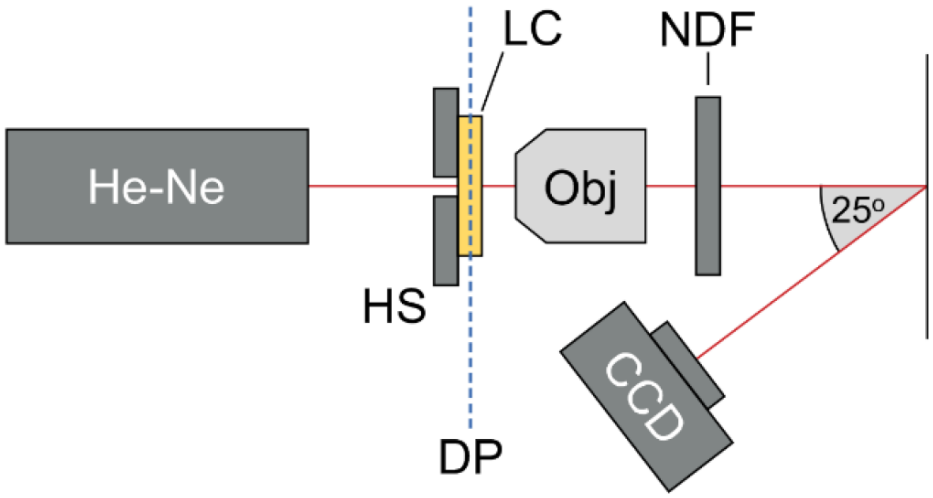

(a)

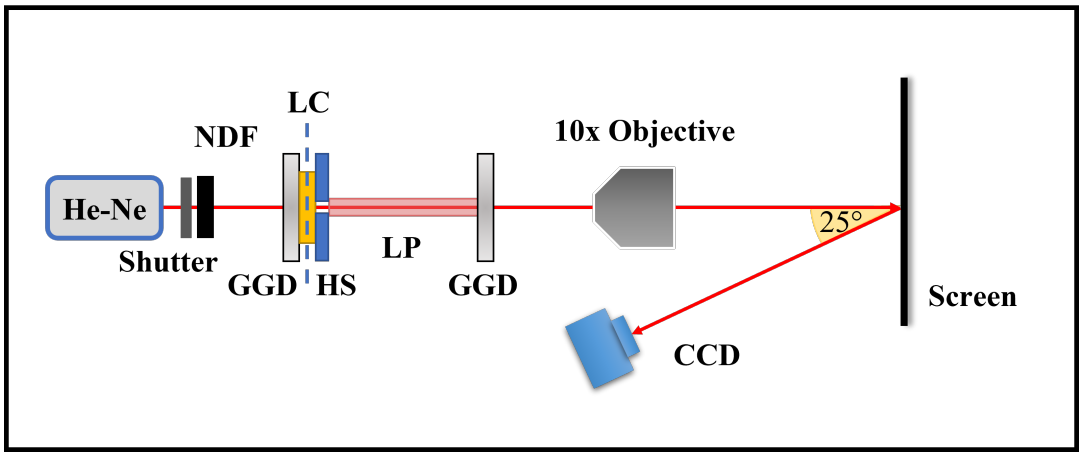

(b)

FIGURE 3.7: The illustration of the speckle characterisation setup (a) built previously [36] and (b) the enhanced version used in this thesis. In (a), the coherent light coming out of the Helium-Neon laser (He-Ne) first passes through the small hole in the middle of Hot-Stage (HS) and is then modulated by the LC device at the Diffuser Plane (DP). The modulated light is collected by the 10x Objective (Obj) and then projected onto the screen after being attenuated by the Neutral Density Filter (NDF). A monochrome, CCD camera is put next to the screen with an angle of 25° subjective to the optic axis. In (b), the system is composed of the He-Ne laser, a shutter for laser safety, and a NDF to attenuate the light at the very beginning of the system. The light pass through a Ground Glass Diffuser (GGD) before being incident on the LC device. The blue-dashed line represents the DP. A Light-Pipe (LP) is put afterwards and another GGD is attached closely to the other end of the LP. The light is collected by the 10x Obj and then projected to the screen and observed by the same CCD camera as the one used in (a). A wooden box, enclosed on all sides covers the setup acting as an enclosure.

1.3 mrad [86]. The system includes a compact and thin ceramic heating element which was purchased from Thorlabs, HT19R (with an inner diameter of 4mm, the maximum temperature is 400°C) and it is controlled by a Thorlabs TC200 Temperature Controller (with a temperature range from 20°C to 200°C and an accuracy of 0.1°C).

The LC devices were operated under an AC electric field, provided by a waveform generator (dual-channel, Tektronix AFG 3022 [82]) and an amplifier (dual-channel, 10x, FLC Electronics F10AD [83]) is introduced in Section 3.2. The objective was produced by Olympus (UPlanFL N) and the NA is 0.3 [87]. It was previously used to restrict the beam divergence after passing through the LC device so that the camera can receive enough light for the determination of the speckle contrast.

The camera is especially important in this characterisation setup. The monochrome CCD camera is from QImaging Co. (QICAM 12/16-bit). The resolution of the pixels is 1392 x 1040, and the dimension of each pixel is 4.65 µm x 4.65 µm. The CCD camera was selected because of its cooling function which is beneficial for reducing the dark noise during the measurement. The camera measures the intensity of light without interpolating the data. To best imitate human perception, the position of the camera relative to the imaging plane (screen), the imaging lens attached to the front of the camera, as well as the integration time of the sensor were carefully adjusted.

The camera lens with an inappropriate f-number can artificially reduce the granular noise due to either spatial averaging or spatial decorrelation [15, 36]. Specifically, reducing the speckle contrast through spatial averaging could happen when the average speckle size A_C observed by the CCD detector after passing through the camera imaging lens is smaller than the pixel's spatial resolution A_P. The following equations show the A_C and the

relative reduction rate N_1 can be written as [15]:

$$A_C = \frac{\lambda^2}{\Omega_l} \tag{3.4}$$

$$N_1 = \frac{A_P}{A_C} \tag{3.5}$$

where Ω_l is the solid angle subtended by the exit pupil of the camera imaging lens as seen by the CCD detector and it is equal to $\Omega_l = \frac{\pi}{4F^2}$ for a circular aperture imaging lens where $F = \frac{f}{D}$ is the f-number of the lens (the ratio of the focal length to the diameter of the lens aperture).

Alternatively, for an artificial reduction in the speckle due to spatial decorrelation, the reduction rate can be defined as

$$N_2 = \frac{\Omega_P}{\Omega_D} \tag{3.6}$$

where the $\Omega_D = \frac{\pi}{4F^2}$ is the solid angle subtended by the exit pupil of the projection system to the screen and the Ω_P is the solid angle subtended by the entrance pupil of the detector to the screen. The Ω_P relates to the dimension of the coherence area on the projection screen. For a fixed size Ω_D, Ω_P represents the angular resolution of the detector. When the Ω_P increases while Ω_D is fixed, then the coherent areas increase in size and overlap, leading to a measured decrease of the speckle contrast.

Now $N_1 \propto \frac{1}{F^2}$, while $N_2 \propto F^2$. Thus, for an accurate speckle contrast measurement, the $f-$number cannot be either too large or too small. The distance between the sensor plane and the screen is also important because of the same reason as the f number and it should be the same among all

measurements. It is important to note that the refocusing effect while moving the camera around relative to the screen while adjusting the distance is negligible considering the distance between the screen and the camera is extremely large compared to the spot size. It has been shown that the closer the camera is to the screen, the higher the speckle contrast. As a result, the camera is placed at a distance such that the distance between the camera and the screen is as short as possible while the laser light path is not blocked [36]. The integration time of the camera was set as 50 ms which has been shown to be a suitable value for comparison with human perception of speckle.

The aperture of the imaging lens was selected to match the pupil diameter when the eyes are perceiving the luminance for an indoor cinema based on the equation [88].

$$d = 5 - 3\tanh(0.4log_{10}L) \tag{3.7}$$

where d represents the pupil diameter and L represents the luminance.

For an indoor cinema scenario, when the light is switched off, the luminance L is around 48 cd/m^2 [89] thus the diameter of the camera imaging lens in this characterisation system was determined to be d= 3.2 mm. The focal length of the eye is reported to be 22.8 mm [90]. However, in our system, the distance between the entrance pupil and the CCD sensor of the camera and the resolution of the sensor are fixed and larger than the human eyeball, the focal length of the camera lens should be adjusted by matching the N_2 parameter. For the case of a human eye, under the luminance considered in this work, the cones dominate over the rods at the retina and it is reported to have a density of at least 100,000 cones/mm^2 [88] at the foveal centralis. Thus, $A_P = 10$ µm^2, $A_C \approx 25.82$ µm^2 and $N_1 \approx 0.387$. To match

N_1 of the system to 0.387, the focal length of the imaging length equals to $f = \sqrt{\frac{(4.6\times10^{-3})^2\times\pi\times3.2^2}{4\times(632.8\times10^{-6})^2\times0.387}} \approx 33.14$ mm.

In summary, the focal length of the imaging lens was selected as 35 mm which is close to the ideal value of 33.14 mm. The CCD camera is set 160 mm away from the screen with an angle of 25° such that it is close enough without inducing spatial decorrelation or blocking the light. The camera was set at a bit depth of 16 which is above the threshold for accurately measuring speckle.

It was also found that the profile of the laser light is a Gaussian distribution and because of that, the measurement area is very crucial in eliminating an artificial increase in the speckle contrast. A uniform intensity is important to accurately determine speckle contrast. For this reason, we include two GGDs and a LP in the system shown in Figure 3.7(b). The first GGD slightly scatters the light so that more light can be modulated by the effective area of the LC device. The LP immediately follows, acting as a 'homogenizer', this guarantees a much more uniform intensity distribution compared with the one obtained in Figure 3.7(a). The rear GGD further enhances the uniformity and conveys the light to the objective. Additionally, the impact of ambient light is reduced by enclosing the setup and it was ensured that the camera was not saturated during any measurement by installing a suitable NDF in front of the laser. The value of the filter was carefully selected so that the full dynamic range of the camera was used.

The whole characterisation system was calibrated every time before carrying out measurements. Additionally, the system was bench-marked by testing with a standard rotating GGD and a depolarising diffusing screen and the resulting measurements were found to be consistent with the literature. Specifically, for laser light without attenuation by an active LC device but

just depolarised by the diffusing screen was found to be C=0.68$\pm$0.01 which is close to the expected value of $\frac{1}{\sqrt{2}}$ [15]. A fundamental error analysis has been carried out while designing the system by D. Hansford [36]. The laser and the hot-stage were switched on 30 minutes in advance to avoid intensity fluctuation and the temperature drifting. A fully automated code written in MATLAB was connected to the system so that a remote control was available to avoid mechanical vibration [36].

3.5 Summary

This chapter details the experimental methods used in this thesis including LC device assembly, mixture preparation, and device characterisation in terms of configuration and performance. The chapter describes the fundamentals of these methods and it emphasizes the function and the novelty of the speckle characterisation system developed previously [36]. The camera has a bit depth of 16 which is above the threshold for accurately measuring speckle. Additionally, the camera is cooled to minimize the impact of noise on the measurements and it is operated with unity gamma correction to provide a linear relationship between the pixel value and the incident optical intensity. The focal length of the lens and the aperture for the camera were selected to ensure speckle values determined closely match human perception. The impact of ambient light is considered and decreased by setting up an enclosure and it was ensured that the histogram of the projected image is neither dim nor saturated for the camera by putting a suitable NDF in front of the laser.

Chapter 4

Redox Doped-Liquid Crystals for Laser Speckle Reduction

In this chapter, two different redox dopants are investigated for a wide range of concentrations in short-pitch chiral nematic LCs, and the improvements in the speckle contrast are considered and compared with previous studies. The results show that the speckle contrast can be reduced to $C = 0.11 \pm 0.02$ at a temperature of 30°C. Finally, an improvement in the quality of an image generated using a modified commercial projector fitted with a monochromatic laser source is then presented. The work presented in this chapter forms the basis of a publication in the journal article, *Advanced Photonics Research*, 2, 2000184 (2021) [17].

4.1 Introduction

The degree of speckle can be quantified by the speckle contrast parameter, C, that was originally introduced by Goodman [91–94] and has been introduced in Equation 2.34. Another relevant quantity is the signal-to-noise ratio $\frac{S}{N} = \frac{\bar{I}}{\sigma_I}$, which is the reciprocal of the speckle contrast C. In other words, the lower the speckle contrast value C is, the more uniform the image intensity is. For

fully developed speckle, where the most severe speckle pattern is present, the speckle contrast parameter C and the signal-to-noise ratio $\frac{S}{N}$ are both equal to 1. It has been reported that the speckle pattern is not typically perceivable to the human eye when C is lower than a value of 0.04 [95].

Different methods of eliminating speckle have been investigated previously in both coherent imaging and high-brightness imaging. These can be loosely divided into four separate categories: polarisation decorrelation [15], angular decorrelation [64–66], wavelength decorrelation [64], and spatial decorrelation [63]. All of these methods aim to reduce the spatial coherence and/or temporal coherence of the laser. Each method can reduce the speckle to a certain degree instantaneously or over an integration time. With an active speckle reducing element placed in the propagation path of the light source, the speckle contrast can be described by Equation 2.35.

Generating decorrelated speckle patterns can be realized by using a range of different practical implementations such as the introduction of a depolarising screen [15], the use of an array of lasers aligned at different angles relative to the receiver [96], an array of lasers emitting at different wavelengths, the use of a low spatial coherence light source such as a random laser [63], or the use of a rotating ground glass diffuser [97]. In recent reports, there are many approaches taken into consideration to improve the imaging quality, which can be classified as either by introducing the optical elements to optimise the laser source and optical system physically or by employing numerical methods in the post-imaging processing procedure, such as neural networks [4], so that the objective information can be reconstructed. The former has the advantage that it fundamentally improves the $\frac{S}{N}$ ratio of the optical system.

The most common approach to introducing a physical optical element to combat speckle is to place a rotating ground glass diffuser (RGGD) before the collection optics in a wide field-of-view imaging system [97]. Previous research has shown that the speckle can be decreased to an acceptable level if the rotation speed of the diffuser is higher than 2π rad/s [98]. While this approach can mitigate the appearance of speckle, it has some considerable drawbacks such as the presence of mechanical vibrations caused by the system with the motor, which is not desirable for measurements/experiments requiring a high degree of sensitivity.

Another approach is to use a mechanically rotating ball lens in a laser projection system, where it was shown that the speckle contrast could be reduced by 54.12%. However, the motor-driven ball lens has a rotating shaft which can deviate from the centre of the ball lens, a series of light spots shifts while the lens is rotating. To obtain a stable light spot on the projection screen while the ball lens is rotating, the speed of rotation must be fast [99]. Additionally, the aberration caused by the deliberate deviation distance from the ball centre to the rotation axis would be a problem when the projection area is large. Again, even though this approach is effective at reducing speckle it comes at the price of mechanically moving components.

An alternative approach is to employ electro-optic materials that can be made compact and free from moving parts which can generate a series of statistically independent speckle patterns within a finite period of time when a voltage is applied. Towards this end, liquid crystalline materials have been shown to be promising candidates [16, 17, 100]. The combination of the birefringence and the reorientation of the director when an external electric field is applied make it particularly appealing for the generation of random phase or polarisation states that can lead to decorrelated speckle patterns.

Numerous works have been published to demonstrate the potential of LC devices and materials for speckle reduction. The first work on this was published by K. Sueda *et al.* where they used a 15 micron-sandwiched-photo-aligned cell and reduced the speckle down to $\frac{1}{\sqrt{2}}$ [67]. Inspired by that, other groups started to investigate LCs in speckle reduction. One example is the work by Zhaomin Tong *et al.* who demonstrated a 55% reduction by using a polymer dispersed nematic LC (PDLC) diffuser [101]. Separately, Hayato Ishikawa *et al.* have shown that ferroelectric LCs (FLC) dispersed with fine SiO_2 particles can reduce the speckle noise by more than 40% when voltages of the order of 150 V were used [71]. A more significant reduction was demonstrated by Andreev *et al.*, who manipulated the spatially and temporally random refractive index across the FLC resulting in a 50% reduction in speckle [102]. These findings were also supported in studies conducted by Furue *et al.* where they were able to show successful speckle reduction using polymerized FLCs or surface stabilized FLCs as well as using photocurable monomer dispersed nematic LCs [103, 104]. Additionally, LC-SLM can be used to generate cyclic random phase masks corresponding to the Hadamard orthogonal functions. This method has been shown to reduce the speckle contract by $\frac{1}{\sqrt{64}}$ when the SLM was programmed to generate 64 separate phase patterns [105]. The performance of the SLM in speckle reduction is impressive, but their sheer cost and size make these impractical for many applications.

Our technique is based on electrohydrodynamic instabilities (EHDI) whereby the application of a low-frequency AC electric field results in competing torques between the conductivity from charged particle impurities and the dielectric coupling to the macroscopic helices in a chiral material.

This can create a dynamic scattering state, after breaking up the William domain structure, for light that can then be used to generate a series of time-sequentially angular decorrelated speckle patterns that average out over the integration time of the detector (e.g., the human observer), which in turn leads to a significant reduction in the speckle.

4.2 Chiral Nematic LCs for Laser Speckle Reduction

4.2.1 Selection of Nematic LCs

In this project, the compositions of the material are a host chiral nematic LC, which forms the base and an ionic/redox dopant supplying cation and anion components. A series of base nematic LCs were considered with different dielectric constants, anisotropy and conductivity. Table 4.1 lists their important physical properties. All materials listed are provided by Merck KGaA.

Nematic LC	n_e	n_o	Δn	$\varepsilon_{\parallel}$	$\varepsilon_{\perp}$	$\Delta\varepsilon$	$\gamma(mPas)$	$T_c(^{\circ}C)$
BL006	1.8148	1.5296	0.2852	20.0	4.7	15.3	426	113
MLC-2172	1.8139	1.52	0.2939	17.8	4.4	13.4	334	111
MLC-7022-000	1.5618	1.4745	0.0873	11.8	3.3	8.4	100	81
MDA-19-3138	1.6695	1.4967	0.1728	44.6	6.1	38.5	242	88

TABLE 4.1: Key physical properties of the nematic LCs considered. Birefringence was obtained at 589.3 nm at 20°C. The dielectric anisotropy is measured under 1 kHz, 20°C. The rotational viscosities for each nematic used in this section are quoted at 20°C as well. Values were taken from the literature [106, 107]

The properties listed in Table 4.1 can potentially influence the performance of the speckle reduction in different ways and it is a balance in selecting the material. According to a previous study [36], as the birefringence values increase the minimum speckle contrast is found to be reduced. However, when the Δn is larger than 0.2, the correlation between the C_{min}

and Δn becomes weaker. Above that value, there is no significant difference for mixtures with different birefringence values. However, a higher birefringence value leads to a decrease in transmission of the device [36]. For these reasons, the nematic LC mixture BL006 was chosen for this work.

4.2.2 Influence of Physical Properties

The speckle reduction is achieved via the EHDI effect which means our devices are operating in the conductive regime, instead of the dielectric regime. The relation between the EHDI regime and the frequency is as follows: for a lower frequency ac electric field, the EHDI forms and the cells turn into a turbid scattering state. While increasing the frequency, the regime will change into a dielectric mode and the change over point is close to the space-charge relaxation $f = \frac{4\pi(\sigma_{\parallel}+\sigma_{\perp})}{\varepsilon_{\parallel}+\varepsilon_{\perp}}$ [41]. Without charge injection from the electrodes or deliberately added ionic dopants, f is relatively small. However, with either redox dopants (or zwitterion dopants mentioned in Chapter 5), the f can be rather high.

Another important parameter is the amplitude of the electric field. The amplitude should be controlled above the periodic perturbation threshold E_{th} and below the critical unwinding threshold E_c. It has been verified [36] that the minimum speckle contrast is achieved around the E_c and it is always above E_{th} and falls in the DSM regime [58, 68]. To conclude, the dielectric constant and the conductivity anisotropy mainly affect the range of the EHDI regime and the electric field condition for the best speckle reduction. This is because E_c, according to Equation 2.17, is proportional to $(\Delta\varepsilon\varepsilon_0)^{-\frac{1}{2}}$. Meanwhile, the threshold for the formation of the periodic perturbation is related to $\frac{\varepsilon_{\parallel}+\varepsilon_{\perp}}{\varepsilon_{\perp}}$ as well as $\frac{\varepsilon_{\parallel}+\varepsilon_{\perp}}{4\pi(\sigma_{\parallel}+\sigma_{\perp})}$ [108].

The aim of this project is to decrease the speckle contrast within the

EHDI regime as much as possible. According to Reference [100], the pitch is of great importance for achieving minimum speckle contrast. The minimum speckle contrast decreases as the pitch decreases until a certain length P_0. For pitches smaller than P_0 will not bring a significant reduction of the minimum speckle contrast but will increase the transmission of the light. This is beneficial for display applications, however, one should notice that the optimum condition of the electric field $E_c \propto P_o^{-1}$. For a shorter pitch, the energy consumption will increase significantly and the required voltage might exceed the maximum amplitude that a setup can supply. Also, when mixing the host nematic LCs with a higher concentration of chiral dopants (for high twisting power dopants > 0.5 wt.% and for low twisting power dopants >20 wt.%), the LC properties relative to the speckle reduction might change because of the large amount of additives. Thus, in the following project, the pitch is not selected as the minimum measurable length of 209 nm but selected as the pitch for which the optimum amplitude of the electric field is below E= 20 V/µm for a 20 µm cell.

4.3 Redox Dopants

According to the research carried out by Herich and Rondelez, in order to boost the EHDI, charge injection is effective and necessary for any material with extremely low conductivities. The motion of these ions through the LC can cause turbulence. To encourage instability in the LC, researchers have investigated different approaches such as the use of ionic dopants in the form of CTAB or redox dopants [16, 72]. In the previous work, even though the reduction in the speckle contrast was encouraging, the degradation of the CTAB-doped thin-films at high electric field amplitudes, due to the irreversible electro-chemical reactions that occur at the electrodes, limits their use in practical applications [109].

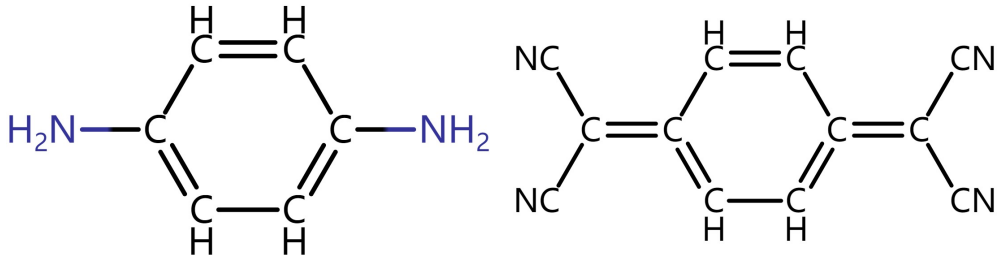

(a) (b)

FIGURE 4.1: The chemical structures of the redox dopants considered in this study, 7,7,8,8-tetracyanoquinodimethane (TCNQ) and *p*-phenylenediamine (PPD).

The purpose of the study in this chapter, therefore, is to consider the impact of using redox dopants instead of conventional ionic dopants such as CTAB, and to demonstrate an improvement in the operating lifetime of the LC diffuser when subjected to a range of electric field conditions. In order to enhance the conductivity properties and avoid permanent electochemical deterioration in the diffuser, a redox dopant in the form of 7,7,8,8-tetracyanoquinodimethane (TCNQ) or *p*-phenylenediamine (PPD) (see Figure 4.1) was added at different concentrations by weight to a chiral nematic LC mixture [110, 111]. TCNQ and PPD are examples of electron acceptor and donor species, respectively, that can effectively increase the density of current carriers (ionic charges) [72].

4.4 LC Speckle Reducer Without Dopants

To characterize the speckle reducer, we have developed an automated system that records the speckle contrast in real-time and is configured in accordance with the recommended practice for the measurement of speckle in laboratory conditions as defined by the Laser Illuminated Projector Association

(this was introduced in Chapter 3, Figure 3.7(b)) [112]. An electric field was applied to the LC devices using a dual-channel function generator (Tektronix AFG 3022) and a voltage amplifier (FLC Electronics F10AD). To identify the optimum operating conditions where the speckle contrast would be reduced to a minimum value, each LC device was subjected to three separate tests. First, the speckle contrast was recorded by sweeping through a range of electric field amplitudes (10-20 V/µm in increments of 2 V/µm) and frequencies (20-100 Hz in increments of 10 Hz). This coarse sweep of the field parameters provided an estimation of the electric field conditions and frequency requirements required to achieve maximum speckle reduction. Based on this quick scan test assessment, the next step was to subject each device to a higher resolution scan to identify precisely the field parameters required for peak speckle reduction. In this peak scan test, the increments of the electric field and frequency were 0.2 V/µm and 1.0 Hz, respectively. Finally, each LC device was subjected to a steady-state response test. For this, the signal generator was set to apply the electric field conditions corresponding to peak speckle reduction and the speckle contrast was recorded every 1 s continuously to determine the variation of the speckle contrast over a period of time. All of the tests mentioned above were carried out at 30 ºC. For the extended lifetime measurements, devices were operated at their peak speckle reduction electric field conditions, and the speckle contrast measurement system was set to record at regular intervals.

An example of the speckle patterns captured on the CCD camera without and with the LC diffuser is presented in Figure 4.2(a) and 4.2(b). For this example, the mixture consisted of the nematic LC (BL006, Merck) and 3.0 wt.% of the high-twisting power chiral dopant, R5011 (Merck). The mixture was found to have a pitch of $P_0 \approx 310$ nm at 30ºC and the peak speckle reduction electric field conditions were found to occur at E_p = 15.3

V/µm and f_p= 38 Hz, where E_p and f_p are respectively the electric field and frequency at which peak speckle reduction is obtained. A variety of amplitudes and frequencies were experimented with to identify the ideal electric field conditions, and the condition that resulted in the least amount of speckle contrast was considered the best. The process consisted of a quick scan test with larger steps, followed by a peak scan test with finer scans. The output for each test is a colour map with the bluest blocks indicating the minimum speckle contrast, as shown in Figure 4.2(c) and 4.2(d). The corresponding electric field conditions were identified as the optimal control conditions for the device under test using these colour maps as a reference.

To illustrate how the speckle contrast varies with the electric field parameters (i.e., amplitude and frequency) applied to the LC diffuser, Figure 4.2(c) and 4.2(d) shows the results for our base mixture (without redox dopants) in the form of colour maps. Figure 4.2(c) shows the result for a low-resolution test used to identify (approximately) the field parameters where the maximum reduction in the speckle contrast is observed. Results are presented for electric field amplitudes ranging from 10 V/µm to 20 V/µm and frequencies from 20 to 100 Hz. The range of the frequency and the amplitude are selected in order to trigger DSM in the device. If the amplitude of the electric field is too low then the scattering state is too weak to break up coherence and reduce speckle. However, if the electric field amplitude is too high the helix will unwind preventing the formation of a scattering state. Meanwhile, the frequency has to be neither too low that the observer perceives flickering of the scattering state, nor too high that the device enters the dielectric regime. In this case, no notable change was observed at field amplitudes below 10 V/µm. It can be seen that the greatest reduction in the speckle contrast is observed for amplitudes around 15 V/µm across frequencies from 20 to 80 Hz. The black boxed region in 4.2(c) and 4.2(d) identifies the electric field

parameters for which the lowest speckle contrast was recorded. Across the range of frequencies shown here, the speckle contrast is found to reduce with increasing electric field amplitude up to the point when the helical structure unwinds, at which point all dynamic scattering ceases, as shown by the dark red regions in Figure 4.2(c) at field amplitudes above ≈ 15 V/µm. At higher fields, the alignment transforms to a homeotropic state, so EHDI ceases and no speckle reduction is observed in this state [100].

Figure 4.2(d) is an example of a high-resolution scan conducted to find the precise field conditions at which the speckle contrast was minimized; in this case, the results show that the lowest speckle contrast was observed for an amplitude of $E = 15.3$ V/µm and a frequency of $f = 38$ Hz. This field is quite large because of the relatively short pitch of the chiral material used (hence a large unwinding field), and the frequency optimises turbulence in the conductive EHDI regime whilst ensuring that any associated flicker is not visible to the human eye. (Note: the results shown in Figure 4.2, and subsequent results discussed in this chapter, are generally obtained at a temperature of 30 °C. This slightly elevated stabilised temperature is used because the actual room temperature fluctuates somewhat.)

4.5 LC Speckle Reducer With Redox Dopants

To determine the impact of the redox dopant on the speckle contrast and the electric field conditions for maximum speckle reduction, sweeps of the electric field amplitude and frequency were carried out for the base mixture consisting of BL006 +3.0 wt.% R5011 and 1.0 wt.% of either redox dopant, TCNQ or PPD. For the purposes of comparison, measurements were also conducted for a sample consisting of 1.0 wt.% of the ionic dopant, CTAB. For these comparisons, the base chiral nematic LC mixture was doped with

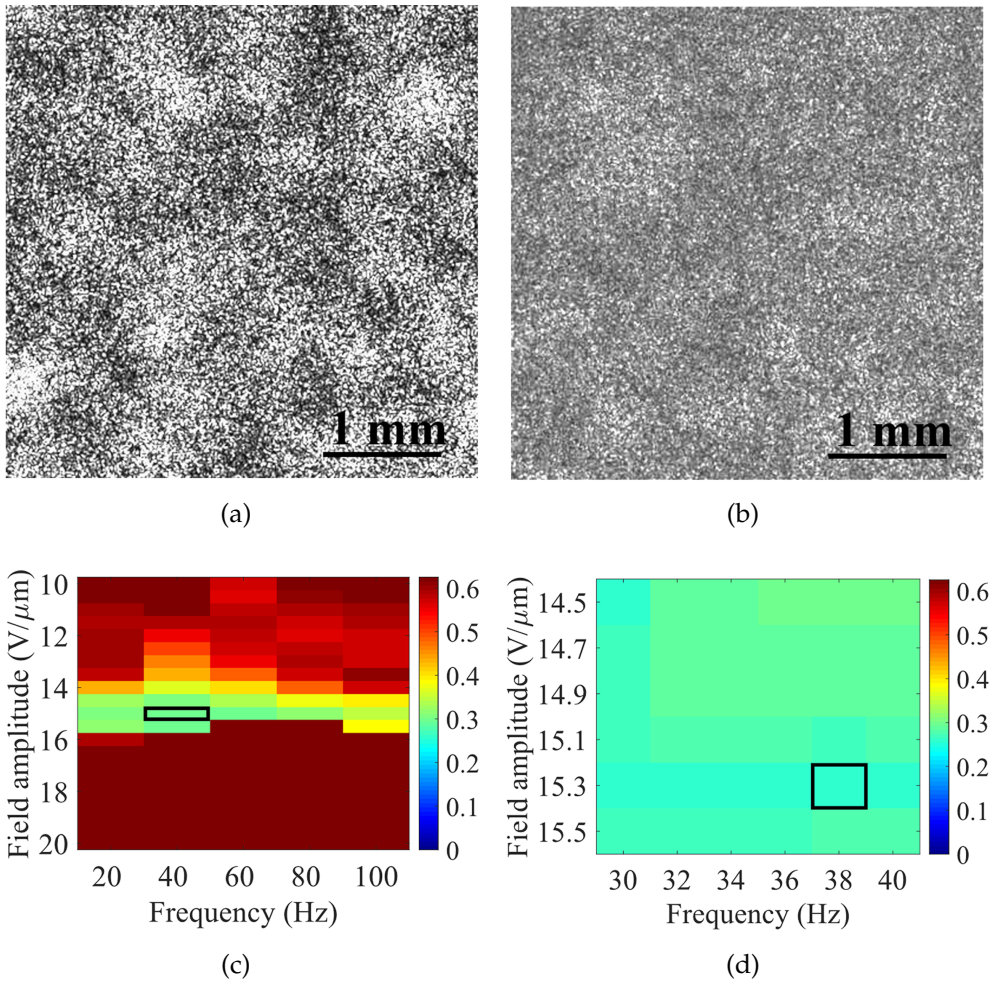

FIGURE 4.2: Examples of the speckle pattern recorded by the CCD camera when (a) there is no LC diffuser ($C = 0.65 \pm 0.02$) or (b)with a LC diffuser inserted in the system (filled with BL006 + 3.0 wt.% R5011; $C = 0.26 \pm 0.02$). (c) and (d) are examples of a speckle contrast colour map for the base mixture (BL006 + 3.0 wt.% R5011) used in this study, which shows the speckle contrast as a function of electric field amplitude and frequency under (c) a low-resolution test and (d) a high-resolution peak scan test. The black boxes in (c) and (d) highlight the minimum speckle contrast for each test which are $C = 0.29 \pm 0.02$ at $E_p = 15$ V/µm, $f = 40$ Hz and $C = 0.26 \pm 0.02$ at $E_p = 15.3$ V/µm, $f = 38$ Hz, respectively. The experiments were taken at a temperature of 30 ºC and the cell gap was 20 µm. The colour bar on the right represents the legend for the speckle contrast. To be clear, (b) shows the speckle pattern observed from the region indicated by the black box in (d).

different concentrations (0.5 wt.%, 1.0 wt.%, 1.5 wt.%, 2.0 wt.%) of either the redox dopant or ionic dopant. It was noted that the ionic doped mixture tended to degrade rapidly during testing if a concentration higher than 1.0 wt.% was used. Therefore, 1.0 wt.% of dopant was used for the initial comparisons. (Note: data showing behaviour at various concentrations of redox dopant are shown later in Figure 4.6, and discussed in the associated text).

The results for a concentration of 1.0 wt.% of the different dopants are presented in Figure 4.3, where it can be seen that the addition of either a redox or ionic dopant greatly increases the range of frequencies and field amplitudes over which speckle reduction is observed. In addition, for the samples including either the redox dopant, TCNQ, or the ionic dopant, CTAB, the field amplitudes required to observe the maximum reduction in the speckle contrast are found to occur at lower values. For example, the sample consisting of the 1.0 wt.% TCNQ dopant, in particular, exhibits a reduction in the speckle contrast across almost all of the range of frequencies and field amplitudes considered here, with the minimum speckle contrast (maximum speckle reduction) of $C = 0.14 \pm 0.02$ being observed for an electric field amplitude of $E = 15$ V/µm and a frequency of $f = 30$ Hz. In comparison, for the base mixture, the minimum speckle contrast recorded was $C = 0.26 \pm 0.02$, which is noticeably higher than that observed for the sample doped with TCNQ. The sample containing the ionic dopant was found to exhibit an even lower speckle contrast of $C = 0.11 \pm 0.02$ at a frequency of 100 Hz and a comparable electric field amplitude. However, it should be noted that this sample was rather unstable, as will be discussed further.

Once the minimum speckle contrast and corresponding electric field conditions had been determined for each sample, each one was then subjected to a 5-minute steady-state response test every day for a period of two weeks. A plot of the minimum speckle contrast measured (at the peak field

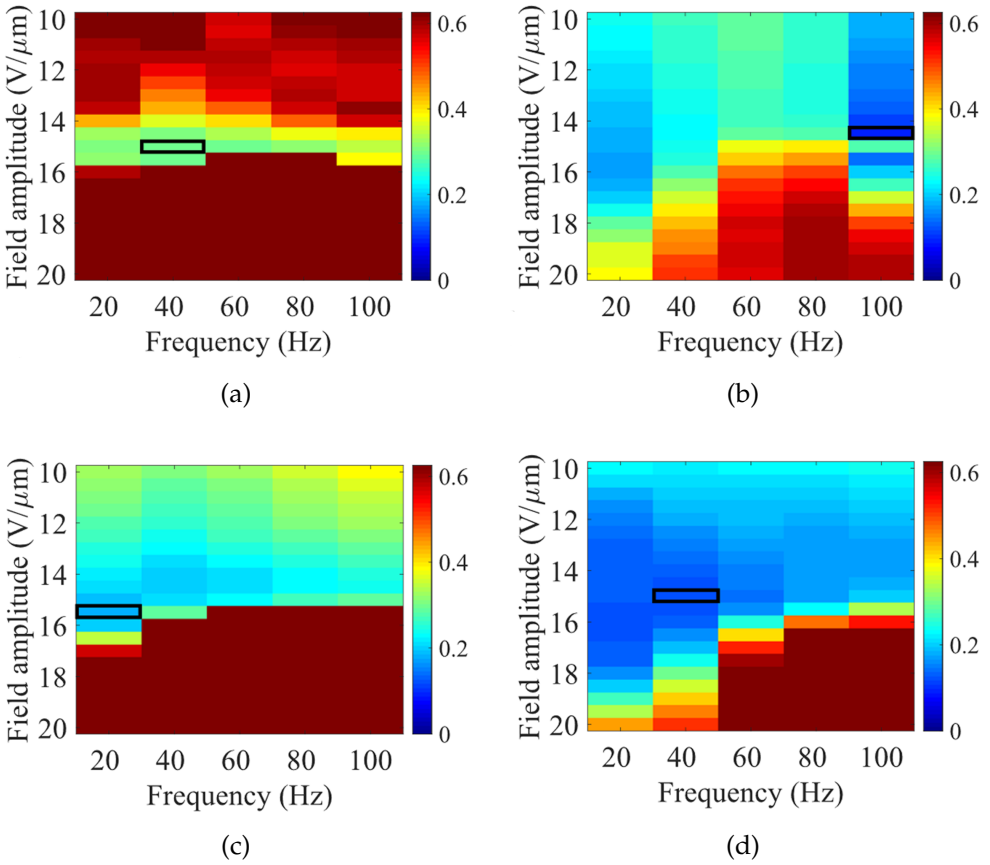

FIGURE 4.3: Colourmaps of the speckle contrast as a function of the electric field amplitude and frequency for the samples: (a) Base mixture (BL006 + 3 wt.% R5011) (repeated here from Figure 4.2(b) for the purposes of comparison); (b) Base mixture + 1.0 wt.% CTAB; (c) Base mixture + 1.0 wt.% PPD; (d) Base mixture + 1.0 wt.% TCNQ. Measurements were conducted at a temperature of 30°C and each sample was 20 µm-thick.

conditions) over this two week period can be seen in Figure 4.4, which shows the variation in the measured speckle contrast for the base chiral nematic LC sample as well as those consisting of either the acceptor or donor redox dopants, PPD and TCNQ. Despite starting from a lower value of the speckle contrast, it is clear that the sample containing the ionic dopant, CTAB, deteriorates over time as the speckle contrast increases notably. By the end of the second week, the speckle contrast approaches the value recorded as if no LC diffuser was present in the experimental system (i.e., $C \approx 0.6$). At this point, due to the irreversible processes taking place, there is substantial degradation and oxidation of the LC material inside the cell. The resultant

significant changes in the composition of the LC mixture in the cell means that EHDI no longer takes place under these conditions, so the dynamic processes cease. Hence, the cell no longer functions as a speckle reducer, and so, the speckle level returns to the "un-reduced" value of around $C = 0.6$. In contrast, for the base mixture and the two samples containing the redox dopants, there was very little change in the speckle suppression performance over time. Furthermore, the speckle contrast for the redox dopants shows a very flat response over the two-week period and the low value of $C = 0.14 \pm 0.02$ was maintained throughout the sample with the TCNQ redox dopant.

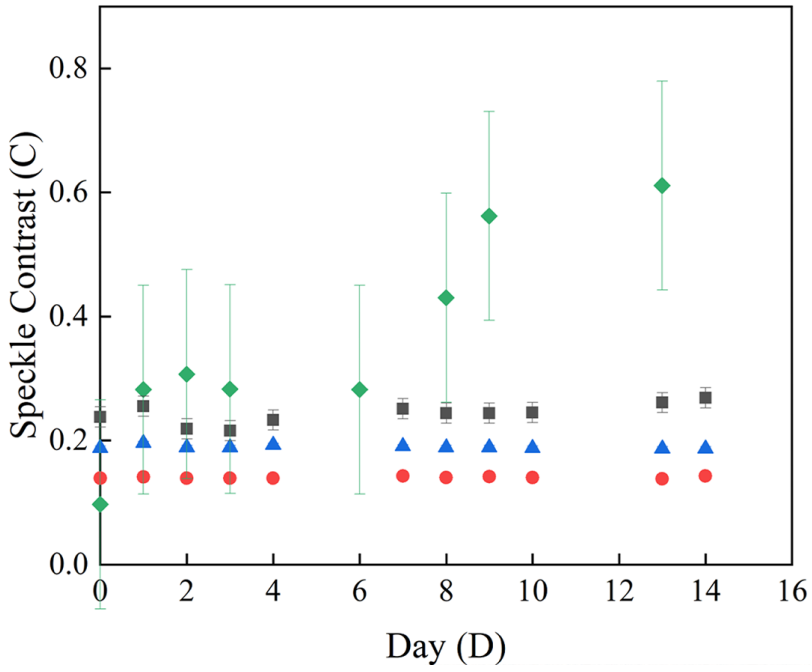

FIGURE 4.4: The speckle contrast as a function of day number over a two week. Data points represent the results for a 5-minute steady-state response on each day for the following LC mixtures: BL006 + 3 wt.% R5011 (black squares); BL006 + 3 wt.% R5011 + 1.0 wt.% CTAB (green diamonds); BL006+ 3 wt.% R5011 + 1.0 wt.% PPD (blue triangles); BL006 + 3wt.% R5011 + 1.0 wt.% TCNQ (red circles). The pitch of the chiral nematic samples were $P_0 \approx 310$ nm and the measurements were carried out at a temperature of 30 °C.

It is clear that with the addition of redox dopants to the base mixtures, the speckle contrast can be significantly reduced. Additionally, due to the reversible electro-chemical reactions, devices containing redox dopants were able to perform better over time, especially compared with the CTAB-doped

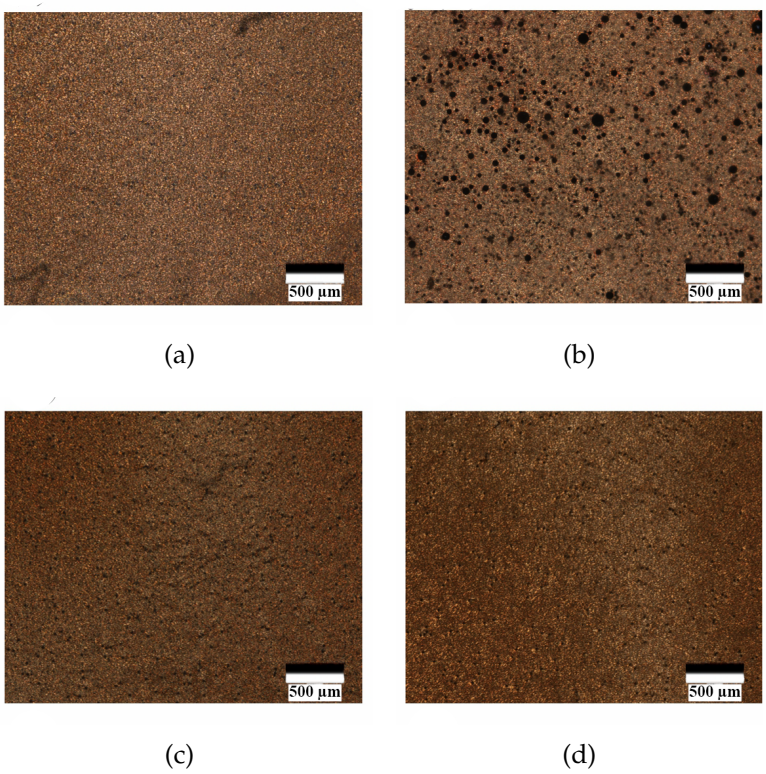

FIGURE 4.5: Polarising optical microscope images of the optical texture of the CTAB-doped mixture recorded in Figure 4.4 on the 1st day (a) and 14th day (b) of testing are also shown. Polarising optical microscope images of the optical texture of the TCNQ-doped mixture recorded on the 1st day (c) and 14th day (d) of testing are also shown. Scale bars on the images are 500 µm.

mixture. The CTAB-doped mixture did allow a reduction of the speckle contrast to values closer to $C = 0.10$ at room temperature where the speckle pattern becomes almost imperceivable to the human eye; however, it is clear from the microscope images in Figure 4.5(a) and 4.5(b) that the sample degraded significantly within a short period of time. In comparison, it is evident from the microscope images in Figure 4.5(c) and 4.5(d) that the TCNQ-doped sample did not show significant degradation.

Having demonstrated an improvement in the device performance with the addition of the redox dopants to the chiral nematic LC host, the next steps were to determine: 1) the optimal concentration for the two different redox dopants; 2) to identify which redox dopant was able to reduce the speckle contrast to the lowest value at room temperature, and 3) how these

mixtures performed over a period of continuous use. Towards this end, Figure 4.6 shows the measured speckle contrast for mixtures consisting of either redox dopant (PPD or TCNQ) at concentrations by weight ranging from 0.2 – 2 wt.%. It is clear from the figure, and in accordance with Figure 4.3 and 4.4, that the addition of either redox dopant results in a dramatic decrease in the speckle contrast, with the lowest values observed for mixtures consisting of <0.5wt.% redox dopant. Specifically, at concentrations by weight of 0.2 wt.%, the speckle contrast was found to be as low as $C = 0.11 \pm 0.02$ for the sample containing the TCNQ dopant (which represents an approximately 60% reduction in the speckle contrast compared to that observed for the base mixtures and an approximately 88% reduction compared to that observed for no LC diffuser).

For higher concentrations of dopant, irrespective of whether it is an acceptor or donor redox dopant, the speckle contrast was found to increase, but was still lower than that observed for devices fabricated using just the base mixture. This trend is both reasonable and expected. It appears that without the injection of cations or anions, the instability caused solely by inherent impurities is limited, resulting in limited scattering and speckle reduction. However, the concentration of dopants that can participate in redox reactions is also limited by two factors: E_c and f, where f should be bigger than 20 Hz (based on average human eye integration time) and smaller than the frequency threshold of the dielectric switching regime. Take the acceptor redox dopant for example, the concentration of the available electron generated by the negative electrodes within one period is limited by the amplitude of the applied voltage and the frequency will influence the time of the reversible reactions and the transition time between two electrodes. Thus, there will be a saturation point where increasing the concentration of the redox dopant has no improvement on the speckle reduction performance.

A more refined concentration exploration could be conducted in the future. Here a proof of concept and general verification are the main objectives.

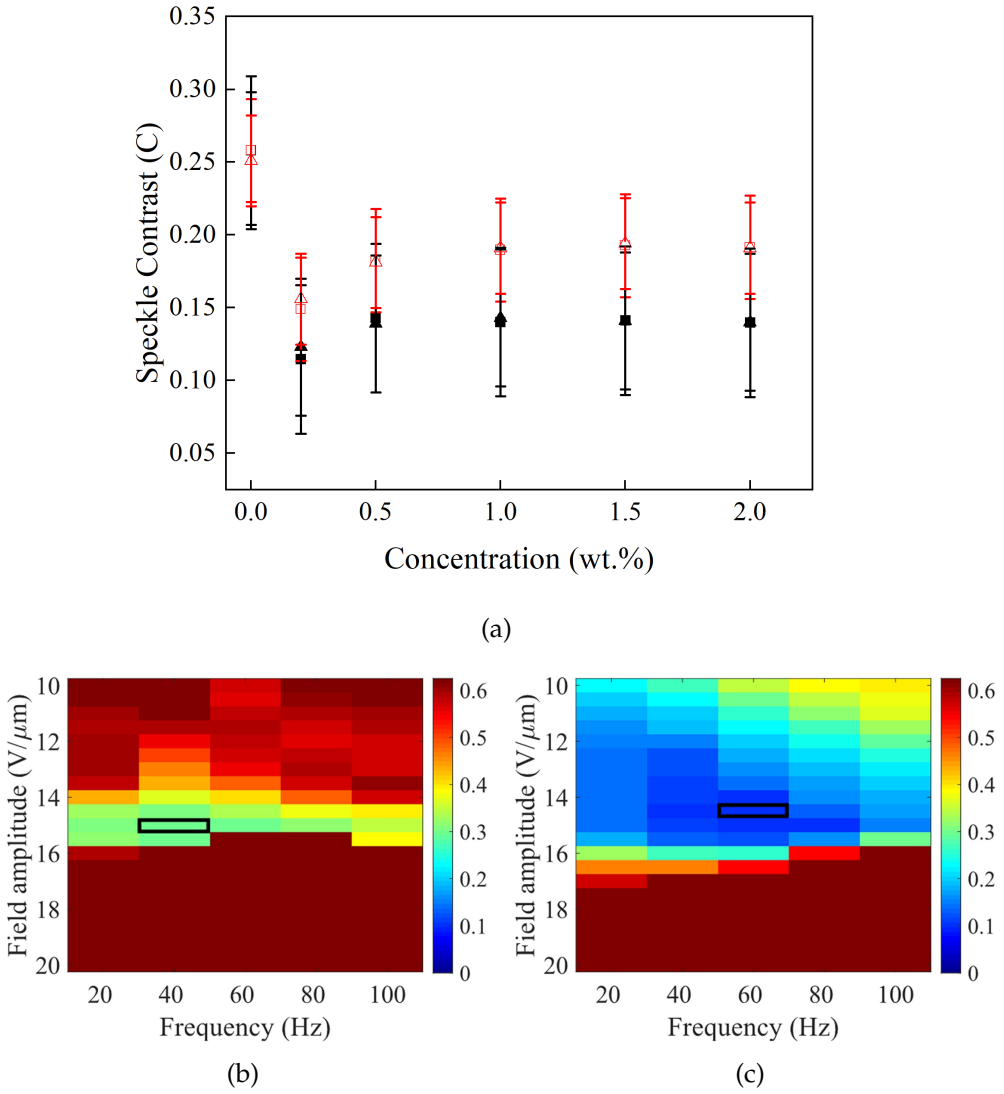

FIGURE 4.6: Plot of the speckle contrast, *C*, as a function of the concentration by weight of the redox dopant for samples consisting of BL006+3 wt.%R5011+PPD (red open symbols) and BL006+3wt%R5011+TCNQ (black solid symbols). Measurements conducted immediately after fabrication of each device are represented with square symbols whereas measurements conducted 7 days after fabrication are represented with triangular symbols. Colourmaps of the speckle contrast in (b) and (c) show the quick-scan result for the concentrations of redox dopant as labelled in (a). These represent the worst-case scenario with just the base mixture (b) and the best-case scenario with the 0.2 wt.% TCNQ in the base mixture (c). The experiments were taken at a temperature of 30 °C and the cell gap in each case was nominally 20 µm.

Figures 4.7 and 4.8. show the variation in the speckle contrast, *C*, as

a function of electric field amplitude and frequency recorded for each concentration of redox dopant immediately after fabrication. The colourmaps make it clear that following fabrication the mixtures containing 0.2wt% of either redox dopant are more desirable in terms of peak speckle reduction, although the range of field parameters over which speckle reduction is observed is found to increase with the concentration of dopant. Moreover, for all concentrations, it can be seen that the mixtures with the TCNQ dopant consistently outperform those containing PPD, both in terms of the minimum speckle contrast and the range of field parameters over which speckle reduction is observed. A possible explanation for this phenomenon is that the chiral nematic LC base mixture used in this work has a certain preference to the category of the redox dopant. Here the PPD is an acceptor whereas the TCNQ is a donor, and by analyzing the results, it appears that the chiral nematic LC mixture (BL006+3 wt.% R5011) is more compatible with the donor than the acceptor.

For the sample that exhibited the lowest speckle contrast (BL006 + 3.0 wt.% R5011 + 0.2 wt.% TCNQ), we also investigated whether this low value for the speckle contrast could be maintained when the device was operated continuously over a period of time. For this experiment, a 20 µm-thick device containing the above mixture was connected to a signal generator and voltage amplifier to apply an amplitude and frequency that matched the peak operating conditions (E_p and f_p) for a continuous period of 7 days. A measurement of the speckle contrast was then recorded each day, which involved conducting a high resolution peak-scan test first to verify whether the E_p and f_p had drifted. It can be seen in Figure 4.9 that the speckle contrast for both the base mixture (BL006 + 3.0 wt.% R5011) and the best-performing redox-doped mixture (Base mixture + 0.2 wt.% TCNQ) increased with time but that

the redox-doped mixture plateaued at around $C \approx 0.13$. In all cases, the values for the base mixture were much higher than that recorded for the redox-doped mixture.

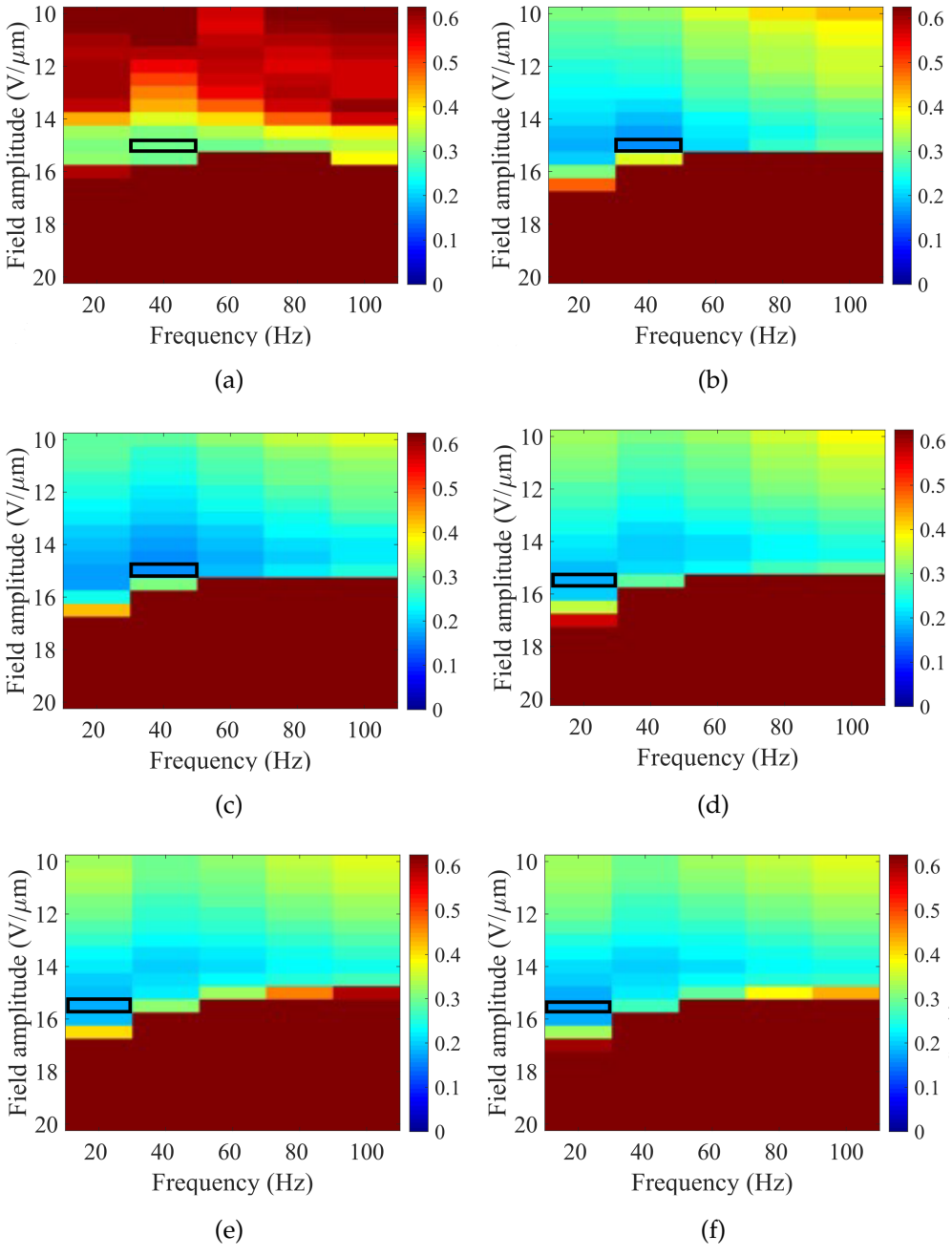

FIGURE 4.7: Colourmaps of the speckle contrast (tested on Day 0 – immediately after fabrication) for a range of electric field amplitude and frequency conditions for samples consisting of the base mixture (BL006 + 3 wt.%R5011) and (a) 0 wt.% PPD; (b) 0.2 wt.% PPD; (c) 0.5 wt.% PPD; (d) 1.0 wt.% PPD; (e) 1.5 wt.% PPD; and (f) 2.0 wt.% PPD. Measurements were carried out at a temperature of 30°C and for cell gaps of 20 µm.

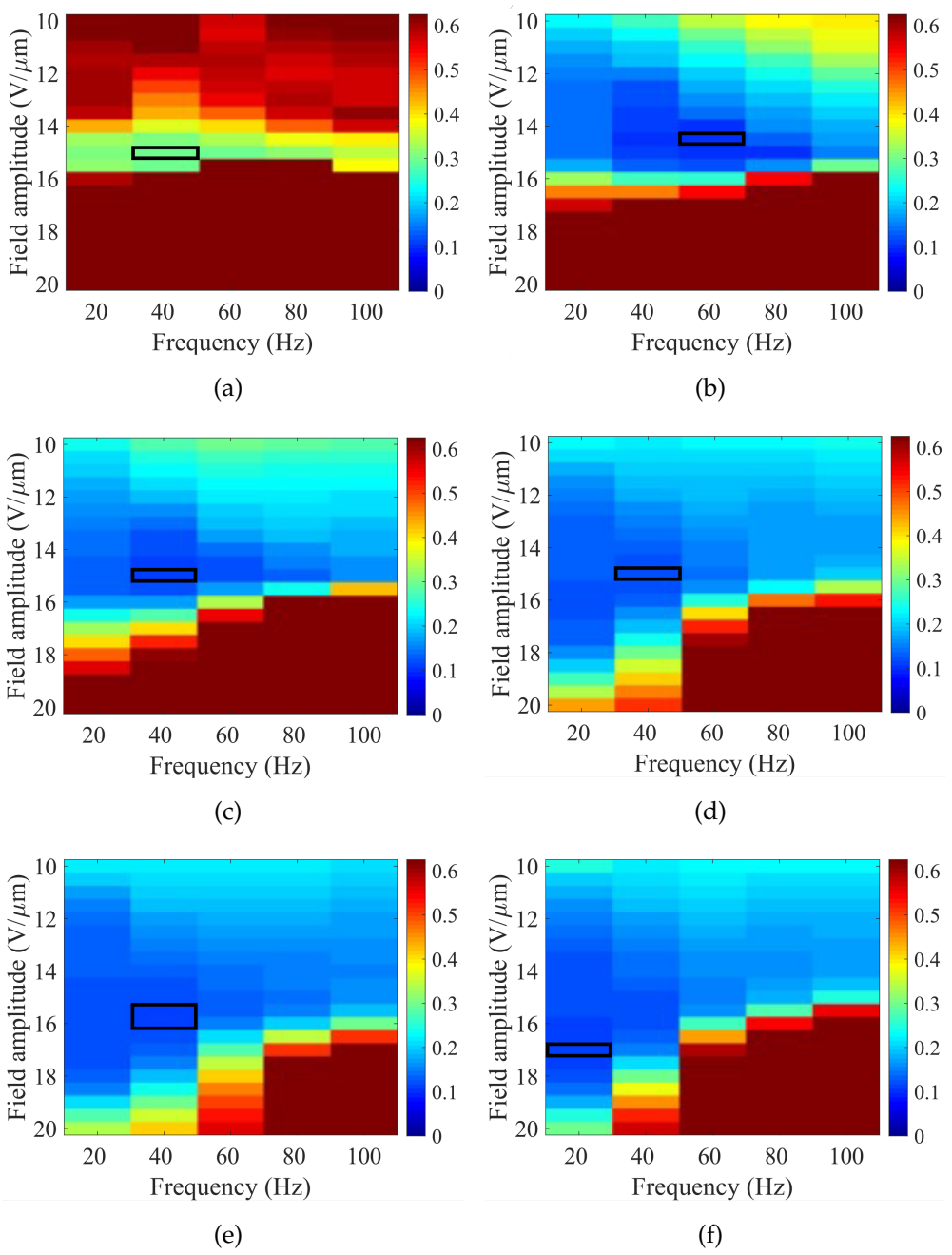

FIGURE 4.8: Colourmaps of the speckle contrast (tested on Day 0 – immediately after fabrication) as a function of the electric field amplitude and frequency for samples consisting of the base mixture (BL006 + 3 wt.%R5011) and (a) 0 wt.% TCNQ; (b) 0.2 wt.% TCNQ; (c) 0.5 wt.% TCNQ; (d) 1.0 wt.% TCNQ; (e) 1.5 wt.% TCNQ; and (f) 2.0 wt.% TCNQ. Measurements were carried out at a temperature of 30°C and for cell gaps of 20 µm.

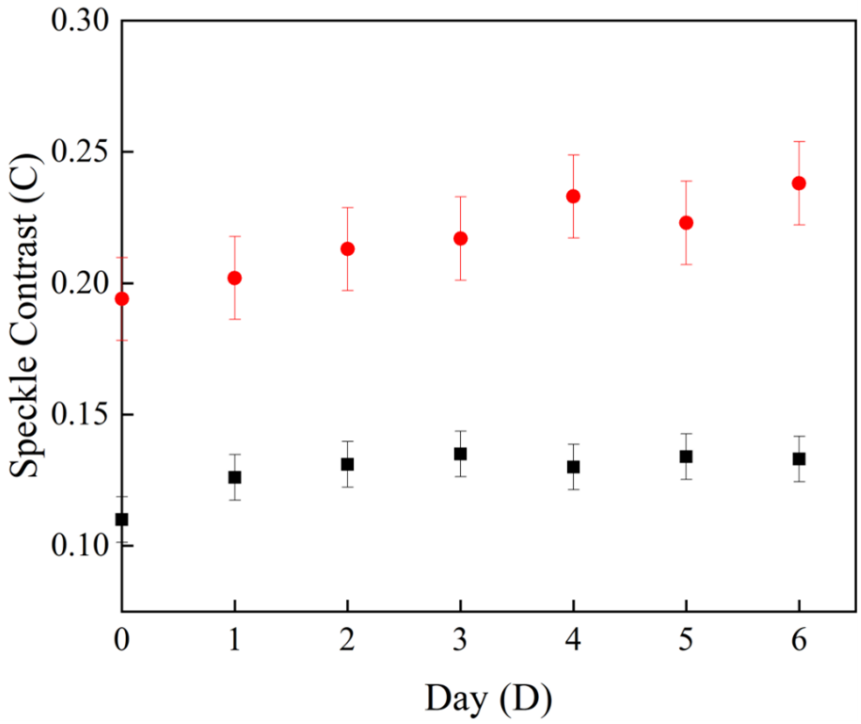

FIGURE 4.9: Plot of the speckle contrast as a function of the day number when the optimum mixture formulation (BL006 + 3.0 wt.% R5011 + 0.2 wt.%TCNQ, black points) was operated continuously over a period of 7 days. For the purposes of comparison, the red data points are data for the base mixture: BL006 + 3.0 wt.% R5011 when operated continuously over the same period of time. The sample was held at a constant temperature of 30°C for the duration of the 7 days and the sample thickness in each case was 20 µm.

4.6 Deployment in a Prototype Projector

To verify the performance of this LC speckle reducer technology in the setting of a practical application, photographs of images generated using a prototype projector system (modelled on a HITACHI CP-X250 Multimedia LCD Projector) with and without our LC technology were recorded. In this projector setup, the light source was a Coherent Genesis MX 561 SLM fibre laser with a wavelength of λ = 561±3 nm and the resultant image was projected onto a white screen using the set-up presented in Figure 4.10. In this case, the LC diffuser consists of the mixture (BL006 + 3.0 wt.% R5011 + 0.2 wt.% TCNQ) and the operating electric field conditions were E_p = 14.8 V/µm and f_p = 64 Hz. Figure 4.11 shows the images observed on the screen with and without the LC diffuser. It is obvious that with the insertion of the LC diffuser, the resolution and features of the projected images are noticeably improved. With the insertion of LC diffuser device, the speckle contrast was reduced by as much as 84%.

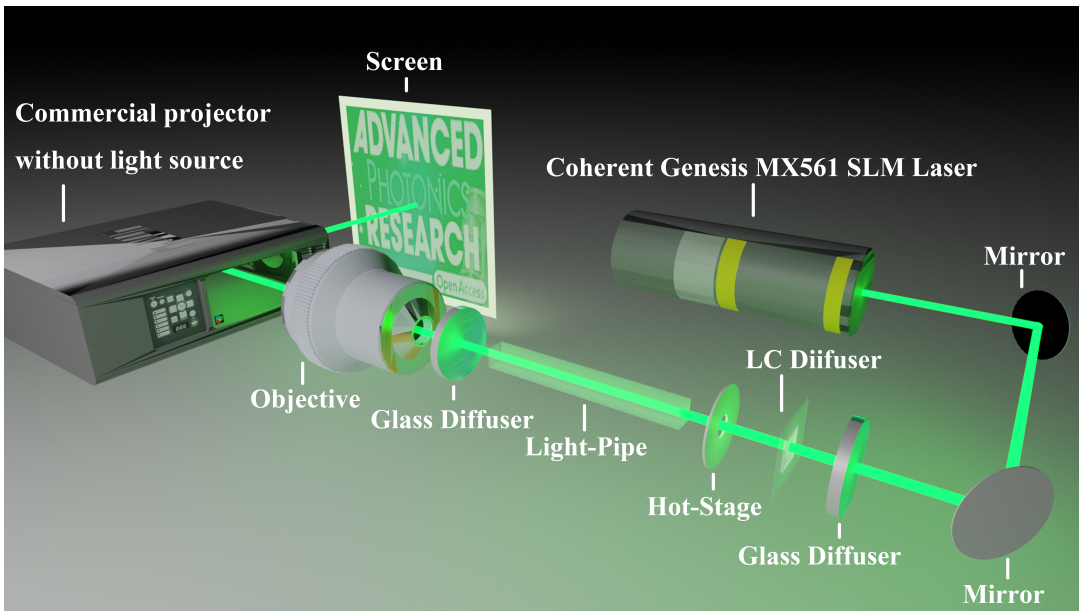

FIGURE 4.10: Schematic of the laser projector demonstrator.

Even lower values of the speckle contrast can be obtained by operating the LC diffuser consisting of the optimal mixture BL006 +3.0 wt.% R5011 + 0.2 wt.% TCNQ at a higher temperature of T = 55 ºC, Figure 4.12. The results show that at this higher temperature, the speckle contrast could be reduced to C = 0.08 ± 0.02 and the performance was stable over a 60 min steady-state response test.

FIGURE 4.11: Photographs of images generated using a prototype projector system (modelled on a HITACHI CP-X250 Multimedia LCD Projector) (a), (d) and (g) without our LC technology; (b), (e), (h) with the LC diffuser operated under suboptimal electric field conditions; (c), (f) and (i) with LC diffuser operated under optimal electric field conditions. The LC diffuser consisted of the mixture (BL006 + 3.0 wt.% R5011 + 0.2 wt.% TCNQ) filled into a nominally 20 µm-thick device. The LC diffuser was operated at T = 55°C.

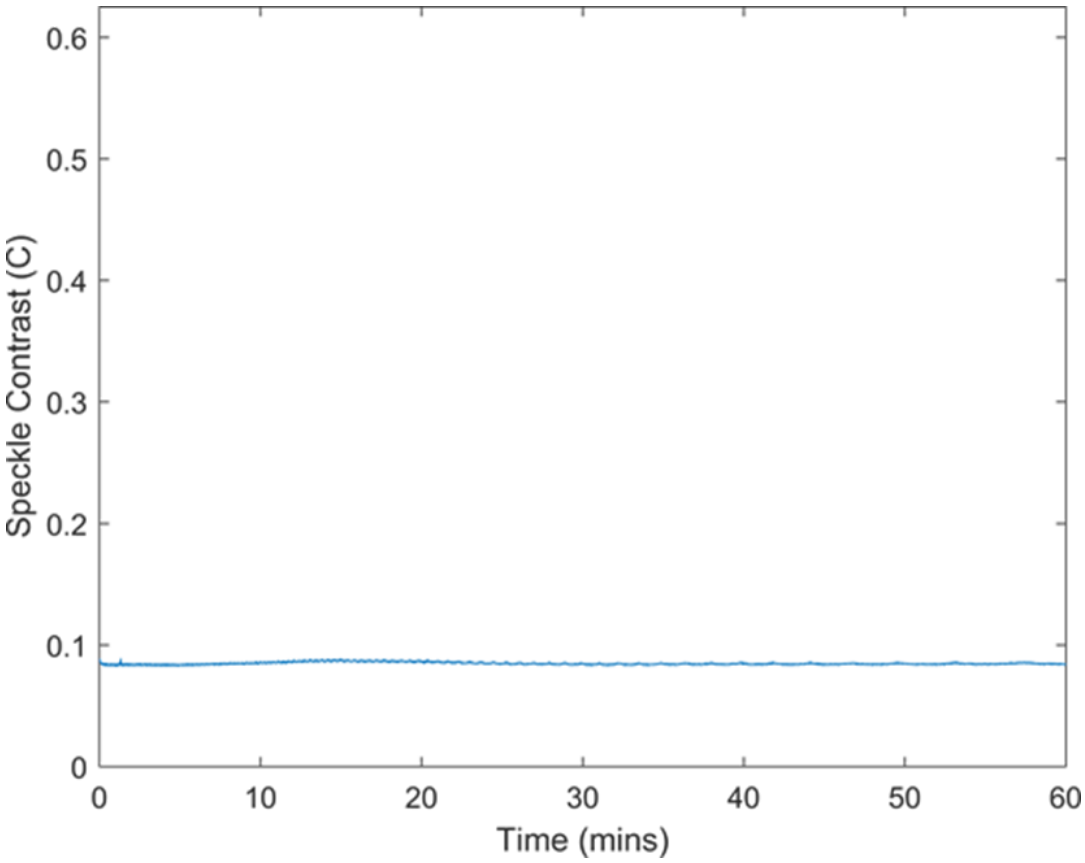

FIGURE 4.12: Speckle contrast, *C*, as a function of time for the optimal mixture consisting of BL006+3 wt.% R5011+0.2 wt.% TCNQ operated at a temperature of 55 ºC. The test was conducted on the 21st day after filling a 20 µm-thick cell.

4.7 Summary

To conclude, in this chapter, it has been demonstrated that the addition of a redox dopant (0.2 wt.% TCNQ) to a chiral nematic LC (composed of BL006 + 3.0 wt.% R5011) can significantly reduce the speckle contrast perceived in a projected image from $C = 0.65 \pm 0.02$ to $C = 0.11 \pm 0.02$ at a temperature of 30ºC when imaging with a CCD camera with an integration time of 50 ms, chosen so as to emulate the response of the human eye. Two different redox dopants were considered (TCNQ and PPD) in this study representing either an electron acceptor or electron donor type dopant. The dependence of the speckle noise reduction was investigated for chiral nematic mixtures containing these dopants at different concentrations by weight and were compared

with devices that contained either an ionic dopant, such as CTAB, or no additional dopants.

Overall, when considered over a period of time there appears to be some dependence of the speckle reduction on the concentration of redox dopant (for the range from 0.2 – 2 wt.%), with the best performance observed for a concentration of 0.2wt%). Also, it was found that for all concentrations considered the samples comprising the electron acceptor dopant exhibited the lowest speckle contrast values. Furthermore, the speckle reduction was considerably better with the addition of either redox dopant when compared to the performance of a LC diffuser consisting of just the base chiral nematic LC mixture. Unlike samples containing an ionic dopant, the performance was consistent over time, both when run intermittently over two weeks or when operated continuously for 7 days.

The LC diffuser device presented herein is compact, portable and easy to integrate into existing commercial systems that currently suffer from speckle noise. To highlight the ease with which the device can be integrated, a notable improvement has been demonstrated for an image generated using a commercial projector that was retro-fitted with a monochromatic laser source and our LC diffuser technology. The upcoming chapter will explore the utilization of an alternative dopant that has a higher likelihood of mitigating permanent electrochemical degradation and offering improved speckle reduction at room temperature. Furthermore, additional applications will be showcased, extending beyond the realm of laser projection scenarios.

Chapter 5

Zwitterion-doped LC Speckle Reducers for Immersive Displays and Vectorial Imaging

This chapter describes the use of zwitterionic dopants in chiral nematic liquid crystal (LC) speckle reducers. To begin with, the chapter demonstrates how the device's performance depends upon a range of material and environmental parameters. The results show that zwitterionic-doped LC speckle reducers (LC-SRs) can substantially reduce the appearance of speckle and such devices are then showcased in five different display and imaging scenarios. The results presented in this chapter form the basis of a paper submitted for publication entitled "Zwitterion-doped Liquid Crystal Speckle Reducers for Head-Up Displays and Vectorial Imaging".

5.1 Introduction

In this study, I demonstrate a new device incarnation that involves the dispersion of zwitterions (in the form of Reichardt's dye) into a chiral nematic LC host and show how this device can reduce the speckle contrast in a range

of different display and imaging applications. Zwitterions have been investigated in different applications previously including in luminescent perovskite nanocrystals [113] and as the supplier of charges in self-targeting nanocarriers for clinical applications [114]. Of relevance to LC-based devices, recent research demonstrated a new smart window technology by doping a negative dielectric anisotropy LC with zwitterions [115]. For the study presented in this chapter, the specific zwitterion dopant chosen was Reichardt's dye, which is an organic dye that was purchased from Sigma-Aldrich.

Commonly used electrolytes, such as ionic dopants suffer from electron accumulation at the surface layers and device degradation after repeated usage because of their unbalanced anionic and cationic composition. Redox dopants, investigated in the previous chapter, are another option that can provide cations or anions while not suffering electrochemical degradation. However, the speckle contrast can not be suppressed to a satisfactory degree for direct human eye perception at room temperature with solely redox dopants added. Zwitterions, with their equal amount of negatively and positively charged functional groups in one molecule, are considered as a great alternative to overcome these issues. In this chapter, results show that these zwitterionic-based LCs have great potential for speckle reduction and that the speckle contrast can be reduced to a level that is imperceptible to the human eye while maintaining transmission of around 50%. This new speckle reducer is then showcased in five different application scenarios: four are related to standard field illumination, which includes a wide-field microscope, holography, Head-Up Display (HUD), and high-intensity laser projector. The final demonstration is the applicability of these LC-SRs to vectorial illumination, in the form of a high resolution polarisation biopsy microscope.

5.2 Speckle Contrast Characterisation

5.2.1 Mixture Preparation and Device Fabrication

The LC-SRs consisted of a short-pitch positive dielectric anisotropy chiral nematic LC mixture dispersed with different concentrations of a zwitterionic dopant (Reichardt's dye) that were capillary filled into glass cells that consisted of transparent conductors coated onto the inner surfaces of the glass substrates to facilitate the application of an electric field. In this study, the base chiral nematic LC was made up from BL006+3.0 wt.% R5011 (both sourced from Merck Ltd) and, Reichardt's dye (purchased from Sigma-Aldrich), which enhances the electrohydrodynamic instabilities (EHDI) and generates a dynamic scattering mode (DSM). Reichardt's dye was chosen and the concentration of the dopant was carefully investigated in order to determine the optimum concentration. Specifically, the dye was added to the base mixture at different concentrations by weight (ranging from 0.1 wt.% to 0.8 wt.%).

These zwitterionic doped LC mixtures were capillary filled into either commercially available INSTEC LC2 cells that have a nominal cell gap of d = 20.0 µm, or home-made Fréedericksz cell with a gap of d = 40.0 µm. The effective area of the device typically had dimensions of 5 mm x 5 mm, The home-made thicker device (d = 40.0 µm) had an anti-parallel alignment pre-treated on the top and bottom indium tin oxide (ITO)-coated glass substrates. Each substrate was washed in acetone for a period of 10 min. The two ITO glass substrates were then separated by 40 µm thick spacer films and sandwiched together using UV polymerizable glue. To characterize the LC-SRs, the experimental configuration described in Chapter 3 (Section 3.4) was used.

As discussed in the previous chapter, the pitch of the chiral nematic LC is an important parameter that influences the performance of the speckle

reduction. Previous work has shown that the size of the scattering domains at low voltage is about the same order of the helical pitch (P) which means a shorter pitch should result in smaller scattering domains [36]. When the pitch is longer than 4 µm, the mixtures will only exhibit an electrically induced fingerprint texture rather than a focal conic scattering state, leading to little if any speckle reduction. Thus, to generate more scattering and uncorrelated speckle patterns, the concentration of the chiral dopant R5011 was carefully selected to be between 2.5 wt.% and 5.0 wt.%. Measurements of the pitch were carried out by determining the spectral location of the reflection band using a UV-vis spectrometer, Agilent Cary 8454, which has been introduced in Section 3.3. Additionally, shorter pitch based-speckle reducers require higher driving voltages. Therefore, to balance the speckle reduction requirements with the resulting power consumption, the pitch was selected such that the voltage was accessible using the equipment available in the lab.

5.2.2 Experimental Methods

The method used to characterise the speckle contrast was exactly the same as that employed in Chapter 4 and as described in Chapter 3. For the purposes of completeness, the process is summarised here. Before testing the devices in different imaging and display applications, the LC-SRs were first characterized in terms of the amount of speckle reduction that was achievable for different mixture compositions, device thicknesses, and operating temperatures. For each mixture formulation, a scan of the speckle contrast was performed for a range of electric field conditions (i.e., amplitude and frequency) in order to identify what conditions were required to obtain the maximum speckle reduction.

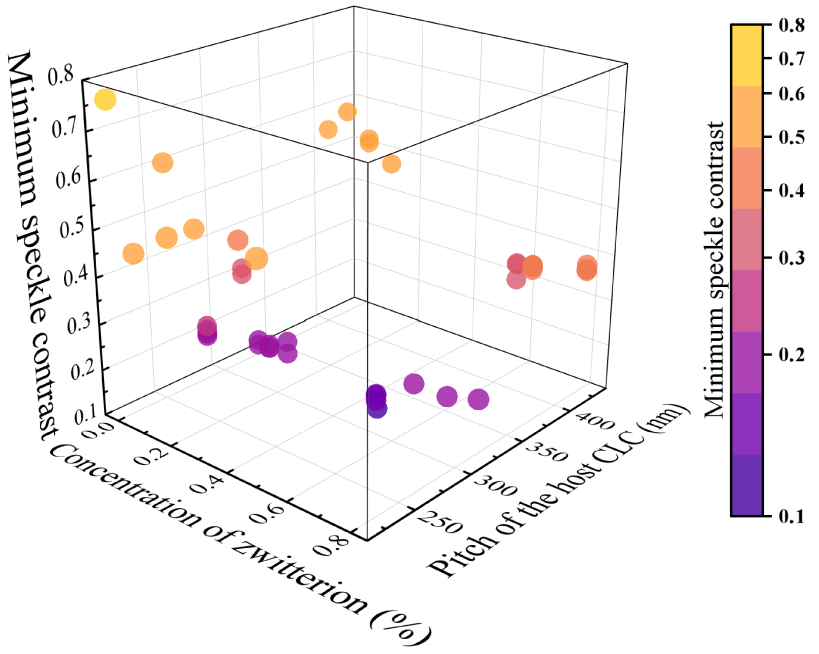

FIGURE 5.1: The minimum speckle contrast obtained for different pitch of the host chiral nematic LC and concentration of zwitterion dopant The optimum receipe is highlighted by the yellow dashed circle.

5.2.3 Concentration of Zwitterionic Dopant

Figure 5.1 shows how the speckle contrast changes subject to the pitch as well as the zwitterion dopant concentration. The coloured markers in Figure 5.1 represent the minimum speckle contrast after going through a quick scan test and a peak scan test (Section 4.4). The colour of the marker indicates the magnitude of the speckle contrast when the cell is operated under optimum driving conditions for each set of physical parameters. The mixture for each test was composed of a nematic LC, BL006, and a variation of chiral dopant ranging from 2.5 wt.% to 5.0 wt.% so that a wide range of pitch tests could be carried out. Each mixture was filled into a 20 µm device and operated at room temperature. Figure 5.1 shows that the best speckle suppression can be realized around P=310±10 nm where the concentration of the chiral dopant R5011 is about 3.0 wt.%. The trend is consistent in the case of different concentrations of the zwitterion dopant Reichardt's dye. Thus, the recipe used in this project is 96.5 wt.% nematic LC BL006, 3.0 wt.% R5011 and 0.5

wt.% Reichardt's dye.

As shown in Figure 5.2(a), the maximum reduction in the speckle contrast that was observed was found to depend upon the concentration of the zwitterionic dopant (Reichardt's dye) dispersed into the chiral nematic LC host. Figure 5.2(a) shows the minimum speckle contrast recorded as a function of the concentration of Riechardt's dye. At low concentrations of dopant, EHDI were insufficient to generate enough light scattering so as to reduce the speckle contrast to 0.1 or less. However, with an increase in the concentration of the zwitterionic dopant, the turbulence and dynamic scattering increased, resulting in a reduction in the speckle contrast. The optimum concentration of the zwitterionic dopant (Reichardt's dye) was found to occur at 0.5 wt.% at which point the speckle contrast was reduced to C = 0.15 ± 0.008 (for a cell gap = 20 µm and a temperature of 20 °C). Increasing the concentration of Reichardt's dye further resulted in a gradual increase in the minimum speckle contrast value but this was still found to be lower than that observed for the base chiral nematic LC mixture on its own.

The mixture that exhibited the lowest speckle contrast (BL006 + 3 wt.% R5011 + 0.5 wt.% Reichardt's dye) was further tested in a glass cell with a larger cell gap, the results of which are shown by the orange star in Figure 5.2(a). The smallest value of the speckle contrast, C = 0.07, recorded in this study was observed using a glass cell with a gap of 40 µm at a temperature of 50 °C. This corresponded to a very large speckle reduction of 90%. Figure 5.2(b), 5.2(c) and 5.2(d) show example scans of the speckle contrast over a range of electric field amplitudes and frequencies for the three data points highlighted in Figure 5.2(a). As described in Chapter 4, each mixture was characterized by first a low-resolution test followed by a high-resolution scan that was concentrated around the electric field conditions relating to

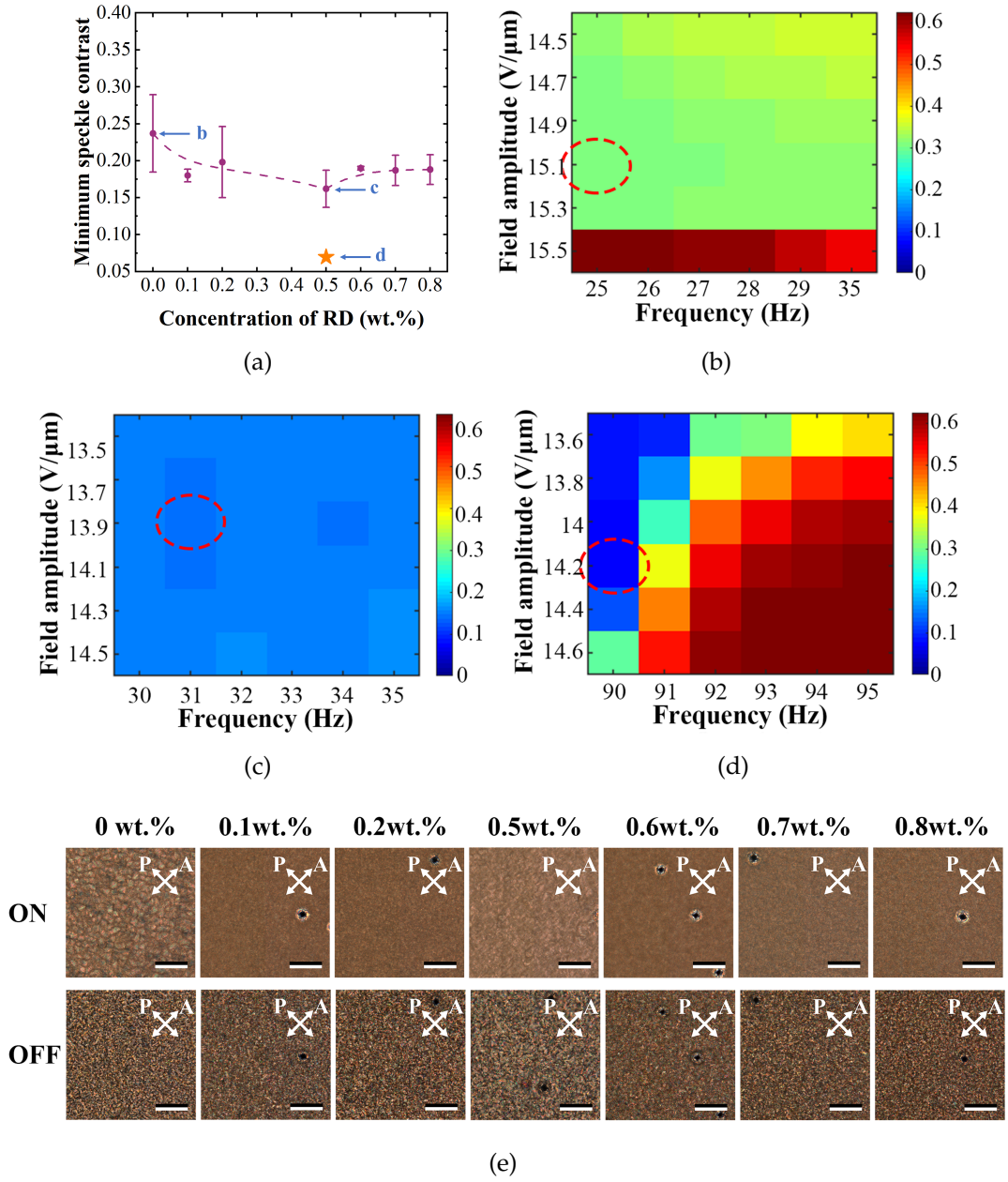

FIGURE 5.2: Reduction in the laser speckle contrast using a zwitterionic-doped chiral nematic LC-SR. (a) The plot of the speckle contrast, C, as a function of the concentration of the zwitterionic dopant (by weight percentage) for LC-SRs that were 20 µm-thick at a temperature of 25 °C (purple dot symbols) and 40 µm-thick devices at a temperature of 50 °C (orange star). The dashed line in the figure is simply to guide the eye and has no physical meaning. (b), (c), (d) Example colourmaps of the speckle contrast for a range of electric field amplitudes and frequencies. These speckle contrast colourmaps correspond to the data points and concentrations of zwitterionic dopant labelled in (a). The smallest speckle contrast value recorded (for a particular combination of electric field amplitude and frequency – referred to as the optimum electric field conditions) are encircled by a red dashed ellipse in each plot. (e) Polarising optical microscope (POM) images of LC-SRs with and without the optimum electric field conditions applied. The devices were 20 µm thick and the images were taken at 25 °C. Scale bars in the POM images are 50 µm.

the largest reduction in the speckle contrast. The red dashed ellipses in Figure 5.2(b) and 5.2(c) show the peak field condition for the case of no zwitterionic dopant (Figure 5.2(b)) and with 0.5 wt.% of zwitterionic dopant (Figure 5.2(c)). Both devices were 20 µm-thick and were operated at 20 °C. It can be seen clearly that the addition of the zwitterionic dopant resulted in a substantial reduction in the speckle contrast (C = 0.15 for the 0.5 wt.% zwitterion doped mixture compared with C = 0.3 for the mixture without zwitterionic dopants) at lower electric field amplitudes. The colourmap in Figure 5.2(d), on the other hand, is for the 0.5 wt.% mixture but in a 40 µm cell operated at 50 °C. Evidently, increasing the thickness of the device as well as the operating temperature can have a significant improvement on the device's performance, which is in accord with the results obtained in previous work [36]. It is important to emphasize that even though the best result in terms of reducing the speckle to C = 0.07 was obtained at an elevated temperature, this 40 µm-thick device also exhibited a very low speckle contrast of C = 0.075 at a temperature of 20 °C, which is an improvement on LC-SRs reported in the previous chapter as well as that reported in the literature ($C \approx 0.09$ at a temperature of 55°C) [17].

Polarising optical microscope (POM) images of the LC mixtures with different concentrations of the zwitterionic dopant with the same cell gap of 20 µm are shown in Figure 5.2(e). After removing the electric field from the device, the chiral nematic LC adopted a stationary focal conic alignment as can be seen in the optical texture in the POM image. Variants of this optical texture were observed in cells with different concentrations of zwitterionic dopant, and it is believed that this static configuration is largely governed by the pitch of the chiral nematic LC host, the cell gap, and the alignment layers. When the electric field was applied, on the other hand, the degree of turbulence and the size of each dynamic scattering unit varied depending

upon the concentration of the zwitterionic dopant. For the device without a zwitterionic dopant, the optical structure observed when the electric field was applied appeared to be a combination of the stationary focal conic state and a dynamic scattering mode where only the areas in the dynamic scattering mode are able to introduce angular decorrelation whereas the stationary focal conic states appear to contribute to no more than two decorrelated patterns, substantially less than that the dynamic scattering areas can generate. In this case, the dimension of the scattering area in an undoped device is not as large as that in a zwitterionic-doped device and this results in less angular decorrelation patterns generating per unit time which leads to an unsatisfactory performance in terms of speckle reduction. However, upon the addition of zwitterionic dopant, the dynamic scattering domains gradually became dominant and maximized at a concentration of 0.5 wt.%.

5.2.4 Transmission of the LC-SR

The transmission of the LC-SR is also an important property. For volume scattering devices, a large reduction in the speckle contrast often occurs with a simultaneous reduction in the transmission of light. To investigate the transmission properties, a series of speckle patterns were captured using a monochrome CCD that imaged the speckle pattern displayed on a white screen. Each speckle pattern was formed by placing the different LC-SR devices (containing different concentrations of zwitterionic dopant) in the path of a He-Ne laser.

The speckle patterns that were observed on a white screen for the different LC-SRs are presented in Figure 5.3(a) - 5.3(h). Figure 5.3(a) shows the speckle pattern that was observed when the LC-SR with no zwitterionic dopant (0 wt.%) was placed in the light path and was not switched on,

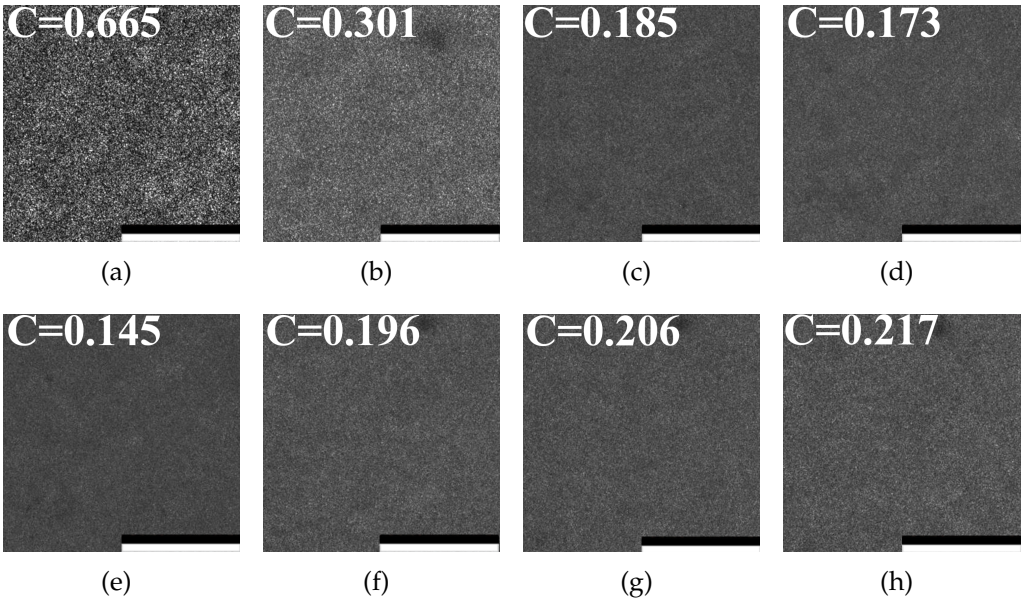

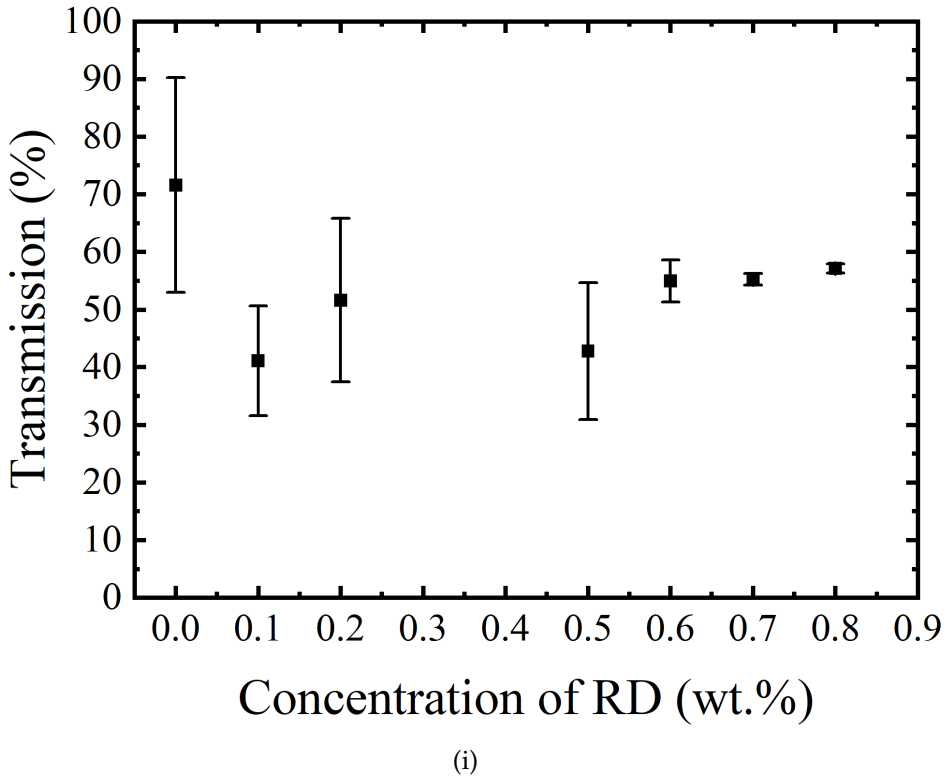

(i)

FIGURE 5.3: Speckle patterns and percentage of transmission with a zwitterionic-doped chiral nematic LC-SR. (a) speckle pattern recorded by the CCD camera when the light from a He-Ne laser passed through an LC-SR that was not switched on. (b) – (h) LC-SR speckle patterns recorded by the CCD camera for different concentrations of zwitterionic dopant: (b) 0.1 wt.%, (c) 0.2 wt.%, (d) 0.3 wt.%, (e) 0.5 wt.%, (f) 0.6 wt.%, (g) 0.7 wt.%, and (h) 0.8 wt.%. The scale bar in the images represents a distance of 2 mm. (i) The corresponding transmission of light after passing through the LC-SR relative to the intensity recorded in (a). All images and data points were captured at 25 °C and the device thicknesses were 20 µm.

where it can be seen that there was a very clear and obvious granular intensity speckle pattern. Figures 5.3(b) to 5.3(h), on the other hand, show the different speckle patterns recorded when the LC-SRs were switched on and as the concentration of zwitterionic dopant increased. Each speckle pattern was obtained when the devices were driven at their respective optimum electric field conditions. The transmission of light after propagating through the different devices was then calculated based on the intensity recorded in the images in Figure 5.3(b) to 5.3(h) relative to the intensity recorded in Figure 5.3(a) when the LC-SR was not switched on. For each data point in Figure 5.3(i), the electric field amplitude and frequency applied to each sample corresponded to the conditions required for maximum speckle reduction. The results show that there is a decrease in the transmittance with the addition of the zwitterionic dopants, and that the lowest transmission was recorded for the sample that also exhibited the lowest speckle contrast (i.e., 0.5 wt.%). Nevertheless, the results presented in Figure 5.3(i) show that the relative transmittance did not drop below 45%, which is important for practical applications.

5.3 LC-SRs in Microscopy and Display Applications

To illustrate the capability of the zwitterionic-doped chiral nematic LC-SR, I now investigate the performance of the technology in five different application scenarios. For what follows, the LC-SR consisting of the 0.5 wt.% zwitterionic dopant was used exclusively unless stated otherwise.

5.3.1 Laser Microscopy Imaging System

Figure 5.4 demonstrates the performance of the LC-SR when it was deployed in a laser microscope imaging system. The continuous wave (CW), He-Ne laser light first passed through a variable attenuator (VA) to adjust the intensity so that the CCD camera was not saturated. The LC-SR device was put right behind the VA so that the laser light could be directly modulated by the LC-SR. The modulated light then propagated through a positive lens and then expanded to a dimension such that the intensity of the laser light was uniform over the area of interest on the target. A mirror was put between the lens and the target to fold the system. The target is composed of a 220-grit ground glass diffuser (GGD) and a O1" 1951 USAF Target to mimic a thick, rough tissue with fine details. A universal 10x objective magnified the patterns on the target. The enlarged pattern was collected by another positive lens and finally captured by a CCD camera. It is immediately discernible that the imaging quality significantly improved when the LC-SR was integrated into the microscope and run at the optimum electric field conditions. The compact size of the diffuser and the absence of any moving mechanical components means that it could be easily integrated into the laser microscope assembly.

As can be seen by comparing Figure 5.4(b) with Figure 5.4(c), the sharpness of the fringes and the visibility of the numbers adjacent to the fringes were significantly improved because of the presence of the LC-SR. Using an edge detection algorithm (Laplacian of Gaussian (LoG) operator) the key features (shapes/numbers) from Figure 5.4(b) and 5.4(c) were extracted. The results for alternative edge detection algorithms are presented in Figure 5.5 and 5.6.

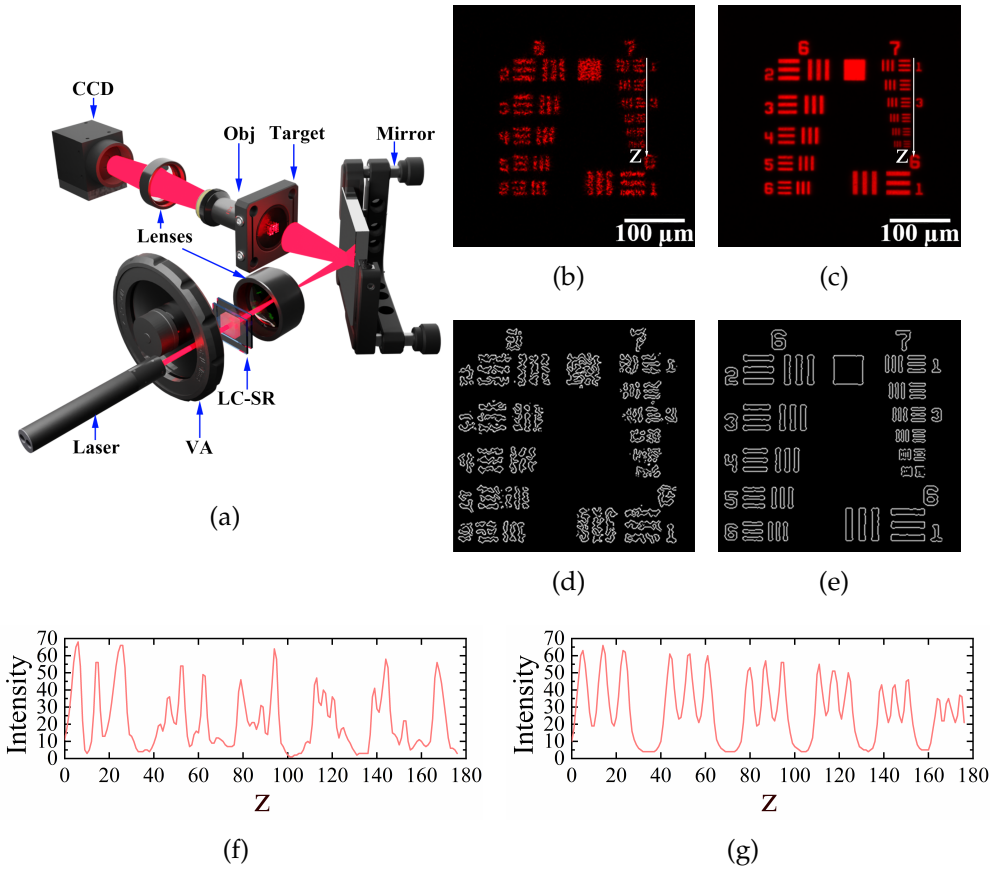

FIGURE 5.4: Zwitterionic-doped chiral nematic LC-SR in a laser microscope imaging system. (a) Schematic of the laser microscope assembly used to demonstrate the LC-SR. The best performing LC-SR was employed for this demonstration (BL006 + 3.0 wt.% R5011 + 0.5wt.% Reichardt's dye, d = 40.0 µm). An objective (Obj) was used to collect the light from the USAF 1951 target before it was directed to the CCD camera by a focusing lens. The target was a combination of a 220-grit ground glass diffuser and a Ø1" 1951 USAF Target. (b) The image captured by the CCD camera without the LC-SR. (c) Image captured when the LC-SR was switched on. (d) The corresponding image after an edge detection algorithm (Laplacian of Gaussian) had been applied to (b). (e) The corresponding image when an edge detection algorithm had been applied to (c). (f) The normalized intensity extracted along a line defined by Z in (b). (g) The normalized intensity extracted along a line defined by Z in (c). The z-axis starts from group 7 element 1 to group 7 element 6.

The results from the edge detection emphasise clearly the adverse impact of speckle noise on the laser microscope imaging capability as shown in Figure 5.4(d) and 5.4(e). When the device was not activated (Figure 5.4(b)) the speckle noise corrupted the images making it difficult for the edge detection algorithm to correctly identify both the shapes and the numbers (Figure 5.4(d)). However, when the LC-SR was switched on (Figure 5.4(c)), the edge

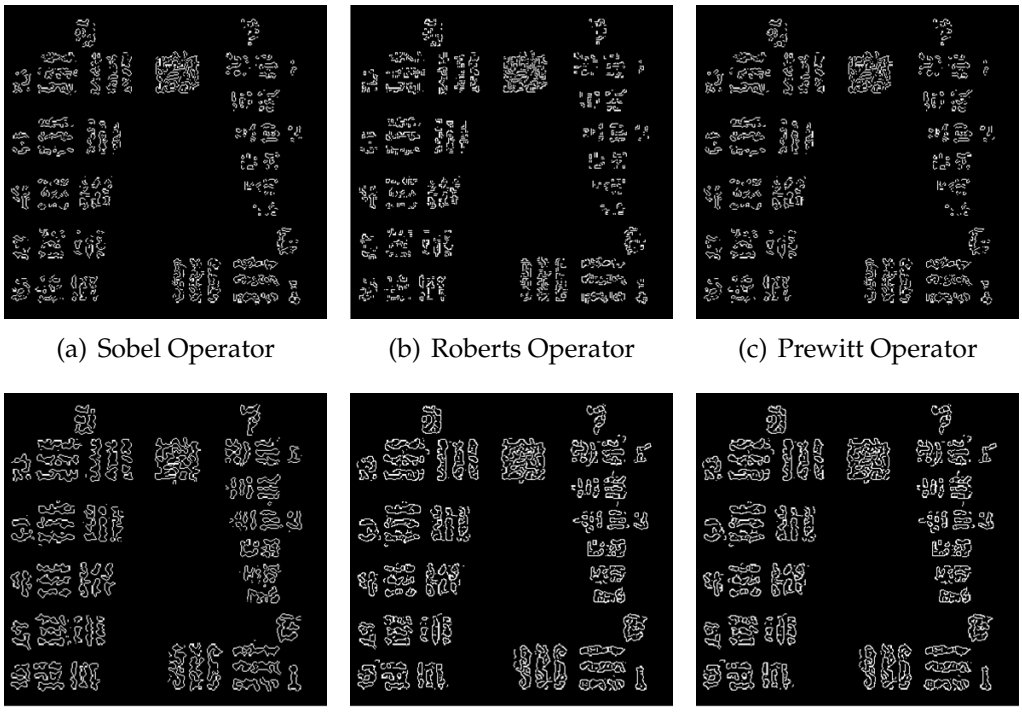

(a) Sobel Operator (b) Roberts Operator (c) Prewitt Operator

(d) LoG Operator (e) Canny Operator (f) Gaussian & Canny Operator

FIGURE 5.5: The edge detection (for different algorithms employed in Matlab) of the target in Figure 5.4 when the illumination is only the laser.

detection correctly extracted and identified both the shapes and the numbers. Line scans along the images in Figure 5.4(b) and 5.4(c) (leading to Figure 5.4(f) and 5.4(g), respectively) show the improvement in uniformity in the intensity distribution when the LC-SR was turned on, as can be seen by the three fringes that are equally separated with the same thicknesses (Figure 5.4(g)). The intensity of the light was also uniform across the same group of elements, and we can see this from the flat and uniform profile of the plot. These results demonstrate that with the inclusion of the LC-SR, the signal-to-noise ratio of the laser microscope system had noticeably increased.

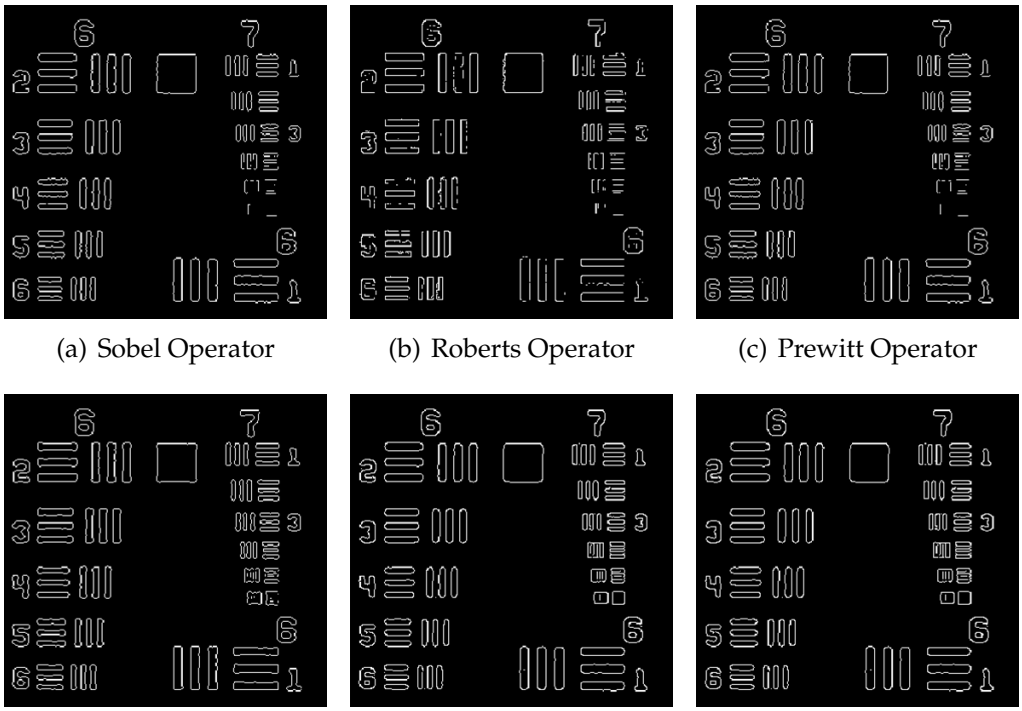

(a) Sobel Operator (b) Roberts Operator (c) Prewitt Operator

(d) LoG Operator (e) Canny Operator (f) Gaussian & Canny Operator

FIGURE 5.6: The edge detection (for different algorithms employed in Matlab) of the target in Figure 5.4 when the laser is the light source, and the LC-SR is inserted and turned on.

5.3.2 Head-Up Display

Another application where lasers are desirable illumination sources, but the presence of speckle noise can corrupt images, is a HUD [116]. For this investigation, a system was assembled and shown in Figure 5.7(a) where a curved piece of plastic (coated with reflective film) was used to mimic an automotive windscreen (this work was conducted in collaboration with another D.Phil student, Nathan Spiller). The laser light from a Helium-Neon laser passed through a variable attenuator (to control the intensity) before it propagated through a ground glass diffuser (GGD) and then the LC-SR. After exiting the LC device, the light propagated through a light pipe (LP) and second GGD before being imaged onto a target mask. The illuminated mask was imaged by a lens and the HUD screen which formed a virtual image 120 mm behind the HUD screen. This image along with background objects was then captured by a CCD placed at the viewing point (VP). A bowl of fruit and other objects were placed behind the windscreen so that they would be visible to the observer. At the same time, labels and signage were displayed on the windscreen that appeared overlaid on the objects in order to simulate augmented reality (in this case the observer was provided with details about what the object is, e.g., an orange).

As can be seen from the CCD camera images in Figure 5.7(b)- 5.7(g), the LC-SR significantly improved the quality of the images. The granular noise was suppressed in accordance with the reduction in the speckle contrast and the intensity distribution across the image became more uniform when the electric field conditions approached those that corresponded to the lowest speckle contrast. This resulted in the content of the display being more intelligible against the background objects for the same average image intensities. For a practical use of a HUD, either in the automotive industry or for an augmented reality headset, the accurate transfer of information from

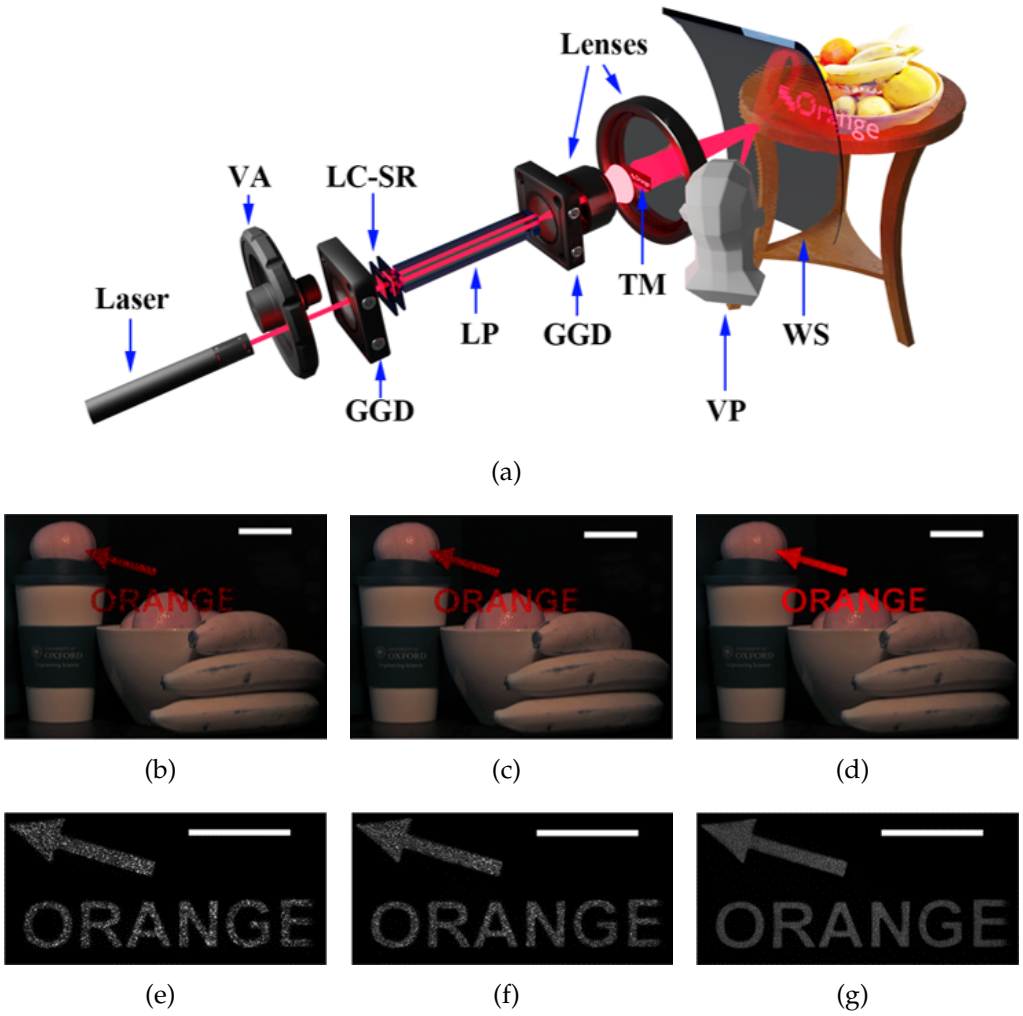

FIGURE 5.7: Zwitterionic-doped chiral nematic LC speckle diffuser in a Head-up Display (HUD). (a) Schematic of the HUD demonstrator. The assembly consisted of a variable attenuator (VA), two ground glass diffusers (GGD), a light pipe (LP), the LC-SR, lenses and a windscreen (WS). A CCD was positioned at the location of the viewer to capture images of the objects behind the WS as well as the labels that are projected onto the WS. (b)-(d) Colour CCD images of the HUD when there was no LC-SR (left image), with the LC-SR but not operated at the optimum electric field conditions (middle image), and with the LC-SR operated at the electric field conditions corresponding to the lowest speckle contrast value (right image). (e)-(g) Monochrome and enlarged images of the HUD when there was no LC-SR (left image), with the LC-SR but not operated at the optimum electric field conditions (middle image), and with the LC-SR operated at the electric field conditions corresponding to the lowest speckle contrast value (right image). The scale bars in (b)-(g) represent a distance of 5 cm.

the display to the observer is of paramount importance. Speckle present in the images can cause a loss of information and make the projection uncomfortable to view. Therefore, the reduction of speckle plays a crucial role in enabling laser illumination within these devices.

5.3.3 Holography

Another important immersive display that is used to reconstruct 3D information of an object is holography [117]. Holography records not only the intensity information of the objects but also the phase information of the objects. Traditionally, holography is realised by sending a reference plane wave generated by a laser light source, with known-intensity and phase profile, to the camera. As the light-wave reflected by the object (which is illuminated by another laser light source with the same wavelength) also propagates towards the camera sensor, the interference between these two light-waves is recorded by a CCD camera or photosensitive media. Illuminating the holographic film with the laser source that possesses the same wavelength as the one used during fabrication, the intensity and phase information of the object will be reconstructed through diffraction.

Speckle can also be an issue in the formation of images in holography [4, 118], here I demonstrate the performance of the LC-SR when it was used to reduce the presence of speckle in the laser illumination of a multi-level phase hologram, the results of which are presented in Figure 5.8 (this work was carried out in collaboration with another D.Phil student, Nathan Spiller). Figure 5.8(a) displays the system employed to demonstrate speckle reduction in a thin-film hologram. The He-Ne laser first passed through a variable ND filter to control the illumination intensity. Following the filter the beam passed through a ground-glass diffuser immediately before the LC-SR. A single lens was used to expand the output beam from the LC-SR to illuminate a

large area of the hologram. A CCD camera was then placed in two positions (VP1 and VP2) to capture images of the hologram at two different angles in order to verify that the speckle reducer performance is not affected by the viewing angle.

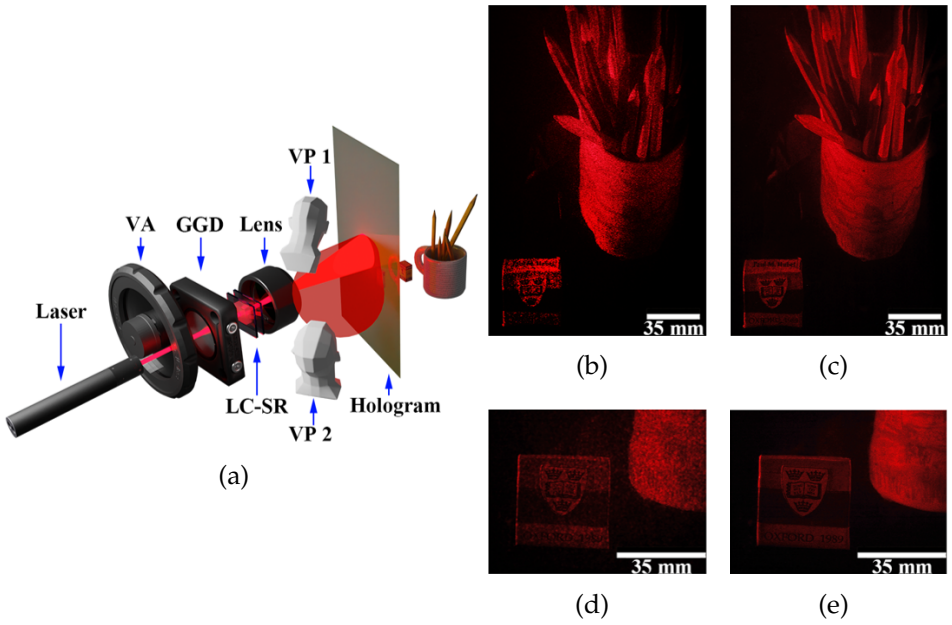

FIGURE 5.8: A zwitterionic-doped chiral nematic LC-SR for holography. (a) Schematic of the experimental assembly used to test the LC-SR with the laser illumination of a thin-film hologram. The system consisted of a He-Ne laser, a variable attenuator (VA), a ground glass diffuser (GGD), the LC-SR and a combination of lenses to expand the beam to illuminate the hologram. the beam is then transported through a positive lens and then projected on a hologram. A CCD camera was positioned at the locations of the two heads so that the mug and the eraser could be viewed from different angles. (b) Image of the hologram when no LC-SR was included in the system and when the CCD camera was placed at location 1 (positioned high up and relatively far away from the hologram). (c) Image taken from location 1 when the LC-SR was inserted and operated at the optimum electric field conditions. (d) Image captured on the CCD when it was located at position 2 (positioned low down and close to the hologram) with no LC-SR included in the system. (e) Image captured from position 2 when the LC-SR was inserted and run at the optimum electric field conditions.

5.3.4 Laser Projection Displays

Laser projectors are particularly desirable for cinema and home entertainment systems as they can provide a high brightness with a potentially high colour gamut [119]. For the demonstration of laser projection, the system is the same one used in Chapter 4. As mentioned previously, the lamp from a HITACHI CP-X250 Multimedia LCD Projector has been removed and replaced with a green laser (Quantel ELBAC-L-559-2-P-M-S-2.0 laser) which emitted at a wavelength of λ = 559.6 nm and had a maximum output power of 2W. A schematic of the laser projector system is presented in Figure 5.9.

For demonstrating the use of a LC-SR in a projection display the standard illumination system (a bulb) was stripped out of a commercial HITACHI projector and replaced with a laser illumination system. This consisted of a homogenisation system similar to the one in the speckle characterisation system. The first GGD was followed by the LC-SR mounted on a hot stage. The beam then propagates through a light pipe before a second GGD. The two GGDs and LP diffuse the light so that the intensity distribution on the projected screen is uniform. The output from this illumination system was passed into the projector and used to display full motion video. A VA was placed at the very beginning of the system to avoid intensity saturation. Examples of the projected image, when the laser was operated at its maximum output, are shown in Figures 5.9(b) and 5.9(c) when the LC-SR was either not switched on or was run at its peak electric field conditions. When the LC-SR was not switched on, it can be seen clearly that the image quality of the white fur on the cat was very grainy. Features such as the whiskers were also more difficult to make out because of the presence of the speckle. On the other hand, when the LC-SR was switched on, the image quality improved dramatically, and the smooth white fur could be seen clearly without being corrupted by a grainy speckle pattern.

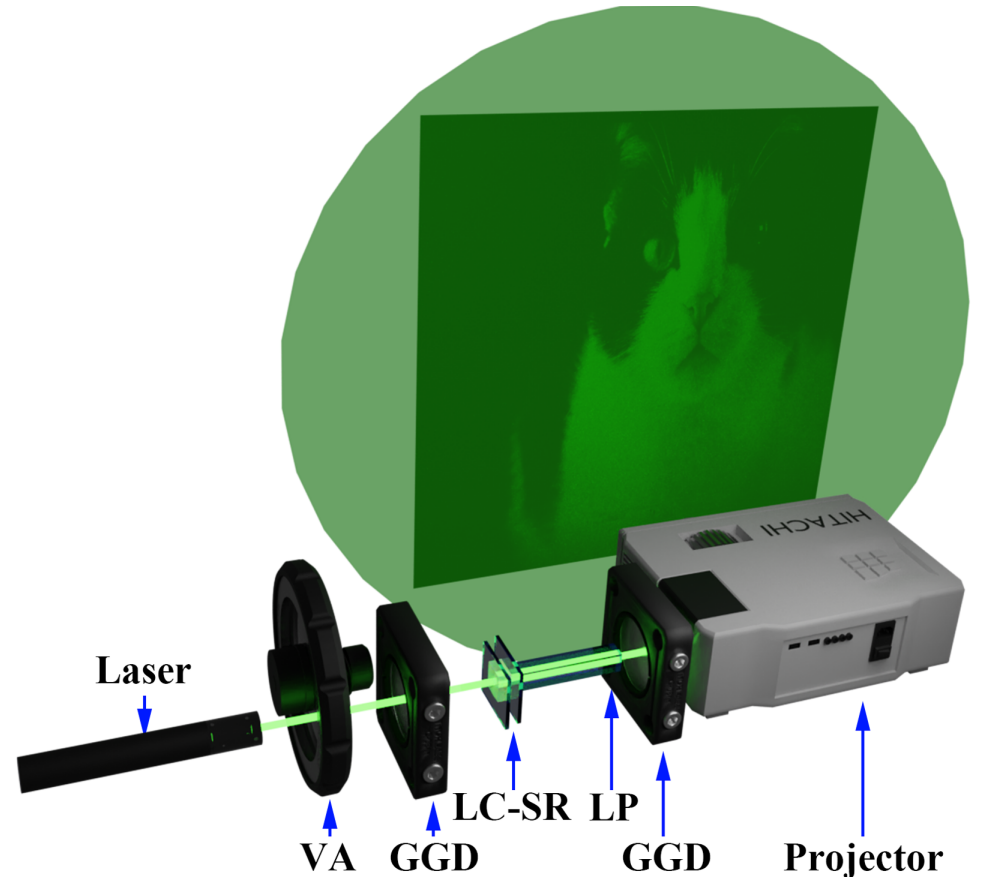

(a)

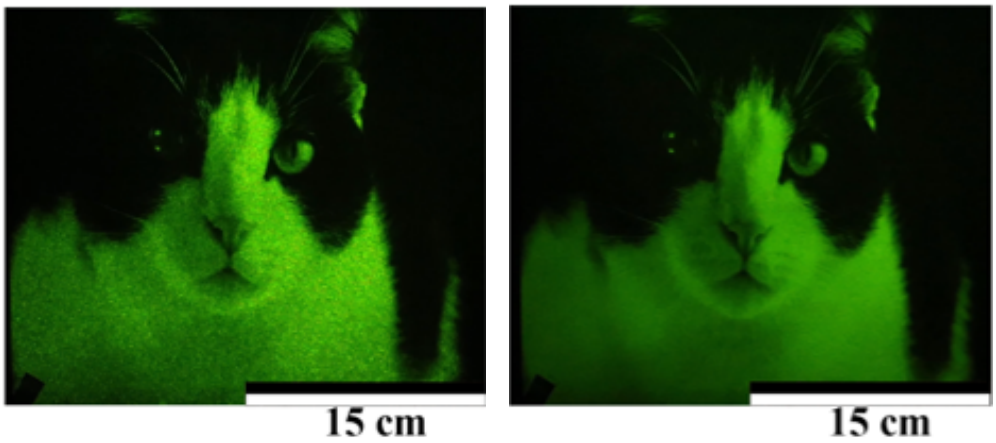

(b) (c)

FIGURE 5.9: Laser projection with a zwitterionic-doped chiral nematic LC-SR. (a) Illustration of the laser projector demonstrator. The demonstrator consisted of a HITACHI CP-X250 Multimedia LCD Projector that was illuminated by a Quantel laser. Also included were ground glass diffusers (GGD), the LC-SR, and a light pipe (LP). (b) A still from the video of the cat when the LC-SR was not switched on. (c) A still from the video when the LC-SR was operated at the optimum electric field conditions. The video of the cat was downloaded from a copyright-free website (pixabay).

5.3.5 Laser-Based Vectorial Imaging

The previous sections have demonstrated the performance of the LC-SR in scalar field illumination systems. However, we have also considered how the LC-SR performs when measurements of the vectorial information of light are needed [120–122]. In the following, we consider a transmissive geometry (for thin samples under investigation) and then a back-scattering geometry (for a bulk sample) (this work was carried out in collaboration with a research fellow, Dr Chao He). For the transmissive geometry, using Mueller Matrix (MM) imaging, vectorial information of light passing through a thin birefringence crystal was extracted enabling properties such as the retardance and fast axis orientation to be determined [120, 123]. The results are also benchmarked with that obtained using an LED illumination source. For the back-scattering geometry, we have validated the vectorial information reconstruction of a bulk porcine liver sample, which is a highly scattering medium, via back-scattering illumination. The MMs and their transformation parameters [103, 120] are taken from previous work, through which we successfully retrieved the fine liver polygon structure.

Numerous MM imaging polarimeters have already been proposed in previous studies [120, 124]. Meanwhile, many MM interpretation methods have been put forward to extract useful polarization parameters to characterize sample information. The widely used decomposition methods [125, 126] – which include Mueller matrix polar decomposition (MMPD) and Mueller matrix transformation (MMT) – interpret the MM in terms of different physical parameters such as diattenuation, depolarization, retardance, linear anisotropy level and so on, have been widely used and validated for both forward and backward geometry detections via a series of Monte Carlo simulations and related experiments [125]. More details can be found in Refs [120, 127].

Figure 5.10 shows the MM polarimeter geometries that were adopted in the vectorial imaging experiments in this chapter, via a dual-rotating wave plate configuration (previously described by *Azzam*, *Goldstein* and *Chipma* [121–123, 126, 128]). Figure 5.10(a) includes an illustration of the transmissive vectorial measurement systems, and an image of the target birefringence crystal sample; Figure 5.10(b) includes an illustration of the back-scattering configuration and an image of the target bulk porcine liver tissue sample.

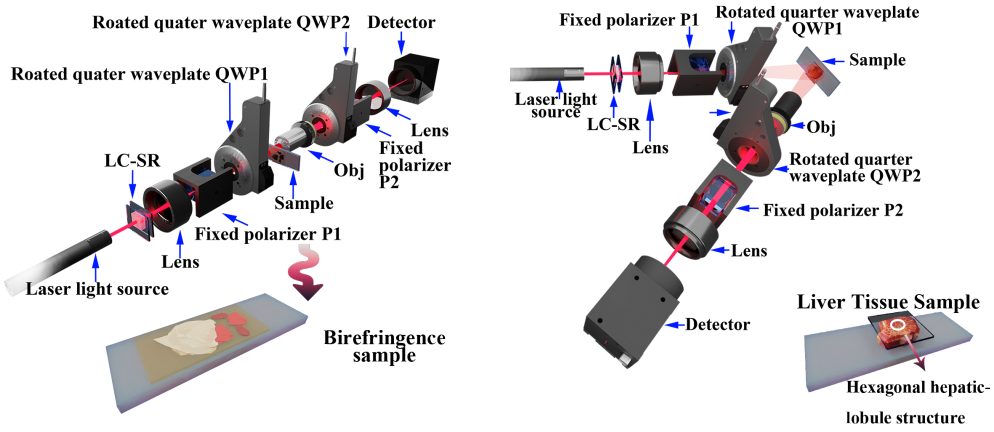

(a) (b)

FIGURE 5.10: (a) Transmissive and (b) back-scattering geometries for MM polarimetry used in this work. (a) The beam comes from the LED (1 W, 633 nm) or He-Ne laser (4 mW, 633 nm) and passes through the polarizer (P1, Thorlabs) and quarter wave plate (QW1, Thorlabs). Then the beam from the sample passes through the analyzing quarter-wave plate (QW2, Thorlabs) and polarizer (P2, Thorlabs), and are recorded by a 10-bit CCD camera (Thorlabs). (b) The beam comes from the LED (1 W, 633 nm) or He-Ne laser (4 mW, 633 nm) and passes through the polarizer (P1, Thorlabs) and quarter wave plate (QW1, Thorlabs). Then the beam is backscattered from the sample and passes through the analyzing quarter-wave plate (QW2, Thorlabs) and polarizer (P2, Thorlabs), and are recorded by a 10-bit CCD camera (Thorlabs). The LC-SR and the lens are inserted and taken out according to the experimental requirements during the measurement process.

Figures 5.11 and 5.12 showcase the performance of the LC-SR in transmissive and back-scattering vectorial imaging applications, respectively. These figures include the experimental results in the form of the MMs, polarisation parameters for three different scenarios: a) laser illumination without the LC-SR (normal coherence light-based imaging); b) laser illumination with

the LC-SR (speckle reduced coherence light-based imaging); and c) LED illumination (standard measurement approach).

For the transmissive configuration (Figure 5.11), one region of the sample was chosen to illustrate the performance of the imaging system for the different illumination scenarios. These birefringent samples consist of crystals with different shapes and orientations of the fast-axes. Measurements of the vectorial information of light upon passing through the birefringent sample enable the retardance values and orientation of the fast axis to be determined. These results are presented as colourmaps where the legend on the righthand side of the images shows the relationship between the colour and the value of either the fast axis orientation (middle image) or the retardance (right image). Considering the data for the MM (first image in Figure 5.11(d)) for LED illumination as an example, it can be seen that the bottom right 3x3 sub-matrix includes information about the spatial variation of the birefringent properties of the sample, which demonstrates that the target sample exhibits a strong optical anisotropy [125]. After implementing a polar decomposition method [126], a quantitative value for the fast axis orientation (middle image in Figure 5.11(d)) and the spatially varying retardance (right image in Figure 5.11(d)) could be extracted.

In contrast, when a CW He-Ne laser was used as the illumination source, we can see clearly that the speckle noise severely affects the intensity distribution leading to significant measurement errors. The MM polarimetry requires multiple intensity measurements to enable the vectorial information to be extracted. If there is significant noise in the intensity then this degrades the precision of the MM polarimetry [120]. It can be seen from Figure 5.11(b) that the MM images (left image) are very blurred, with lower values in the bottom right 3x3 sub-matrix, as well as unwanted noise appearing in the first

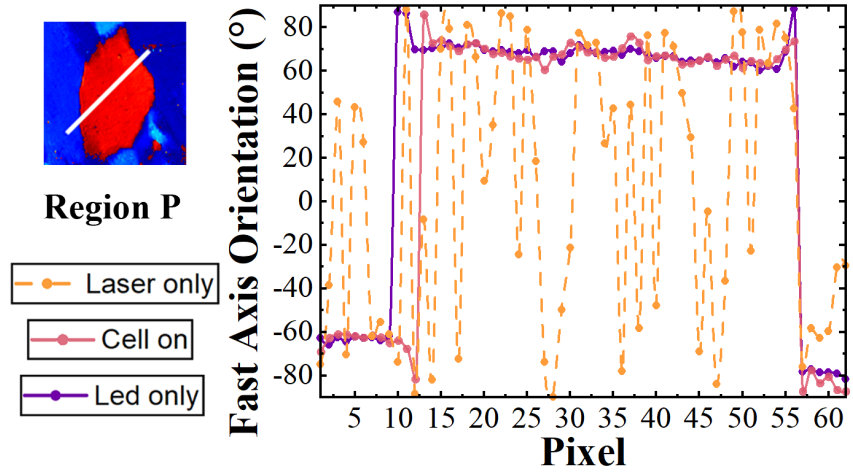

(a) Fast Axis Orientation of Region P

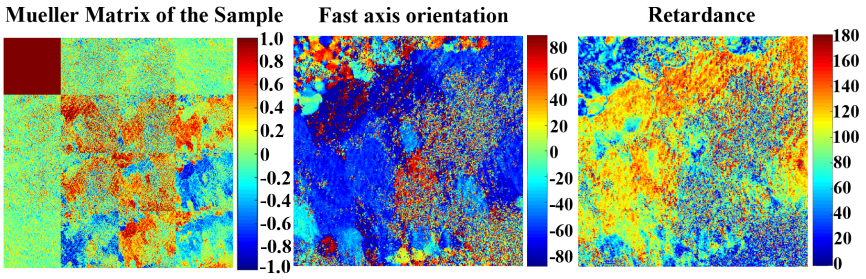

(b) Laser Only

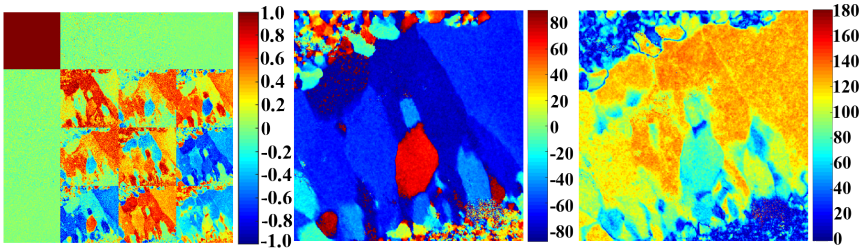

(c) Laser and LC-SR

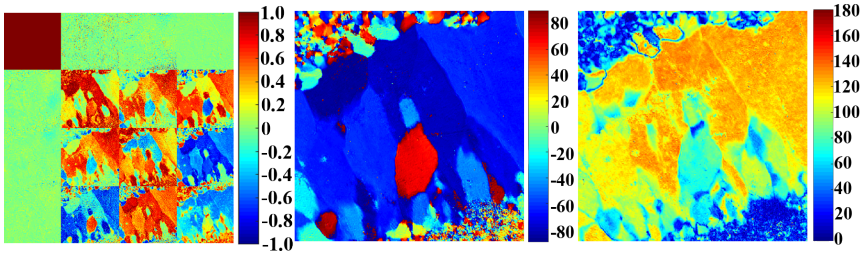

(d) LED Only

FIGURE 5.11: (a) An enlarged image of the fast axis orientation of the crystal defined as P extracted from the LED illumination case and a plot of the fast axis orientation as a function of pixel number for all three illumination scenarios over the distance represented by the white solid line in the crystal region defined as P. (b) Mueller matrix (left image), fast axis orientation (middle image) and retardance (right image) of the sample for the laser illumination case without the LC-SR. (c) Mueller matrix image (left image), fast axis orientation (middle image) and retardance (right image) of the sample for the laser illumination case with the LC-SR operated at the optimum electric field conditions. (d) Mueller matrix image (left image), fast axis orientation (middle image) and retardance (right image) of the sample for the case when an LED (incoherent) is used as the illumination source.

row and column of the MM. In addition, the quality and accuracy of the deconstructed fast axis orientation (middle image) and retardance (right image) are in turn corrupted by the noise present in the intensity, which results from the presence of speckle.

From these images an identified crystal region (defined by P) that has a very distinguishable fast axis orientation relative to the surrounding background and have used this to enable a quantitative comparison of the performance for the three different illumination cases. The crystal defined by P clearly has a very different orientation (which appears red in the colourmap) compared with the surrounding region (which appears blue in the colourmap). When using just the laser as an illumination source the region defined by P cannot be readily identified (Figure 5.11(b) – middle image). In contrast, however, with the assistance of the LC-SR device, the full MM images (Figure 5.11(c) – left image) as well as the fast axis orientation (Figure 5.11(c) – middle image) and retardance (Figure 5.11(c) – right image) are accurately recovered and are in good agreement with the standard incoherent (LED) illumination case (Figure 5.11(d)). Figure 5.11(a) plots a value for the fast axis orientation across the region defined by the white line in the image where it can be seen that using laser illumination the fast-axis value (dashed orange curve) oscillates dramatically across the sample showing no clear signs of a crystal structure. This is in contradiction to the actual sample properties as reflected in the results for the standard LED illumination (blue solid line) and when the LC-SR is combined with the laser source (solid red line). Encouragingly, the results obtained for the LC-SR agree extremely well with those obtained for the LED illumination scenario. Considering the unique properties of a laser light source, such as 1) high intensity, 2) narrow bandwidth and 3) compatibility with the illumination of the fluorescence microscope, a laser light source would be beneficial over an LED, especially with speckle

suppression.

For the back-scattering configuration (Figure 5.10(b)), a porcine liver tissue sample was selected for this demonstration (Figure 5.10(b)). The liver is a very important organ, which performs hundreds of different functions including lymph production, protein metabolism and hormone production [129]. These complicated physiological functions are closely related to the intrinsic microstructure of the liver tissue and the abundance of organelles within cells [130]. MM imaging is an excellent label-free technique for distinguishing the microstructural variations in the surface layer of the liver in order to help diagnose hepatic diseases [131, 132]. Previous studies have shown that the porcine liver is almost isotropic [131, 132]. However, there exist polygonal structures distributed around the isotropic liver tissues, which are highly birefringent connective tissues and are considered to be the boundaries of hepatic lobules [133]. Monitoring such anisotropic structures is beneficial in terms of the detection and diagnosis of the liver condition [131, 132].

As before, results are presented (Figure 5.12) for the three illumination scenarios: laser on its own, laser with LC-SR, and incoherent illumination using an LED. The latter represents the traditional approach and helps to benchmark the performance of the speckle reducing technology presented herein. The use of a MM polarimeter allows each point of the sample captured by the CCD camera and the measurement outputs are the corresponding MMs. Arranging these MMs according to the positions of the sample pixels, and representing them using a colourmap, we can get Figure 5.12(a). Based on the MMs for each point of the sample, a set of MM for each pixel the level of optical anisotropy (Figure 5.12(b)) as well as the fast axis orientation (Figure 5.12(c)) can be determined. It is worth noting that here the back-scattered bulk tissue is an intense light scattering media, and previous laser-based full MM vectorial imaging has not been able to retrieve

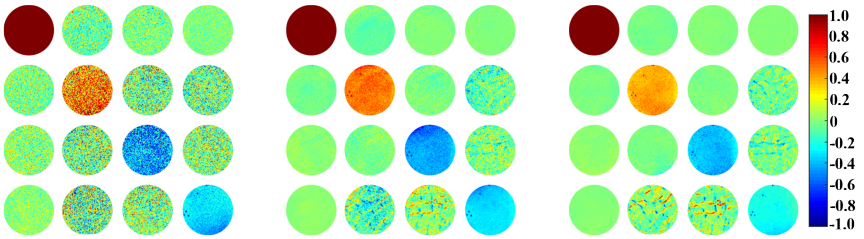

(a) Mueller Matrix of the Sample

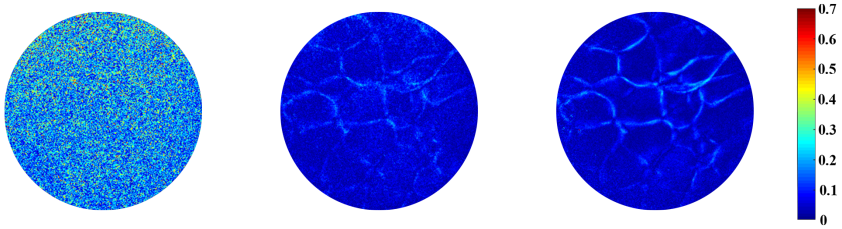

(b) Anisotropy Level

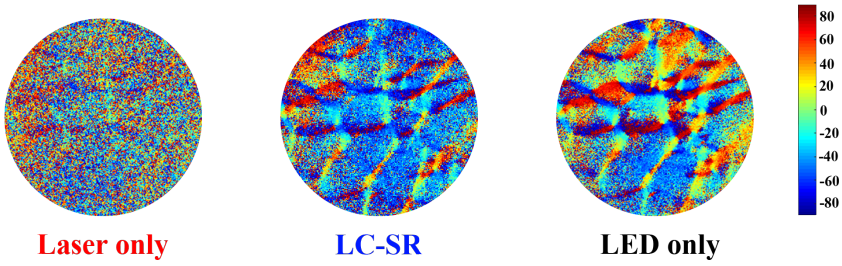

(c) Axis Orientations

FIGURE 5.12: Improving laser-based vectorial imaging of thin-film samples using a zwitterionic-doped chiral nematic LC-SR (back-scattering configuration). (a) Mueller matrices for the laser illumination case (left image), the laser with LC-SR (middle image) and the LED (right image). (b) The level of anisotropy for the laser illumination case (left image), the laser with LC-SR (middle image) and the LED (right image). (c) The orientation of the fast axis across the sample for the laser illumination case (left image), the laser with LC-SR (middle image) and the LED (right image).

the fine polygonal structures shown here (for the laser illumination similar cases have been considered in Reference [66]). Using the LC-SR device, the influence of laser speckle can be significantly reduced enabling accurate reconstruction of the intricate polygonal structures of the liver tissue (see the middle images in Figure 5.12(a), 5.12(b) and 5.12(c)). To the best of my knowledge, this is the first time the image quality as well as the vector information obtained from back-scattering MM polarimetry has been recovered with laser illumination and low speckle $C = 0.07$.

5.4 Summary

The above observations show that the zwitterion doped LC-SR device made a significant improvement for laser-based scalar imaging and vectorial imaging – in both image resolution and the vectorial information correctness – via the significant speckle-reduction. The results demonstrated that upon the addition of 0.5 wt.% Reichardt's dye to a chiral nematic LC (BL006+3.0 wt.% R5011), the speckle noise can be reduced from C=0.7±0.02 to C=0.07±0.01 at best at a temperature of 50°C with a 40 µm cell. These 40 µm-thick devices also exhibited a very low speckle contrast of C=0.075 at a temperature of 20 °C enabling applications requiring lower operating temperature. The performance of the LC-SR is not narrowed by the application scenarios, and has been proven that the ability of the device is not dependent on the specific applications but can be simply inserted into various optical systems including light-field microscopy, HUD, holography to laser projector and still provides a significant improvement of the imaging quality.

In addition to the demonstrations with the scalar field, this is the first time that the LC-SR has been used in a vectorial imaging system and presented promising results. The exciting results shown in Figure 5.11 and 5.12 provides the possibility of improving the resolution of fluorescence polarisation microscopy (FPM) [134, 135] that suffered from the speckle noise due to the coherent nature of the laser light. With this LC-SR, the partially coherent laser light is perfect to provide narrow bandwidth as well as high intensity. Image resolution and the vector information correctness are significantly enhanced in the vectorial domain. The LC-SR device shows good performance for different microscopy configurations encompassing scenarios ranging from the analysis of birefringent materials to the characterisation of thick tissue biopsy.

The LC-SR demonstrated in this chapter is compact, portable and has a low form factor. The tiny dimension of the device makes integration into existing commercial and custom-built systems currently suffering from speckle noise straightforward. The applications presented here cover a range of commonly used imaging systems and also explore its possibility further to a new area of vectorial imaging. The notable change and suppression of the granular noise resulting from the LC-SR make this work of interest for the improvement of laser microscopy, HUD, holography, laser projectors and polarisation microscopy.

Chapter 6

Millisecond Optical Phase Modulation using Multi-pass Configurations with Liquid Crystal Devices

As mentioned in the introductory chapter, the second key part of the thesis focuses on developing analogue phase modulators that have the potential to operate at faster switching speeds than conventional technologies. The following chapters will discuss my work in this area. In this chapter, two configurations have been considered for analogue 0 to 2π optical phase modulation using LC devices, each of which achieves switching times that are 1 ms or less. One configuration is based on the switching behaviour of the so-called nematic pi cell and the other is based on the flexoelectro-optic effect in chiral nematic LCs when operated in the uniform lying helix geometry. Both configurations exploit a multi-pass optical arrangement to enhance the available optical phase range, while maintaining a fast-switching speed. Moreover, these devices can be operated at or close to room temperature. Experimental data were found to be in good agreement with results predicted

from theory for these multi-pass phase-modulation configurations. The results presented in this chapter have been published in part or in their entirety in the journal article *Physical Review Applied* 14, 024007 (2020) [18].

6.1 Introduction

Optical phase modulation is important in many aspects of optical and optoelectronic technology [136]. Phase modulation can be obtained either by changing the refractive index (or effective refractive index) of a material through which light is propagating, or by physically changing the optical path-length for the light. For applications requiring a spatially structured phase modulation of a propagating optical wavefront, a LC spatial light modulator (SLM) is often desirable and has been employed in applications such as micromanipulation and beam-shaping [137–142]. Commercial SLM technology based upon LCs broadly breaks down into two categories: those that provide a digital, binary, or quantized phase modulation with a very limited number of states (e.g. 0 and π phase states are commonly chosen) and those that provide analogue (or at least, multi-level) phase modulation (e.g. a phase range of 0 to 2π is commonly used).

As an example, binary SLM technology [143–145] is often based on the bi-stable switching of ferroelectric LCs (FLCs) and can achieve switching times that are substantially less than 1 ms. A high-speed technology based on anti-FLCs has recently been demonstrated, but this uses rather thick LC layers, thus limiting the potential pixel pitch [146]. Analogue SLM technology, on the other hand, typically involves switching a layer of nematic LC, but the switching times are generally much longer, often being many milliseconds [147, 148], although with careful material and device optimisation 2 ms response times have been obtained in the laboratory [149].

Improving the switching speed, whilst maintaining access to a full range of phase states (from 0 to 2π) enables SLM technology to be used in a wider range of systems, such as in faster optical laser beam tracking/steering [73], and in higher-speed optical aberration correction in imaging systems [74]. There has been much interesting work in this area, with a number of very interesting proposals and demonstrations of configurations which can enhance the switching speed (reduce the response time) in a useful way. For example, work using two-photon techniques to engineer advanced structures inside of LC devices in order to optimise switching times [75–77], and work incorporating polymer networks into LC layers in order to obtain sub-millisecond switching times [14].

An alternative approach has been demonstrated using the flexoelectro-optic effect in chiral nematic LCs as a promising candidate [48]. The electro-optic effect, which was discussed in Chapter 2, Section 2.3.3, can be observed when an electric field is applied perpendicular to the helical axis of the chiral nematic LC, and can exhibit fast electro-optic properties because the characteristic length scale is the helical pitch (which can be of the order of 100s nm) rather than the device thickness. While the electro-optic effect offers sub-millisecond switching times, the optical response is generally quite small for most LC compounds and mixtures, with switching angles of just a few degrees. Bimesogenic LCs, however, can show much larger switching angles, allowing useful electro-optic effects to be exploited [78]. Using a configuration based upon the flexoelectro-optic effect in combination with wave-plates and a reflecting element, work carried out by *JAJFells* and *XWang* has shown that it is possible to achieve 0 to 2π optical phase modulation at temperatures of around 108°C [150].

A drawback with the approach demonstrated in Reference [150] is that the devices had to be operated at somewhat elevated temperatures (in

excess of 100°C), which is impractical for most technological applications. Unfortunately, room-temperature materials showing a large and high-speed flexoelectro-optic effect are not yet commonly available. An LC which shows substantial switching angles at room temperature has recently been demonstrated, but it requires large electric fields (equivalent to 100 V across a 5 µm-thick device to achieve a switching angle of 40°) [78]. Therefore, there is still considerable value in identifying new modes and configurations that can lead to fast switching and full 2π phase modulation. The focus of the work presented in this chapter, therefore, is to report on two alternative approaches that potentially address the shortcomings that are present in existing technologies. The objective is to achieve, full 2π phase modulation operating at switching frequencies much greater than 100 Hz at room temperature.

6.2 Alternative Configurations

6.2.1 Pi-Cell Configuration

In the first configuration, a nematic electro-optic mode is used in a high-speed regime. For nematic LCs the "switch-off" speed is typically the limiting factor in engineering a high-speed optical response. This is because the "switch-on" is driven by an applied voltage and the resulting switching speed is primarily controlled by the corresponding electric field and the viscosity of the LC. Therefore, by ensuring that the field is sufficiently large, high-speed switching can be obtained. However, the "switch-off" speed [151] is primarily controlled by the elasticity and viscosity of the LC, and therefore this is harder to control, other than through material parameter optimisation [152]. Alternatively, the switching speed can be improved through the use of polymer stabilization [153] or by making the device thinner. Polymer stabilization, while it can be effective often leads to larger driving voltages and

increased light scattering, both of which are unwanted side effects. Making the device thinner is a possible solution as the thickness of a nematic LC layer strongly influences the switching speed. In general, the characteristic "switch-off" time constant, τ, is given by $\tau \approx \frac{\gamma d^2}{\pi^2 K}$ [151], where γ is the rotational viscosity, K is an elastic constant, and d is the layer thickness.

There are, however, two problems with the approach of reducing the layer thickness: (i) thin uniform layers are more difficult to engineer, and the devices become difficult to capillary fill; (ii) thin layers show a reduced electro-optic effect, so the degree of phase modulation available may be insufficient. In this chapter, I aim to address these two issues. Firstly, I use an LC layer with a conventional device thickness of 5 microns but exploit the switching of a thin region near the surfaces of the device. Secondly, I use a multi-pass optical arrangement to enhance the electro-optic effect at the surfaces of the device to obtain a full 0 to 2π optical phase modulation.

6.2.2 Flexoelectro-Optic Device Configuration

For the second configuration, a room temperature flexoelectro-optic device is employed that exhibits small tilt angles, but the electro-optic response is enhanced (or amplified) through a multi-pass configuration. Previous work using the flexoelectro-optic effect has shown that by integrating the LC layer between quarter-wave plates and a mirror it is possible to obtain full 0 to 2π optical phase modulation in a device with a switching angle of $\pm 45^\circ$ [150] which was carried out at temperatures close to 108°C. The rather high temperature is not desirable and therefore the goal is to obtain sufficient phase modulation at much lower temperatures. However, as noted, fast-switching materials that operate at room temperature tend to show reduced switching angles. In the work presented in this chapter, a bimesogenic-doped eutectic mixture was employed that exhibits switching angles in the range of $\pm 15^\circ$

to ±20° at room temperature. Results are presented that demonstrate that enhanced optical phase modulation can be obtained by using a multi-pass geometry in combination with such materials

6.3 Theoretical Considerations

6.3.1 Phase Modulation with a Nematic Pi-Cell

In a layer of nematic LC with positive dielectric anisotropy the application of an electric field across the layer causes the reorientation of the director from a planar state towards a state with the director oriented perpendicular to the device surfaces, as described in Chapter 2. At high voltages, the bulk of the layer is reoriented to the perpendicular state, and small transition regions (or boundary layers) remain near the device surfaces which are shown in Figure 6.1

In a conventional anti-parallel rubbed device that exhibits the well-known Fréedericksz threshold, the director tilt in the boundary layers is in the same sense near the two surfaces. On the other hand, in the so-called pi-cell (parallel rubbed surfaces) [154], introduced in Chapter 2, the tilt is in the opposite sense in the two boundary layers. In the limit of very high voltages, and if the tilt of the director out of the cell surface plane is given by the angle θ (the tilt angle θ and coordinate z are defined as Figure 6.1(a) and 6.1(b)), then for understanding the difference of these two device configurations, these states can be simplified as

$$z = 0 \ : \theta = 0^\circ$$

$$0 < z < d \ : \theta = 90^\circ$$

$$z = d \ : \theta = 180^\circ$$

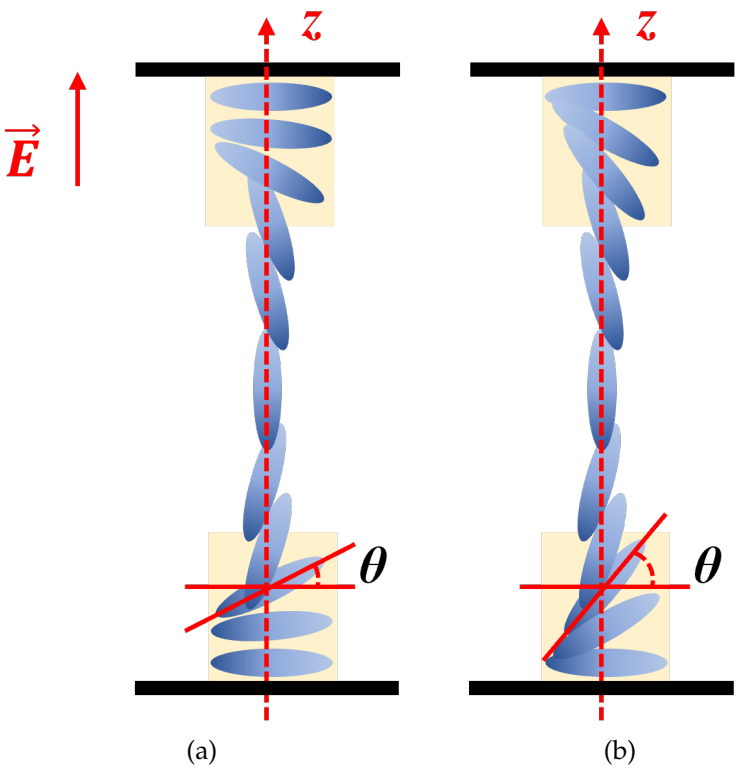

FIGURE 6.1: The orientation of the nematic LC director with an applied electric field in a pi-cell: (a) The side view of the pi-cell device at lower voltage; (b) The side view of the pi-cell device at higher voltage. The yellow highlighted areas are boundary layers.

for the Fréedericksz device and

$$z = 0 \ : \theta = 0^\circ$$
$$0 < z < d \ : \theta = 90^\circ$$
$$z = d \ : \theta = 0^\circ$$

for the pi-cell device, where z measures the position through the LC layer.

In each case, when the electric field is removed, the relaxation of the director from the switched state back towards the planar state begins from the surfaces. Using a one-elastic-constant-approximation (i.e., $K_{11} = K_{22} = K_{33} = K$ to model the LC behaviour then the initial response of the boundary layers at each surface has an analytic solution in terms of the error-function (erf) of the form

$$\theta(z,t) = \theta_s + (\theta_b - \theta_s) erf\left\{ \frac{z\sqrt{\gamma}}{2\sqrt{K}\sqrt{t}} \right\} \tag{6.1}$$

where z is now a coordinate measured from the surface, θ_s and θ_b are the initial surface and bulk director orientations, respectively, and K is the LC elastic constant. This solution is valid at each surface for short timescales provided that the $erf\left\{ \frac{z\sqrt{\gamma}}{2\sqrt{K}\sqrt{t}} \right\}$ term remains close to unity for $z = \frac{d}{2}$.

To determine the magnitude of the optical phase change (modulation) available through this boundary layer behaviour we need to determine the phase, ϕ, of the light propagating through the LC,

$$\phi = \frac{2\pi}{\lambda} \int_0^d n_{eff}(z) dz \tag{6.2}$$

where

$$n_{eff}(z) = \frac{n_e n_o}{\sqrt{n_e^2 \sin^2(\theta) + n_o^2 \cos^2(\theta)}} \tag{6.3}$$

Here λ is the wavelength of light, and n_e and n_o are the extraordinary and ordinary refractive indices of the LC, respectively. Further analytic progress is challenging because the integration of the trigonometric function of the error function is non-trivial. However, further progress can be made if: (a) a piecewise linear approximation to the error function is introduced of the following form:

$$erf(u) \approx \frac{u}{u_0} \; : \; u < u_0 \tag{6.4}$$

$$erf(u) \approx 1 \; : \; u \geq u_0 \tag{6.5}$$

where u_0 is chosen such that the integral of the approximation to the error function is compatible with the experimental results (leading to u_0 =1.12838); and (b) $n_{eff}(z)$ is expanded for small Δn.

Assuming that $\theta_s = 0^\circ$ and $\theta_b = 90^\circ$, $\theta(z,t)$ can now be written as

$$\theta(z,t) \approx 90^\circ \cdot \frac{1}{1.12838} \cdot \frac{z\sqrt{\gamma}}{2\sqrt{K}\sqrt{t}} \; for \; \frac{z\sqrt{\gamma}}{2\sqrt{K}\sqrt{t}} < 1.12838 \tag{6.6}$$

$$\theta(z,t) \approx 90^\circ \; for \; \frac{z\sqrt{\gamma}}{2\sqrt{K}\sqrt{t}} \geq 1.12838 \tag{6.7}$$

and expand Equation 6.3 in series around $\sqrt{A}\cos(\theta)$=0, we can get

$$
\begin{aligned}
n_{eff}(z) &= n_e n_o \left\{ n_o^2 \left(\frac{n_e^2}{n_o^2} \sin^2(\theta) + \cos^2(\theta) \right) \right\}^{-\frac{1}{2}} \\
&= n_e \{1 + A \sin^2(\theta)\}^{-\frac{1}{2}} \\
A &= \frac{n_e^2 - n_o^2}{n_o^2} \\
p &= A \sin^2(\theta)
\end{aligned}
$$

$$
\begin{aligned}
f(p) &= (1+p)^{-\frac{1}{2}} \\
&= \sum_{n=0}^{\infty} \frac{f^{(n)}(0)}{n!} p^n \\
&= 1 + \frac{-\frac{1}{2}}{1!} p + \frac{-\frac{1}{2} \cdot -\frac{3}{2}}{2!} p^2 + \frac{-\frac{1}{2} \cdot -\frac{3}{2} \cdot -\frac{5}{2}}{3!} p^3 + \cdots \\
&= 1 - \frac{1}{2} p + \frac{3}{8} p^2 - \cdots
\end{aligned}
$$

$$
n_{eff}(z) = n_e \cdot f(p)
$$

$$
n_{eff}(z) \approx n_e \left(1 - \frac{A}{2} \sin^2(\theta) + \frac{3A^2}{8} \sin^4(\theta) - \cdots \right) \tag{6.8}
$$

where

$$
A = \frac{n_e^2 - n_o^2}{n_o^2} \tag{6.9}
$$

Substituting these into Equation 6.2 allows ϕ to be determined as

$$\begin{aligned}\phi &= \frac{2\pi}{\lambda} n_e \left(d - \int_0^d \frac{A}{2}\sin^2(\theta) - \frac{3A^2}{8}\sin^4(\theta) + \cdots dz \right) \\ &= \frac{2\pi}{\lambda} n_e \left(d - \int_0^{z_{crit}} \frac{A}{2}\sin^2(\theta) - \frac{3A^2}{8}\sin^4(\theta) + \cdots dz \right. \\ &\left. - \int_{z_{crit}}^d \frac{A}{2}\sin^2(\theta) - \frac{3A^2}{8}\sin^4(\theta) + \cdots dz \right)\end{aligned}$$

$$\begin{aligned}&\int_0^{z_{crit}} \frac{A}{2}\sin^2(\theta) - \frac{3A^2}{8}\sin^4(\theta) + \cdots dz \\ &= \frac{2z_{crit}}{\pi}\int_0^{\frac{\pi}{2}} \frac{A^2}{2} sin^2(\theta) - \frac{3A^2}{8} sin^4(\theta) + \cdots d\theta \\ &= \left(\frac{A}{4} - \frac{9A^2}{64} + \cdots \right) z_{crit}\end{aligned}$$

$$\int_{z_{crit}}^d \frac{A}{2}\sin^2(\theta) - \frac{3A^2}{8}\sin^4(\theta) + \cdots dz = \left(\frac{A}{2} - \frac{3A^2}{8} + \cdots \right)(d - z_{crit})$$

$$\phi = \frac{2\pi}{\lambda} n_e \left\{ \left(1 - \frac{A}{2} + \frac{3A^2}{8} - \cdots \right) d + \left(\frac{A}{4} - \frac{15A^2}{64} + \cdots \right) z_{crit} \right\} \tag{6.10}$$

where

$$z_{crit} = 1.12838 \cdot \frac{2\sqrt{K}\sqrt{t}}{\sqrt{\gamma}} \tag{6.11}$$

In Equation 6.10, the first term in the curly brackets (the $n_e \left(1 - \frac{A}{2} + \frac{3A^2}{8} - \cdots \right) d$ term) represents a fixed phase term whereas the other terms represent a change in the phase. Setting the phase change to $\frac{\pi}{2}$ and using light of wavelength λ = 632.8 nm (He-Ne laser), together with the physical parameters for

the nematic LC, E7, allows for the determination of a time that represents a response for a $\frac{\pi}{2}$ phase modulation, which is then estimated to be $t \approx 1$ms. (There is some variation in the published parameters for E7. Based on the elastic constants published in [155] a one-constant approximation of $K \approx 15$pN is used. The rotational viscosity published in [155] is $\gamma \approx 0.08$Pa.s, but values published elsewhere are typically higher. Here I used a value of $\gamma \approx 0.15$Pa.s. I use $n_o = 1.52$, $n_e = 1.74$ from [156]. (All values are quoted at room temperature.) Note that the response time is independent of the thickness of the LC device provided that its thickness is substantially greater than twice z_{crit} at this point time, which is 0.7 µm for the above case.

The implication of these findings is that $\frac{\pi}{2}$ phase modulation is available on a millisecond timescale in the "switch-off" (relaxation) of individual nematic boundary layers provided that they are switched on at high voltage. In Section 6.4 this behaviour is demonstrated using a pi-cell device. By using a multi-pass configuration, the phase modulation is then enhanced to give a full 0 to 2π range.

6.3.2 Phase Modulation with Flexoelectro-Optic Switching

In the flexoelectro-optic effect, the applied electric field leads to an in-plane rotation of the effective optic axis of the helical structure by an angle, χ (the definition is shown in Figure 6.2(b)), which to first order is given by the equation in Section 2.3.3 [157]

$$\chi = \frac{e_1 - e_3}{K_{11} + K_{33}} \frac{E}{q} \tag{6.12}$$

where e_1 and e_3 are the splay and bend flexoelectric coefficients, respectively, K_{11} and K_{33} are the splay and bend elastic constants, respectively, E is the applied electric field, and $q = \frac{2\pi}{P}$, where P is the pitch of the chiral nematic

helix. The orientation of the chiral nematic LCs without and with imposed electric field are shown in Figure 6.2.

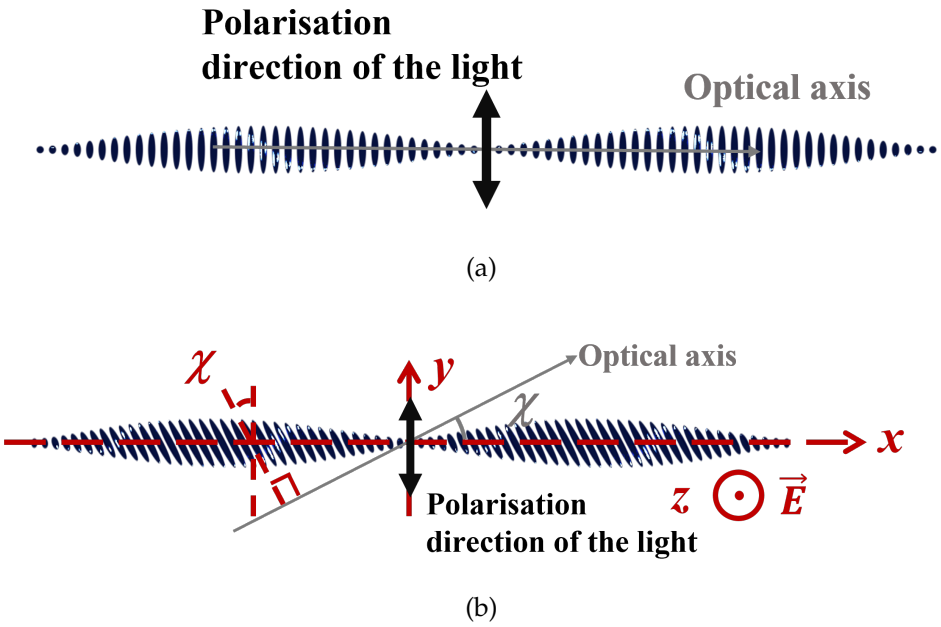

FIGURE 6.2: The geometrical quantities (tilt angle χ, optical axis orientation, polarisation direction of the light and coordinate x, y and z) definition for the configuration based on the flexoelectro-optic effect and the top view of this device: (a) Device without applied electric field; (b) Device with an applied electric field.

If the layer of LC is placed between quarter-wave plates, there is a modulation in the phase of the transmitted light. The magnitude of this phase modulation can be determined using a Jones matrix [158] approach via

$$\begin{aligned}
\vec{E}_{out} &= \vec{Q}\left(-\frac{\pi}{4}\right)\vec{LC}(\chi)\vec{Q}\left(+\frac{\pi}{4}\right)\vec{E}_{in} \\
&= \left\{\frac{\lambda}{4}\angle{-45^\circ}\right\}\left\{\frac{\lambda}{2}\angle\chi\right\}\left\{\frac{\lambda}{4}\angle{+45^\circ}\right\}\vec{E}_{in} \\
&= \frac{1}{2}\begin{pmatrix} 1+i & i-1 \\ i-1 & 1+i \end{pmatrix}\cdot\begin{pmatrix} \cos 2\chi & \sin 2\chi \\ \sin 2\chi & -\cos 2\chi \end{pmatrix}\cdot\frac{1}{2}\begin{pmatrix} 1+i & 1-i \\ 1-i & 1+i \end{pmatrix}\cdot\vec{E}_{in} \\
&= \begin{pmatrix} 0 & e^{i2\chi} \\ -e^{-i2\chi} & 0 \end{pmatrix}\cdot\begin{pmatrix} 0 \\ 1 \end{pmatrix} \\
&= e^{i2\chi}\begin{pmatrix} 1 \\ 0 \end{pmatrix}
\end{aligned} \tag{6.13}$$

$$\begin{aligned}
\vec{E}_{out} = &\left\{\frac{\lambda}{4}\angle{-45^\circ}\right\}\left\{\frac{\lambda}{2}\angle{-\chi}\right\}\cdot\left\{\frac{\lambda}{4}\angle{+45^\circ}\right\} \\
&\{M\}\left\{\frac{\lambda}{4}\angle{-45^\circ}\right\}\left\{\frac{\lambda}{2}\angle\chi\right\}\left\{\frac{\lambda}{4}\angle{+45^\circ}\right\}\vec{E}_{in}
\end{aligned}$$

$$\{M\} = \begin{pmatrix} 1 & 0 \\ 0 & -1 \end{pmatrix} \tag{6.14}$$

$$\begin{aligned}
\vec{E}_{out} &= \begin{pmatrix} 0 & e^{-i2\chi} \\ -e^{i2\chi} & 0 \end{pmatrix}\begin{pmatrix} 1 & 0 \\ 0 & -1 \end{pmatrix}\begin{pmatrix} 0 & e^{i2\chi} \\ -e^{-i2\chi} & 0 \end{pmatrix}\cdot\begin{pmatrix} 0 \\ 1 \end{pmatrix} \\
&= e^{i4\chi}\begin{pmatrix} 0 \\ -1 \end{pmatrix}
\end{aligned}$$

where $\vec{E}_{in}$ is the incoming light field, $\vec{Q}(+\frac{\pi}{4})$ are quarter-wave plates at ±45°, $\vec{LC}(\chi)$ is the flexoelectro-optic LC layer switched to an angle χ, and $\vec{E}_{out}$ is

the outgoing light field. Using Equation 6.13 it can be demonstrated that the optical phase modulation is twice the switching angle of the effective optic axis in the LC layer when the LC is effectively equal to a half-wave plate. So, if the switching angle is $\pm\chi_{max}$ then the phase modulation obtained is $\pm 2\chi_{max}$. Placing a reflector (mirror) behind this system of components, and using the modulator in a reflective mode doubles this further, giving a phase modulation of $\pm 4\chi_{max}$. Therefore, with a switching range of $\pm 45^{\circ}$ a phase range of $\pm\pi$ is available (equivalent to a full optical phase range of 0 to 2π).

This principle can be extended further to a "multi-pass" concept. The single-pass, as shown by Equation 6.13, leads to a phase modulation of $\pm 2\chi_{max}$. The reflection configuration used in previous work [150] is effectively a double-pass arrangement leading to twice this modulation, i.e., $\pm 4\chi_{max}$. Therefore, a three-pass arrangement would lead to $\pm 6\chi_{max}$, and a four-pass arrangement would lead to $\pm 8\chi_{max}$, and so on. In this chapter, I demonstrate the enhancement of the phase modulation by increasing from a single, to a double and finally a four-pass arrangement.

6.4 Experimental Results and Discussion

6.4.1 Pi-cell Phase Modulator

To begin with, the high-speed switching in a nematic pi-cell is demonstrated. The pi-cell's surfaces were treated so that they can provide a surface alignment that will create the opposite pretilt direction on both surfaces so that the flow results in no torque being applied to the LC director in the centre of the cell [154]. When the cell is switched off after applying a voltage, the flow during the relaxing process near the centre of the LC layer is in the same direction making it favourable for the LC director to realign, resulting in a faster switch-off speed. This is in contrast to the common anti-parallel cell

where there will be a 'backwards' torque on the local director near the centre of the cell. The next chapter (Chapter 7) considers the backflow of the pi-cell in more detail. For this chapter, the nematic eutectic mixture, E7 (Synthon Ltd), was capillary filled into a pi-cell, which consisted of glass substrates that were coated in indium tin oxide (ITO) electrodes and parallel rubbed polyimide alignment layers. The thickness of the device was nominally 5 µm. Placing such a device between crossed polarisers, with the alignment direction at 45° to the polariser axis, the transmission tends to zero at high voltage. When the voltage is removed the transmission increases. At the point where the transmission reaches 50%, the phase retardation of the device is equivalent to a quarter-wave plate, which is where the phase for light polarised along the alignment direction has changed by $\frac{\pi}{2}$. This is where the boundary layers have grown to a thickness of z_{crit} at each surface as outlined in Section 6.3.1.

The behaviour described here is shown in Figure 6.3 where the wavelength of light used was λ = 632.8 nm (He-Ne laser). The switching voltage waveform was a 5 kHz square-wave modulated to give a sequence of 50 V_{pp} (drive voltage), 0 V (relax voltage), and 6 V_{pp} (hold voltage) (The waveform generator was a Tektronix AFG 3022). Firstly, the 50 V_{pp} switches the device on before the 0 V then allows the boundary layers to grow from the surface. At the point where the transmission reaches 50% a holding voltage of 6 V_{pp} was applied so that the LC director can be held at a position providing a $\frac{\pi}{2}$ phase modulation in a single pass. The sequence was then repeated. Importantly, the time to "relax" to a transmission of 50% was found to be 0.75ms. This is actually slightly less than the equivalent time for $\frac{\pi}{2}$ phase modulation estimated in Section 6.3.1, but it should be remembered that this was based on a simplified analytic approach.

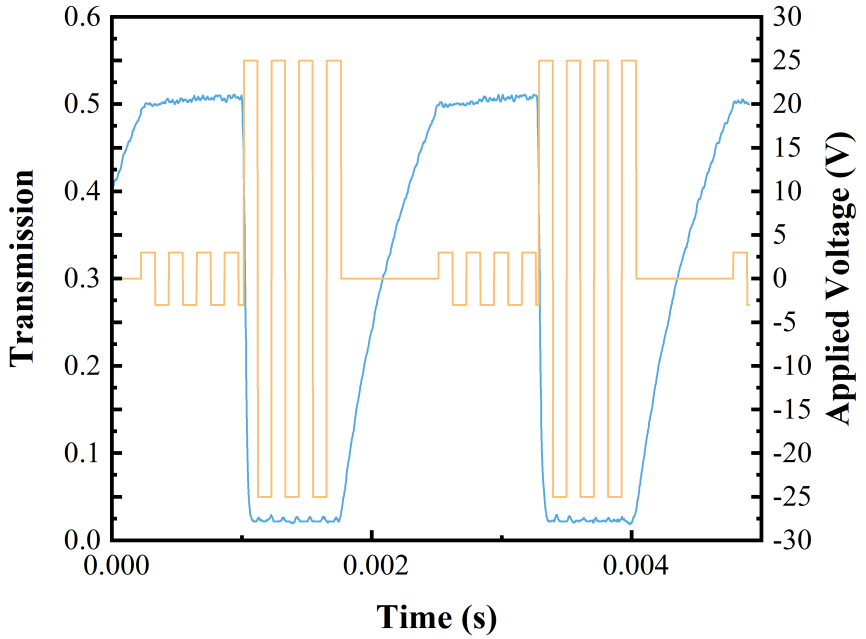

FIGURE 6.3: Transmission as a function of time (blue solid line) for a pi-cell between crossed polarisers when the device was driven by the waveform sequence described in the main text. Modulation of the transmission by 50% corresponds to a phase change of $\frac{\pi}{2}$ in the extraordinary wave. The orange solid line shows the voltage waveform applied to the device.

Next, the pi-cell device was placed in a Mach-Zehnder interferometer [159]. The experimental arrangement was as shown in Figure 6.4(a). The resulting fringes were recorded using a CCD camera as the device was switched through the sequence described previously. The CCD camera had an exposure time of 1ms and in order to capture the position change of the interference fringes (which have a similar frequency as the frame rate of the camera), the frequency of the applied voltage was set to 1 Hz higher than it should be (say for just an experiment consisting of two states, 1 ms for "drive voltage" and 1 ms for "relax voltage", the frequency that was actually applied was 501 Hz). The method of frequency drift for better perception of the change in the interference patterns has little impact on the real phase modulation achieved for each device so in the following discussion, the time of each part is still considered as 1 ms. The time for "drive voltage", "hold voltage", and "relax voltage" of the modulated 5 kHz waveform was now set to be 1

ms (i.e., 1 ms at drive voltage, 1 ms at relax voltage, 1 ms at hold voltage, repeated). The recorded fringes were then analyzed to track the phase-change of the wavefront of the light passing through the pi-cell device. To demonstrate control of the resulting phase of the transmitted light the modulation of the 50 V_{pp}, 0 V, 6 V_{pp} sequence was then adjusted, and the phase-change tracked for each case. (Note: as the modulation of the waveform was decreased the drive voltage reduced and the relaxation voltage increased, but the overall rms voltage remained sufficient to retain the pi-state in the device.)

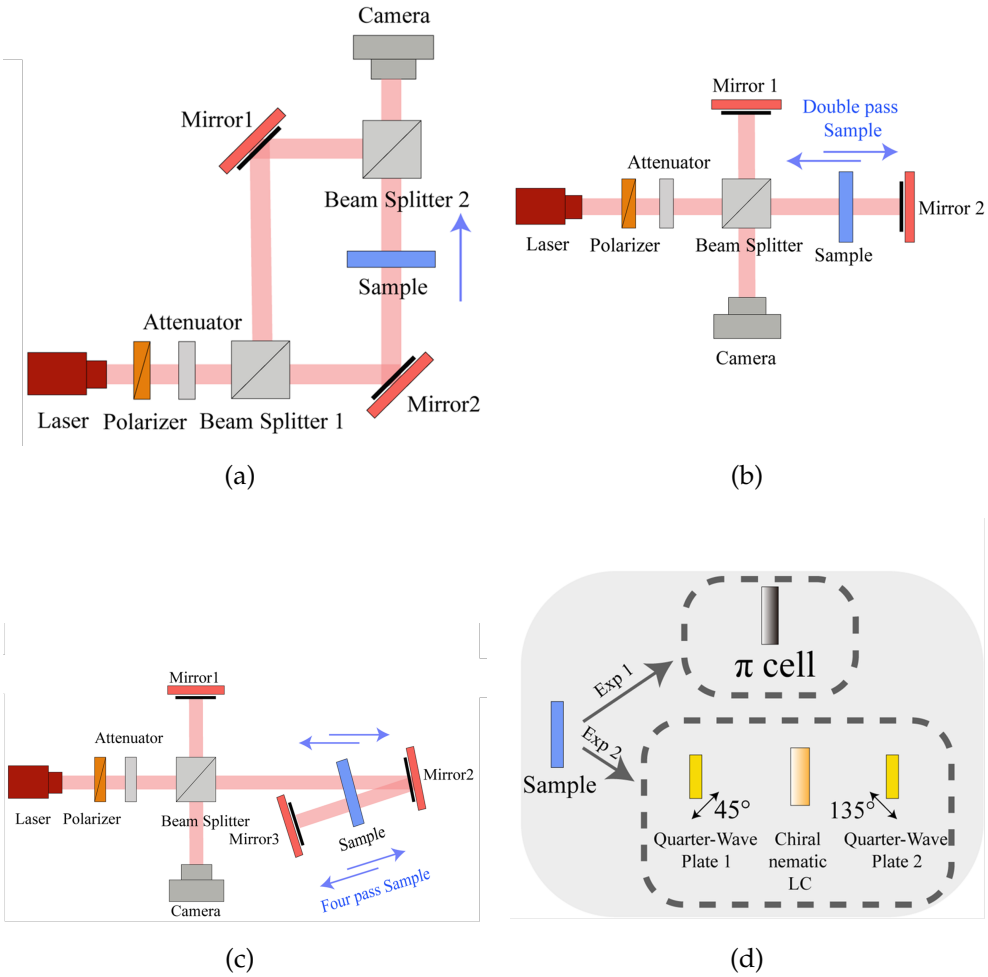

FIGURE 6.4: Schematic diagrams of the experimental arrangements. (a) The one-pass setup (Mach-Zehnder interferometer); (b) The two-pass setup (Michelson configuration); (c) The four-pass setup ("folded" Michelson configuration); (d) The two different device geometries used: a pi-cell and a flexoelectro-optic device between quarter-wave plates.

The results are shown in Figure 6.5 where the x-axis shows the difference between the drive voltage and the relaxation voltage (ΔV), and the duration for each state is 1 ms. In the figure, we can see that a maximum phase modulation of slightly in excess of 90° was obtained and that this varied smoothly as the modulation was changed. This response was obtained in 1 ms. The amplitude (or intensity) modulation in this configuration is minimal because the nematic director is switching in the plane of the incident polarised light. There are small losses due to the reflections at the device surfaces, and the small amount of optical scattering in the nematic LC, but the overall arrangement is very optically efficient.

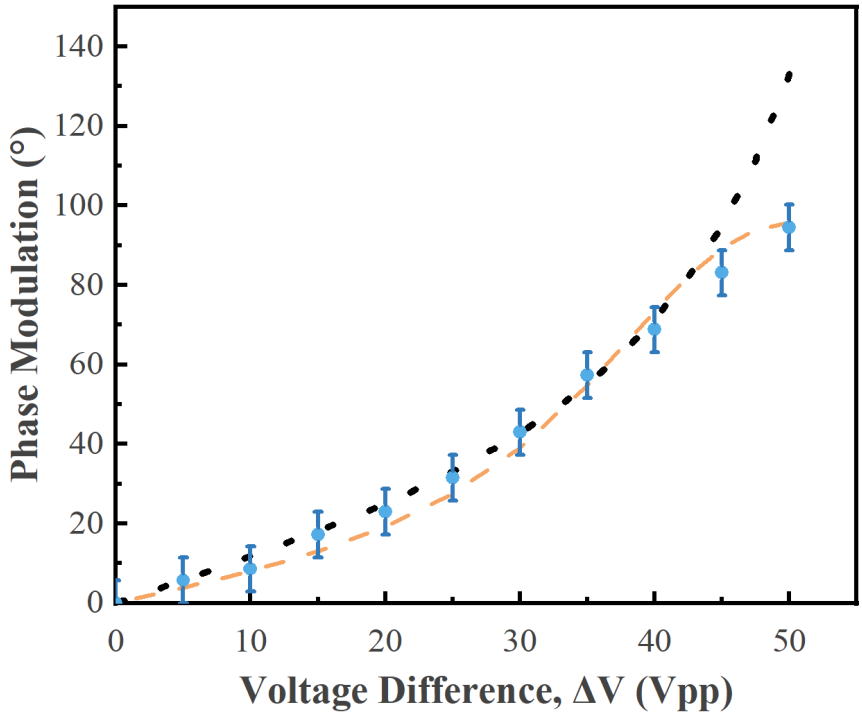

FIGURE 6.5: Phase modulation obtained using a pi-cell, driven by the waveform sequence as described in the main text. The data points (blue circles) are from the experiments and the dashed orange line represents the results from the numerical model. The dotted black line shows the results from a simplified analytic model.

Figure 6.5 also shows the results from modelling the phase behaviour. An analytic model can be developed based on the ideas introduced in Section 6.3.1. In this case, a piecewise linear form was again used, but now the boundary layer thickness, z_{crit}, was determined by minimising the energy

for the driving and holding voltages (this leads to the dotted black line in Figure 6.5). Alternatively, rather than using the analytic estimation outlined in Section 6.3.1, a model can be based on a finite-difference numerical solution to the Euler-Lagrange equations for nematic continuum theory. Only the splay and bend elastic constants are relevant in this model (values of K_{11} = 11.1 pN and K_{33} = 17.1 pN were used for E7 [155], this leads to the dashed line in Figure 6.5). The device thickness was 5 microns, $\Delta\varepsilon$ = 14.0, and Δn = 0.22. The analytic model is reasonable at lower modulation levels but diverges substantially at higher modulation levels. This may be because the dynamic behaviour becomes more important in these cases. For the numerical model it can be seen that whilst the overall trend is reasonable, the model falls slightly outside of the error bars associated with the experimental data (measurement of optical phase from the interferometer). It is not entirely clear why this is so, although it may be due to the lack of inclusion of flow in the model, this being generally considered to enhance the switching speeds in pi-cells [160]. (Some allowance for this effect was included by reducing the rotational viscosity for the fit, where a value of γ = 0.07 Pa·s was used, which is very similar to the value quoted in [155]). In subsequent figures, only the results from the numerical modelling need to be considered.

For the geometry considered here, light only passed through the device once (i.e., it is a one-pass configuration). Next, the interferometer was reconfigured into a Michelson configuration [161] and the device was placed in one arm to give a two-pass arrangement. The diagram of the two-pass set-up is shown in Figure 6.4(b). The light then passed through the device twice, and an enhanced optical phase modulation effect was obtained. The results, for the same driving conditions used previously, are shown in Figure 6.6(a). We can see from the figure that the behaviour follows the same trend as that shown in Figure 6.5, but the optical phase modulation is now twice

as much, reaching a maximum in excess of 180° (π).

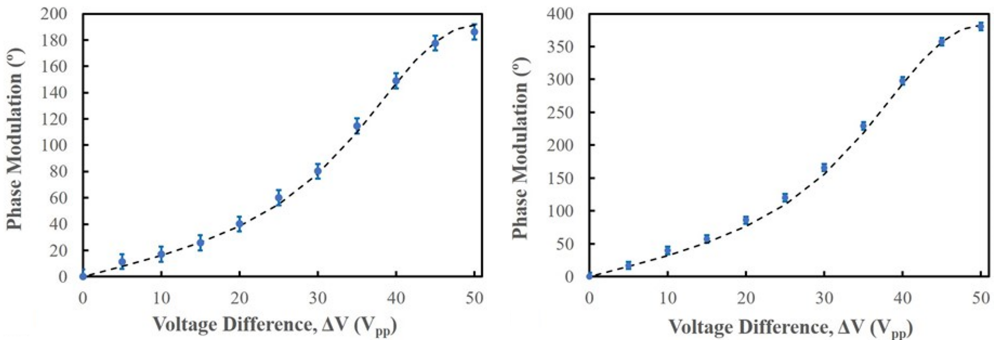

(a) (b)

FIGURE 6.6: Phase modulation obtained using a pi-cell. The points are the experimental data and the dashed lines are based on the results from the model. (a) Two-pass configuration; (b) Four-pass configuration.

To increase the modulation depth further, the arrangement of the interferometer was modified to pass the light through the device four times; this was done by adding an additional mirror into the signal arm of the Michelson arrangement; the diagram is shown in Figure 6.4(c). The result for this four-pass configuration is shown in Figure 6.6(b). Here we can see that an optical phase modulation in excess of 360° (2π) is obtained. Again, the experimental data lie slightly off the line of the model. However, importantly, this configuration has demonstrated a full phase modulation of the light (i.e., a phase range of greater than 0 to 2π) with a 1 ms switching time. Even faster switching times would be available using more optimised materials, such as that used in the work by *Huang et al.* [149]. Such development would be very helpful and wanted in beam steering, free-space communication, adaptive optics and any other that requires fast phase modulation to encode the information into light or SLMs.

6.4.2 Phase modulation with multi-pass flexoelectro-optic switching

The multi-pass phase modulator configuration was also considered for use with the flexoelectro-optic devices. For the flexoelectro-optic effect, I first investigate the switching behaviour of a mixture, consisting of a base chiral nematic mixture comprising E7 + 3 wt.% BDH1281 (Merck) that was doped with 20 wt.% of the bimesogenic (dimer) material 4',4'-(nonane-1,7-diyl)bis-[(1',1"biphenyl)-4"-carbo-nitrile] (CB9CB) [162, 163]. The chiral nematic mixture, which formed a right-handed helical structure with a pitch of about 520 nm, was capillary filled into a nominally 5 µm thick device that consisted of glass substrates that were coated with ITO electrodes (to facilitate the application of an electric field along the normal to the device substrates) and anti-parallel rubbed polyimide alignment layers. To ensure that the electric field was orthogonal to the helical axis (a necessary requirement to observe flexoelectro-optic switching) a uniform lying helix (ULH) geometry was required. To form the ULH alignment, the device was heated up to 50°C in the presence of a 500 Hz, 25 V_{pp} square waveform and then cooled down to room temperature in the presence of an applied electric field. After going through such a process, the helical axis of the ULH structure is aligned perpendicular to the rubbing direction of the cell's pretreatment layer. All measurements were carried out at room temperature.

The resulting mixture shows enhanced flexoelectro-optic switching when compared to the base E7 + 3 wt.% BDH1281 mixture, but in contrast to the neat bimesogenic material which exhibits a nematic phase that is at substantially elevated temperatures (>100 °C), this mixture can still be operated at room temperature. The electro-optic properties were investigated by applying a 500 Hz (ensure a 1 ms switching time for optic axis switching) square wave voltage waveform using a Tektronix AFG 3022 waveform

generator and measuring the switching angle using a combination of a BX51 polarising microscope, a Tektronix TBS1154 oscilloscope and high-speed Si photodiode [164]. This measurement method is used further in Chapter 8 and discussed in more detail in Section 8.4. The results are shown in Figure 6.7(a).

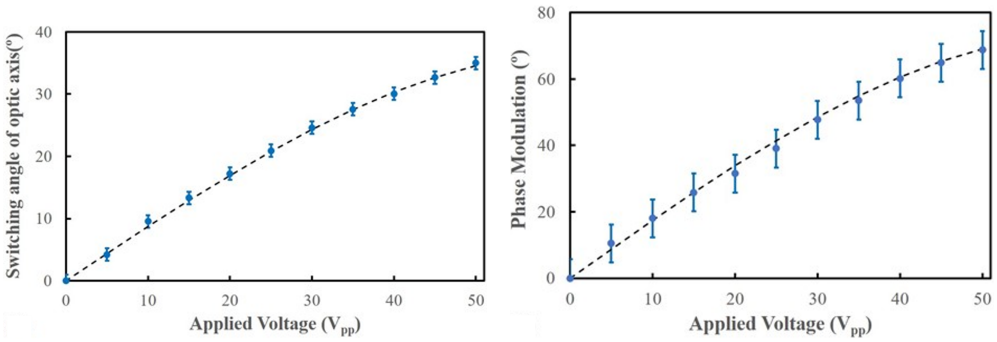

(a) (b)

FIGURE 6.7: Flexoelectro-optic switching in the chiral nematic phase of the mixture E7+3 wt.% BDH1281 + 20 wt.% CB9CB in a 5µm thick device. The applied voltage was a 500 Hz square wave. (a) The flexoelectro-optic switching angle (peak-to-peak, as measured on a polarising optical microscope) is shown as a function of the applied voltage (peak-to-peak) and the dashed line represents a cubic series expansion fit based upon theoretical considerations. (b) The resulting optical phase modulation in transmission for the same range of flexoelectro-optic switching angles when the device was placed between a pair of quarter-wave plates.

In Figure 6.7(a) we can see that a peak switching angle of around 35° (±17.5°) was obtained at a switching voltage of 50 V_{pp} (±25 V). However, at this voltage, the helix of the chiral nematic LC begins to unwind and there is some change in the alignment texture; therefore, operation at slightly lower voltages may be preferred. Due to the dielectric anisotropy of the material, and the resulting helix distortion under electric field application, the overall flexoelectro-optic switching behaviour is complex. However, the switching angle can be approximated in terms of a cubic series expansion [165]-this is the dashed line in Figure 6.7(a). This cubic series can be written in terms of the expression for flexoelectric tilt introduced earlier in Section 6.3.2, plus a

correcting cubic term:

$$\chi = \frac{e_1 - e_3}{K_{11} + K_{33}} \frac{E}{q} + \beta \left\{ \frac{e_1 - e_3}{K_{11} + K_{33}} \frac{E}{q} \right\}^3 \tag{6.15}$$

where β is treated as a fitting parameter, and is a complex combination of elastic, dielectric and flexoelectric properties [165]. From the dashed line in Figure 6.7(a) the ratio $\frac{e_1 - e_3}{K_{11} + K_{33}}$ can be determined, which is sometimes referred to as the flexo-elastic ratio for the material, to be 0.924 V^{-1} and the value of the fitting parameter β which is β = -1.446, the negative value of β indicating that the dielectric coupling tends to suppress (reduce) the flexoelectric tilt angle. To note that the E in Equation 6.15 refers to the amplitude of the electric field and there is a conversion between V_{pp} to E which is $E = V_{pp}/d$ (d is the cell thickness, 5 µm).

The flexoelectro-optic device was then placed between quarter-wave plates (Figure 6.4(d) Exp2) and inserted it into one arm of the Mach-Zehnder interferometer for the purpose of phase modulation enhancement. The device was again driven with a 500 Hz square wave (so the switching response to either polarity is taking place in 1 ms), and the interference fringes were recorded on the CCD camera and tracked to extract the resulting optical phase modulation. The resulting phase modulation is shown in Figure 6.7(b) and a corresponding phase modulation simulation (dashed line in Figure 6.7(b)) was also carried out based on the simulated results in Figure 6.7(a) and the Equation 6.13. We can see that, as expected, the resulting phase modulation is twice the switching angle of the optic axis in the device – this is because the light passes through the device a single time. However, this optical phase modulation is still rather small, with a maximum range of 70° at 50 V_{pp}. There are some losses in this arrangement due to imperfections in

the alignment of the helical axis in the flexoelectro-optic device. These alignment imperfections lead to point defects in the LC structure, which in turn results in considerable optical scattering. The demonstration device is therefore somewhat optically inefficient, although it is expected that improvements to the alignment quality would considerably reduce this problem. By choosing the orientation of the device appropriately there is minimal amplitude (or intensity) modulation in this configuration. This is estimated to be less than 10% in amplitude (less than 1 dB).

The phase modulation depth can be enhanced if the device is instead placed (still between quarter-wave plates) in one arm of the Michelson interferometer. In this case, the light now passes through the device twice. This configuration has been considered previously using a different mixture that exhibited large switching angles but at very high temperatures (108°C) [150]. The result for the present device is shown in Figure 6.8(a). It is immediately noticeable in the figure that the phase modulation has a different curvature from that shown in Figure 6.6 for the switching angle and single-pass phase modulation behaviour, with the curvature being reversed at lower voltages. Figure 6.8(b), which presents the result when the light passes through the device four times, shows similar qualitative behaviour to the two-pass case. This effect happens because of the change in retardation of the LC layer under an applied voltage. The material used here has a significant dielectric anisotropy (as noted earlier, for E7 only at room temperature $\Delta\varepsilon = 14$), and therefore under the application of the electric field there is a tendency for the helix of the chiral nematic LC to distort.

In the configuration used here, with the electric field direction and light propagation direction perpendicular to the helical axis, this leads to a reduction in the effective optical anisotropy as the electric field amplitude

was increased. To first order, this reduction is quadratic in the applied electric field [165]. When the flexoelectro-optic LC device was placed between a pair of quarter-wave plates and the phase shift was measured using polarised light (the configuration for the one-pass transmission measurement results shown in Figure 6.7(b)) then the phase modulation follows the tilt angle of the optical axis, as can be seen by comparing Figure 6.7(a) and Figure 6.7(b). However, when a mirror is placed behind the second quarter-wave plate the behaviour changes. The configuration experienced by the light path is now: quarter-wave plate, LC device (first pass), quarter-wave plate, mirror, quarter-wave plate, LC device (second pass), quarter-wave plate. Now, changes in the effective birefringence of the LC layer under the application of an electric field distort the optical phase change as a function of tilt angle behaviour, making it non-linear, and resulting in the curves seen in Figure 6.8. The shape of these curves would be qualitatively similar to those shown in Figure 6.6 if a polariser were placed between the second quarter-wave plate and the mirror. More details regarding the retardance change of a flexoelectro-optic LC device under an applied electric field will be discussed further in Chapter 8.

In Figure 6.7(a) the switching angle of the flexoelectro-optic LC device for a voltage of 45 V_{pp} ($\pm$22.5 V) at 500 Hz is over a range of 32.5° (i.e., $\pm$16.25°). The resulting optical phase change available in a one-pass configuration is then twice this value, being 65° for 45 V_{pp} as shown in Figure 6.7(b). Although the shapes of the curves are different, we can see that in the two-pass case, the maximum optical phase modulation is again doubled (to a range of 130° for 45 V_{pp} in Figure 6.8(a). In the four-pass case, it is further doubled to a maximum range of 260° for 45 V_{pp}, as seen in Figure 6.8(b). At this point, the optical phase modulation is eight times the flexoelectro-optic

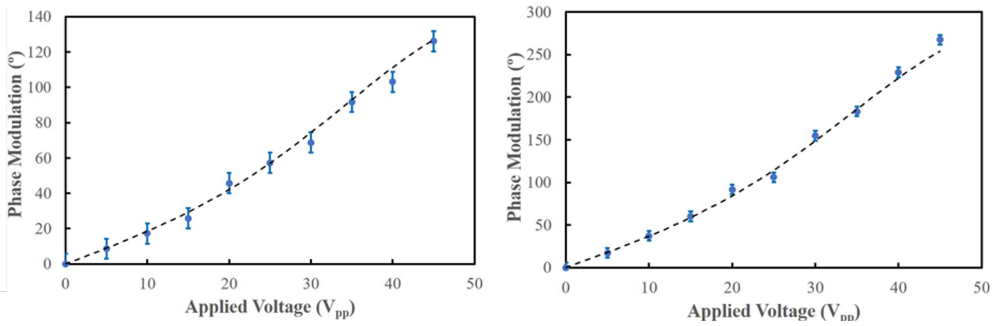

(a) (b)

FIGURE 6.8: Phase modulation as a function of the applied voltage (peak-to-peak) for the flexoelectro-optic device consisting of the chiral nematic mixture E7+3 wt.% BDH1281 + 20 wt.% CB9CB for multi-pass geometries. The thickness of the device was nominally 5 µm (a) two-pass and (b) four-pass configurations. The data points represent the results from the experiments and the result from the model(s) are the black dashed lines. The model is based on the derivation of the Jones matrix that the phase modulation is twice the rotation angle of the optic axis χ where χ can be simulated based on Equation 6.15. The precise form of the behaviour depends on the orientation of the device, which, as mentioned above, has been chosen to minimise the light intensity modulation and keep this below 10%.

switching angle range, which means that full 0 to 2π optical phase modulation would be available in this arrangement using a flexoelectro-optic device with a switching angle of 45° ($\pm$22.5°).

6.5 Summary

In summary, the results presented in this chapter have demonstrated two different configurations that allow substantial optical phase modulation on a millisecond timescale at room temperature. Using a pi-cell driven at high voltages in a multi-pass optical arrangement has allowed a boundary layer high-speed switching effect to be exploited, giving full 0 to 2π optical phase modulation in 1 ms. It should be noted that this device used the well-characterized nematic LC, E7, and therefore substantially faster switching times could be obtained by using an optimised mixture (e.g. one with lower rotational viscosity, higher optical birefringence, and larger elastic constants). This

would therefore pave the way to full 0 to 2π optical phase modulation in sub-millisecond time scales.

Using the flexoelectro-optic effect in chiral nematic LC devices, enhanced multi-pass optical phase modulation has been demonstrated. Modulation of 260° was achieved on a 1 ms time-scale using a material which showed a switching angle of just over 32° at 45 V_{pp} ($\pm$16° at $\pm$22.5 V). Full 0 to 2π optical phase modulation could be achieved either using a slightly more optimised mixture (to give a switching angle of $\pm$22.5°) or by using a six-pass optical arrangement. For example, a material developed by Varanytsia and Chien based on the nematic material MLC-2048 (Merck) doped with the bimesogenic (dimer) material CB7CB showed room-temperature switching angles of up to $\pm$40° [78], although this was at somewhat higher applied fields.

A key application of the ideas proposed here is in the development of SLM technology with sub-millisecond switching over a full phase range. In order to implement the multi-pass configurations using such technology it would be necessary to ensure that each modulating pixel is re-imaged onto the same modulating pixel in subsequent passes. For two-pass operation, this can be achieved by integrating a mirror into the back-plane of the device. For four-pass (and higher) arrangements there are two possible approaches. Firstly, Peng et al. have demonstrated a very interesting integrated multi-pass configuration when optimising the phase modulation available using blue-phase LC technology [166]. The material they used, was a polymer-stabilized blue phase LC (PS-BPLC) that was polarisation independent and the material was sandwiched between a reflective polariser (reflects s-wave but transmits p-wave), broadband quarter-wave plate ($4/\lambda$ placed at 45° with respect to the direction of the reflective polariser), ITO glass substrates and the aluminium (Al) multi-pixel electrode panel mirror.

The linear polarised light changes into left/right-handed circular light when it passes through the quarter-wave plate or is reflected by the Al electrode, and the PS-BPLC adds the same phase shift to both the x and y components of the circular light. After four times of accumulation, the outgoing light recovers its original polarisation (s-wave) but has a 2π phase shift. This solution is very elegant, but the integrated mirrors do substantially reduce the useable mark-space ratio of the pixels in a device. Secondly, an alternative approach to this would necessitate an imaging system, such as a four-f system. In this arrangement light is incident on an SLM with an integrated Al mirror back-plane. The reflected light from the Al mirror is then passed through a lens, which is placed one focal length away from the back-plane, and another lens is put two focal lengths away from the first lens. The mirror is then put one focal length behind the second lens. The light is hence reflected and precisely imaged back through the two lenses onto the same pixel in the SLM. The light, therefore, passes four times through each individual pixel. Further higher-pass multi-pass configurations can be envisaged, although the imaging arrangements would not be convenient to implement.

A further concern for the practical technological implementation of the ideas presented in this chapter is the drive voltages used. These are up to 50 V_{pp} ($\pm$25 V), which are somewhat higher than normally used in SLMs with integrated silicon back-planes. However, it is anticipated that these drive voltages could be reduced through material choice and/or optimisation. In the pi-cell demonstration, the work was undertaken with the standard nematic material E7. Choosing (or potentially developing) a material with higher dielectric anisotropy and high optical birefringence would allow the drive voltages to be substantially reduced. The flexoelectro-optic phase modulator was constructed using an in-house developed mixture. Again, optimisation of the material to enhance the flexoelastic ratio and increase its

birefringence would allow the use of thinner layers at reduced voltages.

Chapter 7

Backflow-assisted Time-resolved Phase Modulation in Nematic Liquid Crystal Devices

In this chapter, an experimental method is presented to extract the time-resolved phase modulation of three different nematic liquid crystal (LC) devices: pi-cell (parallel-rubbed alignment layers), Fréedericksz cell (anti-parallel rubbed alignment layers), and a hybrid aligned nematic (HAN) device. Results are shown to be in good agreement with simulations of the phase modulation for the three nematic devices when backflow is taken into consideration. Results from this chapter have been published in the journal article *Optics&LaserTechnology*156(2022) : 108596 [19].

7.1 Introduction

Like Chapter 6, the subject of this chapter is optical phase modulation in LC devices. Here the focus is on the time-dependent phase modulation behaviour, with the aim of investigating and demonstrating the benefits of

backflow on the phase modulation depth of nematic LC devices. As mentioned in the previous chapter and the introductory chapter, LC-SLMs have become an enabling technology for shaping the wavefront of light in a range of different applications including laser micromachining [167], optical communications [168], and biomedical imaging [169]. A key reason why LC-SLM technology is of significant value is that it enables direct control over the structure of the optical illumination through the application of a voltage to a thin pixelated LC layer.

There are various modes that an LC-SLM can be operated in, such as only modulating intensity, only modulating the phase or modulating intensity and phase simultaneously. In this chapter, the phase-only optical modulation was studied in particular, as phase-only optical modulation is found to be important for augmented reality (AR) near-eye displays [149, 170–172] and free-space optical beam steering [173–175]. When considering which LC phase to use in LC-SLMs, the choice has historically been between nematic [176] and ferroelectric [177] materials, although other LC phases have been considered in recent years [178].

In terms of the technology requirements for current commercial applications, both the nematic and ferroelectric phases have their advantages and disadvantages, such as depth of modulation versus speed, and the trade-off between these properties depends upon the nature of the application. Ferroelectric LC (FLC) systems can be operated in a number of modes, but it is common in SLM applications to use in a bi-stable arrangement. Depending on the choice of input and output optical polarisation states this then allows either amplitude modulation or phase modulation or a combination of both. For example, a previous study demonstrates a FLC device for optical modulators that can switch between two molecular aligned states using a surface-stabilized FLC arrangement [179]. More recent work reports a free

space adaptive optical interconnect with a vertical-cavity surface-emitting laser transmitter module operating at 1.25 Gb/s and a bi-state FLC-SLM which can provide a retardation of approximately 0.8π at 850 nm and a refresh time of 192 µs for each 1280x768 frame [180]. A critical feature that is essential for AR display applications as well as for optical communications is the switching speed, which is determined by both the LC phase that is used and the fundamental configuration of the LC layer (e.g., the alignment of the director in the case of a nematic LC). In the case of nematic LC devices that consist of anti-parallel rubbed planar alignment layers (e.g., rubbed polyimide), the result is a uniformly-aligned nematic LC layer with the director aligned approximately parallel to the device substrates. When an electric field is applied, and for a positive dielectric anisotropy nematic LC, the director rotates to align with the electric field (as discussed in Chapter 2). The threshold voltage above which the LC director reorients is known as the Fréedericksz transition voltage. Due to the two different principal refractive indices along and perpendicular to the director, the result is a modification in the effective birefringence (as discussed in Chapter 2), which in turn alters the difference in the optical path length and consequently the phase difference, thus making optical phase modulation possible. If the LC layer is operated in a phase-only mode, then ideally the incident light should be polarised along the n_e direction.

Even though the ferroelectric phase has excellent fast switching speed in a practical device application, analogue phase modulation is generally much more useful than bi-state modulation, which in turn requires a continuous rotation of the LC director under an applied electric field. The detailed nematic LC device behaviour is complicated by the various physical processes that take place during switching, which are influenced by both the material and device behavioural properties such as the elasticity, viscosity, and

backflow. Combined with the initial device configuration, these properties determine the speed of the phase modulation and have significant impacts on the switching speed of LC-SLMs [181]. For example, flow-reorientation coupling in nematic director switching (commonly referred to as backflow) tends to slow down the switch-off process in nematic LC-based device technology. This is because during switch-off the director reorientation induced LC flow tends to work against the required reorientation process, slowing down the behaviour. This is unfortunate because slow modulating LC-SLMs impede higher information bandwidth and limit high-speed applications – for example, this can result in a breakup in field sequential colour operation [182]. Understanding the time-resolved response of the phase modulation is therefore of crucial importance in terms of improving the response time and selecting the best-performing configurations. This, in turn, requires a direct measurement of the time-resolved response of the optical phase modulation of these LC phase modulators.

Whilst in many of the practical applications involving LC phase modulation, such as in SLMs, it is the relative phase of the propagating wavefront between different pixels which is important. In order to study phase modulation behaviour directly it is beneficial to measure the induced phase change relative to a reference wave. A convenient way to do this is, for example, to use a Michelson interferometer whereby the LC device to be investigated is placed in one "arm" of the interferometer. Other methods that have been explored include Young's double slit configuration [183] or by introducing a Ronchi grating in the object plane and observing the variation in the diffraction pattern in the imaging plane so as to infer the phase modulation depth [184]. Another approach is to use a Twyman-Green interferometer, which can provide quantitative information about the phase shift [185, 186]. In previous work on LC phase measurement, a method of tracking the changes in

the phase by imaging the interference fringes was adopted [18]. However, this method is not ideal because for LC devices that reorient at millisecond timescales, it is necessary to use either high-speed imaging of the fringes or else to use a stroboscopic imaging approach. Additionally, the process of phase modulation extraction from the data, through image processing and fitting of line samples from images, adds additional complexity and potential sources of error, particularly as highly uniform images of the fringes are required.

To address these issues a more direct measurement of the phase as a function of time is needed. Previous work has used a heterodyne interferometer to measure optical phase over time [187]. This manipulated a heterodyne interferometer and acousto-optic frequency shifters to measure the phase shift of the light directly. The system can capture and measure the signal without time-averaging but needs rather complex signal processing and expensive hardware support. In this chapter a variation on this approach is used, such that a piezoelectric scanning mirror is placed in the reference arm of a Michelson interferometer to provide a continuous phase shift in the reference signal. The interference signal intensity is then recorded and the phase modulation can be extracted directly. Using this technique, the time-dependent phase modulation behaviour for three technologically-important nematic LC alignments are presented, which are shown in Figure 7.1.

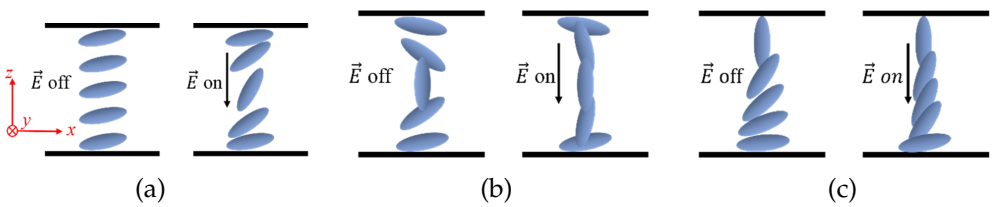

FIGURE 7.1: Illustration of the three different configurations of the LC director for the nematic LC devices considered studied in this chapter: (a) Fréedericksz device (anti-parallel rubbed alignment layers); (b) Pi-cell (parallel-rubbed alignment layers); (c) HAN device. All configurations are shown with and without an applied electric field. It is considered that the director only rotates within the x-z plane.

Figure 7.1(a) illustrates anti-parallel rubbed planar aligned nematic LC (this work refers to this as the Fréedericksz cell) [188] - this is actually the most commonly used nematic alignment in phase modulation nematic SLMs. Figure 7.1(b) illustrates parallel-rubbed planar alignment (the pi-cell configuration) [188] – this has been shown to exhibit fast switching, and results for a multi-pass configuration were presented in the previous chapter. Early work on this operating mode showed that the relaxation time from the switched state to the bend state (shown as the E on and E off states in Figure 7.1(b)) could take place on millisecond time scales [154]. Further investigations showed that the unique geometry of the pi-cell configuration allows more favourable nematic director switching dynamics (flow-reorientation coupling) than other switching modes, enhancing the switching speed and making the mode potentially useful for high-speed applications such as field-sequential colour displays [160, 189]. This mode is therefore also interesting for current and future optical phase modulation technologies. In Figure 7.1(c) a hybrid aligned nematic (HAN) [190] cell arrangement is shown.

In the work presented in this chapter, a comparison is made of the experimental findings with simulations of the phase modulation behaviour when backflow is taken into account, and the combined effect of backflow with the elasticity and viscosity properties is typically discussed in the context of response time studies. By modelling the influence of backflow for these three different nematic LC device configurations, and making comparisons with experiments, it is possible to identify the optimum configurations and understand their resultant behaviour. These dynamic phase response measurements demonstrate that backflow hinders the response of the Fréedericksz cell but not the response for the pi-cell. The findings and experimental technique presented would be of importance for commercial LC devices

and could, in the future, lead to the development of faster, analogue phase-only optical modulation.

7.2 Phase Measurement Configurations

7.2.1 Experiment Configuration

A schematic of the Michelson interferometer that is equipped with the piezo-electric scan mirror arrangement used in this study is shown in Figure 7.2.

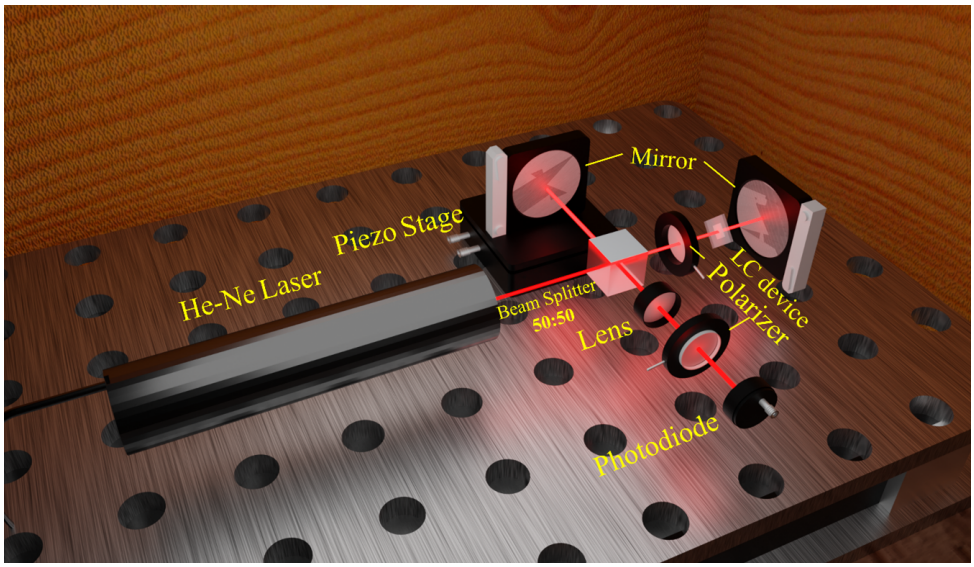

FIGURE 7.2: Pictorial representation of the Michelson interferometer with a piezo-electric scan mirror placed in one arm of the interferometer.

A continuous wave He-Ne laser (Thorlabs, HNL505L) operating at 632.8 nm is passed through a 50:50 beam splitter (Thorlabs, BS016-50:50 Non-Polarising Beamsplitter Cube, 400-700 nm, 20 mm) where the beam is split into two: one beam passes through a linear polariser and then the LC device under test before being reflected back by a mirror. The orientation of the LC device is such that the surface alignment direction is parallel to the incident polariser in order to lead to optimum phase modulation. The other beam, on the other hand, propagates towards a second mirror that is mounted on a

piezoelectric stage (Melles Griot, 17 TFJ001/D) that is controlled by a waveform generator (Multicomp PRO, MP750510) via a Melles Griot Piezoelectric Controller (17 PCW002). The 0-10 V dc signal from the waveform generator can drive the Melles Griot Piezoelectric Controller to output a signal from 0-to-75 V in order to control the Melles Griot piezoelectric stage. By carefully adjusting the frequency, shape and amplitude of the control waveform, the piezoelectric stage that is fitted with the mirror can move along the optical axis back and forth smoothly. The piezoelectric stage is controlled by a triangular waveform with a 10% symmetry, 30 mHz frequency so that the mirror travels from 30 µm to 35 µm (the total travel distance of the piezo stage is 50 µm and has a good linearity between 8 µm and 45 µm, here the control output of the waveform generator is 6-7 V.) over a period of 30 seconds and quickly moves back to the start position (30 µm) in 3.33 seconds.

The principle of this method is generally referred to as phase shifting interferometry. This approach can be used in a range of applications, such as in axial surface and position measurement and in high-resolution interference microscopy [191–193]. The method is generally based on changing the optical path length smoothly and continuously in the reference arm, resulting in intensity in the interference pattern which will continuously change. The resulting signal (or series of images in an imaging system) can then be analysed to extract the required phase information. For example, in this system, this approach leads to a sine wave profile being captured for a fixed signal beam phase. The frequency of this sine wave depends on the characteristics of the movement of the scanning stage. The LC phase modulator under investigation is then controlled by an external waveform signal. The phase shift waveform from the signal arm will then effectively be overlaid on top of the sine wave to form a new waveform with a different shape. By selecting, extracting, and analysing the new waveform at some key feature points,

then the value of the phase shift can be extracted, as explained in the analysis in the next section. The material chosen for this investigation is the widely studied LC nematic mixture E7 (Synthon Chemicals Ltd.), which has been used in the previous chapters. The clearing temperature of this mixture is 58°C [194] and the ordinary and extraordinary refractive indices are quoted to be n_o=1.52 and n_e=1.74 [195], respectively, at a wavelength of 632.8 nm and room temperature. The dielectric anisotropy of E7 at room temperature is reported to be $\Delta\varepsilon$=14 [196].

7.2.2 Theoretical Considerations: Extraction of the Optical Phase

In general, the single point intensity observed on an imaging plane resulting from the interference between two light waves can be written as a short-term average $I = \langle\{E_1(t) + E_2(t)\}^2\rangle$, where $E_1(t)$ and $E_2(t)$ are the instantaneous electric fields generated by the waves from the two interfering light sources, and the average is taken over a time which is large compared with the period of a light wave, but small compared with the time-scale of modulating signals of interest.

The light at the detector in this system is the sum of the light propagating along the reference arm and the light propagating along the signal arm of the interferometer as presented in Figure 7.2. Ignoring the phase change due to the propagation of the light along its path, the light from the reference arm can simply be expressed as

$$E_{ref}(t) = A\cos(wt) \tag{7.1}$$

whereas the light for the signal arm is given by

$$E_{sig}(t) = B(t)\cos(wt + kt + \Delta + \phi(t)) \tag{7.2}$$

where E_{ref} and E_{sig} represent the electric field component of the reference and signal arm light, respectively, t is time, A and $B(t)$ are the amplitudes of the reference and signal light beam, respectively (where the signal is shown as time-dependent because the modulator may introduce amplitude/intensity modulation as well as phase modulation), w is the angular frequency of the light, kt is the term for the continuous phase change resulting from the piezo-electric scan mirror, Δ is the system optical path difference which results from the system construction process, and $\phi(t)$ is the time-dependent phase modulation induced by the LC device.

Assuming that the photodiode is not responsive to the frequency of the light, but has a sufficient bandwidth to respond to the modulating signals, then based on Equation 7.1 and Equation 7.2, the light intensity can be determined by calculating the average over a short time of the square of the sum of these two equations, which leads to the following:

$$I = \frac{A^2}{2} + \frac{B(t)^2}{2} + A \cdot B(t)\cos(kt + \Delta + \phi(t)) \tag{7.3}$$

where the average is taken over a period that is much shorter than that of the modulating signals. First, let us consider the case when there is no modulation. In this case, the signal will simply be an offset sine wave, as can be seen in Figure 7.3(a) where the period is controlled by K and depends on the mirror scan speed. Here four specific points are chosen where the phase term, $kt + \Delta$, is equal to $n\pi$ and $\frac{\pi}{2} + n\pi$, labelled as I_x, I_y, I_z and I_k in Figure 7.3(a).

Around the corresponding four specific points labelled in Figure 7.3(a), the intensity from Equation 7.3 becomes:

$$I_x(t) = \frac{A^2}{2} + \frac{B(t)^2}{2} + A \cdot B(t)\cos(\phi(t)) \tag{7.4}$$

$$I_y(t) = \frac{A^2}{2} + \frac{B(t)^2}{2} - A \cdot B(t)\sin(\phi(t)) \tag{7.5}$$

$$I_z(t) = \frac{A^2}{2} + \frac{B(t)^2}{2} - A \cdot B(t)\cos(\phi(t)) \tag{7.6}$$

$$I_k(t) = \frac{A^2}{2} + \frac{B(t)^2}{2} + A \cdot B(t)\sin(\phi(t)) \tag{7.7}$$

Subtracting Equation 7.5 from Equation 7.7 and Equation 7.6 from Equation 7.4 separately, and then dividing, we can obtain the value of the phase modulation from:

$$\phi(t) = \arctan[\frac{I_k(t) - I_y(t)}{I_x(t) - I_z(t)}] \tag{7.8}$$

It can also be noted that

$$A^2 + B(t)^2 = I_x(t) + I_z(t) \tag{7.9}$$

In practice, it is necessary to identify and select the data around the points labelled in Figure 7.3(a) when a modulating signal is applied to the device. In order to do this, well-defined reference points are added to the modulating signal. In post-processing, these can then be identified, and the signals

(shown in Figure 7.3(b)) can then be extracted from the points labelled and can then be "processed" using Equation 7.8. The extracted and realigned data subsets from around the points I_x, I_y, I_z and I_k are shown in Figure 7.3(b). The resulting extracted optical phase as a function of time is then of the form shown in Figure 7.3(c), the details relating to its shape and values will be analysed and discussed in the following sections. The raw data was collected by an A/D converter with a 200000-point-per-sec sample rate, allowing sufficient resolution to study the LC phase modulation.

7.3 Modelling of the LC director

The number of LC molecules is enormous even in a device of a few microns thick. Therefore, simulation at an atomistic or molecular level is not appropriate in this case. Thus, a macroscopic continuum method based on Ericksen-Leslie-Parodi's [33, 197, 198] theory has been used for the simulations of the phase modulation. The LC director is thus treated as continuous which allows gradients to be specified. In many simulations that are undertaken for interpreting the switching behaviour of nematic LC devices, the influence of backflow is not commonly discussed in detail. Some of the literature has discussed how backflow can influence the dynamics in nematic LC disclinations [199] and twist cell configurations [200]. However, for a rigorous understanding of the modulation, the backflow cannot be ignored, and the flow gradients have a significant impact on the dynamic behaviour of the system. Generally, backflow has a negative impact on switching times in a Fréedericksz device due to the flow-reorientation coupling, but this can have a more positive impact on pi-cell performance. H. G. Walton and M. J. Towler's work makes a direct comparison between pi-cell switching times with and without the inclusion of flow-reorientation coupling in simulations

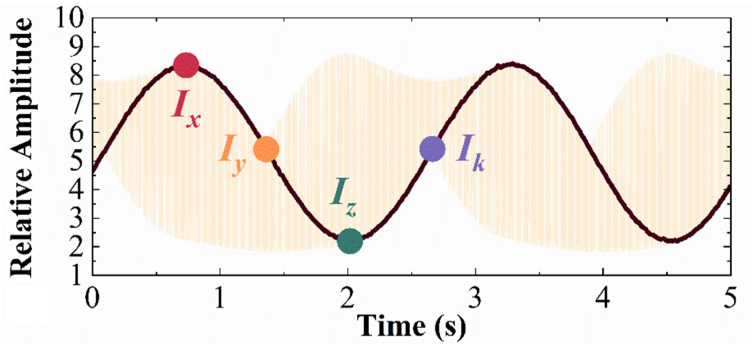

(a)

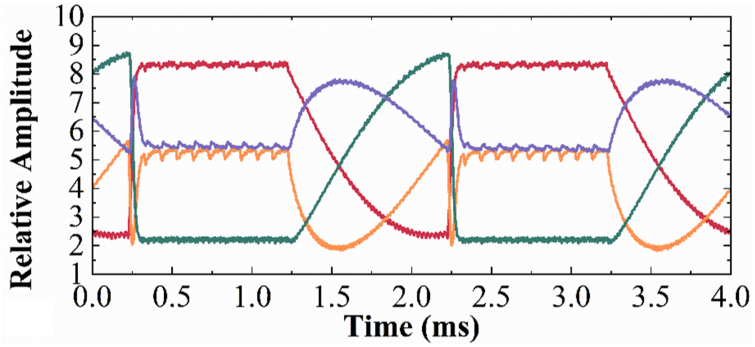

(b)

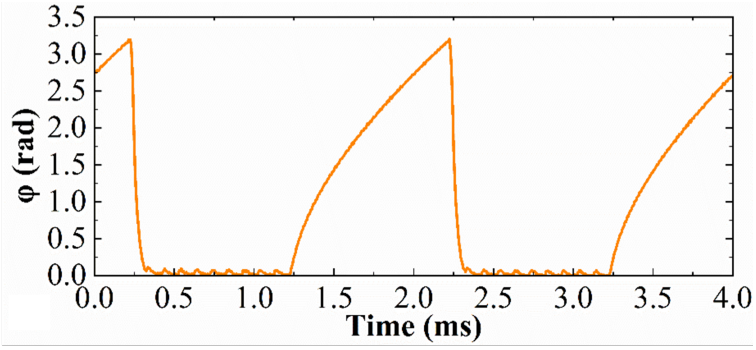

(c)

FIGURE 7.3: (a) Example waveforms of the interference signal and the specific regions of interest. The black solid line depicts the sine wave obtained when an LC phase modulator is placed in the signal arm but not modulated by an external electric field and the light yellow is an example envelope of the signal modulated by the LC device. (b) The realigned extracted signals from around the four specific points highlighted in (a). The dark red solid line is the waveform around I_x; the orange solid line represents the waveform around I_y; the dark green solid line is the waveform around I_z; and the purple line is the waveform around I_k. (c) An example of the time-resolved modulation of the optical phase of a 5 µm E7 nematic pi-cell when subjected to an applied voltage of V= 10 V at room temperature. The device was driven with a 5 kHz square wave, which is itself amplitude modulated with a second lower frequency wave that results in 1 ms duration bursts of the 5 kHz signal, followed by 1 ms spacings whereby V = 0 V. This data has been extracted according to Equation 7.8. (The sample rate used for the data presented here is 200,000 per second.)

[160]. This shows that when the backflow effect is not included in simulations, a slower switching response is observed in the pi-cell, emphasising the importance, and positive benefit of back-flow effects in pi-cell switching. Taking this into consideration, the modelling here simulates the Frank elastic energy density function(s), as well as the effects of dielectric coupling and backflow. A numerical approach is then employed to determine the phase modulation behaviour.

The director profile of a volume of LC material is defined in this work based on the coordinate system illustrated in Figure 7.4. Here the structures under consideration are untwisted, and $\phi = 0$ and the director remains in the $x - z$ plane.

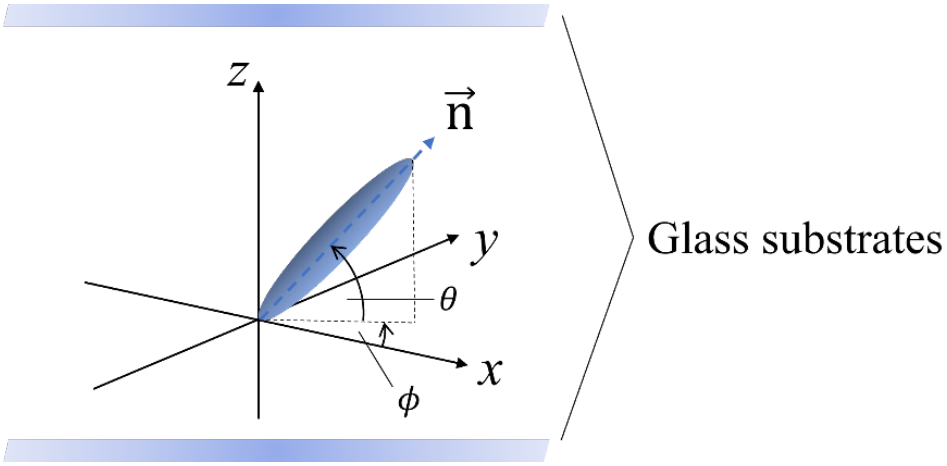

FIGURE 7.4: The geometry of the LC director in a glass cell. The two substrate surfaces are in the $x - y$ plane and are perpendicular to the z-axis.

The HAN cell is intrinsically untwisted due to the homeotropic anchoring at one surface, therefore in such a device, when using an achiral nematic LC, the director is confined to a single switching plane. The Fréedericksz device has a small surface tilt angle of 4°, but is untwisted, although in practical devices small errors in device assembly can lead to small twists within the device. In this work devices are carefully chosen that show very little residual twist. Additionally, relatively high amplitude electric fields are

applied in this work, ensuring that the director is perpendicular to the substrates in the centre of the cell, and hence effectively decoupling the top and bottom halves of the cell – hence the assumption that the director remains in the $x-z$ plane is reasonable. The pi-cells studied in this chapter also have small surface tilt angles of 4°, and in these devices, twisted states can occur when the electric field is removed. However, such states take time to form and do not occur on the timescales of the modulation investigated here. Again, the top and bottom halves of the device are effectively decoupled by applying relatively high amplitude electric fields, and the assumption that the director remains in the $x-z$ plane is reasonable. The general Frank elastic energy density equation is then given by Equation 2.2:

$$\begin{aligned} f_{elastic}(\vec{n}) &= f_{splay}(\vec{n}) + f_{twist}(\vec{n}) + f_{bend}(\vec{n}) \\ &= \frac{1}{2}K_{11}[\nabla \cdot \vec{n}]^2 + \frac{1}{2}K_{22}[\vec{n} \cdot (\nabla \times \vec{n}) + q_0]^2 + \frac{1}{2}K_{33}[\vec{n} \times (\nabla \times \vec{n})]^2 \end{aligned}$$

The materials used in this study are not chiral, so $q_0 = 0$. The electric field is applied across the cell, parallel to the z-axis in Figure 7.4, and perpendicular to the substrates. The size of the active electrodes of the cells in the $x-y$ plane is around 2.5 cm^2 whereas the gaps of the cells are under 10 µm. Therefore, because of the large aspect ratio between the length scale in the z-direction and the length scales in the $x-y$ plane, the electric field $\vec{E}$ can be considered as consisting of only the component E_z, while $E_x = E_y = 0$. The electrostatic energy density of the device then takes the form

$$f_{electro} = -\frac{1}{2}\vec{D} \cdot \vec{E} = -\frac{1}{2}D_z E_z = -\frac{1}{2}\varepsilon_0 \varepsilon_{zz} E_z^2 \tag{7.10}$$

which is the z-component of the original Equation 2.8 and ε_0, ε_{zz} represent

the free space permittivity and the z-component of the relative dielectric permittivity tensor, respectively, $\vec{D}$ is the electric field displacement vector and $\vec{E}$ is the electric field vector. In this system this becomes

$$f_{electro} = -\frac{1}{2}E_z^2\varepsilon_0(\Delta\varepsilon \sin^2\theta + \varepsilon_\perp) \tag{7.11}$$

Considering the device contains barely any ions, there are no free charges in the system, then $\nabla \cdot \vec{D} = 0$ and $\nabla \times \vec{E} = 0$. Therefore, with the large pixel assumption $\frac{\partial E_x}{\partial z}$=$\frac{\partial E_y}{\partial z}$=$\frac{\partial D_z}{\partial z}$=0, then the electric field along the z direction and the electric displacement in the z direction are

$$\begin{aligned} D_z &= \varepsilon_0\varepsilon_{zz}E_z \\ E_z &= \frac{D_z}{\varepsilon_0\varepsilon_{zz}} \\ -V &= \int_0^d E_z dz \\ &= \int_0^d \frac{D_z}{\varepsilon_0\varepsilon_{zz}} dz \\ &= \frac{D_z}{\varepsilon_0}\int_0^d \frac{dz}{\varepsilon_{zz}} \end{aligned}$$

then we can rearrange the equation above and we can get

$$D_z = \frac{-\varepsilon_0 V}{\int_0^d \frac{dz}{\varepsilon_{zz}}}$$

$$E_z = \frac{\frac{-\varepsilon_0 V}{\int_0^d \frac{dz}{\varepsilon_{zz}}}}{\varepsilon_0\varepsilon_{zz}} \tag{7.12}$$

The objective of the simulation is to determine how the LC alignment behaviour changes over time, so using a computational method which is based

on the work of a previous group member, Dr Paul Brimicombe, [201], to solve the rate of the change of the free-energy of the system is essential. The approach is to describe the rate of the energy dissipation ($\mathcal{D}$) as equal to the change rate of the free-energy (L) which can be written as

$$\frac{dL}{dt} = \mathcal{D}$$
$$\frac{dL}{dt} = \frac{dL}{dn_x}\frac{dn_x}{dt} + \frac{dL}{dn_y}\frac{dn_y}{dt} + \frac{dL}{dn_z}\frac{dn_z}{dt}$$

utilizing the Euler-Lagrange equations from calculus of variations [201], the $\frac{dL}{dn_x}$, $\frac{dL}{dn_y}$ and $\frac{dL}{dn_z}$ can be given as

$$\frac{dL}{dn_x} = \frac{d}{dz}\left(\frac{\partial L}{\partial n'_x}\right) - \frac{\partial L}{\partial n_x}$$
$$\frac{dL}{dn_y} = \frac{d}{dz}\left(\frac{\partial L}{\partial n'_y}\right) - \frac{\partial L}{\partial n_y}$$
$$\frac{dL}{dn_z} = \frac{d}{dz}\left(\frac{\partial L}{\partial n'_z}\right) - \frac{\partial L}{\partial n_z}$$

$$n'_x = \frac{dn_x}{dz}; n'_y = \frac{dn_y}{dz}; n'_z = \frac{dn_z}{dz}$$

Thus $\frac{dL}{dt} = \mathcal{D}$ can be written as

$$\frac{dL_x}{dt} = \left(\frac{d}{dz}\left(\frac{\partial L}{\partial n'_x}\right) - \frac{\partial L}{\partial n_x}\right)\frac{dn_x}{dt} = \mathcal{D}_x$$
$$\frac{dL_y}{dt} = \left(\frac{d}{dz}\left(\frac{\partial L}{\partial n'_y}\right) - \frac{\partial L}{\partial n_y}\right)\frac{dn_y}{dt} = \mathcal{D}_y$$
$$\frac{dL_z}{dt} = \left(\frac{d}{dz}\left(\frac{\partial L}{\partial n'_z}\right) - \frac{\partial L}{\partial n_z}\right)\frac{dn_z}{dt} = \mathcal{D}_z$$

If we replace the differentials with respect to t with dots and the differentials with respect to z with dashes, the equations become

$$\frac{d}{dz}\left(\frac{\partial L}{\partial n_x'}\right) - \frac{\partial L}{\partial n_x} = \frac{\partial \mathcal{D}_x}{\partial \dot{n}_x}$$
$$\frac{d}{dz}\left(\frac{\partial L}{\partial n_y'}\right) - \frac{\partial L}{\partial n_y} = \frac{\partial \mathcal{D}_y}{\partial \dot{n}_y}$$
$$\frac{d}{dz}\left(\frac{\partial L}{\partial n_z'}\right) - \frac{\partial L}{\partial n_z} = \frac{\partial \mathcal{D}_z}{\partial \dot{n}_z}$$

The director can be either expressed in terms of n_x, n_y and n_z or θ and ϕ. In order to correspond to the illustration in Figure 7.4 as well as simplify the following derivations, we replace the n_x, n_y and n_z with θ and ϕ in the following set of equations and we then get two dissipation equations:

$$\frac{d}{dz}\left(\frac{\partial L}{\partial \theta'}\right) - \frac{\partial L}{\partial \theta} = \frac{\partial \mathcal{D}_\theta}{\partial \dot{\theta}}$$
$$\frac{d}{dz}\left(\frac{\partial L}{\partial \phi'}\right) - \frac{\partial L}{\partial \phi} = \frac{\partial \mathcal{D}_\phi}{\partial \dot{\phi}}$$

As the change in ϕ is considered to be zero, there is no change in the dissipation in the ϕ direction, so $\mathcal{D} = \mathcal{D}_\theta$ and then we replace the differentiation with respect to z with a partial derivative with respect to z, then we get the energy dissipation equation of the whole system which is

$$\frac{\partial}{\partial z}\left(\frac{\partial L}{\partial \theta'}\right) - \frac{\partial L}{\partial \theta} = \frac{\partial \mathcal{D}}{\partial \dot{\theta}} \tag{7.13}$$

where L is the free-energy density and $\mathcal{D}$ is the dissipation function.

Using the standard Einstein summation convention, the general form of the dissipation function can be written as [202]

$$\begin{aligned}\mathcal{D} =& \left(\frac{\alpha_4}{4}\right)(v_{j,i}v_{j,i} + v_{j,i}v_{i,j}) + \left(\frac{\alpha_5-\alpha_2}{4}\right)(n_i n_j v_{k,i} v_{k,j} - 2\dot{n}_k n_i v_{k,i}) \\ &+ \left(\frac{\alpha_2+2\alpha_3+\alpha_5}{4}\right)(n_i n_j v_{i,k} v_{j,k} - 2\dot{n}_k n_i v_{i,k}) \\ &+ \left(\frac{\alpha_2+\alpha_5}{2}\right)(n_i n_j v_{k,i} v_{j,k} + \dot{n}_k n_i v_{k,i} - \dot{n}_k n_j v_{j,k}) \\ &+ \left(\frac{\alpha_1}{2}\right) n_i n_j n_k n_p v_{j,i} v_{p,k} \\ &+ \left(\frac{\alpha_3-\alpha_2}{2}\right)\dot{n}_k^2\end{aligned} \tag{7.14}$$

where the α_1 to α_5 coefficients are the Leslie viscosities [33]. Assuming in a real device the LC flow is incompressible, then the only non-zero flow terms are the velocity of the fluid, $v_{x,z}$=v'_x and $v_{y,z}$=v'_y. However, here we only consider the velocity within the $x-z$ plane, then the only non-zero flow term is $v_{x,z}$=v'_x. Firstly, we simplify Equation 7.14 based on $\vec{n} = (n_x, n_y, n_z)$, then the dissipation function can be written as

$$\begin{aligned}\mathcal{D} =& \frac{v'^2_x}{4}[2\alpha_1 n_x^2 n_z^2 + \alpha_2(n_x^2 - n_z^2) + 2\alpha_3 n_x^2 + \alpha_4 + \alpha_5(n_x^2 + n_z^2)] \\ &+ v'_x \dot{n}_x \alpha_2 n_z + v'_x \dot{n}_z \alpha_3 n_x \\ &+ (\dot{n_x}^2 + \dot{n_y}^2 + \dot{n_z}^2)\left[\frac{\alpha_3-\alpha_2}{2}\right]\end{aligned}$$

where we replace n_x with $\cos\theta$, n_y with 0 and n_z with $\sin\theta$, and differentiate $\mathcal{D}$ with respect to the time differentiation of θ, we then get

$$\mathcal{D} = \frac{v_x'^2}{4}[2\alpha_1 \cos\theta^2 \sin\theta^2 + \alpha_2(\cos\theta^2 - \sin\theta^2) + 2\alpha_3 \cos\theta^2 + \alpha_4 + \alpha_5(\cos\theta^2 + \sin\theta^2)]$$
$$- v_x'\alpha_2 \sin\theta^2 \cdot \dot{\theta} + v_x'\alpha_3 \cos\theta^2 \cdot \dot{\theta} + \dot{\theta}^2\left[\frac{\alpha_3 - \alpha_2}{2}\right]$$

$$\frac{\partial \mathcal{D}}{\partial \dot{\theta}} = (\alpha_3 - \alpha_2)\dot{\theta} + v_x'(\alpha_3 \cos^2\theta - \alpha_2 \sin^2\theta) \tag{7.15}$$

For the right hand side of Equation 7.15 there are two unknowns $(\dot{\theta}, v_x')$. Therefore, it is necessary to introduce the Navier-Stokes equation

$$\rho \dot{v}_i = F_i + \sigma_{ji,j} \tag{7.16}$$

where ρ is the density of the fluid, $\dot{v}_i = \frac{\partial v_i}{\partial t}$, F_i is the external body force, and σ_{ji} is the stress tensor. It is assumed that in this system the external body force can be neglected, as a result, F_i=0. Additionally, for the left-hand side of Equation 7.16, it is assumed that inertial terms ($\rho\dot{v}_i$) only act over a timescale significantly shorter than the LC relaxation. As a result, in the Equation 7.16 $\rho\dot{v}_i$=0. Thus, Equation 7.16 is further reduced to $\sigma_{ji,j}$=0. In this study, the only non-zero dynamic portion of the stress tensor in an untwisted nematic system is $\tilde{\sigma}_{zx}$, which is given as

$$\begin{aligned}\tilde{\sigma}_{zx} = \frac{\partial \mathcal{D}}{\partial v_x'} = &\frac{v_x'}{2}[2\alpha_1 \sin^2\theta \cos^2\theta + \alpha_2(\cos^2\theta - \sin^2\theta) \\ &+ 2\alpha_3 \cos^2\theta + \alpha_4 + \alpha_5] \\ &+ \dot{\theta}(\alpha_3 \cos^2\theta - \alpha_2 \sin^2\theta)\end{aligned} \tag{7.17}$$

Equation 7.17 can now be combined with Equation 7.15 to obtain a pair of equations for $\dot{\theta}$ and v_x' [201] - this system can then be solved numerically to

determine the director's behaviour. Furthermore, based on the time dependence of the director profile, the intensity modulation can also be modelled along with the phase modulation using a Jones matrix approach to represent the light propagation through the nematic LC layer. The key elasticity, dielectric and refractive index coefficients used for the model here are K_{11}=11.1 pN, K_{33}=17.1 pN, $\varepsilon_{\perp}$=5.4, $\varepsilon_{\parallel}$=17.4, n_o=1.5, n_e=1.72 and the wavelength is set to λ=632.8 nm [203].

7.4 Results: Experiments and Simulations

The devices investigated here are three different, but well-known, configurations of nematic LC devices: a Fréedericksz cell [188], a pi-cell [188], and a HAN cell. In each case, the LC modulators are placed in the signal arm of the Michelson interferometer arrangement illustrated in Figure 7.2. Each device is typically driven with a 5 kHz square wave, which is itself amplitude modulated with a second lower frequency wave. In the data presented in the following, this configuration is used in order to provide 1 ms duration bursts of the 5 kHz signal, followed by 1 ms "gaps" at 0 V. An example of the driving signal is shown in Figure 7.5(a). The voltage amplitude used in this case is V=25 V ($V_{pp} = \pm 25$ V).

Alongside the driving waveform, Figure 7.3 also shows a set of data that demonstrates the time-resolved phase modulation behaviour of a 5 µm nematic pi-cell at room temperature. The phase modulation response shown in Figure 7.5(b) is a result of the on-off external electric field which is shown in Figure 7.5(a). It can be seen in Figure 7.5(b) that a phase depth of around 3.7 radians is achieved over a timescale of 1 ms. Following the switch-on state is a 1 ms period when the LC device is switched off (this is represented by the black line parts in Figure 7.5(b)) where the LC device modulates the

phase of the incident light from 0 to 3.7 rads in 1 ms (see, for example, the response over the time period from 1.5 ms to 2.5 ms in Figure 7.5(b)), before rapidly dropping back to 0 rad when the electric field is re-applied. This behaviour would easily lead to a phase modulation that was greater than 2π with a sub-millisecond timescale using the four-pass configuration that was presented in Chapter 6 [18].

Because the nematic pi-cell behaves as a capacitor, which is driven through the resistance of the indium tin oxide (ITO) electrodes, when the electric field reverses at 5 kHz between 25 V and -25 V, the capacitor charging time leads to a ripple in the signal which is the red line in Figure 7.5(b). It is more noticeable in Figure 7.5(c) when the voltage driving conditions were set to a square wave of V= 25 V, f = 5 kHz, but without the 500 Hz amplitude modulation. Figure 7.5(d) shows the residual intensity modulation. The data shown in Figure 7.5(d) was extracted using Equation 7.9.

To investigate the behaviour of the three different nematic LC devices, a series of experimental tests were carried out and the measurements were then compared with the results from simulations. In the simulations, the surface anchoring conditions are "strong", with a no-slip condition in the flow at the surfaces and infinity strength surface tilt anchoring with a small surface pretilt angle of 4°. The Leslie coefficients used in the model are α_1=-21 mPa·s, α_2=-282 mPa·s,α_3=-1 mPa·s, α_4=225 mPa·s and α_5=92 mPa·s, taken from Reference [204].

Figure 7.6 shows direct comparisons between the experimentally determined phase modulation and the phase modulation predicted from simulations. Two sets of results are shown, one with an AM modulating frequency of 500 Hz (i.e., with the 5 kHz signal on for 1 ms, and off for 1 ms) (Figure 7.6(a) - 7.6(c)), and one with an AM frequency of 50 Hz (i.e., with the 5 kHz

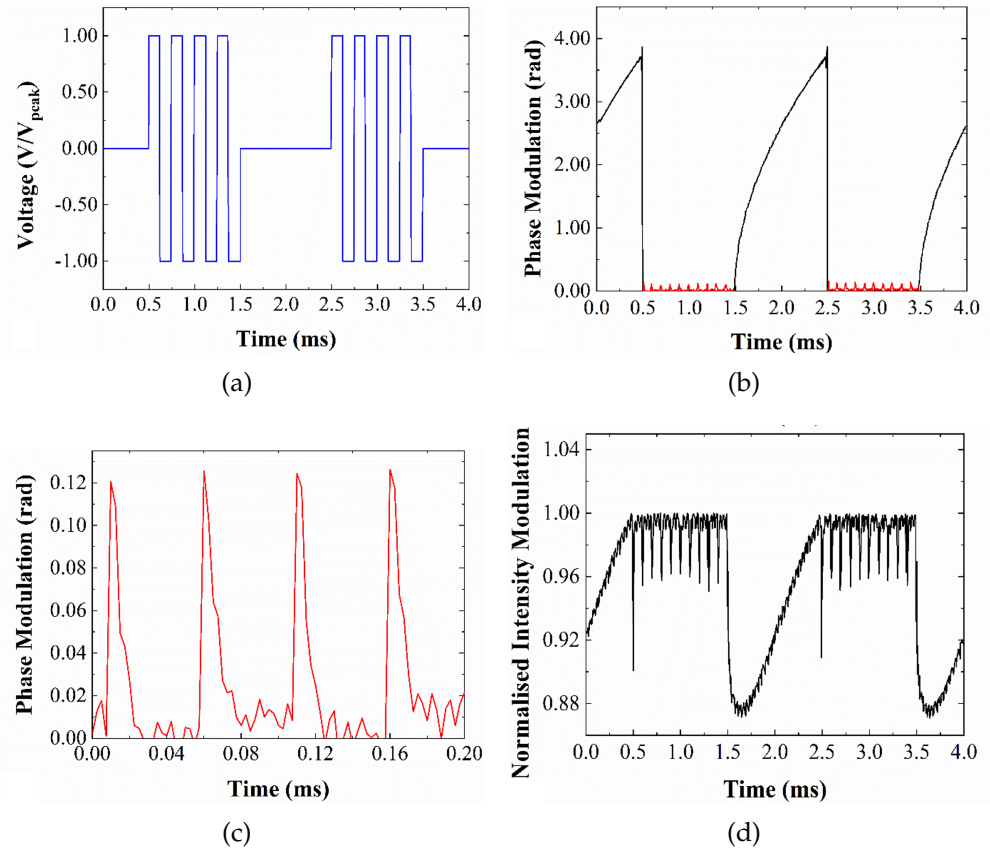

FIGURE 7.5: An example of the experimental data for the time dependence of the phase modulation for a nematic LC pi-cell with a gap of 5 µm. (a) An example of the modulated square wave, the square wave frequency is 5 kHz and the amplitude modulated (AM) frequency is 500 Hz. Note that the voltage amplitude is varied depending on the experiment and the value is specified in each case. (b) The extracted phase modulation using Equation 7.8 as a function of time for the electric field conditions: V=25 V and f = 5 kHz, AM frequency 500 Hz and (c) V= 25 V, f = 5 kHz without the application of the AM square wave. (d) corresponding intensity modulation as a function of time for a modulated square wave, V= 25 V, AM frequency 500 Hz. The value of the intensity has been normalized to the maximum intensity value.

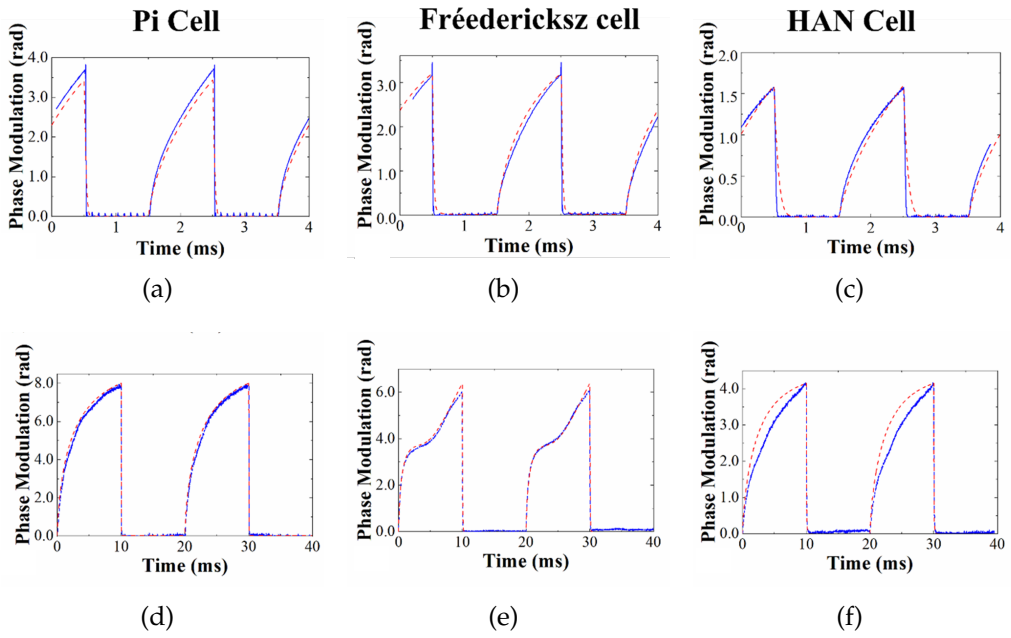

FIGURE 7.6: Experimental measurements (blue solid lines) and simulations (red dashed lines) of the phase modulation as a function of time for the three different nematic LC configurations considered in this study: nematic pi cell (parallel rubbed alignment layers), Fréedericksz device (anti-parallel rubbed alignment layers), and a hybrid aligned nematic (HAN). The cell gap used in the simulation for the pi and Fréedericksz cells were 5.78 µm and 5.12 µm respectively, whereas for the HAN cell, the gap was 7.44 µm. Each cell was filled with the nematic LC, E7. The time when the modulating signal is applied and when the voltage is zero in (a), (b) & (c) were 1 ms, but were 10 ms in (d), (e) & (f). The amplitude of the applied voltage in all cases was V= 25 V. Measurements were carried out at room temperature.

signal on for 10 ms, and off for 10 ms) (Figure 7.6(d) - 7.6(f)). The behaviour for 1 ms bursts illustrates the available phase modulation over a target time scale of 1 ms, whereas the response for the 10 ms bursts serves to illustrate the impact of backflow on the resulting device behaviour.

The results from simulations are found to be in good agreement with the experimental results for the different switching conditions. It can be seen that the shapes of the phase modulation response are very similar for all three devices when driven with 1 ms bursts. Furthermore, the nematic pi-cell (parallel rubbed) and the Fréedericksz device (anti-parallel rubbed) show similar phase modulation over a timescale of 1 ms (Figure 7.6(a) and 7.6(b)), with the Fréedericksz device being just slightly less responsive. In contrast, the HAN device shows somewhat less phase modulation (Figure 7.6(c)), though the gap is 7.44 µm which is much thicker than the other two devices, and is thus less promising for commercial phase modulation technology.

The behaviour observed can be understood in terms of the high voltage response of nematic LC devices. When high voltages are applied, the LC director in the bulk of the device is switched to a near-homeotropic alignment. When the voltage is removed, however, the device returns towards the corresponding pi, planar or HAN states, depending upon the original configuration of the nematic LC. Initially, this relaxation occurs as boundary layer regions growing from planar-aligned surfaces [18]. In the nematic pi-cell and the Fréedericksz device, these boundary layers grow from both surfaces, but in the HAN device, this only occurs at one surface, the corollary of which is that the level of phase modulation obtained is lower (compare Figure 7.6(c) with Figure 7.6(a) and 7.6(b)). It can also be verified by comparing the phase modulation shown in Figure 7.6(a), 7.6(b) with that in Figure 7.6(c): the HAN cell phase modulation is half of that for the other two cell configurations. This behaviour is largely independent of the device gap.

At longer time scales, however, the backflow becomes more important, as is evident in the response of the devices when driven with 10 ms bursts (Figure 7.6(d)- 7.6(f)). In these cases, we see substantially different responses between the pi-cell (Figure 7.6(d)) and the Fréedericksz (Figure 7.6(e)) devices. For the Fréedericksz device, it can be seen that the phase modulation increases rapidly when the field is removed before increasing at a slower rate up until approximately 5 ms when the phase modulation increases at a greater rate. This behaviour is also reproduced in the simulations and is an effect that is caused by backflow, which tends to hinder the switch-off response in Fréedericksz devices. This behaviour is not apparent in the pi-cells because in these devices the backflow tends to work with the switch-off response (i.e., with the reorientation of the director) rather than against it. As noted above, this concept has been demonstrated previously by H.G. Walton and M.J. Towler in work where a direct comparison was made between the flow-influenced pi-cell director relaxation and the behaviour when ignoring flow [160].

It is clear that the limiting effect in terms of the available phase modulation depth is the phase change that occurs during the switch-off period after the device has been driven on. Therefore, the investigation further focuses on the available phase modulation depth of the devices under different applied voltages. Five experimental points were chosen, with the driving voltages varying from V= 5 V to V= 25 V in increments of 5 V. The magnitude of the deviation between the theory and the measurement was 0.14 rads for the HAN cell and 0.09 rads for the pi and Fréedericksz cells.

Figure 7.7 presents both experimental and modelling results of the achievable phase modulation depth as a function of the applied voltage amplitude. The waveform that was applied was the same shape as that illustrated in Figure 7.5(a) and here the black squares represent the results from

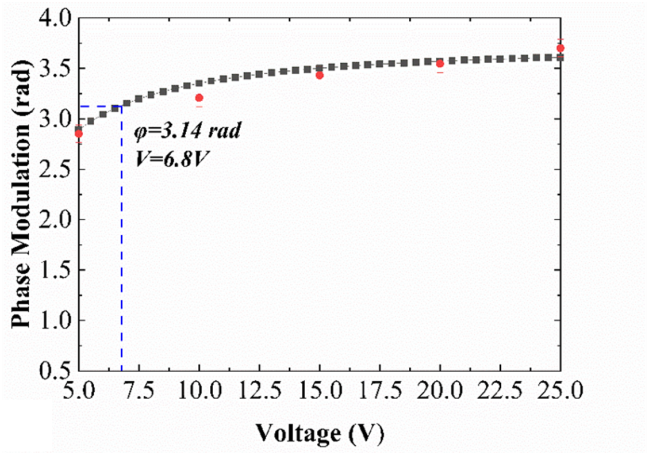

(a)

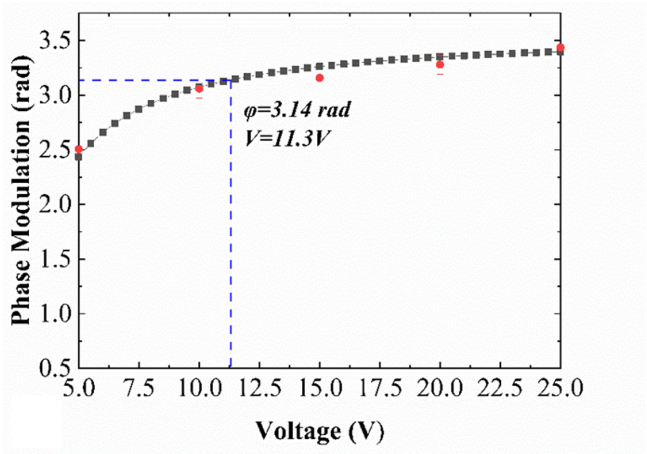

(b)

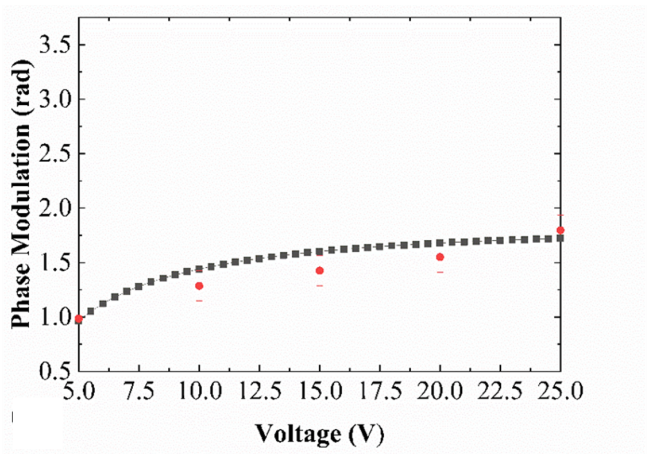

(c)

FIGURE 7.7: The available phase modulation as a function of voltage when driven with voltage waveforms of the same shape as that shown in Figure 7.5(a). The black squares represent the simulation results and the red dots represent the experimental results recorded at five different voltage amplitudes for the switching on state. (a) a nematic pi cell, (b) a Fréedericksz cell, and (c) a HAN cell. The experimental results were obtained at room temperature.

simulations while the red dots represent the experimental results at the five different voltages. The results also show that for the same applied voltage amplitude, the nematic pi cell performs best in terms of the available phase modulation compared with both the Fréedericksz cell and the HAN cell. Similarly, and as shown here, the pi-cell can achieve more than a π (ϕ=3.14 rads) phase modulation (or 2π phase modulation if the device is implemented in a four-pass configuration of the type discussed in the previous chapter (Chapter 6) at a lower voltage amplitude (V = 6.9 V) and can achieve the largest phase modulation of all three devices (ϕ=3.7 rads). For the nematic pi-cell and the Fréedericksz device, the dashed blue lines in the plot indicate the voltage that corresponds to a π phase modulation. It can also be seen that the HAN cell used here cannot reach a full π phase modulation in a timescale of 1 ms, even though the cell gap is around 3 µm thicker than that of the pi-cell and Fréedericksz cell. For each configuration, as the drive voltage is increased, the phase modulation increases, but above a certain level the increase is only small. This is because once the applied voltage reaches a level such that the boundary layer between the bulk homeotropic state and the planar surface state is substantially less than the wavelength of light, a further voltage increase does not substantially increase the change in the phase.

Finally, the illustration of experimental measurements of the time-dependent behaviour of the phase modulation when switching between arbitrary phase modulation depths for the nematic LC pi-cell is demonstrated. In this case, the applied 5 kHz square wave is modulated by a pseudo-random pattern, and the resulting time-dependent phase was extracted. This is shown in Figure 7.8. The electric field was set such that the waveform was the same form as that shown in Figure 7.5(a), and the amplitude of the applied voltage was varied every 1 ms, which can be seen in the yellow plane in Figure 7.8. A voltage sequence was then applied as follows: the voltage is switched

on (the dark red areas), a lower voltage that behaves as a switch-off voltage (the lightest red areas) and then a hold voltage (the red colour bar in between). The director will remain at a certain orientation that results in a specific, steady phase modulation for 1 ms when subjected to the voltage sequence. By adjusting the relative value of voltage amplitude during the three periods, the phase modulation can be varied on demand. Figure 7.8 clearly shows that for a practical phase modulation application scenario, the phase can still be modulated by up to 3.7 rads within a sub-millisecond timescale. Therefore, it is seen that the available pseudo-random phase modulation is consistent with the range observed above.

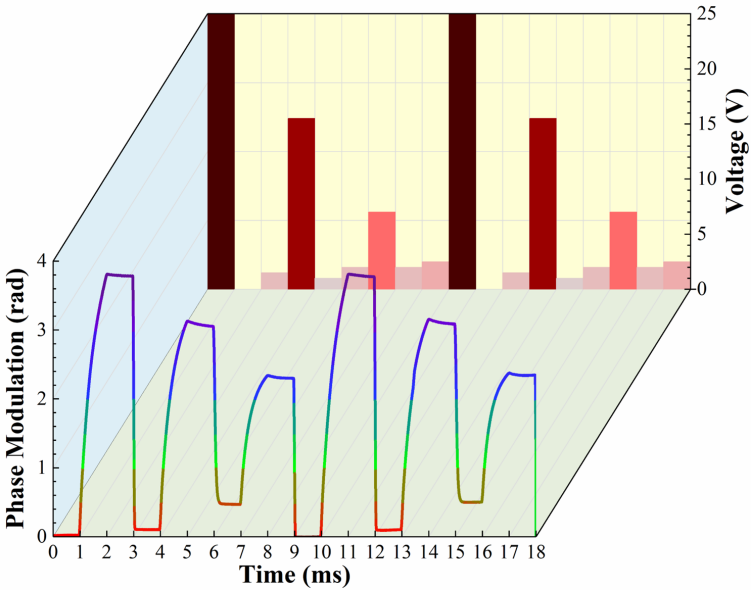

FIGURE 7.8: The phase modulation as a function of time for the nematic pi-cell in an arbitrary phase-modulation sequence. The plot on the yellow panel represents the rms voltage applied to the cell and the applied waveform is a 5 kHz square wave but in this case, the amplitude changes every 1 ms according to the plot on the yellow panel. The darker red bars indicate a higher voltage amplitude. Each red bar is 1 ms in duration and the corresponding relative phase shift is shown in the front panel, where the colour of the line reflects the depth of the modulated phase. The purple parts indicate that the modulation is greater than π. The phase modulation changes along with the 'switch on- switch off- hold' electric field sequence so that the phase depth is lowest (red parts) at first and then increases to a high value (the gradient changes colour from red to green to purple or blue) and then remains held at that level for another 1 ms without any significant change (the purple or blue parts). Hence, by controlling the amplitude modulation of the applied waveform, different levels of phase modulation can be achieved.

7.5 Summary

In this chapter, a method which can experimentally measure the time-dependent phase modulation of LC devices is presented. This method was then used to study and characterise the response of three different nematic LC devices: pi-cell (parallel-rubbed alignment layers), Fréedericksz cell (anti-parallel rubbed alignment layers), and a hybrid aligned nematic (HAN) LC. The results presented have shown that both the intensity and phase properties can be determined by simply recording and analysing the signal captured by the photodiode in a Michelson interferometer when the reference arm is modified to provide a phase ramp.

In order to understand fully how the alignment configuration and the initial director orientation of the LC can affect the phase modulation behaviour, simulations were conducted based upon the Frank elastic energy density, effects of dielectric coupling, and importantly, the impact of backflow. In this study, a range of device driving voltages have been explored, with driving voltages up to 25 V. For the nematic LC E7 in each of the three different configurations, the "useful" range of driving voltages is determined, defined here as when π phase modulation is achieved in the test arrangement discussed above. The results show that different cell configurations have different impacts on LC relaxation and thus have significant influences on director reorientation speed. For a quick phase modulation application, say the switching time is shorter than 1 ms, a π phase modulation is achieved at a driving voltage of 6.8 V for the nematic pi-cell, compared with 11.3 V for the Fréedericksz device. However, π phase modulation is not achieved in the HAN cell.

By increasing the switching time to 10 ms, all of these three devices can provide a full π phase modulation, though, at a sacrifice of refresh speed.

Under 1 ms rapid switching condition, those results would lead to full 2π phase modulation in the four-pass configuration presented in the previous chapter (Chapter 6) for the pi and Fréedericksz devices at reasonable driving voltages (less than 10 V in the case of the pi-cell). In contrast, the HAN cell does not reach a π phase modulation despite the LC layer being nearly twice as thick. It is also shown that when backflow is prevalent there is a negative impact on the dynamic phase response of the Fréedericksz device but not the pi-cell. The experimental results and simulations both suggest that the pi-cell is potentially better suited for phase modulation when fast switching speeds and a wide optical phase change are required.

This chapter primarily explores the advantageous cell configurations that promote greater phase shift in the nematic LC material, one of the two materials investigated in Chapter 6. The next chapter will also address the second issue discussed in Chapter 6, namely, the enhancement of phase modulation in flexoelectro-optic materials and the mitigation of amplitude modulation.

Chapter 8

Optical Phase Modulation of optimised Fast-Switching Flexoelectro-optic Liquid Crystal Devices

In this Chapter, I demonstrate that by carefully considering and selecting various device parameters, the phase modulation depth of a flexoelectro-optic phase modulator can be elevated to a significantly higher degree. It is shown that by adopting such a technique in a phase modulator, it is possible to demonstrate a substantial optical phase modulation, even though the tilt angle of the optic axis is less than $\pm 22.5°$. Modelling is used to determine the phase shift for the chiral nematic LC mixture and the experimental results show a good agreement with the simulation results. This chapter has been written up for publication.

8.1 Introduction

The importance of modifying the optical phase properties of light is a critical process in a large range of photonics applications which has been discussed in Chapter 6 and 7. Chapter 6 provided a design of an optical system to amplify the phase shift of either a nematic pi-cell device or a chiral nematic flexoelectro-optic device by a factor of four. Chapter 7 further investigated the possibilities of optimising the nematic LC phase modulators by demonstrating phase modulation for three different device configurations (pi-cell, Fréedericksz cell, and HAN cell). However, the optimisation of the other device, the flexoelectro-optic device, presented in Chapter 6 has thus far not been studied further.

Here, in this Chapter, I will show a comprehensive investigation of how to achieve enhanced high-speed phase modulation by combining a uniform lying helix (ULH) chiral nematic flexoelectric LC device with quarter-wave plates. The approach of time-resolved measurements of phase modulation is adapted so that we can extract the change in the optical phase (Equation 7.8) as well as changes in the intensity (Equation 7.9) as a function of time. Factors, including the orientation of the helical axis relative to the quarter-wave plates, applied electric field conditions, and the impact of dielectric coupling on the observed response for a chiral nematic LC mixture dominated by flexoelectric coupling, are analysed.

8.2 Flexoelectro-optic Effect and Optimisation for Phase-only Modulation

In general, LC-SLMs have been based upon either nematic [176] or ferroelectric LC technologies, as discussed in Chapters 2, 6 and 7. However, for other

applications such as Lidar and optical communications, high-speed modulators are required that simultaneously offer full analogue control of the phase. Towards this end, there have been a number of reports that describe different methodologies that have been developed to achieve high-speed analogue phase modulation. An approach that the group at Oxford has adopted in recent years is to consider alternative LC electro-optics modes that inherently possess a fast response time but can also exhibit analogue switching of the optical properties. Even though it was discovered more than three decades ago, the flexoelectro-optic effect in chiral nematic LCs remains an interesting electro-optic mode for phase modulation as the in-plane rotation of the optic axis, which is linear in the applied electric field, combined with the sub-millisecond response times, offers a desirable combination of properties for next-generation phase modulators. Moreover, with the development of high twisting power chiral additives, which lead to fast response times as a result of the short pitch of the chiral nematic helix, and new compounds in the form of LC bimesogens (dimers), large rotations of the optic axis combined with fast response times have been realised [150, 178].

A flexoelectro-optic device in isolation does not readily enable 2π phase modulation. Instead, one way to obtain full 2π phase modulation is to place quarter-wave plates on either side of the flexoelectro-optic LC layer positioned with the appropriate relative orientations of the optic axis of the LC and the fast axes of the quarter-wave plates [150, 178, 205]. Furthermore, the LC layer must behave as a tuneable half-wave plate and the second quarter-wave plate must be followed by a reflector to enable a double-pass of the incident light. For this configuration, which was introduced in Chapter 6, and which takes its inspiration from Stockley et al. who pursued 2π phase modulation using ferroelectric LCs [206, 207], the first quarter-wave plate generates circularly polarised light that is then incident on the flexoelectro-optic

LC layer. The LC layer then induces a phase change that is equal to twice the rotation of the optic axis [207]. In the work of Stockley et al, the LC layer was a ferroelectric LC, which did not quite exhibit a full 2π phase modulation and other issues such as high nonlinearity, a steep transition with voltage as well as large amplitude modulation also hindered the device performance.

Achieving 2π phase modulation does place strict requirements on the flexoelectro-optic switching. In particular, the tilt angle of the optic axis (for one electric field polarity) must be as large as 45°. Fortunately, LC bimesogens (dimers) such as CB7CB, which is from the same homologous series as that used in Chapter 6 (CB9CB), have been shown to exhibit large rotations of the optic axis when employed in flexoelectro-optic devices operating in a ULH mode[150]. Therefore, using chiral nematic LC mixtures containing 1",7"-bis(4-cyano-biphenyl-4'-yl)heptane (CB7CB) and a low concentration of high twisting power chiral additive, full 2π phase modulation operating at kHz switching frequencies was observed for an LC layer that was 5 µm-thick [150]. In this first demonstration, the chiral nematic phase only existed above 100°C and so the device could only be operated at very high temperatures over a limited temperature range. It was later shown that the second quarter-wave plate and reflector (mirror), which were bulky external components to the LC layer, could be replaced with either a chiral nematic LC reflector [208] or a combination of a polymer quarter-wave plate and a mirror in the form of an integrated device [208]. As shown in Chapter 6, an alternative strategy was developed whereby 20 wt.% of CB9CB was dispersed into a short pitch wide-temperature range chiral nematic LC host and combined with a multi-pass configuration. In this case, the tilt angles of the chiral nematic LC were below 45° but with the multi-pass arrangement it was still possible to obtain 2π phase modulation, and the device could be operated at lower temperatures.

Despite these advances, as mentioned before, my previous studies demonstrated in Chapter 6 lack investigation into the modulation in the amplitude that occurs in tandem with changes in the phase. For phase-only modulation, any changes in the amplitude are unwanted and need to be suppressed. Moreover, the requirement for the LC layer to tilt by angles as large as 45° at relatively low electric field amplitudes and low operating temperatures (e.g. 20 °C) places a considerable strain on the mixture and material development. The purpose of the study discussed in this chapter is to investigate the time-resolved phase modulation of the flexoelectro-optic effect in chiral nematic LCs to better understand how both the phase and amplitude modulation behaviour depend upon material properties and device configurations.

8.3 Flexoelectro-optic Phase Modulator

The configuration of the flexoelectro-optic phase modulator is shown diagrammatically in Figure 8.1 (assuming that the incident light (E_{in}) is linearly polarised along the perpendicular (y) direction). Specifically, the complete phase modulation device consists of a quarter-wave plate oriented with its fast axis at 45° relative to the x-axis, a ULH flexoelectro-optic LC layer that behaves as a half-wave plate for the incident light, and a quarter-wave plate aligned with its fast axis at -45° relative to the x-axis, as introduced in Chapter 6. The grey elements represent the preset angle of the optical axis, θ; the red elements show the flexoelectric effect induced angle χ, which will rotate around the preset optical axis and the black elements are the resultant angle of the optical axis of the device relative to the x-axis, α.

The incident light propagates along the z-axis and the LC is aligned such that its optical axis lies in a plane that is normal to the z-axis (in the

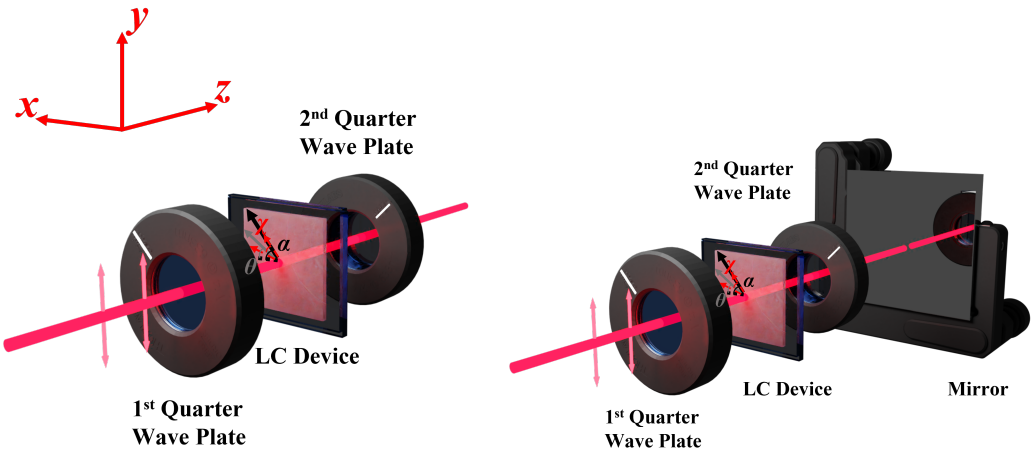

FIGURE 8.1: (a) A schematic showing the flexoelectro-optic LC half-wave plate placed between quarter-wave plates and (b) the same configuration but with the addition of a mirror so that the incident light passes through the LC half-wave plate twice resulting in a factor of two increase in the phase modulation.

plane defined by the x and y-axes in Figure 8.1) as well as has an angle of $\alpha = \theta + \chi$ relative to the x-axis (ideally, if the LC device is fabricated as an exact half-wave plate then the θ should be set at zero at the beginning of the experiment). If here the θ is set as zero and the LC device is an ideal half-wave plate, then the configuration used here is exactly the same as the one used in Chapter 6 where

$$\begin{aligned} E_{out} &= \left\{\frac{\lambda}{4}\angle -45^\circ\right\}\left\{\frac{\lambda}{2}\angle \alpha\right\}\left\{\frac{\lambda}{4}\angle +45^\circ\right\} E_{in} \\ &= \left\{\frac{\lambda}{4}\angle -45^\circ\right\}\left\{\frac{\lambda}{2}\angle \chi\right\}\left\{\frac{\lambda}{4}\angle +45^\circ\right\} E_{in} \\ &= e^{i2\chi}\begin{pmatrix}1\\0\end{pmatrix} \end{aligned} \tag{8.1}$$

where $\left\{\frac{\lambda}{4}\angle +45^\circ\right\}$ and $\left\{\frac{\lambda}{4}\angle -45^\circ\right\}$ are the Jones matrices for the first and second quarter-wave plates with the fast axes aligned at an angle of 45° and -45° to the horizontal direction, respectively. $\left\{\frac{\lambda}{2}\angle \alpha\right\} = \left\{\frac{\lambda}{2}\angle \chi\right\}$ is the Jones matrix for the flexoelectro-optic LC layer, which is designed to behave as a

rotatable half-wave plate and $\alpha = \chi$ represents the angle between the fast axis of the LC and the x axis. In most real applications, a reflective mode is commonly used to obtain a larger phase shift. This can be achieved by placing a mirror behind the second quarter-wave plate (Figure 8.1(b)). The double pass then results in a phase shift that is four times the rotation of the optic axis of the LC half-wave plate, χ. In this case ($\theta = 0$, ideal half-wave plate), the Jones vector for the output is the same as Equation 6.14:

$$\begin{aligned} E_{out} &= \left\{\frac{\lambda}{4}\angle -45^\circ\right\}\left\{\frac{\lambda}{2}\angle -\alpha\right\}\left\{\frac{\lambda}{4}\angle +45^\circ\right\}\{M\}\left\{\frac{\lambda}{4}\angle -45^\circ\right\}\left\{\frac{\lambda}{2}\angle \alpha\right\}\left\{\frac{\lambda}{4}\angle +45^\circ\right\}E_{in} \\ &= \left\{\frac{\lambda}{4}\angle -45^\circ\right\}\left\{\frac{\lambda}{2}\angle -\chi\right\}\left\{\frac{\lambda}{4}\angle +45^\circ\right\}\{M\}\left\{\frac{\lambda}{4}\angle -45^\circ\right\}\left\{\frac{\lambda}{2}\angle \chi\right\}\left\{\frac{\lambda}{4}\angle +45^\circ\right\}E_{in} \\ &= e^{i4\chi}\begin{pmatrix} 0 \\ -1 \end{pmatrix} \end{aligned} \tag{8.2}$$

Encouragingly, the phase shift increases by a factor of four but the polarisation remains the same,i.e., along the y-axis.

Practically, it has been observed that because of dielectric coupling, the helix will unwind when the amplitude of the applied electric field is greater than the critical field required for the chiral nematic-nematic transition. This process does not happen all of a sudden but instead the helix unwinds gradually. When the applied voltage approaches the critical electric field amplitude, the dielectric coupling will become significant, and the result is a decrease in the effective retardance. Furthermore, fabricating the LC device so that it has a thickness that matches the ideal conditions for a half-wave plate can be challenging. As a result, in most cases, the retardance of the LC device does not correspond to an ideal half-wave plate and the

retardance will decrease by a certain percentage when the electric field is increased to large magnitudes. Additionally, θ cannot be ideally zero and in this work, the θ is actually set not to be zero on purpose to find the best angle which shows minimum amplitude modulation as well as full 2-π phase modulation. Taking these factors into account in an analytic model, Equation 8.2 then becomes

$$
\begin{aligned}
&\left\{\frac{\lambda}{4}\angle -45^\circ\right\}\{LC\angle\alpha\}\left\{\frac{\lambda}{4}\angle +45^\circ\right\} \\
=&\frac{(1+i)^2}{4}\begin{pmatrix}1 & i\\ i & 1\end{pmatrix}\begin{pmatrix}\cos^2\alpha + A\sin^2\alpha & (1-A)\cos\alpha\sin\alpha\\ (1-A)\cos\alpha\sin\alpha & \sin^2\alpha + A\cos^2\alpha\end{pmatrix}\begin{pmatrix}1 & -i\\ -i & 1\end{pmatrix} \\
=&\frac{i}{2}\begin{pmatrix}1+A & (1-A)(\sin 2\alpha - i\cos 2\alpha)\\ (1-A)(\sin 2\alpha + i\cos 2\alpha) & 1+A\end{pmatrix} \\
=&\frac{i}{2}\begin{pmatrix}1+e^{i\delta} & -i\cdot e^{i2\alpha}(1-e^{i\delta})\\ i\cdot e^{-i2\alpha}(1-e^{i\delta}) & 1+e^{i\delta}\end{pmatrix}
\end{aligned}
$$

$$
\begin{aligned}
&\left\{\frac{\lambda}{4}\angle -45^\circ\right\}\{LC\angle -\alpha\}\left\{\frac{\lambda}{4}\angle +45^\circ\right\} \\
=&\frac{(1+i)^2}{4}\begin{pmatrix}1 & i\\ i & 1\end{pmatrix}\begin{pmatrix}\cos^2\alpha + A\sin^2\alpha & (A-1)\cos\alpha\sin\alpha\\ (A-1)\cos\alpha\sin\alpha & \sin^2\alpha + A\cos^2\alpha\end{pmatrix}\begin{pmatrix}1 & -i\\ -i & 1\end{pmatrix} \\
=&\frac{i}{2}\begin{pmatrix}1+A & -(1-A)(\sin 2\alpha + i\cos 2\alpha)\\ -(1-A)(\sin 2\alpha - i\cos 2\alpha) & 1+A\end{pmatrix} \\
=&\frac{i}{2}\begin{pmatrix}1+e^{i\delta} & -i\cdot e^{-i2\alpha}(1-e^{i\delta})\\ i\cdot e^{i2\alpha}(1-e^{i\delta}) & 1+e^{i\delta}\end{pmatrix}
\end{aligned}
$$

$$E_{out} = \frac{1}{4}\begin{pmatrix} i \cdot (1 - e^{i2\delta}) \cdot (e^{i2\alpha} - e^{-i2\alpha}) \\ (1 + e^{i\delta})^2 - e^{i4\alpha} \cdot (1 - e^{i\delta})^2 \end{pmatrix} \tag{8.3}$$

where $A = e^{i^{\delta}}$, and δ is the arbitrary retardation of the LC phase modulator. As according to the measurement setup illustrated in Figure 7.2, the reference wave has the same polarisation direction as the $E_{in} = (0, 1)^T$. Thus the E_{out} modulated by the flexoelectric effect is $E_{out} = \frac{1}{4}(1 + e^{i\delta})^2 - e^{i4\alpha} \cdot (1 - e^{i\delta})^2$.

Using Equation 8.3 along with the expression for the retardance $\delta = \frac{2\pi\Delta n_{eff} d}{\lambda}$, we can calculate the output phase shift after defining the wavelength, cell thickness and the dielectric anisotropy of the LC host. By varying δ together with the orientation of the half-wave plate, θ, the optimum combination of angles can be found for the configuration shown in Figure 8.1(b). To accurately simulate the behaviour of the LC, there are two more factors that need to be taken into consideration: (i) the angle between the fast-axis of the LC device and the quarter wave plate with applied voltage, which is no longer linear with the applied electric field, even at lowish amplitudes; this is because the rotation of the optic axis results from a combination of flexoelectric and dielectric coupling [165]; (ii) The retardance of the LC will also change during the switching process when the amplitude of the electric field increases as a result of the dielectric-driven distortion of the helical structure, which influences Δn_{eff} [38, 39]. Meanwhile, to provide more flexibility so that the optimum configuration can be identified, one more degree of freedom to the model is also introduced. This is the orientation of the first quarter-wave plate relative to the x-axis and the angle between the two quarter-wave plate elements remains fixed at 90° so that the configuration in this study is similar to the original arrangement presented in Chapter 6.

8.4 Chiral Nematic LC Retardance

The reduction in the retardance is also taken into consideration in this study because for a real device helix unwinding is inevitable unless the dielectric anisotropy of the LC is zero. The critical unwinding field, E_c , can be calculated by considering the free-energy equation, which was derived independently by Meyer and de Gennes and found to be [38, 39], and has been introduced in Equation 2.17

$$E_c = \frac{\pi^2}{P_0}\sqrt{\frac{K_{22}}{\Delta\varepsilon\varepsilon_0}}$$

where P_0 represents the natural pitch of chiral nematic LC phase, K_{22} is the twist elastic constant, $\Delta\varepsilon$ is the dielectric anisotropy and ε_0 is the dielectric permittivity of free space. With the exception of an LC that possesses a dielectric anisotropy that is zero, this equation shows that every chiral nematic LC exhibits a critical unwinding field. However, Equation 2.17 only considers the impact of dielectric coupling on the unwinding process and ignores flexoelectric coupling, which can combine with dielectric coupling to unwind the helix. Taking flexoelectricity into account, Equation 2.17 then becomes [48],

$$E_c = \frac{\pi q_0}{2}\sqrt{\frac{K_{22}}{\Delta\varepsilon\varepsilon_0 - \frac{\pi^2(e_1-e_3)^2}{16K_{11}}}} \tag{8.4}$$

where K_{11} is the splay elastic constant, and assuming K_{11}=K_{33} [48]. e_1 and e_3 are the splay and bend flexoelectric coefficients, respectively, and q_0 is the wavenumber of the helix, which is equal to $\frac{2\pi}{P_0}$. In the simulations presented in this chapter, we consider the impact of both dielectric and flexoelectric coupling on the critical electric field amplitude.

When simulating the behaviour of the flexoelectro-optic LC layer, the dependence of the rotation of the optic axis, χ, on the electric field amplitude also needs to be taken into consideration alongside the retardance, δ, and the critical unwinding field, E_c. An established analytic method used to model the electric field-induced tilt of the optic axis of a ULH chiral nematic LC that undergoes flexoelectro-optic switching (which is also introduced in Chapter 2) takes the form

$$\tan\chi = \frac{(e_1 - e_3)E}{2q_0K_{22}} - \frac{(K_{11} - 2K_{22} + K_{33})}{2K_{22}}\sin\chi \tag{8.5}$$

For small angles, this can be approximated neatly as

$$\chi(E) = \frac{e_1 - e_3}{K_{11} + K_{33}}\frac{E}{q_0} \tag{8.6}$$

It should be stressed that Equation 8.6 only considers the influence of flexoelectric coupling on the rotation of the optic axis- the change in the helical structure for this case is illustrated in Figure 8.2(a).

The distortion in the helix that results from just flexoelectric coupling will not have an impact on the value of the optical anisotropy, but it does result in a tilt in the optic axis of the LC device, the magnitude of which is represented by the flexoelectro-optic tilt angle, χ.

If dielectric coupling is included, however, then the overall distortion to the helical structure will have a significant influence on the optical anisotropy. Outram and Elston previously derived an expression for the helix distortion [209] which can be written as (considering a ULH structure that the optical axis along x-axis initially according to the configuration in Figure 8.1)

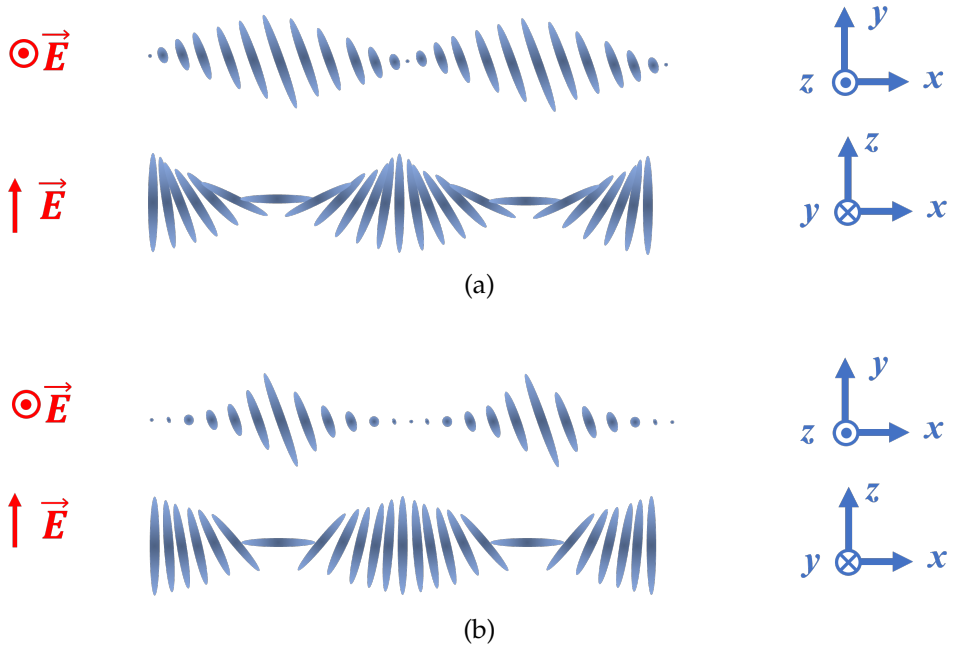

FIGURE 8.2: Illustration of the distortion in the macroscopic helical structure of chiral nematic LC when (a) only flexoelectric coupling is taken into account and (b) flexoelectric and dielectric coupling are included in the model.

$$\eta(x) = q_0 x + \eta_0 \sin(2q_0 x) \tag{8.7}$$

$$\eta_0(E) = \frac{\Delta\varepsilon\varepsilon_0}{8K_{22}q_0^2}E^2 \tag{8.8}$$

where η is the rotation angle of the director along the helix and η_0 is the twist distortion perturbation amplitude. Using these analytical expressions, the resultant biaxial refractive index components can then be written as

$$\begin{bmatrix} n_1 \\ n_2 \\ n_3 \end{bmatrix} = \begin{bmatrix} n_o \\ \sqrt{\frac{n_e^2+n_o^2}{2}}\sqrt{1+\eta_0\left(\frac{n_e^2-n_o^2}{n_e^2+n_o^2}\right)} \\ \sqrt{\frac{n_e^2+n_o^2}{2}}\sqrt{1-\eta_0\left(\frac{n_e^2-n_o^2}{n_e^2+n_o^2}\right)} \end{bmatrix} \tag{8.9}$$

where n_1, n_2 and n_3 are the refractive indices corresponding to the x, y and

z axes, respectively, and n_e and n_o are the extraordinary refractive index and ordinary refractive index of the LC, respectively.

In our numerical model, we include the effects of flexoelectric and dielectric coupling on the director distortion in a chiral nematic LC by taking into account the refractive indices described by Equation 8.9. An illustration of the simulated rotation of the helix is presented in Figure 8.2(b). The phase modulation and intensity modulation of devices with this director configuration agrees well with the theoretical analysis of the phase and intensity modulation values when the applied electric field is below the critical electric field.

To convert the analytical model to a numerical model, the optic axis tilt angle χ, which is relative to the applied field, was simplified to be linear in the field with the aid of a cubic correction term. The model was first tested by using a chiral nematic LC (E7 + 3 wt.% BDH1281) so that experimental results could be compared with those obtained from the simulations. The nematic LC mixture, E7, was chosen as its macroscopic physical properties are widely available across a range of temperatures and incident wavelengths, and the low concentration of chiral additive (BDH1281, Merck) has only a very small impact on these physical properties. The chiral nematic LC mixture was capillary filled into a glass cell that consisted of rubbed polyimide alignment layers and indium tin oxide (ITO) electrodes that were coated onto the inner surfaces of each glass substrate. The ITO layers, which are transparent conductors, enabled the application of an electric field along the normal of the glass substrates and thus perpendicular to the helix axis when the LC was aligned in a ULH configuration. The cell gap in this case was 5µm.

The plot in Figure 8.3(b) is taken with the device on a polarisation optical microscope with crossed polarisers. When no electric field is applied

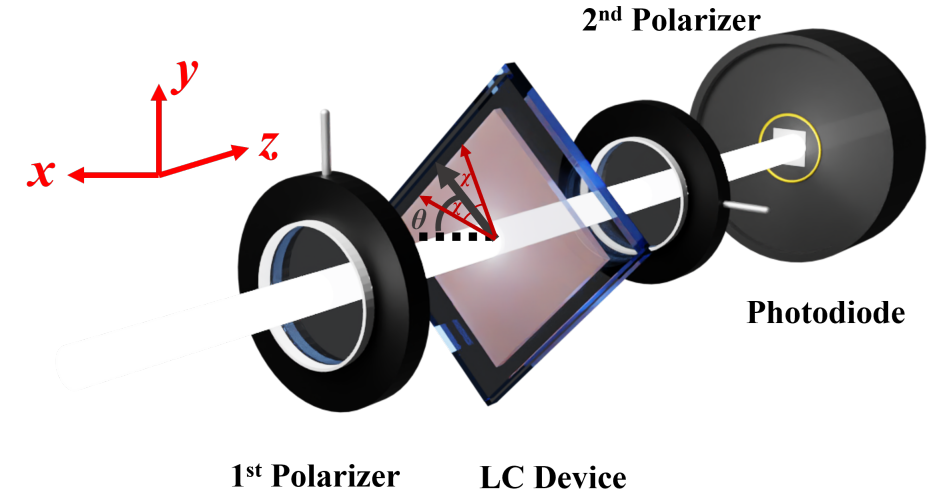

(a)

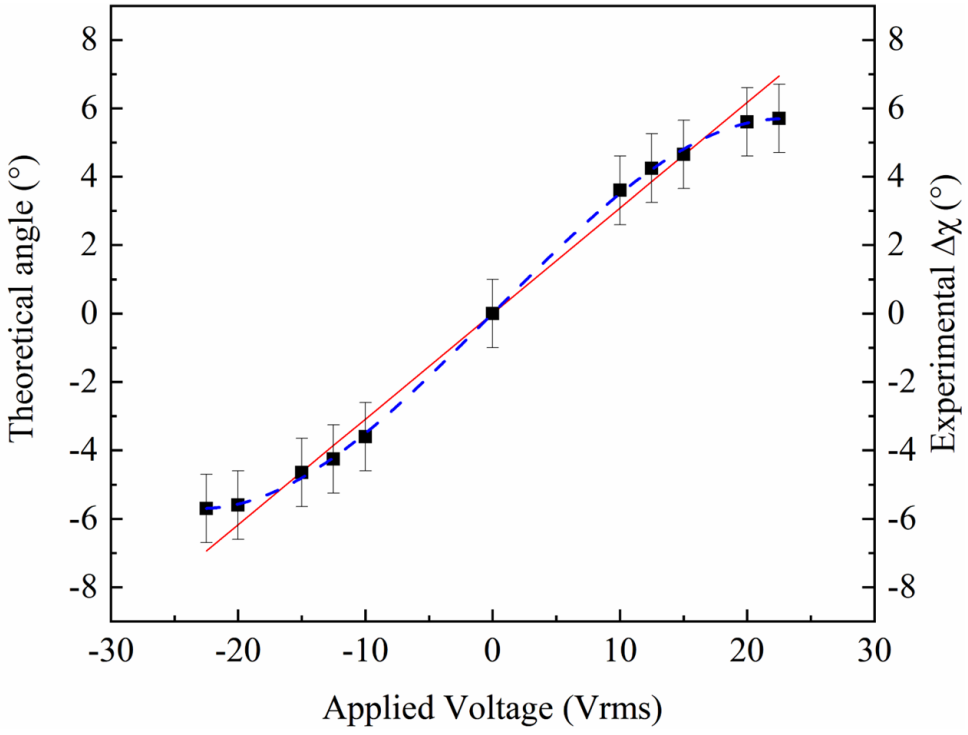

(b)

FIGURE 8.3: (a) Illustration of the setup for measuring the flexoelectro-optic switching angles. The LC device is placed between a pair of crossed-polarisers and the photodiode is positioned at the end to record the intensity change while applying different voltages to the LC device. (b) A comparison between the results from simulations (primary y-axis) and experiments (secondary y-axis) of the electro-optic switching behaviour (tilt angle of the optic axis) of a short-pitch chiral nematic LC (E7 + 3 wt.% BDH1281). The cell thickness is 5μm and the frequency of the applied electric field is 500 Hz, square wave, at room temperature. The red solid line represents the tilt angle extracted from Equation 8.6, the blue dashed line represents the results from simulations after adding the cubic form due to dielectric coupling, and the solid black squares are the experimental results.

to the LC device, the device's optic axis makes an angle of θ with the x-axis. The transmission of light received by the photodiode behind the second linear polariser after going through the LC device with certain phase retardation δ can be described as,

$$\begin{aligned} &\begin{pmatrix} 1 & 0 \\ 0 & 0 \end{pmatrix} \begin{pmatrix} \cos^2\alpha + \sin^2\alpha \cdot A & \sin\alpha\cos\alpha \cdot (1-A) \\ \sin\alpha\cos\alpha \cdot (1-A) & \sin^2\alpha + \cos^2\alpha \cdot A \end{pmatrix} \begin{pmatrix} 0 \\ 1 \end{pmatrix} \\ &= \begin{pmatrix} \sin\alpha\cos\alpha \cdot (1-A) \\ 0 \end{pmatrix} = \frac{1}{2} \begin{pmatrix} \sin 2\alpha \cdot (1-e^{i\delta}) \\ 0 \end{pmatrix} \end{aligned} \tag{8.10}$$

and the resultant transmission collected by the photo-diode is calculated as

$$T = \left\{ \frac{1}{2} \sin 2\alpha \cdot (1-e^{i\delta}) \right\} \cdot \left\{ \frac{1}{2} \sin 2\alpha \cdot (1-e^{-i\delta}) \right\} = \sin^2 2\alpha \cdot \sin^2 \frac{\delta}{2} \tag{8.11}$$

$$\delta = \frac{2\pi \Delta n_{eff} d}{\lambda} \tag{8.12}$$

where Δn_{eff} represents the effective refractive index of the LC mixture, d is the thickness of the wave plate and λ is the wavelength of the incident light.

Considering the switching angle $\pm\chi$ (derived from Equation 8.6), then $\alpha = \theta \pm \chi$ and Equation 8.11 turns into

$$T = \sin^2(2\theta \pm 2\chi) \sin^2(\delta/2) \tag{8.13}$$

The transmission curve is illustrated in Figure 8.4.

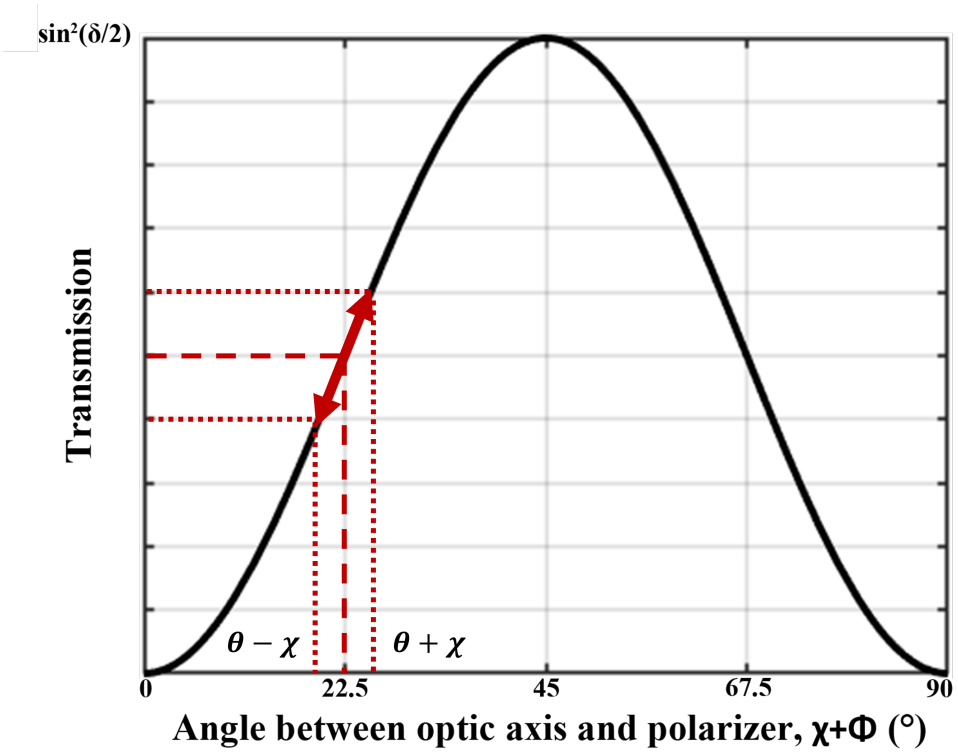

FIGURE 8.4: The transmission curve for a ULH device placed between two crossed polarisers. The LC device is a waveplate with δ retardation and an electric-switchable optic axis which makes an angle of $\theta \pm \chi$ relative to the first polariser. The maximum transmission occurs at $\theta \pm \chi = 45°$.

As can be seen from Figure 8.4, the greatest light modulation happens around the highlighted area (highlighted with the red double arrow area). Thus, the LC device is first placed on the stage with an angle of 22.5°. For a small flexo-tilt angle, the angle χ is linear with the transmission of the light, in this way, we can measure the actual flexoelectro-optic switching angle.

The agreement between simulations and experiments is highlighted in Figure 8.3(b) where the tilt angle of the optic axis is presented as a function of the electric field amplitude. Dielectric coupling is accounted for by a cubic form. The change in the effective refractive index Δn_{eff} resulting from an applied electric field E was also simulated based on Equations 8.7 to 8.9, and compared with experiments. Increasing the amplitude of the electric field resulted in a change in the appearance of the LC when observed between

crossed polarisers on a polarising optical microscope (POM). The change in colour observed in Figure 8.5 is a direct consequence of a change in Δn_{eff}. To simulate the phenomenon observed in the figure, an 'inset' (red_{rate} in Equation 8.15) is included with quadratic form in the change in the refractive index. The simplification is acceptable and reasonable compared with the experimental results in the following section. The next stage is to explore how different combinations of director tilt and the effects of a reduction in the device retardation would have on phase and intensity modulation in the flexoelectro-optic phase modulator.

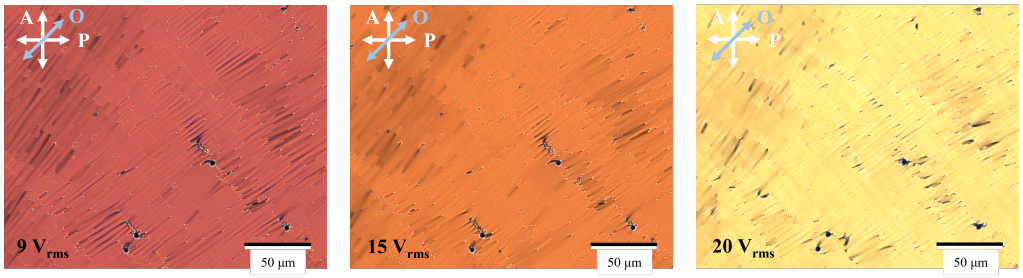

(a) (b) (c)

FIGURE 8.5: Polarisation optical microscopy images of a short pitch chiral nematic LC (E7 + 3 wt.% BDH1281) at different electric field amplitudes when the electric field is applied perpendicular to the helix axis: (a) 9 V_{rms}; (b) 15 V_{rms}; (c) 20 V_{rms}. P represents the first polariser; A represents the second polariser, which is the analyzer. O denotes the initial optic axis (θ) of the device which is at 45° to the polarisers. The measurements are carried out at room temperature and the cell gap is 5 µm. The scale bar represents a length of 50 µm.

8.5 Optical Phase Modulation

8.5.1 Small flexoelectric coupling

Here, the results from numerical simulations of a chiral nematic LC phase modulator using the mixture, E7 + 3 wt.% BDH1281 with a thickness of 5 µm is first demonstrated. These results are then compared with results from measurements of the phase and amplitude modulation of the LC phase modulator using a phase-shift interferometry experiment that was described in

more detail in Chapter 7. Figure 8.6 presents results of the modulation in the phase and intensity that were obtained both from simulations and experiments, which are found to be in good agreement with one another. For this part of the investigation, the LC was set at two specific angles to show how the device orientation can have a significant impact on the device performance.

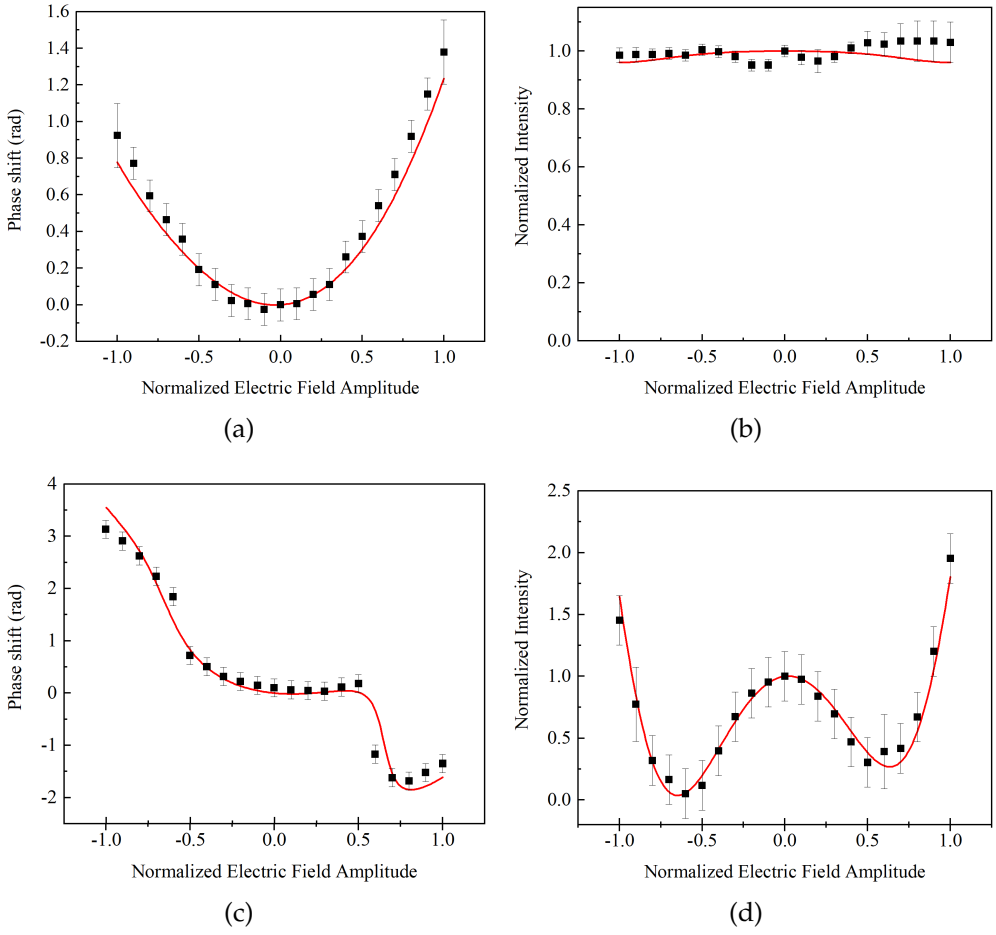

FIGURE 8.6: Phase ((a) and (c)) and amplitude ((b) and (d)) modulation of a chiral nematic LC phase modulator: experiments and simulations. The chiral nematic LC is based on the mixture of E7 + 3 wt.% BDH1281, which has a cell gap of 5µm. The experimental results (solid black squares) and simulation results (solid red line). The configuration of the setup follows the arrangement in Figure 8.1(b). The first and second quarter-wave plates are set at 45° and -45°, respectively. For (a) and (b) the initial LC optic axis (θ in Figure 8.1(b)) is set initially at 0° whereas in (c) & (d) it is set at 45°.

It is clear from the results presented in Figure 8.6 that the device orientation is highly influential on the resultant amplitude modulation and

the symmetry of the phase shift. As can be seen, the amplitude modulation is nearly zero if the LC optic axis is set to 0° relative to $x-$axis in Figure 8.1(b), but the phase shift falls far short of the π modulation. In this case, the tilt angle of the optic axis is relatively small ($\chi \approx 6.5°$ as shown in Figure 8.3). However, if the device is set at 45°, the phase modulation can increase to more than a π shift, which comes at the expense of a considerable modulation in the amplitude.

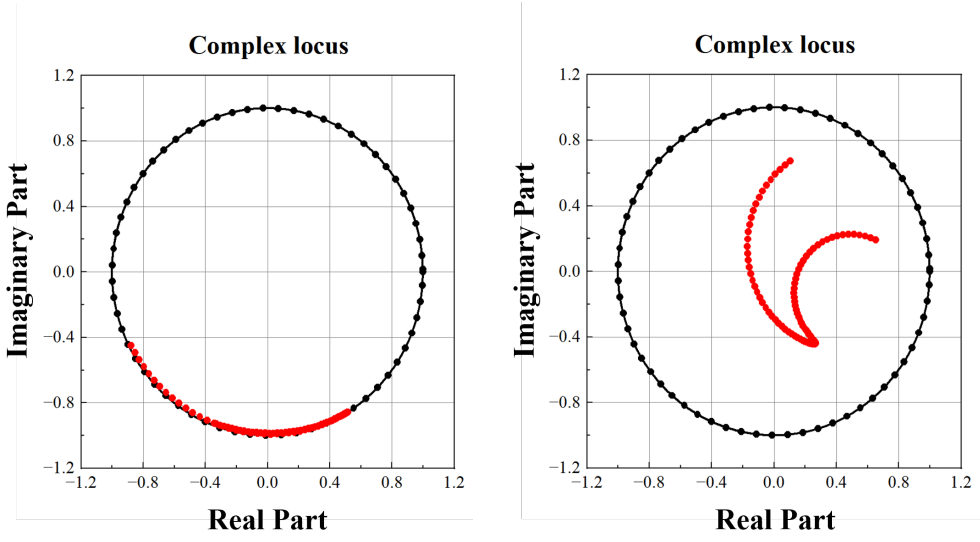

(a) (b)

FIGURE 8.7: The complex locus plot of a chiral nematic flexoelectro-optic LC device based on the mixture E7+ 3 wt.% BDH1281. The initial angle between the optical axis of the device and the x- axis (θ in Figure 8.1(b)) is set as (a) 0° and (b) 45°, respectively. The black dots and lines are the reference and the red dots and the lines are the experimental data.

The reason for the phenomena observed in Figure 8.6 can be explained by Figure 8.7. The x and y axes of plots in Figure 8.7(a) and 8.7(b) represent the real part and the imaginary part of the coherent light recorded at the photodiode,

$$
\begin{aligned}
E_{out} = \frac{1}{4}[&1 + 2\cos\delta + \cos 2\delta - \cos 4\alpha \\
&+ 2\cos\delta\cos 4\alpha - \cos 4\alpha\cos 2\delta - 2\sin 4\alpha\sin\delta + \sin 4\alpha\sin 2\delta \\
&+ i(2\sin\delta + \sin 2\delta + 2\cos 4\alpha\sin\delta \\
&- \cos 4\alpha\sin 2\delta - \sin 4\alpha + 2\cos\delta\sin 4\alpha - \sin 4\alpha\cos 2\delta)]
\end{aligned}
\tag{8.14}
$$

here, the δ is calculated based on the measured flexoelectric tilt angle and the initial retardance (based on the thickness (d) and the Δn_{eff} of the E7) as well as an estimation of the reduction in retardance (red_{rate}) because of the dielectric effect. In this case, δ can be written as

$$
\delta = \frac{2\pi\Delta n_{eff} d}{\lambda}\left(1 - red_{rate}(\frac{\chi}{\chi_{max}})^2\right) \tag{8.15}
$$

and $\alpha = \theta \pm \chi$ as mentioned previously.

By plotting the data in this manner, it becomes easier to understand the phase and intensity modulation for different arrangements. The distance between each data point and the origin represents the intensity amplitude, while the angle between the x-axis and the radius indicates the corresponding phase shift for that χ under relative E. The outer perfect circle serves as a reference, representing a total phase shift of 2π, where there is no intensity modulation. It allows us to directly gauge the performance of the device at different angles. In Figure 8.7(a), we observe that the intensity modulation is relatively small, as indicated by the red line nearly overlapping with the reference circle. However, the available range of the phase shift is limited compared to Figure 8.7(b). Contrastingly, in Figure 8.7(b), the red line deviates significantly from the reference plot, which aligns with the findings in

Figure 8.6(d). This suggests a dramatic intensity jump during phase modulation.

These results indicate that by optimising the device orientation, as well as the absolute angles of the quarter-wave plates angle, a trade-off can be made between the depth of phase modulation and the amplitude modulation. This is important because it potentially relaxes the requirement for LC mixtures that exhibit a 45° tilt angle, which is challenging.

8.5.2 Larger flexoelectric coupling

The next stage of the study was to test a mixture that exhibited larger flexoelectric coupling. For this, we chose the compound CB9CB (α, ω-bis(4,4'-cyanobiphenyl)nonane) as this has been shown to exhibit large flexoelectric coupling (large flexoelastic ratios). The previous investigation done by former group members involved using the LC dimer CB7CB dispersed with a low concentration of high twisting power chiral additive [178]. However, this mixture had to be operated at 100°C as this was where the chiral nematic phase was found to occur, although it did show nearly full π modulation within a response time of 1 ms when used in the single pass configuration shown Figure 8.1(a). To ensure that the chiral nematic phase appeared at lower temperatures and also continuing with the work carried out in Chapter 6, CB9CB (from the same homologous series as CB7CB) was dispersed directly into the chiral nematic LC mixture (E7 + 3 wt.% BDH1281) at an initial concentration of 20 wt.%. The LC mixture was then capillary filled into a glass cell of the type described previously (with a cell gap of 5μm) and placed in a 4 pass configuration, demonstrated in Chapter 6, Figure 6.4(c) to extract the level of phase modulation. A full 2π phase shift was achieved within 1 ms, however, the level of amplitude modulation was not negligible

and it was deemed that one way to overcome this was to reduce the concentration of CB9CB in the host mixture and carefully adjust the angles between the x-axis and the quarter-wave plates and the initial angle of the LC device θ.

A 2π phase shift with a response time that was less than 1 ms was obtained by using a similar mixture to the one above but with a lower concentration of CB9CB. In this case, the amplitude modulation could be decreased to almost zero by optimising the orientation of the different optical components. Figure 8.8 shows the device (E7 + 3 wt.% BDH1281 + 15 wt.% CB9CB with a cell thickness of 5µm) on a POM before and after applying an electric field that was greater than the E_c.

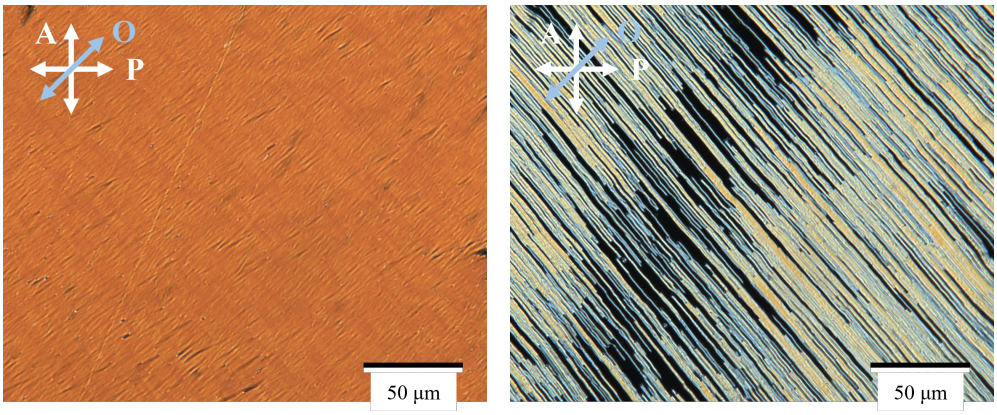

(a) (b)

FIGURE 8.8: Polarising optical microscope images of E7 + 3 wt.% BDH1281 + 15 wt.% CB9CB, (a) is the ULH structure before unwinding the helix, (b) is the structure after increasing the voltage above the critical voltage and the helix starts to unwind. The measurements are carried out at room temperature and the cell gap is 5 µm.

Using this device and placing it in a reflective system shown in Figure 8.1(b), the simulation code was adapted to demonstrate that device orientation can vary the resultant amplitude and phase modulation. The simulation results show that if the variable is the device orientation only, the amplitude and phase modulation cannot satisfy both requirements, so two

quarter-wave plates are also set as variables in the process of finding the optimum combination. The numerical procedure uses the Jones matrix model instead of the analytic method. The results of all possible combinations are shown in Figure 8.9(a).

Figure 8.9(a) shows the degree of amplitude modulation fluctuation in a colour map format when the device orientation and the first quarter wave plate rotation vary from 0° to 360° respectively (the angle for the second quarter-wave plate is consistently set 90° greater than that of the first one). The colour bar is designed such that the data points become increasingly red as the corresponding amplitude modulation decreases. Figure 8.9(b) is a subset of Figure 8.9(a) obtained by applying a filter to isolate and plot the set of two angles that result in a phase shift greater than π. As the data point becomes redder, it indicates a reduced presence of amplitude modulation when the device undergoes a monotonic full π phase shift. Among all the possible points, the point chosen for experimental verification is when the first quarter wave plate = 90°, and device orientation = 74.5°. The results of the phase modulation and the relative amplitude change are shown in Figure 8.9(c), 8.9(d).

Now with the guidance of the numerical simulation model, the yellow rectangle highlighted in Figure 8.9(c) and 8.9(d) shows that we can operate the cell between -25 V and 0 V to obtain full π phase modulation in a reflective configuration with only a small amount of amplitude modulation, which would not be detectable to the naked eye.

8.6 Summary

This study explores potential improvements to the device configurations of chiral nematic LC flexoelectro-optic phase modulators to enable lower-perfo-

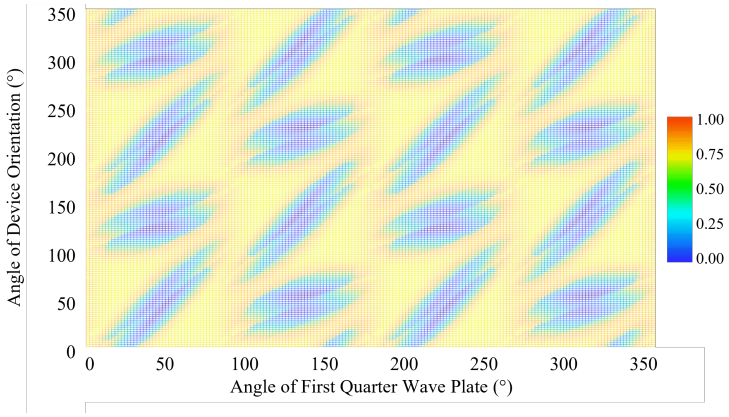

(a)

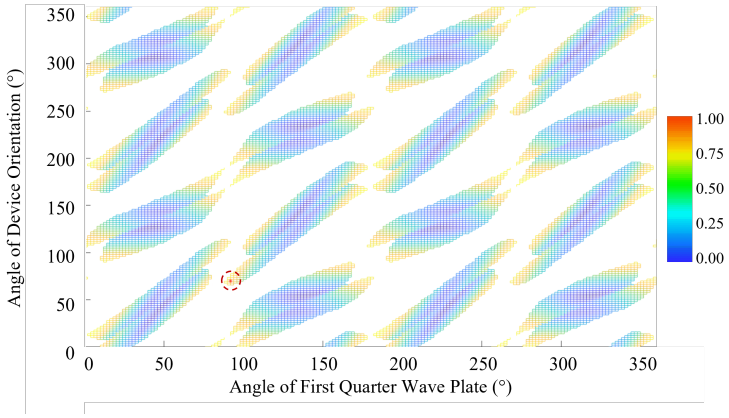

(b)

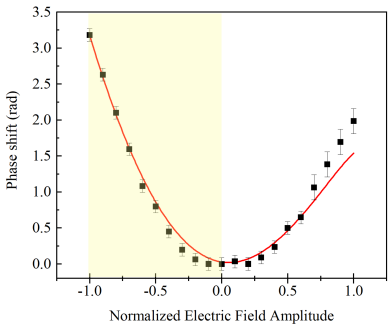

(c)

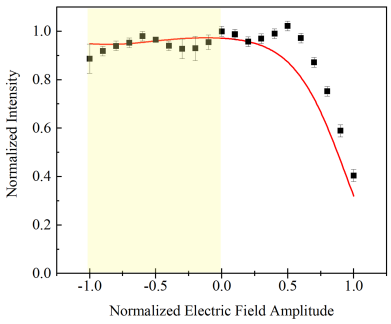

(d)

FIGURE 8.9: The selection of the optimum combination of relative orientations of the optical elements in the flexoelectro-optic phase modulator configuration. (a) shows the amplitude modulation for all combinations of orientations of the device and quarter-wave plates. (b) shows the amplitude modulation at all possible full π phase modulation elements orientation combination. The colour bar represents the average intensity value for the normalized intensity modulation achieved by the device at a specific electric field amplitude that enables it to generate a π phase shift. When the mean intensity value is closer to 1.0 (displayed in red), the intensity modulation is lower. (c) & (d) shows the experimental and simulation results of the phase shift and intensity shift, respectively. The maximum voltage applied to the cell is ± 25 V ($25\ V_{rms}$).

rmance mixtures to be used. In Section 8.3, analytical equations are presented to model the behaviour of the LC device. Furthermore, Section 8.4 delves into the discussion of how the chiral nematic LC responds to external electric fields. The simulation takes into account the impact of dielectric coupling on helix distortion and reduction of the retardance, offering valuable insights.

The study also addresses the implications for material, device, and system optimisation in real-world scenarios. The correctness of the analytical model and its conversion into a numerical approach enables the identification of the optimal arrangement of the optical elements for achieving a full π phase-only modulation from numerous possibilities. Remarkably, these findings suggest that it may be possible to achieve or even surpass the phase shift range of materials with enhanced flexoelectric-coupling at room temperature, using more conventional LC mixtures and compounds.

Chapter 9

Conclusions and Future Work

This thesis aims to investigate techniques and provide solutions to enhance the optical phase (wavefront) in either a random way or controlled way through liquid crystal (LC) thin film devices. The first part of the thesis described the process of manipulating the wavefront in a stochastic way and evaluated the performance in suppressing the laser speckle through generating a set of decorrelated speckle patterns. Different types of dopants and device structures were studied and several practical applications including an optical microscope, Head-Up Display, holographic images, laser projector and MM polarimeter, were considered and demonstrated. The second part of this thesis focused on developing sub-millisecond analogue full 2π phase modulation. This part involved both simulation and experimental work. Various factors that may influence the switching speeds and phase shift depth as well as the suppression of intensity modulation were studied.

This final chapter will summarise the key findings from the chapters presented in the thesis and will outline a route forward for future work. As the collective purpose of this work is to utilize different types of LC technologies for wavefront control, Chapter 2, served as a background introduction, which discussed the fundamentals of LC phases and their related physical

properties, different types of electro-optic effects, and the definition of optical phase. The chapter also outlined the current obstacles that formed the motivation for the work presented in the thesis and ended with a review of laser speckle and optical phase modulation and spatial light modulators.

Chapter 3 then introduced the experimental tools used throughout the thesis. Several commonly used techniques as well as specifically designed measurement & characterisation setups were discussed in detail. As this thesis is mainly concerned with the interaction between different types of LC mixtures and visible light, a comprehensive introduction of the various categories of LC mixtures and standard glass cell configurations used in the following chapters was presented. This was followed by a description of polarising optical microscope and the associated equipment that was used (hot-stage etc.). A parameter of great importance in this work is the pitch of the chiral nematic LC helix and thus the concept of UV-Vis spectroscopy and the approach used to measure the pitch were introduced. The last part of this chapter summarized the purpose-built speckle characterisation system. This system has been specifically tailored so that the system mimics human observer conditions. In this case, the laser light passes through a series of optical elements and is finally captured by a low-dark current CCD camera to provide a quantitative measure of the speckle contrast.

As mentioned previously, the first part of the thesis was about laser speckle reduction and in Chapter 4 different types of redox dopants and their impact on enhancing speckle reduction was discussed. An optimised LC speckle reducer was then demonstrated in a couple of practical scenarios. Chapter 4 not only considered key parameters of the nematic LC host (e.g., refractive index, dielectric constant, rotational viscosity and the clearing point), but also considered the pitch of the chiral nematic LC and its

influence on speckle suppression. A large range of redox dopant concentrations of both acceptor and donor types were investigated along with the performance over a period of time to demonstrate improved stability compared with conventional ionic dopants. It was demonstrated that the devices filled with mixtures composed of electron acceptor redox dopants showed the lowest speckle contrast and also demonstrated a consistent performance over time when run either intermittently over two weeks or continuously for 7 days. The device is thin, vibration free and can be assembled into an optical microscope or laser projector.

Following on from Chapter 4, Chapter 5 then focused on the potential of a new dopant, a zwitterionic dopant. Instead of providing either positive ions or negative ions, zwitterion dopants can provide both as well as automatically control the concentration in a way to avoid permanent electrochemical degradation. This chapter described the device fabrication process along with an investigation of the dopant concentration and pitch. Here it was demonstrated that the speckle contrast could be further decreased to C = 0.07. In addition to the device characterisation, this chapter further expanded the demonstrators from scalar field imaging to vectorial field imaging. As well as verifying the LC speckle reducer's capability in traditional imaging systems and laser displays, this chapter also demonstrated how the speckle reducer performed in a Mueller Matrix polarimeter. The LC speckle reducer is portable and has a small form factor which is easy to retrofit in normal imaging systems and in more advanced vectorial optical microscopes.

Although the above results demonstrate good, speckle reduction, there are still a few drawbacks that have a negative impact on its potential for widespread commercial use. A key drawback is the high amplitude of the applied electric field. For either redox dopant doped or zwitterion dopant doped devices, under room temperature or high temperatures, the optimum

operating condition of the amplitude of the electric field is usually around $20V/\mu m$. For a 20 µm cell, the absolute value of the applied voltage would therefore be $400V$. The amplitude of the electric field required is linearly related to the cell thickness and inversely proportional to the pitch of the helix. However, the minimum speckle contrast that can be achieved is linearly proportional to the pitch and inversely proportional to the cell thickness, which means the shorter the pitch is and the thicker the cell is, the lower the minimum speckle contrast can be reduced. Of course, the chiral pitch can not be infinitely short otherwise the turbulence induced by the random rotation of the chiral nematic LC would not be strong enough to decrease the speckle contrast. Additionally, there is a threshold for the cell thickness for each pitch that further increases the thickness won't bring any more speckle reduction. For a pitch equal to 300 nm mixture, the cell thickness threshold is between 35 to 40 µm.

In order to obtain maximum speckle reduction at room temperature, the cell has to be thick, the pitch has to be short and the device requires high electric field amplitude. However, this problem can be reduced by increasing the temperature to near the clearing point and another merit of doing this is that the transmission at the optimum speckle suppression point can be improved by 15% to 20%. The high temperature may cause the degradation to become faster, hence, the subsequent endeavour to enhance the lifetime at high temperatures would involve not only the injection of electrons but also the incorporation of small particles capable of generating equal or greater vibrations without experiencing degradation near the electrodes. Future work could also consider testing the LC speckle reducer's performance when imaging living cells in a laser-based fluorescence microscope as well as testing the device in a range of clinical diagnosis applications such as endoscopes and fluorescence optical microscopes.

The second part of this thesis was devoted to the investigation of new LC technologies and configurations for optical phase modulation. This included considering a range of different geometries and electro-optic effects in nematic and chiral nematic LCs as well as carrying out both experiments and simulations to establish the optimum configurations. Towards this end. Chapter 6 demonstrated two different configurations that could provide a continuous phase shift within 1 ms. These two configurations were deployed in a multi-pass reflective setup and the resulting phase shift was extracted through the aid of a Mach- Zehnder interferometer. The experimental results showed that for two different device configurations, the multi-pass system could enhance the phase shift by four times. The key achievement of this study was the demonstration of two possible phase modulators for next-generation SLM technologies that could exhibit sub-millisecond switching over a full 2pi phase range. The results presented in the chapter demonstrated a proof of concept of a multi-pass configuration for both nematic and chiral nematic LCs (operating in the flexoelectro-optic mode), although the results only demonstrated phase modulation for a single-pixel device. However, this approach could be extended to multi-pixel configurations. Future work in this area would therefore be to demonstrate a multi-pixel phase modulator. A sub-millisecond reflective multi-pixel phase modulator can have exciting applications in areas such as optical beam steering in free space communication, adaptive optics, and programmable diffractive elements.

Carrying on from the work described in Chapter 6, Chapter 7 extended the research to test a range of device configurations for nematic LC materials in order to elevate the phase modulator performance. In addition, in order to extract the phase modulation and analyse its response with time,

a new measurement setup was presented. This is in contrast to the measurement approach used in Chapter 6, which depended on capturing the movement of the interference pattern with a relatively low frame rate CCD camera. With this new method in Chapter 7, the phase modulation was recorded using phase-shifting interferometry and by analysing the signal obtained via a fast photodiode. This experiment was used to characterise the response of three different nematic LC devices: a Pi-cell, a Freedericksz cell, and a HAN cell. The first step was to compare the intensity and the phase modulation of these three different devices under different amplitudes and frequencies of the applied electric field. Additionally, in order to understand fully the reason for the different responses observed for the three different devices, such as how the cell configurations, pre-tilt angles, amplitude of the electric field as well as the switching time can influence the director behaviour and thus influence the phase and intensity shift, simulations were carried out that consider the Frank elastic energy, the effects of dielectric coupling, and the role of backflow. The results showed that the Pi-cell configuration works best for both 1 ms and 10 ms switching times. The reason is that the backflow has a negative effect on the dynamic director response for the Freedericksz device but not the Pi-cell. The simulation results and the experimental results agreed with each other well and both suggested that a Pi-cell is potentially better suited for phase modulation when rapid switching speeds and a large phase modulation are required.

Further investigation of phase modulation with the goal of solving the unwanted intensity modulation observed for the chiral nematic flexoelectro-optic device (a problem mentioned in Chapter 6) as well as simulating and predicting the optical response under different configurations was presented in Chapter 8. The relative orientation of the ULH axis relative to that of two quarter-wave plates were simulated and discussed. It was shown that

because of the small errors in the thickness of the cell (which means that the LC deviates from the ideal half-wave condition), intensity modulation would appear when the two quarter-wave plates were set to the original configuration. After utilizing the numerical model to calculate the phase shift and intensity modulation for different arrangements of the quarter wave plates and the chiral nematic LC device, and considering all possible combinations of the relative angles, the optimum configuration was chosen which could provide a π phase modulation in a reflective device and would provide full 2π phase modulation within millisecond switching times with nearly zero intensity modulation if it is placed in a four-pass configuration. The experimental results agreed well with the predictions from simulations. A key result of this work is that it has demonstrated that full 2π phase modulation can be achieved even when chiral nematic LC mixtures with relatively weak flexoelectric coupling are employed. Future work in this area could involve finding a way to stabilize the ULH alignment with a polymer network that is written into the LC device using either bulk ultraviolet illumination or using more advanced fabrication techniques in the form of direct laser writing. The impact of the quality of the ULH alignment on the performance of single and multi-pixel phase modulators would also be something that could be investigated further in the future.

To conclude, the work presented in this thesis has targeted the use of different types of LC material and device configurations to modulate the optical wavefront in either a pseudo random way or a controlled way for enhanced optical system functionalities. The first part was about breaking the wavefront coherence of the incident light in order to improve laser-based optical system imaging quality, which is an important contribution to laser

displays, optical microscopy and polarimeters. The technique that was presented is based on electrohydrodynamic instabilities (EHDI), and this thesis has considered the impact of different dopants on the EHDI behaviour and the resulting dynamic scattering mode. The second part of the thesis considered LCs for optical phase modulation. This thesis mainly focused on electro-optic modes in nematic LCs as well as the flexoelectro-optic effect in chiral nematic LCs. Simulation, as well as experimental verification, have been carried out, and a new measurement system has been established to characterize the phase modulation capabilities of these LC devices. The thesis has presented advances in both the speckle reducing capabilities and phase modulation capabilities of LC devices. Notably, in terms of speckle reduction, this thesis has demonstrated a reduction in the speckle contrast to an impressive level of C = 0.07 at room temperature, demonstrating stable performance across diverse application scenarios ranging from laser HUD to polarimetry. A variety of new dopants have been investigated in terms of the concentration therefore and the operating conditions.

In the realm of optical phase modulation, key contributions from this work are the novel multi-pass configuration and the time-resolved phase measurement method. Additionally, various factors that could contribute to submillisecond switching and achieve full 2π analogue phase modulation in thin LC devices have been studied. To support the validity of the research, simulations incorporating boundary layer properties, backflow effects, dielectric coupling, and flexoelectric coupling have been considered. These simulations have proven to be both practical and consistent with real-world observations, offering valuable guidance for future studies in related areas. Overall, the work presented in this thesis has achieved some promising results in speckle reduction and optical phase modulation using LC devices. The significant reduction in speckle contrast and the development of a rapid

analogue full-range phase-only modulator showcase the potential impact of this research. The practical simulations further strengthen the validity and applicability of the findings, providing a foundation for future advancements in LC technologies and the associated applications.

Bibliography

1. Xiong, J., Hsiang, E.-L., He, Z., Zhan, T. & Wu, S.-T. Augmented reality and virtual reality displays: emerging technologies and future perspectives. *Light: Science & Applications* **10,** 216. (2021).
2. Yin, K. *et al.* Advanced liquid crystal devices for augmented reality and virtual reality displays: principles and applications. *Light: Science & Applications* **11,** 161. (2022).
3. Zhao, Z., Duan, J. & Liu, J. Speckle reduction in holographic display with partially spatial coherent illumination. *Optics Communications* **507,** 127604. (2022).
4. Bianco, V. *et al.* Strategies for reducing speckle noise in digital holography. *Light: Science & Applications* **7,** 48. (2018).
5. Lee, D. *et al.* Speckle Reduction for Holographic Display Using Optical Path Difference and Random Phase Generator. *IEEE Transactions on Industrial Informatics* **15,** 6170–6178. (2019).
6. Huang, Y., Liao, E., Chen, R. & Wu, S.-T. Liquid-Crystal-on-Silicon for Augmented Reality Displays. *Applied Sciences* **8,** 2366. (2018).
7. Nakagawa, J., Yamaguchi, H. & Yasuda, T. *Head up display with laser scanning unit* in *ODS 2019: Industrial Optical Devices and Systems* (eds Katayama, R. & Takashima, Y.) **11125** (SPIE, 2019), 12.
8. Lv, Z., Li, J., Yang, Y. & Liu, J. 3D head-up display with a multiple extended depth of field based on integral imaging and holographic optical elements. *Optics Express* **31,** 964. (2023).

9. Kumar, V. *et al.* Speckle noise reduction strategies in laser-based projection imaging, fluorescence microscopy, and digital holography with uniform illumination, improved image sharpness, and resolution. *Optics & Laser Technology* **141,** 107079. (2021).
10. Lo, C.-K. & Pan, J.-W. Speckle reduction with fast electrically tunable lens and holographic diffusers in a laser projector. *Optics Communications* **454,** 124301. (2020).
11. Bahk, S.-W., Fess, E., Kruschwitz, B. E. & Zuegel, J. D. A high-resolution, adaptive beam-shaping system for high-power lasers. *Optics Express* **18,** 9151. (2010).
12. Friedmann, D., Lee, A. F., Wilson, K., Jalili, R. & Caruso, R. A. Printing approaches to inorganic semiconductor photocatalyst fabrication. *Journal of Materials Chemistry A* **7,** 10858–10878. (2019).
13. Morris, R., Jones, C. & Nagaraj, M. Liquid Crystal Devices for Beam Steering Applications. *Micromachines* **12,** 247. (2021).
14. He, Z. *et al.* Liquid Crystal Beam Steering Devices: Principles, Recent Advances, and Future Developments. *Crystals* **9,** 292. (2019).
15. Goodman, J. W. *Speckle Phenomena in Optics:Theory and Applications* second edition. (SPIE PRESS, Bellingham, Washington USA, 2020).
16. Hansford, D. J., Fells, J. A. J., Elston, S. J. & Morris, S. M. Speckle contrast reduction of laser light using a chiral nematic liquid crystal diffuser. *Applied Physics Letters* **109,** 261104. (2016).
17. Jin, Y., Hansford, D. J., Elston, S. J. & Morris, S. M. Laser Speckle Reduction Using a Liquid Crystal Diffuser Enhanced with Redox Dopants. *Advanced Photonics Research* **2,** 2000184. (2021).
18. Jin, Y. *et al.* Millisecond Optical Phase Modulation Using Multipass Configurations with Liquid-Crystal Devices. *Physical Review Applied* **14,** 024007. (2020).

19. Jin, Y. *et al.* Backflow-assisted time-resolved phase modulation in nematic liquid crystal Pi-Cells. *Optics & Laser Technology* **156,** 108596. (2022).
20. Collings, P. J. & Hird, M. *Introduction to liquid crystals : chemistry and physics* (Taylor & Francis, London, UK, 2009).
21. Akagi, K. *et al.* Helical Polyacetylene Synthesized with a Chiral Nematic Reaction Field. *Science* **282,** 1683–1686. (1998).
22. Depp, S. W. & Howard, W. E. Flat-Panel Displays. *Scientific American* **268,** 90–97 (1993).
23. Frank, F. C. I. Liquid crystals. On the theory of liquid crystals. *Discussions of the Faraday Society* **25,** 19 (1958).
24. Zocher, H. The effect of a magnetic field on the nematic state. *Transactions of the Faraday Society* **29,** 945. (1933).
25. Yang, D.-K. & Wu, S.-T. *Fundamentals of Liquid Crystal Devices* second edition. (Wiley, Chichester, West Susex, UK, 2015).
26. Salter, P. S. *Flexoelectricity and chirality in complex liquid crystal systems* PhD thesis (University of Oxford, Oxford, 2010).
27. Oseen, C. W. *Beiträge zur Theorie der anisotropen Flüssigkeiten* 1–19 (Almquist & Wiksells Boktryckeri A.-B., 1931).
28. Oseen, C. W. The theory of liquid crystals. *Trans. Faraday Soc.* **29,** 883 (1933).
29. Zocher, H. The effect of a magnetic field on the nematic state. *Transactions of the Faraday Society* **29,** 945 (1933).
30. Friedel, G. Les états mésomorphes de la matière. *Ann. Phys.* **9,** 273–474 (1922).
31. Ericksen, J. L. Conservation laws for liquid crystals. *Transactions of the Society of Rheology* (1961).
32. Leslie, F. M. Some constitutive equations for anisotropic fluids. *Journal of Mechanics and Applied Mathematics* (1966).

33. Leslie, F. M. Some constitutive equations for liquid crystals. *Arch. Ration. Mech. Anal.* **28,** 265–283 (1968).
34. Kirsch, P., Bremer, M., Heckmeier, M. & Tarumi, K. Liquid Crystals Based on Hypervalent Sulfur Fluorides: Pentafluorosulfuranyl as Polar Terminal Group. en. *Angew. Chem. Int. Ed Engl.* **38,** 1989–1992 (1999).
35. Demus, D. 100 Years Liquid Crystal Chemistry. *Molecular Crystals and Liquid Crystals Incorporating Nonlinear Optics* **165,** 45–84 (1988).
36. Hansford, D. J. *A liquid crystal device for speckle reduction in coherent light* PhD thesis (University of Oxford, 2018).
37. Outram, B & Outram, B. *Flexoelectric and dielectric phenomena in helicoidal liquid crystals* en. PhD thesis (University of Oxford, 2013).
38. Meyer, R. B. DISTORTION OF A CHOLESTERIC STRUCTURE BY A MAGNETIC FIELD. *Appl. Phys. Lett.* **14,** 208 (1969).
39. De Gennes, P. G. Calcul de la distorsion d'une structure cholesterique par un champ magnetique. *Solid State Commun.* **6,** 163–165 (1968).
40. Meyer, R. B. Piezoelectric Effects in Liquid Crystals. *Phys. Rev. Lett.* **22,** 918 (1969).
41. Helfrich, W. Inherent Bounds to the Elasticity and Flexoelectricity of Liquid Crystals. *Mol. Cryst. Liq. Cryst.* **26,** 1–5 (1974).
42. Hinov, H. P. & Marinov, Y. An electro-magneto-optical resonance method for determination of the value and sign of the flexoelectric coefficients in nematics. *J. Optoelectron. Adv. Mater.* **9,** 435 (2007).
43. Ghosh, S. K. A model for the orientational order in liquid crystals. *Nuovo Cimento C* **4,** 229–244 (1984).
44. Petrov, A. G. Measurements and interpretation of flexoelectricity. *EMIS DATAREVIEWS SERIES.*
45. Fan, C. Comments on Piezoelectric Effect in Liquid Crystals. *Mol. Cryst. Liq. Cryst.* **13,** 9–15 (1971).

46. Derzhanski, A, Petrov, A. G. & Mitov, M. D. One-dimensional dielectric-flexoelectric deformations in nematic layers. en. *Journal de Physique* **39,** 273–285 (1978).
47. Bouligand, Y. SUR L'EXISTENCE DE "PSEUDOMORPHOSES CHOLESTÉRIQUES" CHEZ DIVERS ORGANISMES VIVANTS. fr. *J. Phys., Colloq.* **30,** C4–90–C4–103 (1969).
48. Patel, J. S. & Meyer, R. B. Flexoelectric electro-optics of a cholesteric liquid crystal. *Phys. Rev. Lett.* **58,** 1538 (1987).
49. Patel, J. S. & Lee, S.-D. Fast linear electro-optic effect based on cholesteric liquid crystals. *J. Appl. Phys.* **66,** 1879–1881 (1989).
50. Lee, S. D., Patel, J. S. & Meyer, R. B. Effect of flexoelectric coupling on helix distortions in cholesteric liquid crystals. *J. Appl. Phys.* **67,** 1293–1297 (1990).
51. Rudquist, P, Carlsson, T, Komitov, L & Lagerwall, S. T. The flexoelectro-optic effect in cholesterics. *Liq. Cryst.* **22,** 445–449 (1997).
52. Wang, C.-T., Wang, W.-Y. & Lin, T.-H. A stable and switchable uniform lying helix structure in cholesteric liquid crystals. *Appl. Phys. Lett.* **99** (2011).
53. Kim, S. H., Chien, L. C. & Komitov, L. Short pitch cholesteric electro-optical device stabilized by nonuniform polymer network. *Appl. Phys. Lett.* (2005).
54. Broughton, B. J., Clarke, M. J., Morris, S. M. & others. Effect of polymer concentration on stabilized large-tilt-angle flexoelectro-optic switching. *Journal of applied* (2006).
55. Carbone, G. *et al.* Short pitch cholesteric electro-optical device based on periodic polymer structures. *Appl. Phys. Lett.* **95** (2009).
56. Coles, H. J., Musgrave, B, Coles, M. J. & Willmott, J. The effect of the molecular structure on flexoelectric coupling in the chiral nematic phase. en. *J. Mater. Chem.* **11,** 2709–2716 (2001).

57. Musgrave, B., Coles, M. J., Perkins, S. P. & Coles, H. J. ENHANCED FLEXOELECTRIC SWITCHING BEHAVIOUR IN THE CHIRAL NEMATIC PHASE. *Mol. Cryst. Liq. Cryst. Sci. Technol. Sect. A* **366,** 735–742 (2001).
58. Blinov, L. M. & Chigrinov, V. G. *Electrooptic Effects in Liquid Crystal Materials* en (Springer Science & Business Media, 1996).
59. Schadt, M. Milestone in the History of Field-Effect Liquid Crystal Displays and Materials. en. *Jpn. J. Appl. Phys.* **48,** 03B001 (2009).
60. Miniewicz, A, Gniewek, A & Parka, J. Liquid crystals for photonic applications. *Opt. Mater.* **21,** 605–610 (2003).
61. Austin, E. *et al.* Visible light. Part I: Properties and cutaneous effects of visible light. en. *J. Am. Acad. Dermatol.* **84,** 1219–1231 (2021).
62. Roelandt, S. *et al.* Standardized speckle measurement method matched to human speckle perception in laser projection systems. en. *Opt. Express* **20,** 8770–8783 (2012).
63. Redding, B., Choma, M. A. & Cao, H. Speckle-free laser imaging using random laser illumination. *Nature Photonics 2012 6:6* **6,** 355–359 (2012).
64. Zheng, G. *et al.* Laser Digital Cinema Projector. *Journal of Display Technology, Vol. 4, Issue 3, pp. 314-318* **4,** 314–318 (2008).
65. Li, J. Design of optical engine for LCOS laser display with rotated diffuser plate. *Microw. Opt. Technol. Lett.* **55,** 138–141 (2013).
66. Shin, S. C. *et al.* Removal of hot spot speckle on laser projection screen using both the running screen and the rotating diffuser. *Displays* **27,** 91–96 (2006).
67. Sueda, K, Tsubakimoto, K, Miyanaga, N & others. Speckle suppression of laser light using liquid crystals aligned by photoisomerization of dye molecules. *J. Phys. D Appl. Phys.* (2002).

68. Heilmeier, G. H., Zanoni, L. A. & Barton, L. A. Dynamic scattering: A new electrooptic effect in certain classes of nematic liquid crystals. *Proc. IEEE* **56,** 1162–1171 (1968).
69. Chang, K.-H. *et al.* 54-1: Laser speckle reduction using nanoparticle-embedded liquid crystals. en. *Dig. Tech. Papers* **48,** 804–807 (2017).
70. Lin, J.-H. *et al.* Investigation of laser speckle noise suppression by using polymer-stabilized liquid crystals within twisted nematic cell. en. *Appl. Phys. Express* **10,** 031701 (2017).
71. Ishikawa, H., Shibase, A., Weng, W., Ono, M. & Furue, H. Reduction of laser speckle noise by using particle-dispersed liquid crystals. *Mol. Cryst. Liq. Cryst.* **646,** 93–98 (2017).
72. Lim, H. S. & Margerum, J. D. Improved dc dynamic scattering with redox dopants in ester liquid crystals. *Appl. Phys. Lett.* **28,** 478–480 (1976).
73. Haellstig, E., Stigwall, J., Lindgren, M. & Sjoqvist, L. *Laser beam steering and tracking using a liquid crystal spatial light modulator* en. in *Laser Systems Technology* **5087** (SPIE, 2003), 13–23.
74. Jesacher, A. & Booth, M. J. Parallel direct laser writing in three dimensions with spatially dependent aberration correction. en. *Opt. Express* **18,** 21090–21099 (2010).
75. Lee, Y.-H. *et al.* Two-photon polymerization enabled multi-layer liquid crystal phase modulator. en. *Sci. Rep.* **7,** 16260 (2017).
76. He, Z., Tan, G., Chanda, D. & Wu, S.-T. Novel liquid crystal photonic devices enabled by two-photon polymerization [Invited]. en. *Opt. Express* **27,** 11472–11491 (2019).
77. He, Z. *et al.* Polarization-independent phase modulators enabled by two-photon polymerization. en. *Opt. Express* **25,** 33688 (2017).
78. Varanytsia, A. & Chien, L.-C. Giant Flexoelectro-optic Effect with Liquid Crystal Dimer CB7CB. en. *Sci. Rep.* **7,** 41333 (2017).

79. *LC CELLS LC SYSTEM ACCESSORIES Instec Inc* https://instec.com/portal/article/index/id/93/cid/66.html. Accessed: 2023-7-13.

80. Hiltrop, K, Hasse, J & Stegemeyer, H. On the alignment of thermotropic nematic and smectic liquid crystals on lecithin coated surfaces. en. *Ber. Bunsenges. Phys. Chem.* **98,** 209–213 (1994).

81. Mettler-Toledo International Inc. all rights reserved. *AB104-S Analytical Balance* https://www.mt.com/gb/en/home/phased_out_products/Laboratory_Weighing_Solutions/Analytical/AB-S/AB104-S.html. Accessed: 2023-7-13. 2020.

82. *050-3664-XX and 050-3665-XX AFG3021 and AFG3022* en. https://www.tek.com/en/afg3021-manual/050-3664-xx-and-050-3665-xx-afg3021-and-afg3022. Accessed: 2023-7-13.

83. *F10AD* en. https://pendulum-instruments.com/products/dual-channel-high-voltage-linear-amplifiers/f10ad/. Accessed: 2023-7-13. 2022.

84. *Agilent Cary 8454 UV-Visible Spectroscopy System Operator's Manual* https://www.agilent.com/cs/library/usermanuals/public/G1115-90002_OperatorManual_online.pdf.

85. Li, J. *Refractive Indices Of Liquid Crystals And Their Applications In Display And Photonic Devices* PhD thesis (University of Central Florida, 2005).

86. *JDS Uniphase Helium-Neon Laser Heads 1100 Series* https://www.utwente.nl/en/tnw/slt/documentation/Equipment/Lasers/helium_neonlaserheads_1100s.pdf.

87. *UPLFLN/PLFLN* en. https://www.olympus-lifescience.com/en/objectives/uplfln/. Accessed: 2023-7-13.

88. Pokorny, J & Smith, V. C. in *Colour Vision Deficiencies XIII: Proceedings of the thirteenth Symposium of the International Research Group on Colour*

Vision Deficiencies, held in Pau, France July 27–30, 1995 (ed Cavonius, C. R.) 491–511 (Springer Netherlands, Dordrecht, 1997).

89. *Digital Cinema Initiatives (DCI) - DIGITAL CINEMA SYSTEM SPECIFICATION* en. https://www.dcimovies.com/Recommended_Practice/. Accessed: 2023-7-13.
90. Smith, W. J. *Modern Optical Engineering. New York, 1966* (McGraw-Hill International Book Co, New York, 1966).
91. Goodman, J. W. Probability density function of the sum of N partially correlated speckle patterns. *Opt. Commun.* **13,** 244–247 (1975).
92. Goodman, J. W. Dependence of image speckle contrast on surface roughness. *Opt. Commun.* **14,** 324–327 (1975).
93. Goodman, J. W. Some fundamental properties of speckle. *J. Opt. Soc. Am.* **66,** 1145 (1976).
94. Goodman, J. W. in *Laser Speckle and Related Phenomena* 9–75 (1975).
95. Yu, N. E. *et al.* Speckle noise reduction on a laser projection display via a broadband green light source. *Optics Express, Vol. 22, Issue 3, pp. 3547-3556* **22,** 3547–3556 (2014).
96. Furukawa, A. *et al.* Effective speckle reduction in laser projection displays. *https://doi.org/10.1117/12.760860* **6911,** 183–189 (2008).
97. Zhang, H., Wiklund, K., Andersson, M., Stangner, T. & Dahlberg, T. Step-by-step guide to reduce spatial coherence of laser light using a rotating ground glass diffuser. *Applied Optics, Vol. 56, Issue 19, pp. 5427-5435* **56,** 5427–5435 (2017).
98. Chen, C. Y. *et al.* Reduction of speckles and distortion in projection system by using a rotating diffuser. *Optical Review 2012 19:6* **19,** 440–443 (2012).
99. Deng, L. *et al.* Speckle reduction in laser projection based on a rotating ball lens. *Opt. Laser Technol.* **135,** 106686 (2021).

100. Hansford, D. J., Jin, Y., Elston, S. J. & Morris, S. M. Enhancing laser speckle reduction by decreasing the pitch of a chiral nematic liquid crystal diffuser. *Scientific Reports* **11,** 4818. (2021).

101. Tong, Z. *et al.* Electroactive despeckle diffuser using polymer dispersed liquid crystal in-plane switched by interdigitated electrodes. *Opt. Laser Technol.* **145,** 107541 (2022).

102. Andreev, A. A. *et al.* Speckle-noise suppression due to a single ferroelectric liquid-crystal cell. *J. Soc. Inf. Disp.* **17,** 801–807 (2009).

103. Furue, H., Sugimoto, Y., Iwami, K., Weng, W. & Ono, M. Control of Laser Speckle Noise by Using Polymer-Dispersed LC. *Mol. Cryst. Liq. Cryst.* **612,** 245–250 (2015).

104. Furue, H., Terashima, A., Shirao, M., Koizumi, Y. & Ono, M. Control of Laser Speckle Noise Using Liquid Crystals. *Jpn. J. Appl. Phys.* **50,** 09NE14 (2011).

105. Gao, W. *et al. The matrices used to reduce speckle in laser projector system* in *Optical Metrology* (eds Albertazzi Goncalves Jr, A. & Kaufmann, G. H.) **7387** (2010), 73871R.

106. Huang, Y., Jin, M. & Zhang, S. Polarization-independent bandwidth-variable tunable optical filter based on cholesteric liquid crystals. en. *Jpn. J. Appl. Phys.* **53,** 072601 (2014).

107. Lorenz, A *et al.* Electrical addressing of polymer stabilized hyper-twisted chiral nematic liquid crystals with interdigitated electrodes: Experiment and model. *Appl. Phys. Lett.* **104** (2014).

108. Rondelez, F, Arnould, H & Gerritsma, C. J. Electrohydrodynamic Effects in Cholesteric Liquid Crystals under ac Electric Fields. *Phys. Rev. Lett.* **28,** 735–737 (1972).

109. Gosse, B & Gosse, J. P. Degradation of liquid crystal devices under d.c. excitation and their electrochemistry. *J. Appl. Electrochem.* **6,** 515–519 (1976).

110. Torrance, J. B., Scott, B. A. & Kaufman, F. B. Optical properties of charge transfer salts of tetracyanoquinodimethane (TCNQ). *Solid State Commun.* **17,** 1369–1373 (1975).

111. Sakamoto, M *et al.* Enhanced electrical conductivity of polydiacetylene crystals by chemical doping and ion implantation. *J. Appl. Phys.* **60,** 2788–2796 (1986).

112. *Speckle Metrology* en. https://www.lipainfo.org/laser-illumination-sources/speckle-metrology/. Accessed: 2023-7-13. 2018.

113. Cohen, T. A. *et al.* Modular Zwitterion-Functionalized Poly(isopropyl methacrylate) Polymers for Hosting Luminescent Lead Halide Perovskite Nanocrystals. *Chem. Mater.* **33,** 3779–3790 (2021).

114. Wang, D. Y. *et al.* Self-targeting of zwitterion-based platforms for nano-antimicrobials and nanocarriers. *J. Mater. Chem. B Mater. Biol. Med.* **10,** 2316–2322 (2022).

115. Zhang, Y. *et al.* Electroconvection in zwitterion-doped nematic liquid crystals and application as smart windows. en. *Adv. Opt. Mater.* **9,** 2001465 (2021).

116. Kress, B. & Hejmadi, V. *Speckle reduction technique for laser based automotive Head Up Display (HUD) projectors* in *Proc. SPIE 8026, Photonic Applications for Aerospace, Transportation, and Harsh Environment II* (eds Kazemi, A. A., Kress, B., Chan, E. Y., Riza, N. A. & Kempen, L. U.) **8026** (SPIE, 2011), 80260P.

117. Gabor, D. A new microscopic principle. en. *Nature* **161,** 777 (1948).

118. Golan, L. *et al.* Speckle elimination using shift-averaging in high-rate holographic projection. *Optics Express, Vol. 17, Issue 3, pp. 1330-1339* **17,** 1330–1339 (2009).

119. Chen, H.-A., Pan, J.-W. & Yang, Z.-P. Speckle reduction using deformable mirrors with diffusers in a laser pico-projector. *Opt. Express* **25,** 18140 (2017).

120. He, C. *et al.* Revealing complex optical phenomena through vectorial metrics. *Advanced Photonics* **4,** 026001 (2022).

121. Goldstein, D. H. & Chipman, R. A. Error analysis of a Mueller matrix polarimeter. *JOSA A, Vol. 7, Issue 4, pp. 693-700* **7,** 693–700 (1990).

122. Goldstein, D. H. Mueller matrix dual-rotating retarder polarimeter. *Applied Optics, Vol. 31, Issue 31, pp. 6676-6683* **31,** 6676–6683 (1992).

123. Azzam, R. M. A. Photopolarimetric measurement of the Mueller matrix by Fourier analysis of a single detected signal. *Opt. Lett.* **2,** 148–150 (1978).

124. He, C. *et al.* Polarisation optics for biomedical and clinical applications: a review. *Light: Science & Applications 2021 10:1* **10,** 1–20 (2021).

125. He, H. *et al.* Mueller Matrix Polarimetry—An Emerging New Tool for Characterizing the Microstructural Feature of Complex Biological Specimen. *Journal of Lightwave Technology, Vol. 37, Issue 11, pp. 2534-2548* **37,** 2534–2548 (2019).

126. Chipman, R. A. & Lu, S.-Y. Interpretation of Mueller matrices based on polar decomposition. *JOSA A, Vol. 13, Issue 5, pp. 1106-1113* **13,** 1106–1113 (1996).

127. He, C., Shen, Y. & Forbes, A. Towards higher-dimensional structured light. en. *Light Sci. Appl.* **11,** 205 (2022).

128. Chipman, R. A. Depolarization index and the average degree of polarization. *Appl. Opt.* **44,** 2490–2495 (2005).

129. Asrani, S. K., Devarbhavi, H., Eaton, J. & Kamath, P. S. Burden of liver diseases in the world. *J. Hepatol.* **70,** 151–171 (2019).

130. Guicciardi, M. E., Malhi, H., Mott, J. L. & Gores, G. J. Apoptosis and Necrosis in the Liver. *Compr. Physiol.* **3,** 977–1010 (2013).

131. Liu, T. *et al.* Comparative study of the imaging contrasts of Mueller matrix derived parameters between transmission and backscattering

polarimetry. *Biomedical Optics Express, Vol. 9, Issue 9, pp. 4413-4428* **9,** 4413–4428 (2018).

132. Sun, M. *et al.* Characterizing the microstructures of biological tissues using Mueller matrix and transformed polarization parameters. *Biomedical Optics Express, Vol. 5, Issue 12, pp. 4223-4234* **5,** 4223–4234 (2014).
133. Vilas-Boas, V. *et al.* Primary hepatocytes and their cultures for the testing of drug-induced liver injury. *Adv. Pharmacol.* **85,** 1–30 (2019).
134. Guan, M. *et al.* Polarization modulation with optical lock-in detection reveals universal fluorescence anisotropy of subcellular structures in live cells. en. *Light Sci Appl* **11,** 4 (2022).
135. Zhanghao, K. *et al.* Super-resolution imaging of fluorescent dipoles via polarized structured illumination microscopy. en. *Nat. Commun.* **10,** 4694 (2019).
136. Mias, S & Camon, H. A review of active optical devices: II. Phase modulation. en. *J. Micromech. Microeng.* **18,** 083002 (2008).
137. Grier, D. G. A revolution in optical manipulation. *Nature* **424,** 810–816 (2003).
138. Maurer, C, Jesacher, A, Bernet, S & Ritsch-Marte, M. What spatial light modulators can do for optical microscopy. en. *Laser Photon. Rev.* **5,** 81–101 (2011).
139. Eriksen, R., Daria, V. & Gluckstad, J. Fully dynamic multiple-beam optical tweezers. en. *Opt. Express* **10,** 597–602 (2002).
140. McKnight, D. J., Johnson, K. M. & Serati, R. A. 256×256 liquid-crystal-on-silicon spatial light modulator. en. *Appl. Opt.* **33,** 2775–2784 (1994).
141. Davis, J. A., McNamara, D. E., Cottrell, D. M. & Sonehara, T. Two-dimensional polarization encoding with a phase-only liquid-crystal spatial light modulator. en. *Appl. Opt.* **39,** 1549–1554 (2000).

142. Chattrapiban, N., Rogers, E. A., Cofield, D., Hill 3rd, W. T. & Roy, R. Generation of nondiffracting Bessel beams by use of a spatial light modulator. en. *Opt. Lett.* **28,** 2183–2185 (2003).

143. Broomfield, S. E., Neil, M. A. A., Paige, E. G. S. & Yang, G. G. Programmable binary phase-only optical device based on ferroelectric liquid crystal SLM. en. *Electron. Lett.* **1,** 26–28 (1992).

144. Vicari, L. *Optical Applications of Liquid Crystals* en, 41–57 (CRC Press, Boca Raton, Florida, USA, 2016).

145. Kotova, S. P., Mayorova, A. M., Pozhidaev, E. P. & Samagin, S. A. Simulation of spatial phase light modulators based on the ferroelectric liquid-crystals. en. *J. Phys. Conf. Ser.* **1096,** 012017 (2018).

146. Feng, Z. & Ishikawa, K. Phase modulator mode based on the pre-transitional effect of antiferroelectric liquid crystals. en. *Opt. Lett.* **43,** 251–254 (2018).

147. Efron, U, Wu, S. T. & Bates, T. D. Nematic liquid crystals for spatial light modulators: recent studies. *J. Opt. Soc. Am. B* **3,** 247 (1986).

148. Albero, J., García-Martínez, P., Luis Martínez, J. & Moreno, I. Second order diffractive optical elements in a spatial light modulator with large phase dynamic range. *Opt. Lasers Eng.* **51,** 111–115 (2013).

149. Huang, Y., He, Z. & Wu, S.-T. Fast-response liquid crystal phase modulators for augmented reality displays. *Opt. Express* **25,** 32757 (2017).

150. Fells, J. A. J. *et al.* Flexoelectro-optic liquid crystal analog phase-only modulator with a 2π range and 1 kHz switching. en. *Opt. Lett.* **43,** 4362–4365 (2018).

151. Wu, S.-T. & Wu, C.-S. High-speed liquid-crystal modulators using transient nematic effect. en. *J. Appl. Phys.* **65,** 527–532 (1989).

152. Chen, R. *et al.* High-frame-rate liquid crystal phase modulator for augmented reality displays. *Liq. Cryst.* **46,** 309–315 (2019).

153. Love, G. D., Kirby, A. K. & Ramsey, R. A. Sub-millisecond, high stroke phase modulation using polymer network liquid crystals. en. *Opt. Express* **18,** 7384–7389 (2010).

154. Bos, P. J. & Koehler/beran, K. R. The pi-Cell: A Fast Liquid-Crystal Optical-Switching Device. *Mol. Cryst. Liq. Cryst.* **113,** 329–339 (1984).

155. Ye, W. *et al.* Accurate measurement of the twist elastic constant of liquid crystal by using capacitance method. *Liq. Cryst.* **46,** 349–355 (2019).

156. Chao, P. C.-P., Kao, Y.-Y. & Hsu, C.-J. A new negative liquid crystal lens with multiple ring electrodes in unequal widths. *IEEE Photonics J.* **4,** 250–266 (2012).

157. Outram, B. I. & Elston, S. J. Frequency-dependent dielectric contribution of flexoelectricity allowing control of state switching in helicoidal liquid crystals. en. *Phys. Rev. E Stat. Nonlin. Soft Matter Phys.* **88,** 012506 (2013).

158. Yeh, P. & Gu, C. *Optics of Liquid Crystal Displays* en, 173–277 (John Wiley & Sons, 2009).

159. Caldwell, C. S., Hall, J. R. & Babb, A. L. Mach-Zehnder Interferometer for Diffusion Measurements in Volatile Liquid Systems. *Rev. Sci. Instrum.* (1957).

160. Walton, H. G. & Towler, M. J. On the response speed of pi-cells. *Liq. Cryst.* **27,** 1329–1335 (2000).

161. Sun, C. Multiplexing of fiber-optic acoustic sensors in a Michelson interferometer configuration. en. *Opt. Lett.* **28,** 1001–1003 (2003).

162. Bacchiocchi, C. *et al.* EPR study of the polydomain structure of the twist-bend nematic phase of CB9CB in the bulk. *Liq. Cryst.* **45,** 2109–2120 (2018).

163. Panov, V. P. *et al.* Microsecond linear optical response in the unusual nematic phase of achiral bimesogens. *Appl. Phys. Lett.* **99** (2011).

164. Castles, F, Green, S. C., Gardiner, D. J., Morris, S. M. & Coles, H. J. Flexoelectric coefficient measurements in the nematic liquid crystal phase of 5CB. en. *AIP Adv.* **2,** 022137 (2012).

165. Corbett, D. R. & Elston, S. J. Modeling the helical flexoelectro-optic effect. *PHYSICAL REVIEW E* **84,** 41706 (2011).

166. Peng, F., Lee, Y.-H., Luo, Z. & Wu, S.-T. Low voltage blue phase liquid crystal for spatial light modulators. en. *Opt. Lett.* **40,** 5097–5100 (2015).

167. Beck, R. J. *et al.* Application of cooled spatial light modulator for high power nanosecond laser micromachining. *Opt. Express* **18,** 17059–17065 (2010).

168. Ahderom, S, Raisi, M, Lo, K, Alameh, K. E. & Mavaddat, R. *Applications of liquid crystal spatial light modulators in optical communications* in *5th IEEE International Conference on High Speed Networks and Multimedia Communication (Cat. No.02EX612)* (2002), 239–242.

169. Kubby, J., Gigan, S. & Cui, M. *Wavefront Shaping for Biomedical Imaging* (eds Kubby, J., Gigan, S. & Cui, M.) 1–21 (Cambridge University Press, 2019).

170. Matsuda, N., Fix, A. & Lanman, D. Focal surface displays. *ACM Trans. Graph.* **36,** 86:1–86:14 (2017).

171. Maimone, A., Georgiou, A. & Kollin, J. S. Holographic near-eye displays for virtual and augmented reality. *ACM Trans. Graph.* **36,** 85:1–85:16 (2017).

172. Li, Y.-W. *et al.* 18.5L:Late-news paper: Front-lit LCOS for wearable applications. en. *Dig. Tech. Papers* **45,** 234–236 (2014).

173. Zhang, H., Zhang, Z., Lv, J., Peng, C. & Hu, W. Fast beam steering enabled by a chip-scale optical phased array with 8 $\times$ 8 elements. *Opt. Commun.* **461,** 125267 (2020).

174. Gozzard, D. R., Roberts, L. E., Spollard, J. T., Sibley, P. G. & Shaddock, D. A. Fast beam steering with an optical phased array. *Opt. Lett.* **45,** 3793 (2020).

175. Gao, X. *et al.* 2D optically controlled radio frequency orbital angular momentum beam steering system based on a dual-parallel Mach–Zehnder modulator. *Opt. Lett.* **44,** 255 (2019).

176. Turtaev, S. *et al.* Comparison of nematic liquid-crystal and DMD based spatial light modulation in complex photonics. *Opt. Express* **25,** 29874 (2017).

177. Drabik, T. J. *et al.* 2D silicon/ferroelectric liquid crystal spatial light modulators. *IEEE Micro* **15,** 67–76 (1995).

178. Wang, X. *et al.* Fast and low loss flexoelectro-optic liquid crystal phase modulator with a chiral nematic reflector. *Scientific Reports 2019 9:1* **9,** 1–8 (2019).

179. Kurokawa, T & Fukushima, S. Spatial light modulators using ferroelectric liquid crystal. *Opt. Quantum Electron.* **24,** 1151–1163 (1992).

180. Henderson, C. J., Leyva, D. G. & Wilkinson, T. D. Free space adaptive optical interconnect at 1.25 Gb/s, with beam steering using a ferroelectric liquid-crystal SLM. *J. Lightwave Technol.* **24,** 1989–1997 (2006).

181. Pivnenko, M., Li, K. & Chu, D. Sub-millisecond switching of multi-level liquid crystal on silicon spatial light modulators for increased information bandwidth. en. *Opt. Express* **29,** 24614–24628 (2021).

182. Luo, Z. *et al.* Fast-response liquid crystals for high image quality wearable displays. *Opt. Mater. Express* **5,** 603 (2015).

183. Hyman, R. M., Lorenz, A., Morris, S. M. & Wilkinson, T. D. Polarization-independent phase modulation using a blue-phase liquid crystal over silicon device. *Appl. Opt.* **53,** 6925 (2014).

184. Zhang, Z., Lu, G. & Yu, F. T. S. Simple method for measuring phase modulation in liquid crystal televisions. *Opt. Eng.* **33,** 3018 (1994).

185. Zhang, H., Zhang, J. & Wu, L. Evaluation of phase-only liquid crystal spatial light modulator for phase modulation performance using a Twyman–Green interferometer. *Measurement Science and Technology* **18,** 1724 (2007).

186. Gupta, A. K. & Nishchal, N. K. *Phase characterization of a liquid crystal spatial light modulator* in *2018 3rd International Conference on Microwave and Photonics (ICMAP)* (IEEE, 2018), 1–2.

187. Fells, J. A. J. *et al.* Dynamic phase measurement of fast liquid crystal phase modulators. *Opt. Express* **30,** 24788 (2022).

188. Zhang, Z., You, Z. & Chu, D. Fundamentals of phase-only liquid crystal on silicon (LCOS) devices. *Light: Science & Applications* **3,** e213–e213 (2014).

189. Huang, Y., Bos, P. J., Kim, K. H., Jang, J. K. & Kim, H. S. Factors affecting the dynamics of a π-cell (Invited Paper). *J. Soc. Inf. Disp.* **16,** 939 (2008).

190. Wang, Y., Zhou, X., Ye, W. & Zhang, Z. New surface order reconstruction induced by electric field application in a nanoconfined HAN cell with a topological defect. *AIP Adv.* **5,** 107127 (2015).

191. Aizen, A., Ney, M., Safrani, A. & Abdulhalim, I. A compact real-time high-speed high-resolution vibrometer, surface profiler and dynamic focus tracker using three wavelengths parallel phase-shift interferometry. *Opt. Lasers Eng.* **107,** 304–314 (2018).

192. Nazarov, A., Ney, M. & Abdulhalim, I. Compact and fast sub-nm scale displacement probe using a phase mask and parallel phase-shift interferometry. *J. Phys. D Appl. Phys.* **51,** 335102 (2018).

193. Safrani, A. & Abdulhalim, I. Real-time phase shift interference microscopy. *Opt. Lett.* **39,** 5220 (2014).

194. Kamal, W. *et al.* Spatially Patterned Polymer Dispersed Liquid Crystals for Image-Integrated Smart Windows. *Advanced Optical Materials,* 2101748 (2021).

195. Li, J., Baird, G., Lin, Y.-H., Ren, H. & Wu, S.-T. Refractive-index matching between liquid crystals and photopolymers. en. *J. Soc. Inf. Disp.* **13,** 1017 (2005).

196. Lin, F.-C., Wu, P.-C., Jian, B.-R. & Lee, W. Dopant Effect and Cell-Configuration-Dependent Dielectric Properties of Nematic Liquid Crystals. en. *Advances in Condensed Matter Physics* **2013** (2013).

197. Allen, M. P. & Frenkel, D. Calculation of liquid-crystal Frank constants by computer simulation. *Phys. Rev. A* **37,** 1813 (1988).

198. Parodi, O. Stress tensor for a nematic liquid crystal. *Journal de Physique* **31,** 581–584 (1970).

199. Blanc, C, Svenšek, D, Žumer, S & Nobili, M. Dynamics of Nematic Liquid Crystal Disclinations: The Role of the Backflow. *Phys. Rev. Lett.* **95,** 097802 (2005).

200. Berreman, D. W. Liquid-crystal twist cell dynamics with backflow. *J. Appl. Phys.* **46,** 3746–3751 (1975).

201. Brimicombe, P. *Fast-switching nematic liquid crystal devices* en. PhD thesis (University of Oxford, 2006).

202. Vertogen, G. & de Jeu, W. H. *Thermotropic Liquid Crystals, Fundamentals* eng (Springer Berlin Heidelberg, Berlin, Heidelberg, 1988).

203. Kischka, C. *Flexoelectricity in nematic liquid crystals* eng. PhD thesis (University of Oxford, 2011).

204. Wang, H., Wu, T. X., Gauza, S., Wu, J. R. & Wu, S.-T. A method to estimate the Leslie coefficients of liquid crystals based on MBBA data. *Liq. Cryst.* **33,** 91–98 (2006).

205. Fells, J. A. J. *et al.* Dynamic response of large tilt-angle flexoelectro-optic liquid crystal modulators. en. *Opt. Express* **27,** 15184–15193 (2019).

206. Stockley, J. E. *Chiral smectic liquid crystal beam deflector with large analog phase modulation* PhD thesis (1996).

207. Stockley, J. E., Sharp, G. D., Serati, S. A. & Johnson, K. M. Analog optical phase modulator based on chiral smectic and polymer cholesteric liquid crystals. en. *Opt. Lett.* **20,** 2441 (1995).

208. Wang, X. *et al.* A Compact Full 2π Flexoelectro-Optic Liquid Crystal Phase Modulator. *Advanced Materials Technologies* **5,** 2000589 (2020).

209. Outram, B. I. & Elston, S. J. Flexoelectric and dielectric in-plane switching behaviour of Grandjean liquid-crystal structures. *EPL* **99,** 37007 (2012).